Electrochemical and High Temperature Characterizations of Hafnium and Zirconium Diboride Solid Solutions with Different Additives

A Dissertation

Presented in Partial Fulfilment of the Requirements for the

Degree of Doctorate of Philosophy

with a

Major in Materials Science & Engineering

in the

College of Graduate Studies

University of Idaho

by

Steven J. Sitler

Major Professor: Krishnan S. Raja, Ph.D.

Committee Members: Indrajit Charit, Ph.D., Mark Roll, Ph.D., Thomas Williams, Ph.D.

Department Administrator: Eric Aston, Ph.D.

August 2017

Authorization to Submit Dissertation

This dissertation of Steven J. Sitler, submitted for the degree of Doctorate of Philosophy with a Major in Materials Science & Engineering and titled "**Electrochemical and High Temperature Characterizations of Hafnium and Zirconium Diboride Solid Solutions with Different Additives**," has been reviewed in final form. Permission, as indicated by the signatures and dates given below, is now granted to submit final copies to the College of Graduate Studies for approval.

Major Professor: _____ Date: _____
Krishnan Raja, Ph.D.

Committee Members: _____ Date: _____
Indrajit Charit, Ph.D.

_____ Date: _____
Mark Roll, Ph.D.

_____ Date: _____
Thomas Williams, Ph.D.

Department Administrator: _____ Date: _____
Eric Aston, Ph.D.

Abstract

HfB_2, ZrB_2, and their solid solution mixtures were studied, primarily for electrode coating applications in coal-fired magnetohydrodynamic (MHD) direct power extraction plants. MHD works by directly extract current from superheated plasma flame (2725 °C) seeded with potassium salts. Obviously, the electrodes near this flame are subject to extreme temperatures and corrosive environments. The coating material needs to protect the electrodes from salt corrosion, oxidation, and melting, while still providing electrical conductivity. Transition metal diborides have many of the desired properties but need improvement for oxidation resistance above 1200 °C. Two main methods of oxidation resistance improvements were investigated during this research. The first was through electrochemical anodization, a process where a thin protective oxide layer is grown on the surface to prevent further detrimental oxidation at high temperatures. Several solutions, voltages, and methods were used to find an oxide layer that would protect at high temperatures. The second method was to use various additives and mixture ratios to improve densification and oxidation resistance. Ratios of HfB_2 and ZrB_2 tested were 1:4, 1:1, 4:1 and 1:1 with additives of Ta, Hf, and Zr metals, bringing the boron to metal ratio down to 1.86. Additionally, 1.8 mol% Gd_2O_3 and LaB_6 were added the 1:1 ratio. Hydrogen evolution reaction kinetics were also investigated to shed some light on the ability of these materials to resist corrosion. Aqueous corrosion was also done in several solutions of different pH. The opinion of the author is that the 1:1 ratio sample with LaB_6 gave the best overall results both in high temperature and aqueous experiments. More work is needed to determine if this material is viable to use as an electrode coating and it would be important to do so. Coal power currently makes up almost 40% of global electricity production. This method of extracting energy from coal can be added to any coal plant, improving its energy output. Not only would this

prepare us to keep up with the ever-increasing energy demands but it could allow us to significantly cut the greenhouse gas emissions for the coal power industry.

Acknowledgements

I want to acknowledge my major professor, Krishnan Raja, for all the time, advice, and help has given me, and for the time and advice that my dissertation committee members, Dr. Charit and Dr. Roll, have given me along the way. I would especially like to thank Dr. Williams, who is also on my dissertation committee, for all his help using the electron microscopy lab. I also want to thank Charles Cornwall who made countless gadgets throughout the project. I would also like to thank the DOE under grant number DE-FE0022988 for funding my education and research. Thank you all.

I would also like to thank Dr. Dev Chidambaram and his student Zachary Karmiol at the University of Nevada, Reno for the experimental help. In addition, I would like to thank Robert Miner, Colin Lunstrum, and James Zillinger for their amazing help with sample preparations and general lab work.

DEDICATION

This dissertation is dedicated to my loving wife for her support and patience through all the long nights and busy days. I would also like to dedicate it to my son for giving me a sense of what it is to be full of wonder and life. Thank you for rubbing off on me a little.

Table of Contents

List of Figures

List of Tables

CHAPTER 1: Introduction

1.1 Background

The goal of this dissertation is to develop a deeper understanding of the materials hafnium diboride and zirconium diboride with respect to their usefulness as high-temperature electrode materials. The intended application is coal-fired magnetohydrodynamic direct power extraction from a plasma flame seeded with salts to improve conductivity. It seems to be widely believed that coal power is a dyeing source of energy but that is simply not true. Since 1980, coal power has produced an average of 39% of the global electricity,[1] the largest source by far and that number has never varied more than a couple of percent. Global production of coal power has continued to increase and there is more coal power now than ever before.

Magnetohydrodynamic (MHD) direct power extraction is a method where power is extracted directly through electrodes from a coal plasma.[2] The plasma flame is usually seeded with potassium salts to increase the conductivity.[3] The plasma flame flows through a transverse magnetic field whereby the current is extracted by electrodes normal to the directions of both the magnetic field and the flame flow. The advantage of this system is that it can be added on to current coal-fired steam power plants allowing that steam plant to still operate at full capacity while generating extra energy with the MHD process. The conditions inside of the MHD current extraction chambers are very aggressive due to the high-temperature plasma (~3000 K), high mass flow rate, and corrosion due to the added potassium salts. Although cooled internally, it is still estimated that the exteriors of the electrodes will be exposed to temperatures in the range of 1700 K-2200 K.[3]

Because of the aggressive conditions inside the extraction chamber, these electrodes must possess several unique properties. They must be able to resist melting, resist high-temperature corrosion, resist high-temperature oxidation, and conduct electricity relatively well.

1.2 Materials

1.2.1 Diborides

ZrB_2 or zirconium diboride and HfB_2 or hafnium diboride are transition metal (TM) diborides and are considered ultra-high temperature ceramics (UHTC) because of their (> 3200 °C) and their oxide counterparts' high melting temperatures (2700 - 2800 °C).[4] In addition to their high melting point, these two transition metal diborides also have good thermal and electrical conductivity, and

thermal shock resistance.[5-7] However, the main concern with these materials is their limited resistance to oxidation at temperatures above 1200 °C. For example, at 1500 °C, the oxidation rate is reported by Seong et al. [8] to be 125,442 $\mu m^2/h$ in air. Several methods can be found in literature for improving the oxidation resistance, however, most of the literature is applicable for hypersonic aerospace applications designed for improving the short-term oxidation resistance with no interest in conductivity.[9-12]

In order to improve the oxidation resistance, two methods were investigated: The addition of chemical dopants and pre-anodizing the materials which, in theory, creates a protective oxide layer. The dopants used are discussed in turn below.

1.2.2 Dopants

Chemical dopants were added to help with improving the high-temperature oxidation resistance of these materials. Some of the additives were chosen because they were reported to aid in densification during the sintering process others because they were supposed to help improve high-temperature oxidation regardless of density. Silicon Carbide (SiC) was initially added to diboride samples for both of these reasons. However, it was determined that SiC created the wrong kind of oxidation resistance, a liquid protective layer.

Corrosion expert Denny Jones writes "The key to corrosion resistance is a dense adherent surface film or scale that forms a protective barrier between the underlying metal and the corrosive environment. Cracked, porous or soluble films do not protect the metal and result in relatively high corrosion rates."[13] Because B_2O_3 begins melting at 450 °C, it is able to create just such a liquid protective layer against oxygen diffusion over the $(TM)B_2$. This protection is effective up to temperatures of around 1100 °C, where the high vapor pressure of B_2O_3 causes it to begin to evaporate as shown in Equation (1).[14,15]

$$B_2O_{3(l)} \rightarrow B_2O_{3(g)} \quad (1)$$

Once B_2O_3 (vapor pressure (VP) = 223 Pa at 1500 °C[16]) begins to evaporate, the protective layer becomes compromised. With continued elevation in temperature up to about 1400 °C, oxygen diffusion can stay quite limited. At temperatures higher than 1400 ^oC, there is a rapid degradation of the protective layer and a $(TM)O_2$ porous layer is left behind leading to detrimental material recession of the ceramic core. A true operating limit would be below 1100 °C, before the B_2O_3 begins to volatilize.

Therefore, without any additives, $(TM)B_2$ is quite limited in high-temperature applications. It has been found, however, that the addition of 10% to 30% SiC has a significant impact on the performance of $(TM)B_2$ due to SiC's reaction with oxygen at temperatures above 1100 °C as shown in Equation (2).[14]

$$SiC + {}^{3}/_{2}\, O_2 \rightarrow SiO_{2(l)} + CO_{(g)} \quad (2)$$

At temperatures higher than 1100 °C, the B_2O_3 layer mixes with liquid SiO_2 (VP = $3x10^{-4}$ Pa at 1500 °C[16]) to create a borosilicate layer. As in the case with no SiC additive, the B_2O_3 is evaporated off as the temperature is increased, but a liquid glassy layer of SiO_2 is left which continues to protect the $(TM)B_2$ from oxidation. This protection is expected to last to temperatures of just over 1500 °C.[10,17-20] Unfortunately, given the high flow rate of the plasma, and the fact that 1500 °C is at the very low end of the operating range, a liquid protection layer will not suffice because it will evaporate off over time leading to electrode coating failure. Therefore, the addition of SiC was abandoned and not reported in any of the manuscript chapters.

In addition to densification during the sintering process, oxidation resistance may be improved generally by adding chemical dopants through what is called the 3rd element effect or reaction element effect. [21] This occurs when additives are used which pin dislocations, this not only can improve the oxide adhesion but also reduce the "diffusivity of metals" to the sample surface. The individual chemical dopants used are discussed below.

1.2.2.1 Lanthanum Hexaboride (LaB_6)

In a report by Zhang et al,[22] the addition of LaB_6 to ZrB_2-SiC composites was reported to improve oxidation resistance for short term applications. They attributed this to the strength of the oxide adhesion. The addition of LaB_6 forms, in theory, a cubic pyrochlore lanthanum zirconate ($La_2TM_2O_7$) coating which resists further oxidation into the sample. This coating forms on the surface through the formation of an oxide layer as given in the following reactions:[23]

$$LaB_{6(s)} + \frac{21}{4}O_{2(g)} \rightarrow \frac{1}{2}La_2O_{3(s)} + 3B_2O_{3(l)} \quad (3)$$

$$La_2O_{3(s)} + (TM)O_{2(s)} \rightarrow La_2(TM)_2O_{7(s)} \quad (4)$$

The addition of La in the form of LaB_6 is also expected to improve the high-temperature oxidation resistance by impeding the outward diffusion of transition metals into the oxide layer by

segregated La^{3+} ions pinning the misfit edge dislocations.[21,24] In addition to the benefits of oxide adhesion dislocation pinning it was also believed that since LaB_6 is a well-known thermionic emitter, it may help improve the conductivity of the diborides as well as the ionization of the plasma flame.

1.2.2.2 Gadolinia (Gd_2O_3)

Gadolinium(III) oxide was chosen as a dopant as it was reported to increase the oxidation resistance of transition metal diborides up to 1600 °C.[10] The most intriguing part of this study was their desire to stay away from a liquid oxidation protection and move toward a solid Rare Earth protective oxide layer. The additions of Gd in the form of Gd_2O_3 was also expected to improve the high-temperature oxidation resistance by impeding the outward diffusion of transition metals into the oxide layer by segregated Gd^{3+} ions pinning the misfit edge dislocations.[21,24]

1.2.2.3 Tantalum

The addition of Ta helps improve the high-temperature oxidation resistance when present in the surface oxide as Ta^{5+} by decreasing the concentration of oxygen vacancies based on the following reaction given in standard Kroger-Vink notation:[12, 24]

$$Ta_2O_5 + V_O^{\bullet\bullet} \xrightarrow{2\,(TM)O_2} 2\,Ta_{(TM)}^{\bullet} + 5\,O_O \qquad (3)$$

where $V_{Ö}$ represents the oxygen vacancy with a +2 charge and TM represents the transition metal.

In another study, Talmy et al.[25] showed that the addition of TaB_2 may improve the oxidation resistance of ZrB_2-SiC composite mixtures. The improved oxidation resistance was, however, shown to only last up to 1500 ˚C. The authors believed that the improved oxidation resistance of ZrB_2-$20_{vol\%}$ SiC with TaB_2 additions was caused by the formation of an immiscible liquid Ta_2O_5 layer and the phase separation which followed in the borosilicate glassy oxide layer.

1.2.3 Metal-rich Diborides

In a study by Manlabs Inc.,[26] the effects of boron/metal ratios on the electrical and chemical properties of hafnium diboride and zirconium diboride were addressed. The effect of boron/metal ratios on oxidative properties and sinterability was also studied. Metal rich hafnium boride and zirconium boride were found to reach higher final densities during similar sintering studies. $HfB_{1.89}$ exhibited the highest oxidation resistance throughout the range of study. Electrical resistivity was seen to decrease when boron/metal ratios were less than two. At boron/metal ratios above two, electrical resistivity increased, sinterability decreased, and oxidation resistance decreased.

1.3 Experimental

1.3.1 Sample Identifiers

Throughout this dissertation, sample identifiers will be used to name samples with different dopants or diboride ratios. Table 1.1 gives an overview of those sample identifiers and the chemical composition associated with them.

Table 1.1: Sample identifiers used throughout the dissertation.

Sample Identifier	*Composition*
A	HfB_2
B	ZrB_2
AB	1:1 HfB_2 - ZrB_2
A4B	1:4 HfB_2 - ZrB_2
4AB	4:1 HfB_2 - ZrB_2
ABT	1:1 HfB_2 - ZrB_2 + Ta (B/Me = 1.86)
ABZ	1:1 HfB_2 - ZrB_2 + Zr (B/Me = 1.86)
ABH	1:1 HfB_2 - ZrB_2 + Hf (B/Me = 1.86)
ABL	1:1 HfB_2 - ZrB_2 + 1.8 mol % LaB_6
ABG	1:1 HfB_2 - ZrB_2 + 1.8 mol % Gd_2O_3

1.3.2 Ball Milling

A Spex Mixer/Mill 8000M was used for all of the ball milling. A specialized zirconia vial was used to prevent contamination of iron in the powders. With a 1:10 powder-to-ball weight ratio, each load held approximately 5 grams of powder and 50 grams of yttria-stabilized zirconia (YSZ) spherical grinding media of 6.5 mm diameter (Inframat Advanced Materials LLC, Manchester, CT). Each load was milled for 3 hours for all sample mixtures.

1.3.3 Glovebox

Working with pure zirconium and hafnium metals requires using a glove box with a controlled atmosphere. The zirconia vial used in the ball milling process was hermetically sealed after adding the grinding media and powder in a glovebox (M. Braun Inert Gas-Systeme GmbH) using a high-purity argon atmosphere.

1.3.4 Spark Plasma Sintering (SPS)

Traditional sintering was used initially but with unsatisfactory results as expected. All of the samples used in the following chapters were created by spark plasma sintering (SPS) using a Dr. Sinter SPS-515S machine (Fuji Electronic Industrial Co., Ltd., Japan) available at the Center for Advanced

Energy Studies (CAES) in Idaho Falls. SPS was used to produce two sets of samples. The first set was prepared using a 20.6 mm isocarb-85 graphite die with 5 kN of applied force. These samples were cut into smaller pieces and used in the manuscripts for Chapters 2, 3, 5, and 6. For the electrochemical testing, sample pieces were connected to wires with highly conductive silver epoxy and coated in a non-conductive acrylic mount exposing only one surface of the samples. The second set of SPSed samples was prepared using a 12.6 mm isocarb-85 graphite die with 5 kN of applied force. These samples were used in the manuscript for Chapter 4.

1.3.5 Polishing

Samples were polished in accordance with each chapter's experimental section using an Allied TwinPrep 3 polishing machine. Grinding discs were used sequentially down to 9 µm after which a Velcloth (Allied High-Tech Products, Inc.) was used with diamond suspensions of 1 µm and then either 0.5 or 0.3 µm.

1.3.6 Anodization

Anodization was used to create an oxide layer on the samples which would protect them from detrimental oxidation at high temperatures. A controlled DC power supply (Sorensen XPF 60–20 DC) was used to apply the required potential for anodization. Several potentials and solutions were used to determine the initial and final anodization parameters as defined in Chapter 2 and Chapter 4. These initial anodization tests were done on AB samples which were mounted in acrylic and electrically connected to wires using highly conductive silver epoxy. Once the optimum parameters had been determined from electrochemical testing and scanning electron microscopy, the samples were prepared without the acrylic. The samples prepared for high-temperature testing were again connected to wires with highly conductive solver epoxy and then anodized by submerging the samples as close as possible to the silver epoxy. Only about 60% to 80%, was able to be anodized depending on the exact sample shape and epoxy application. Prior to high-temperature testing, all silver epoxy was removed.

As mentioned in the introduction, transition metal diborides have good oxidation resistance up to about 1200 °C. This is due to the protection of a liquid boria layer mixed with a solid transition metal oxide layer. The melting point of pure B_2O_3 is low at 450 °C. Exposure of diborides to temperatures below 930 °C results in the formation of a continuous B_2O_3 liquid layer on the surface. Diffusion of oxygen is therefore hindered through this liquid layer. At higher temperatures in the

range of 930 - 1400 °C, B_2O_3 begins to volatilize, but the volatilization rate of B_2O_3 is comparatively low. Although evaporation of the B_2O_3 layer is occurring at lower temperatures at temperatures higher than 1425 °C, linear oxidation kinetics are reported due to an increased volatilization rate of B_2O_3, leaving a non-protective, porous $(TM)O_2$ layer.[27-29] This porous columnar layer leads to the diffusion of oxygen into the sample and the unhindered oxidation of the entire sample as any B_2O_3 that is formed immediately evaporates and does not protect.

The anodic oxide layer was designed to avoid this mixture of $(TM)O_2$/liquid boria, which at high temperatures leaves the only the unprotective porous $(TM)O_2$ layer. Therefore, the goal was to create a solid $(TM)O_2$ layer at temperatures below 450 °C where B_2O_3 becomes liquid. This goal was not however attained. Some significant oxidation resistance was gained, but it is believed that this benefit occurs through enrichment and depletion layers of either the boron or the transition metals caused by the anodization process more so than through an impervious $(TM)O_2$ layer created on the top surface.

1.3.7 High-temperature Oxidation

1.3.7.1 Tube Furnace

Two different types of high-temperature oxidation were employed during the testing involved in this dissertation. The first, more basic type was done with a Sentro Tech STT-1700C-1.5-6 tube furnace. It is relatively easy to control the atmosphere in a tube furnace and most of the testing was done using a high purity argon inert atmosphere. The benefit of using the tube furnace was its ability to reach 1700 °C.

1.3.7.2 Thermogravimetric Analysis (TGA)

The second type of high-temperature oxidation was done using Netzsch STA 409 PC Luxx furnace. Using the thermogravimetric analysis (TGA) setting, in situ weight change data was made available during the heating cycle and at the maximum temperature of the furnace. Unfortunately, the maximum temperature of the furnace was only 1500 °C. The tube furnace was used at higher temperatures, but at the expense of not being able to acquire real-time weight change data during the heating cycles.

1.3.8 Salts

In order to study the corrosion resistance of the various mixtures of the diborides, two different salts were used. Prior to high-temperature corrosion testing either KCl and K_2SO_4, having

been mixed into a solution, were applied to the top surface of the samples using a micropipette. The liquid was allowed to dry and the process was repeated until the surface was covered with a thin layer of salt at a loading of ~ 2.5 mg/cm^2.

1.4 Characterization

1.4.1 Electrochemical Characterization

All electrochemical characterization techniques were done with a Gamry Interface 1000 unit using a two or three electrode setup as described in each Chapter's experimental section. When a three-electrode setup was used, Ag/AgCl immersed in saturated KCl was used as the reference electrode.

1.4.1.1 Electrochemical Impedance Spectroscopy (EIS)

1.4.1.1.1 EIS

Electrochemical Impedance Spectroscopy is a method of gaining information on the response of the sample with an imposed potential through a range of frequencies. There are two main ways of reporting EIS data: Bode plots and Nyquist plots. Bode plots show frequency vs. the impedance modulus which is the square root of the squared imaginary portion added together with the squared real portion of the sample's response or resistance. The Nyquist plots show the imaginary resistance vs. the real resistance of the sample. In addition to these two methods of presenting the EIS data, equivalent circuit modeling can also be used to elucidate information on the system response.

1.4.1.1.2 Equivalent circuit modeling (ECM)

ECM can be very useful for understanding why a system responds the way it does. The term system is used here because EIS is done in solution and the solution resistance also plays a role in the response, not just the sample. By modeling the system as a combination of idealized capacitors, resistors, inductors, etc., ECM is not only capable of showing which portion of the response can be attributed to the solution resistance but also can give detailed information about layers and interfaces on the sample and how they change with either temperature or time.

1.4.1.2 Potentiostatic polarization (PS)

Potentiostatic electrochemistry is used to measure the current or current density of a sample at an applied voltage. By displaying the information in a time vs current density, steady state or quasi-

steady state current densities can be determined. The slopes of current decay can also be determined by plotting the PS data in the log-log scale, which is helpful for understanding the corrosion kinetics.

1.4.1.3 Potentiodynamic polarization (PD)

Potentiodynamic polarization is used to measure the current or current density of a sample while scanning a potential range. It is plotted as potential vs. log(current). Most often it is used for understanding corrosion details of a sample such as pitting potential, breakaway potential, passivation potential, and corrosion rate. In addition, Figure 1.1 shows an ideal data set and schematics on obtaining some of the other types of data from PD polarization such as exchange current densities, overpotentials, and Tafel slopes. For further reading see "Principles and Preventions of Corrosion" by Denny Jones.[13]

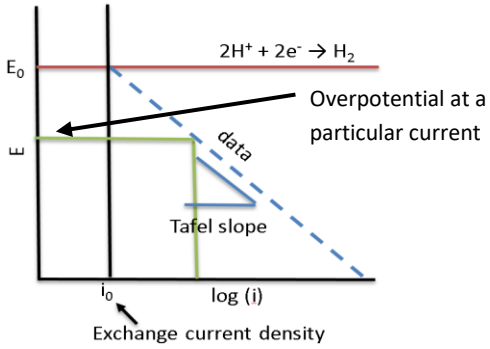

Figure 1.1: Diagram of potentiodynamic polarization on how to determine data values.

1.4.1.4 Cyclic voltammetry (CV)

Although cyclic voltammetry has many uses, for this dissertation it was only used in Chapters 5 and 6 to activate the samples. Oftentimes, in electrochemistry, a material will not behave as expected until it has gone through several charge/discharge cycles. It was to avoid these "transient" responses that the samples were activated with cyclic voltammetry.

1.4.1.5 Electrical conductivity/resistivity

The electrical resistivity of several of the samples was measured at temperatures ranging from up to 1000 °C to up to 1500 °C. This measurement was accomplished by using specialized clamps designed to maintain electrode contacts at high temperatures. The two clamps are shown in Figure 1.2 (a) and (b). The first one was made of Kanthal and was able to withstand temperatures up to around 1100 °C. The second clamp was made from a Zircalloy-4 alloy and could withstand

temperatures up to about 1500 °C. Polarization resistance tests were run at 100 °C increments along with EIS as described in Chapter 4.

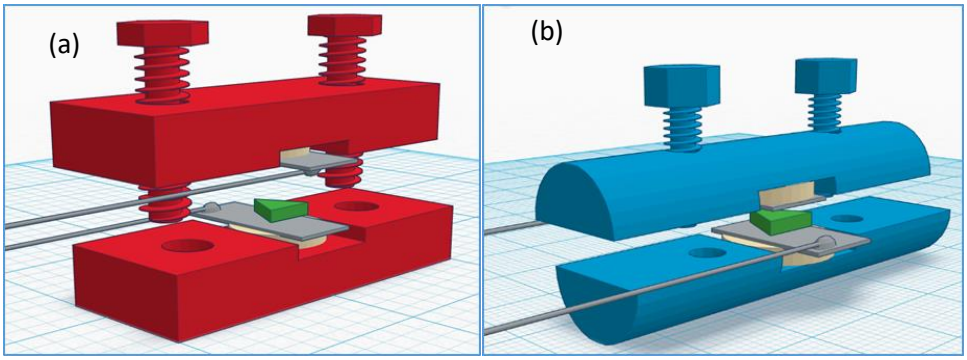

Figure 1.2: Specialized clamps used for maintaining electrode contact during high temperature polarization resistance and EIS testing for conductivity measurements.

1.4.2 Field Emission Scanning Electron Microscopy (FESEM)

Field Emission Scanning Electron Microscopy is a method of imaging the surface of a sample using a thermionic emitter and an electron detector. A LEO Supra 35VP (Zeiss, Jena, Germany) was used for all FESEM imaging done in this dissertation. Depending on the applied voltage the FESEM or SEM image may change as it is displaying information from deeper into the sample with higher voltages.

1.4.3 Energy-dispersive X-ray Spectroscopy (EDS)

EDS is an attachment to the FESEM which allows the user to quantify within limitations the chemical composition of the sample surface. Caution with this technique must be exercised as many of the low atomic number elements such as boron, oxygen, and carbon are not well detected. EDS was used in this dissertation to analyze and compare the chemical composition of the samples and oxide layers. All spectra were obtained using an accelerating voltage of 20 kV. A higher accelerating voltage is required for EDS as it is detecting the signature emission of X-rays for a particular element. Based on the total number of counts the software can determine the % of that element on the surface of the samples.

1.4.4 X-Ray Diffraction (XRD)

X-Ray Diffraction as used to understand the crystallographic structures present on the surface layer of the samples and compare them both with other samples and with the same sample under different conditions. Longer scans were typically used to reduce the noise. All spectra were

obtained using a D5000 Diffractometer (Siemens AG, Munich, Germany) typically at a scan rate of 0.02° with a hold time of 5 seconds.

1.4.5 Density Functional Theory (DFT)

Density Functional Theory (DFT) calculations of individual diborides and HfB_2-ZrB_2 solid solutions with additives were performed under the framework of DFT as implemented in the CASTEP module of Materials Studio™ software package. This modeling was used to estimate lattice parameters, understand band structure, and determine density of states (DOS) at the Fermi level to understand how chemical stability and catalytic activity interplay with different diborides and additives. The details of the specific calculations are given in the appropriate chapters.

1.5 Chapter Descriptions

1.5.1 Overview

Chapter 2 presents the results of the initial investigation into the oxidation resistance mitigation methods proposed in the introduction, namely: anodization and chemical dopants. The experiments presented in Chapters 3, 5, and 6 were designed in some fashion to aid in understanding and selecting the samples to be tested for high-temperature corrosion resistance and high-temperature electrical conductivity. Chapter 4 is considered the pinnacle of the work presented in this dissertation and describes the results of the high temperature corrosion and oxidation testing with respect to the two oxidation mitigation methods used: the addition chemical dopants and pre-anodization of the samples.

1.5.2 Chapter 2: Transition Metal Diborides as Electrode Material for MHD Direct Power Extraction: High-temperature Oxidation of ZrB_2-HfB_2 Solid Solution with LaB_6 Addition

The work in Chapter 2 is the compilation of the data that confirmed that both oxidation mitigation methods employed were worth pursuing more in-depth. The anodization process gave improved oxidation resistance as did the addition of LaB_6. ABL was the only dopant sample tested in this manuscript as it was anticipated that it would perform the best.

1.5.3 Chapter 3: Room Temperature Corrosion Behavior of ZrB_2-HfB_2 Solid Solutions in Acidic and Basic Aqueous Environments

The work in Chapter 3 was performed not only to understand the applicability of these boride materials as room temperature electrodes, but also because a correlation can be drawn between the

room temperature corrosion resistance and high temperature corrosion resistance. Therefore, this data was also used to determine which samples to test in the manuscript in Chapter 4. All 10 samples from Table 1.1 were tested and it was found that ABL tended to perform the better than the other sample in the various aqueous environments tested. This was one of the main reasons other samples were not chosen for testing in Chapter 4.

1.5.4 Chapter 4: Hot Corrosion Behavior of ZrB_2-HfB_2 Solid Solutions in KCl and K_2SO_4 at 1500 °C

Chapter 4 describes the ultimate findings with regards to oxidation resistance, corrosion resistance, and electrical resistivity of the three chosen diboride samples, AB, ABL and ABH, and their anodized counterparts.

1.5.5 Chapter 5: ZrB_2-HfB_2 Solid Solutions as Electrode Materials for Hydrogen Reaction in Acidic and Basic Solutions

The work in Chapter 5 correlates with the work in Chapter 6 but is more focused on ZrB_2:HfB_2 ratios rather than additives or dopants. Of the ratios tested, sample AB performed the best in this manuscript. This finding coupled with the corrosion resistance from chapter 3 are the reasons sample AB was chosen for further testing in Chapter 4. Additionally, although not a decisive factor, it was convenient to use sample AB as a control sample.

1.5.6 Chapter 6: Metal-rich Transition Metal Diborides as Electrocatalysts for Hydrogen Evolution Reactions in a Wide Range of pH

The work in Chapter 6 correlates with the work in Chapter 5 but is more focused on additives or dopants rather than ZrB_2:HfB_2 ratios. The performance of sample ABH in this manuscript when coupled with its corrosion resistance performance in Chapter 3 were the main reasons it was chosen for further testing in Chapter 4.

1.6 Bibliography

[1] [Online]. Available: http://www.tsp-data-portal.org/Breakdown-of-Electricity-Generation-by-Energy-Source.

[2] J. K. Wright, “The Science of M.H.D. Generators-A Critical Survey,” *Philos. Trans. R. Soc. Lond. Ser. Math. Phys. Sci.*, vol. 261, no. 1123, pp. 347–359, 1967.

[3] D. B. Meadowcroft, “Electronically-Conducting, Refractory Ceramic Electrodes for Open Cycle MHD Power Generation,” *Energy Convers*., vol. 8, no. 4, pp. 185–190, Dec. 1968.

[4] D. L. Poerschke, M. D. Novak, N. Abdul-Jabbar, S. Krämer, and C. G. Levi, “Selective Active Oxidation in Hafnium Boride-Silicon Carbide Composites above 2000 °C,” *J. Eur. Ceram. Soc.,* vol. 36, no. 15, pp. 3697–3707, Nov. 2016.

[5] G. V. Samsonov, B. A. Kovenskaya, and T. I. Serebryakova, “Some Physical Characteristics of the Diborides of Transition Metals of Groups IV and V,” *Sov. Phys. J.,* vol. 14, no. 1, pp. 11–14, Jan. 1971.

[6] R. P. Tye and E. V. Clougherty, “Thermal and Electrical Conductivities of Some Electrically Conducting Compounds.,” Pp 396-401 Proc. Fifth Symp. Thermophys. Prop. Bonilla C F Ed N. Y. *Am. Soc. Mech. Eng.* 1970, Jan. 1970.

[7] R. Telle, L. S. Sigl, and K. Takagi, “Boride-Based Hard Materials,” in Handbook of Ceramic Hard Materials, R. Riedel, Ed. *Wiley-VCH Verlag GmbH*, 2000, pp. 802–945.

[8] Y.-H. Seong and D. K. Kim, “Oxidation Behavior of $ZrB_{2-x}SiC$ Composites at 1500 °C under Different Oxygen Partial Pressures,” *Ceram. Int.,* vol. 40, no. 9, Part B, pp. 15303–15311, Nov. 2014.

[9] M. M. Opeka, I. G. Talmy, and J. A. Zaykoski, “Oxidation-Based Materials Selection for 2000°C + Hypersonic Aerosurfaces: Theoretical Considerations and Historical Experience,” J. *Mater. Sci.*, vol. 39, no. 19, pp. 5887–5904, Oct. 2004.

[10] D. D. Jayaseelan, E. Zapata-Solvas, P. Brown, W. E. Lee, and J. Halloran, “In situ Formation of Oxidation Resistant Refractory Coatings on SiC-Reinforced ZrB_2 Ultra High Temperature Ceramics,” J. Am. Ceram. Soc., vol. 95, no. 4, pp. 1247–1254, Apr. 2012.

[11] L. Silvestroni and D. Sciti, “Densification of ZrB_2–$TaSi_2$ and HfB_2–$TaSi_2$ Ultra-High-Temperature Ceramic Composites,” *J. Am. Ceram. Soc*., vol. 94, no. 6, pp. 1920–1930, Jun. 2011.

[12] E. Opila, S. Levine, and J. Lorincz, “Oxidation of ZrB_2- and HfB_2-Based Ultra-High Temperature Ceramics: Effect of Ta Additions,” J. Mater. Sci., vol. 39, no. 19, pp. 5969–5977, Oct. 2004.

[13] D. A. Jones, Principles and Prevention of Corrosion, 2nd edition. Upper Saddle River, NJ: Prentice Hall, 1995.

[14] W.-M. Guo and G.-J. Zhang, “Oxidation Resistance and Strength Retention of ZrB_2–SiC Ceramics,” *J. Eur. Ceram. Soc.,* vol. 30, no. 11, pp. 2387–2395, Aug. 2010.

[15] C. M. Carney, P. Mogilvesky, and T. A. Parthasarathy, “Oxidation Behavior of Zirconium Diboride Silicon Carbide Produced by the Spark Plasma Sintering Method,” *J. Am. Ceram. Soc.,* vol. 92, no. 9, pp. 2046–2052, Sep. 2009.

[16] K. Shugart, W. Jennings, and E. Opila, “Initial Stages of ZrB_2–30 vol% SiC Oxidation at 1500°C,” *J. Am. Ceram. Soc.,* vol. 97, no. 5, pp. 1645–1651, 2014.

[17] X. Zhang, L. Xu, S. Du, W. Han, and J. Han, “Preoxidation and Crack-Healing Behavior of ZrB_2–SiC Ceramic Composite,” *J. Am. Ceram. Soc.,* vol. 91, no. 12, pp. 4068–4073, Dec. 2008.

[18] S. N. Karlsdottir and J. W. Halloran, “Formation of Oxide Films on ZrB_2–15 vol% SiC Composites During Oxidation: Evolution with Time and Temperature,” *J. Am. Ceram. Soc.,* vol. 92, no. 6, pp. 1328–1332, Jun. 2009.

[19] D. Gao, Y. Zhang, C. Xu, Y. Song, and X. Shi, “Oxidation Kinetics of Hot-Pressed ZrB_2–SiC Ceramic Matrix Composites,” *Ceram. Int.,* vol. 39, no. 3, pp. 3113–3119, Apr. 2013.

[209] Y. Niu et al., “Oxidation and Ablation Resistance of Low Pressure Plasma-Sprayed ZrB_2-Si Composite Coating,” *J. Therm. Spray Technol.*, vol. 23, no. 3, pp. 470–476, Oct. 2013.

[21] B. Pieraggi and R. A. Rapp, “A Novel Explanation of the ‘Reactive Element Effect’ in Alloy Oxidation” J. Phys. IV, vol. 03, no. C9, pp. C9-275-C9-280, Dec. 1993.[22] X. Zhang, P. Hu, J. Han, L. Xu, and S. Meng, “The Addition of Lanthanum Hexaboride to Zirconium Diboride for Improved Oxidation Resistance,” *Scr. Mater.*, vol. 57, no. 11, pp. 1036–1039, Dec. 2007.

[23] E. Eakins, D. D. Jayaseelan, and W. E. Lee, “Toward Oxidation-Resistant ZrB_2-SiC Ultra High Temperature Ceramics,” *Metall. Mater. Trans. A*, vol. 42, no. 4, pp. 878–887, Apr. 2011.

[24] S. J. Sitler, I. Charit, and K. S. Raja, “Room Temperature Corrosion Behavior of ZrB_2-HfB_2 Solid Solutions in Acidic and Basic Aqueous Environments,” *Electrochimica Acta*, vol. 246, pp. 173–189, Aug. 2017.

[25] I. G. Talmy, J. A. Zaykoski, M. M. Opeka, and S. Dallek, “Oxidation of ZrB_2 Ceramics Modified with SiC and Group IV–VI Transition Metal Borides,” *High Temp. Corros. Mater. Chem. III Proc. Int. Symp. Electrochem. Soc.*, vol. 2001, no. 12, p. 144, 2001.

[26] L. Kaufman and E. V. Clougherty, “Investigation of Boride Compounds for Very High Temperature Applications, Part II,” *Air Force Materials Laboratory*, Technical Documentary Report No. RTD-TDR-63-4096, RTD-TDR-63-4096, Part II, Feb. 1965.

[27] W. C. Tripp and H. C. Graham, “Thermogravimetric Study of the Oxidation of ZrB_2 in the Temperature Range of 800° to 1500°C,” *J. Electrochem. Soc.,* vol. 118, no. 7, pp. 1195–1199, Jul. 1971.

[28] A. K. Kuriakose and J. L. Margrave, “The Oxidation Kinetics of Zirconium Diboride and Zirconium Carbide at High Temperatures,” J. Electrochem. Soc., vol. 111, no. 7, pp. 827–831, Jul. 1964.

[29] W. C. Tripp, H. H. Davis, and H. C. Graham, “Effect of SiC Addition on Oxidation of ZrB_2,” *Am. Ceram. Soc. Bullitin*, vol. 52, no. 8, pp. 612–616, 1973.

CHAPTER 2: Transition Metal Diborides as Electrode Material for MHD Direct Power Extraction: High-temperature Oxidation of ZrB_2-HfB_2 Solid Solution with LaB_6 Addition[1]

2.1 Abstract

Transition metal borides are being considered for use as potential electrode coating materials in magnetohydrodynamic direct power extraction plants from coal-fired plasma. These electrode materials will be exposed to aggressive service conditions at high temperatures. Therefore, high-temperature oxidation resistance is an important property. Consolidated samples containing an equimolar solid solution of ZrB_2-HfB_2 with and without the addition of 1.8 mol% LaB_6 were prepared by ball milling of commercial boride material followed by spark plasma sintering. These samples were oxidized at 1773 K (1500 °C) in two different conditions: (1) as-sintered and (2) anodized (10 V in 0.1 M KOH electrolyte). Oxidation studies were carried out in 0.3 x 10^5 and 0.1 Pa oxygen partial pressures. The anodic oxide layers showed hafnium enrichment on the surface of the samples, whereas the high-temperature oxides showed zirconium enrichment. The anodized samples without LaB_6 addition showed about 2.5 times higher oxidation resistance in high-oxygen partial pressures than the as-sintered samples. Addition of LaB_6 improved the oxidation resistance in the as-sintered condition by about 30% in the high-oxygen partial pressure tests.

2.2 Introduction

Magnetohydrodynamic (MHD) direct power extraction is a process whereby power is extracted directly from the combustion of coal.[1] The combustion flame is generally seeded with potassium salts to increase the conductivity leading to plasma formation.[2] The superheated plasma flows through a transverse magnetic field and the current is extracted by electrodes normal to the directions of both the flame flow and the magnetic field as illustrated schematically in Figure 2.1. The advantage of this design is that it can be retrofitted onto existing coal-fired steam plants allowing

[1] This chapter has been published and is reproduced with permission from Springer as shown in Appendix A: Sitler, S. J., Hill, C. D., Raja, K. S. & Charit, I. "Transition Metal Diborides as Electrode Material for MHD Direct Power Extraction: High Temperature Oxidation of ZrB_2-HfB_2 Solid Solution with LaB_6 Addition" *Metall. Mater. Trans. E.* **3**, 90–99 (2016), DOI: 10.1007/s40553-016-0072-2.

that steam plant to still operate at full capacity while generating additional current by the MHD process. The operating conditions of MHD current extraction chambers are very aggressive due to high temperatures of the flame (~3000 K (2727 °C)), high mass flow rate, and corrosive attack by the potassium salts. Even though the electrodes which extract current are cooled internally, the exteriors of the electrodes are exposed to very arduous conditions and temperatures in the range from 1700 K to 2200 K (1427 °C to 1927 °C).[2] Specific operating parameters for these systems have not yet been determined as no commercial MHD plants are currently operating. This testing phase is designed to understand the viability of the electrode coating material under the expected arduous parameters; specifically, high temperatures in the range from 1700 K to 2200 K (1427 °C to 1927 °C), corrosive attacks from the potassium salts, and an atmosphere containing a mixture of CO/CO_2 from the combustion of coal.

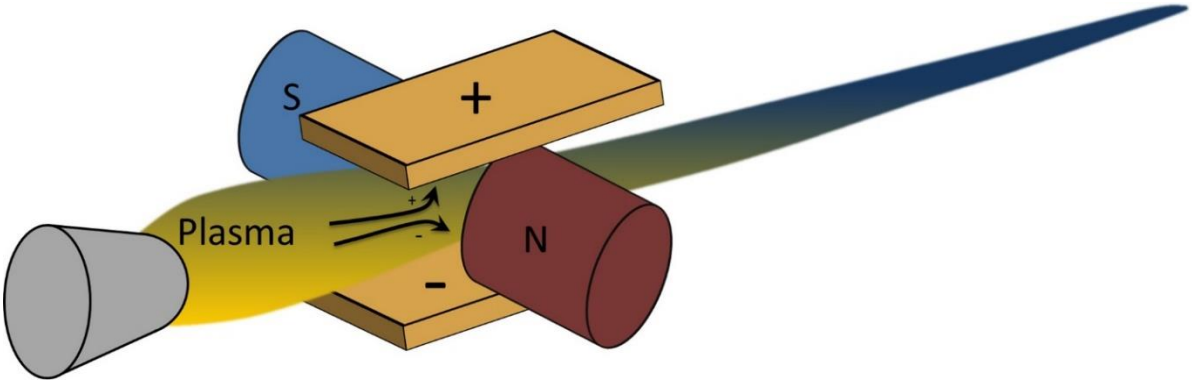

Figure 2.1: Schematic diagram showing the orientation of components of the MHD plasma flame, magnets, and electrodes for current extraction.

Oxide-based materials, such as strontium-doped $LaCrO_3$, have traditionally been considered candidate electrode materials for MHD power generation.[3] However, these conventional oxide materials show high electrical resistivity, low thermal conductivity, and high volatility at MHD operating temperatures, which limit their functionality. Therefore, development of next generation electrode materials that show high electrical and thermal conductivity in combination with better stability in the aggressive environment is required.

In this study, hafnium- and zirconium-based diborides have been tested for use as electrode materials. These materials were chosen based on their extremely high melting point, low electrical resistivity, and high thermal conductivity.[4,5] However, the primary concern of borides is their limited resistance to air oxidation. Several methods of improving the oxidation resistance of the transition

metal diborides have been discussed in the literature such as addition of SiC, $TaSi_2$, $MoSi_2$, and LaB_6. However, most of the available literature pertains to the hypersonic aerospace applications.[6–9]

Two separate methods for limiting the high-temperature oxidation were chosen for this study: (1) creating a thin impervious oxide layer by electrochemical anodization and (2) the addition of 1.8 mol% LaB_6. LaB_6 is a well-known thermionic emitter used in field emission guns of scanning electron microscopes. Also, the addition of LaB_6 to the (Zr, Hf)B_2 composite is supposed to increase the oxidation resistance by forming an impervious cubic pyrochlore lanthanum zirconate ($La_2Zr_2O_7$) coating.[10] The pyrochlore phases are thought to significantly reduce the oxygen permeability. For anodization, Lavrenko et al.[11] observed a triple-layered anodic oxide structure of HfB_2 when anodically polarized at about 1.74 V in 3% NaCl solution. It is suggested that anodization of transition metal (TM) diborides at higher potentials (~10 V) in basic solution would result in a boron-free oxide film by dissolution of the B_2O_3 as boric acid by the following reaction:[12,13]

$$(TM)B_2 + 8OH^- \rightarrow (TM)O_2 + 2\,H_3BO_3(aq) + 2H^+ + 6\,e^- \quad (1)$$

As mentioned earlier, the electrodes are required to have high electrical conductivity. Formation of an anodic oxide layer will adversely affect the electrical conductivity of the diborides at room temperature. However, if the anodic oxide layer is going to hinder the oxygen diffusion at high temperature, the resultant total oxide thickness at high temperature will be much thinner than that observed on the samples not anodized and thus the electrical conductivity would improve at high temperature. Seong and Kim[14] reported parabolic oxidation behavior of ZrB_2 with and without addition of SiC at 1773 K (1500 °C) in air and very low oxygen partial pressure. The reported parabolic rate constant of ZrB_2 yielded an oxidation depth of 354 µm in 1 hour. The addition of 20 vol% SiC reduced the parabolic rate significantly decreasing the oxidation depth to 20.8 µm in 1 hour. Carney et al.[15] reported similar results with the addition of SiC.

For many applications, oxidation is prevented by a borosilicate glassy liquid layer formed on top of the boride. This, however, would be detrimental in MHD applications due to the extreme temperatures being high enough to evaporate this layer. In addition, liquid top layers will not be stable under the stresses caused by the high plasma velocities. Therefore, the addition of SiC[16] has been specifically avoided in this study. While other additives, such as Ta,[17] $TaSi_2$, $MoSi_2$,[8,18] yttrium aluminum garnet and alumina,[19] are being considered, this particular study has been limited to LaB_6.

2.3 Experimental

2.3.1 Materials

ZrB_2, HfB_2, and LaB_6 powders were obtained from Alfa Aesar. The purity of all as-received powders was ≥99.5%. The required quantities of these powders were added to a 100 mL zirconia vial in a glovebox (M. Braun Inert Gas-Systeme GmbH) under high-purity argon atmosphere. The vial was then hermetically sealed before unloading from the glovebox and high energy ball milled for 3 hours using a mixer mill (Spex 8000M). The powder-to-ball mass ratio used during the process was 1:10, utilizing yttria-stabilized zirconia (YSZ) spherical grinding media of 6.5 mm diameter (Inframat Advanced Materials LLC, Manchester, CT). Table 2.1 shows a list of the powder mixtures. The sample identifiers will be used throughout this paper. Only ZrB_2-HfB_2 equimolar solid solution denoted as AB, and ZrB_2-HfB_2 solid solution with the addition of 1.8 mol% LaB_6 denoted as ABL are compared for oxidation resistance in this study.

Table 2.1: Nomenclature of various powder compositions studied and SPS dwell times at 1973 K (1700 °C).

Sample Identifier	*Composition*	*Hold Time (s)*
A	HfB_2	180
B	ZrB_2	600
AB	1:1 HfB_2 - ZrB_2 (equimolar)	600
ABL	1:1 HfB_2 - ZrB_2 + 1.8 mol% LaB_6	300

2.3.2 Spark Plasma Sintering

After the powders were ball milled, they were sintered into pellets by spark plasma sintering (SPS) using a Dr. Sinter SPS-515S machine (Fuji Electronic Industrial Co., Ltd., Japan). The powder was loaded into an Isocarb-85 graphite die with an inner diameter of 20.6 mm. The graphite dies were lined with graphite foil. Before loading into the die, the graphite foil was coated in boron nitride (ZYP Coatings, Inc., Oak Ridge, TN). A heating rate of 100 °C/min was applied during SPS. The SPS tooling was kept under a vacuum of at least 103 Torr for the entirety of SPS operation. For all runs, 5 kN force was applied to the SPS tooling. Enough powder was added to the graphite dies to yield a 5-mm thick disk of each respective composition. All samples were held for 3 to 10 minutes at 1973 K (1700 °C) as shown in Table 2.1.

2.3.3 Anodization

Select numbers of spark plasma-sintered samples were anodized in 0.1 M KOH at 10 V for 60 minutes for comparison to the as-sintered samples. These parameters were experimentally determined to provide the highest likelihood of achieving a protective anodic oxide layer. Samples

were electrochemically anodized using a typical two-electrode setup with a 2 cm x 3 cm platinum flag as the counter electrode and the ~150 mm^2 samples as the working electrodes. A controlled DC power supply (Sorensen XPF 60–20 DC) was used to apply the required potential for anodization. Samples which have undergone this step are referred to as ‘‘anodized’’ or ‘‘Anod,’’ as opposed to samples that were not anodized which are labeled ‘‘as-sintered,’’ ‘‘as-received,’’ or ‘‘AsRec.’’

2.3.4 High-temperature Oxidation

Oxidation studies were carried out using a thermogravimetric analyzer (Netzsch STA 409). Samples were heated at a ramp rate of 3 °C/min to 1773 K (1500 °C). The samples were held at 1773 K (1500 °C) for 2 hours and then cooled at the same rate of 3 °C/min. Four samples were tested: as-sintered ZrB_2-HfB_2 solid solution (denoted as as-received AB), as-sintered ZrB_2-HfB_2 solid solution with addition of LaB_6 (denoted as as-received ABL), anodized AB, and anodized ABL. The samples were tested in a purified argon atmosphere (p_{O2} = 0.1 Pa) and in a mixture of argon+ oxygen. The oxygen was introduced only after 1 hour of soaking at 1773 K (1500 °C) in the argon atmosphere. The oxygen was admitted into the furnace sample chamber for 15 minutes at p_{O2} = 0.3 x 10^5 Pa, after which the pure argon purging continued.

2.3.5 Characterization

The density measurements were performed in accordance to ASTM B962-08 standard based on the Archimedes principle using the following Equation (2):

$$\rho = \frac{M_{air}}{M_{air} - M_{water}}(\rho_{water} - \rho_{air}) + \rho_{air} \quad (2)$$

where M_{air} is the mass of the object in air, M_{water} the mass of the object in water, ρ_{water} the density of water, and ρ_{air} the density of air, which is taken to be 0.0012 g/cm^3. Scanning electron microscopy was carried out by using a field emission scanning electron microscope (FESEM) LEO Supra 35VP (Zeiss, Jena, Germany). X-ray diffraction patterns (XRD) were obtained using a D5000 Diffractometer (Siemens AG, Munich, Germany) at a scan rate of 0.02° and a hold time of 5 seconds. Energy-dispersive X-ray spectroscopy (EDS) was used to analyze chemical composition of the samples and oxide layers. Spectra were obtained using an accelerating voltage of 20 kV. The grain sizes of the samples were measured by the mean linear intercept method using the backscattered electron images after polishing the samples to a surface finish of 1 µm.

2.4 Results and Discussion

Before critical testing of the sample could commence, solid solutionizing of the sample needed to be demonstrated. XRD patterns were taken of both individual diborides and compared to the supposed solid solution mixture. Although ZrB_2-HfB_2 solid solutionizing has been studied by Otani et al.,[20] proof was desired that the specific conditions used in this study would also produce complete solid solutionizing. AB peak values falling directly in-between A and B values with no peak splitting proved such solid solutionizing as shown in Figure 2.2.

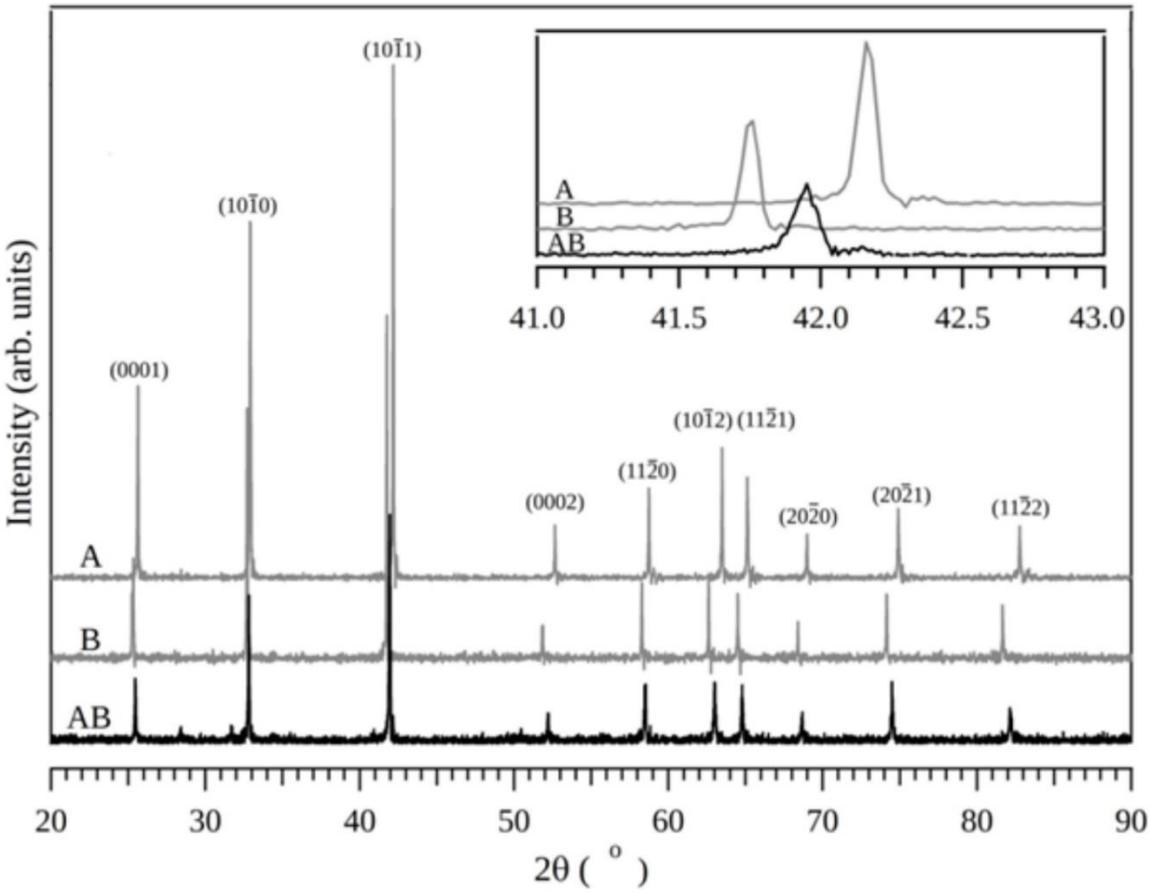

Figure 2.2: XRD spectra comparing ZrB_2, HfB_2, and 1:1 equimolar mixture of HfB_2-ZrB_2 showing complete solid solution. The inset shows how the peak of the solid solution lies in-between the peaks of ZrB_2 and HfB_2.

The SPSed samples AB and ABL showed 76.2 and 97.2% of their theoretical densities, respectively. Densities were calculated using the ASTM standard procedure as mentioned in the experimental section. With SPS, fully dense or near fully dense samples are achievable. Therefore, with the samples in this study, the target densities with sintering agents were set to >95%. Although some surface porosity can be noted on the SEM images, due to the density measurements, it is

expected that this porosity does not continue into the bulk of the material but is simply an effect of polishing. In addition, the backscatter detector used, causes the slightly lowered areas to appear as deep pores. From the shape of the dark features (apparent pores), it is evident that these are actually grain pull-outs rather than actual porosity. The SEM micrographs in Figure 2.3(a) and (b) are included only to give the size scale and microstructure of the grains of AB and ABL in the as-sintered condition, respectively. The grain sizes were calculated by the mean linear intercept method, averaging the results of 10 lines. The grain sizes of the AB and ABL samples were observed to be 3.3 ± 2.1 and 2.7 ± 2.2 µm, respectively. The morphologies of the anodic oxide layers formed on the AB and ABL samples are, respectively, shown in Figure 2.4(a) and (b). The thickness of the anodic oxide layer of the ABL sample can be observed from Figure 2.4(b) which is ~20 µm.

A summary of metal-based energy-dispersive X-ray analyses of various samples after different experimental conditions is given in Table 2.2. The as-sintered AB sample showed marginal enrichment of zirconium on the surface, and the as-sintered ABL sample showed almost equimolar concentrations of Zr and Hf on the surface. After anodization, the surface compositions of the samples showed different trends. The anodized AB sample showed significant enrichment of hafnium at the surface as compared to the anodized ABL sample. The anodized ABL sample showed slightly lower Zr and La concentrations at the surface than that of the as-sintered samples, as shown in Table 2.2. It should be noted that the analyses were based on the metals, and the intensities of the non-metals such as oxygen and boron were not included in the calculation. Therefore, the results are used only for comparative purpose with the as-sintered samples.

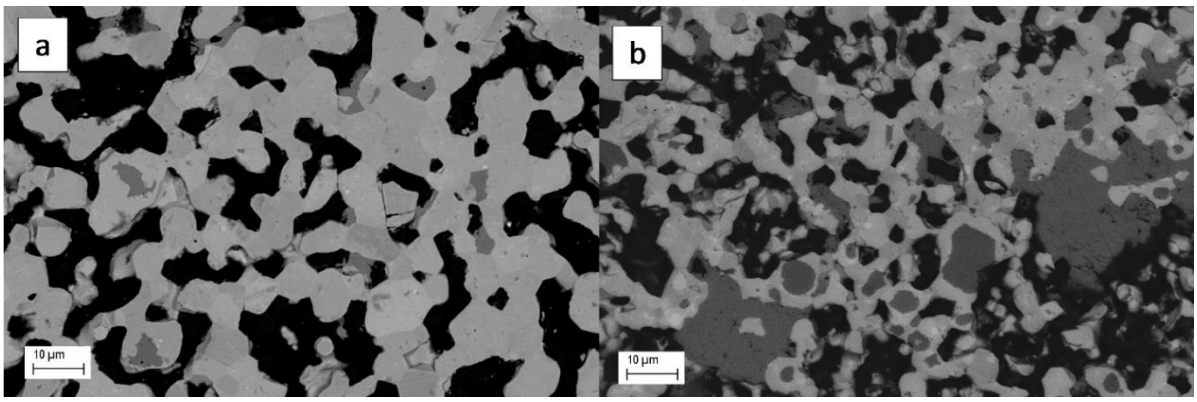

Figure 2.3: Polished and etched FESEM micrographs of samples. (a) 1:1 ZrB_2-HfB_2 solid solution (sample AB), and (b): 1:1 ZrB_2-HfB_2 solid solution with 1.8 mol% LaB_6 (sample ABL).

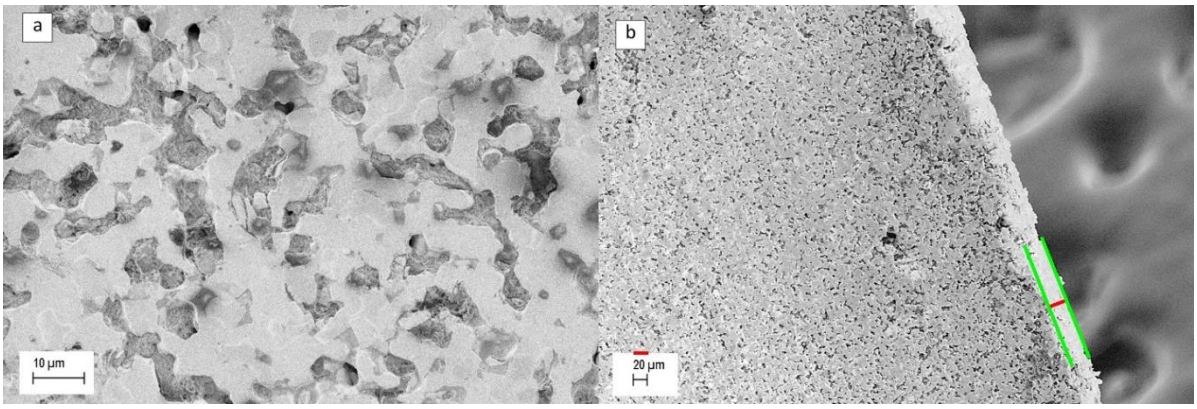

Figure 2.4: FESEM micrographs of the samples anodized at 10 V in 0.1 M KOH for 1 hour: (a) Top surface of 1:1 ZrB_2-HfB_2 solid solution (sample AB), and (b) Cross section of the 1:1 ZrB_2-HfB_2 solid solution with 1.8 mol% LaB_6 (sample ABL).

Table 2.2: Average metal-based composition of the samples by energy-dispersive x-ray analyses after different experimental conditions.

Sample	*Element*	*Base*	*As-Anodized*	*Oxidized in argon*	*Oxidized in oxygen*
Anodized AB (mole %)					
	Zr	-	39.1	65.2	53.1
	Hf	-	60.9	34.8	46.9
Anodized ABL (mole %)					
	Zr	-	46.7	-	57.0
	La	-	1.4	-	0.1
	Hf	-	52.0	-	42.9
As-sintered AB (mole %)					
	Zr	54.5	-	55.0	55.4
	Hf	45.5	-	45.0	44.6
As-sintered ABL (mole %)					
	Zr	48.9	-	48.9	-
	La	02.0	-	0.6	-
	Hf	49.1	-	50.6	-

The energy peaks of non-metal elements such as boron and oxygen were not included in the analyses

The enrichment of Hf on the surface of the anodized AB and ABL samples could be attributed to the electrochemical conditions during anodization. The oxidation reaction of hafnium in the basic solution (pH ~ 13) at 10 V could be given as[21]:

$$Hf \rightarrow Hf^{4+} + 4e^- \quad (3)$$

$$Hf^{4+} + 4OH^- \rightarrow HfO_2 + 2H_2O \quad (4)$$

Reaction (3) ionizes the Hf and causes anodic current to flow from the sample through the circuit to the counter electrode. The tetravalent Hf ions produced by Reaction (3) combine with the hydroxyl ions available on the surface of the boride sample and form HfO_2 layer. The $HfO_2 \bullet H_2O$ type species that is formed on the surface of the sample is stable in a wide range of pH and potentials according to the Hf-H_2O Pourbaix diagram.[21] Therefore, the surface enrichment of Hf on the anodized samples could be attributed to the high stability of the HfO_2 phase. In addition, a quick examination of the stability of the zirconium and boron species under the anodization conditions indicates lower stability of these species. The anodic reactions of Zr can be given as[21]:

$$Zr \rightarrow Zr^{4+} + 4e^- \quad (5)$$

$$Zr^{4+} + 2H_2O \rightarrow ZrO_2 + 4H^+ \quad (6)$$

$$Zr^{4+} + 3OH^- \rightarrow HZrO_3^- + 2H^+ \quad (7)$$

$$ZrO_2 + H_2O \rightarrow HZrO_3^- + H^+ \quad (8)$$

Reactions (5) and (6) indicate the ionization of Zr and formation of an oxide layer in low alkaline conditions (pH < 12.78), respectively. When the pH is above 12.78, the stability of ZrO_2 is affected by dissolution as $HZrO_3^-$ species as given in the Reactions (7) and (8). Since the anodization was carried out in 0.1 M KOH solution in this investigation, dissolution of the anodically formed ZrO_2 could have occurred, and therefore, lower concentrations of Zr were observed on the anodized samples as shown in Table 2.2.

As mentioned earlier, the glassy liquid oxidation protection offered by borosilicate is not viable for the MHD system. The oxidation of transition metal borides results in the formation of ZrO_2-type crystalline transition metal oxide and liquid boron oxide following Reaction (9).

$$ZrB_{2(c)} + 5/2O_{2(g)} \rightarrow ZrO_{2(c)} + B_2O_{3(l,g)} \quad (9)$$

At temperatures higher than 1373 K (1100 °C), rapid evaporation of liquid boron oxide occurs which transforms the ZrO_2 oxide into a porous layer. Diffusion of molecular oxygen occurs at a faster rate through these porous structures than the liquid boria.[22] Around 20 to 30 vol% of silicon carbide is often added as a sintering aid and to improve the oxidation resistance of the ZrB_2/HfB_2. However,

at high temperatures, SiC is also oxidized and forms several liquid and gaseous phases, such as SiO_2, SiO, etc., by following Reactions (10) and (11).[23]

$$SiC + 3/2O_2 \rightarrow SiO_{2(l)} + CO_{2(g)} \quad (10)$$

$$SiO_{2(l)} \rightarrow 2\ SiO_{(g)} + O_{2(g)} \quad (11)$$

It is well established that a silica-rich borosilicate liquid layer is present in the porous structure of the transition metal oxide layer during high-temperature oxidation.[24] The silica-based glass is considered to protect against excessive evaporation of B_2O_3 until temperatures reach around 1773 K (1500 °C).[25] Li et al.[26] proposed a model for the oxidation resistance of the composite structure based on the solid pillars of ZrO_2 and liquid roof of borosilicate glass layer that acts as a barrier to oxygen diffusion. The porous ZrO_2 skeleton acts as a condensing substrate and mechanical support to the borosilicate liquid.

In this investigation, attempts have been made to control the formation of porous oxide structure that occurs due to volatilization of B_2O_3 at high temperature. One strategy was to electrochemically anodize the surface of the diborides in order to form a thin, continuous, and impervious layer of transition metal oxide at room temperature that would impart superior oxidation resistance at high temperature.

The major objective of anodizing the transition metal diboride samples was to obtain an oxide layer free from boron species so that during high-temperature exposure the volatilization of boron oxide could be avoided and a pore-free oxide layer could be maintained. During anodization in mild alkaline solution, the boron oxidation reactions can be given as:[21]

$$B + 5OH^- \rightarrow HBO_3^{2-} + 2H_2O + 3e^- \quad (12)$$

$$B + 3H_2O \rightarrow H_3BO_3 + 3H^+ + 3e^- \quad (13)$$

The above reactions suggest that boron can be preferentially dissolved from the surface of the anodized samples. Since the borate phases such as ZrB_2O_5 and HfB_2O_5 are stable only at high pressure (7.5 GPa) and temperature 1373 K (1100 °C),[27] the presence of these phases in the anodic oxide is excluded. The EDS and XRD analyses did not reveal the presence of borate-related phases in the anodic oxide. However, it is noted that these techniques are not generally sensitive enough to

detect the borate species. Future studies will focus on the analyses of boron species using surface analysis spectroscopic techniques such as FTIR, Raman, and XPS.

The addition of LaB_6 to the AB composite was also done to increase the oxidation resistance by forming an impervious pyrochlore lanthanum zirconate ($La_2Zr_2O_7$) coating.[10] The pyrochlore phases are thought to significantly reduce the oxygen permeability. The oxidation of lanthanum from the addition of LaB_6 during the anodization process can be given by the following reactions:[21]

$$La \rightarrow La^{3+} + 3e^- \quad (14)$$

$$La^{3+} + 3OH^- \rightarrow La(OH)_3 \quad (15)$$

$$2\ La(OH)_3 \rightarrow La_2O_3 \bullet 3H_2O \quad (16)$$

The $La(OH)_3$ is considered to be very stable in alkaline conditions. The presence of La_2O_3 on the sample surface is suggested based on the dehydration Reaction (16) followed by anodization. The results of XRD analyses carried out on the AB and ABL samples after high-temperature oxidation studies are, respectively, shown in Figure 2.5(a) and (b). The oxide layers present on the samples were identified as ZrO_2 and HfO_2 with monoclinic lattice structure. Presence of pyrochlore phases in the ABL samples was anticipated but not identified because only 1.8 mol% of lanthanum was added which was less than the detection limit of the XRD. The addition of LaB_6 helps sintering, improves ionization, and results in smaller grain sizes. Since the cubic LaB_6 has no mutual solubility in hexagonal ZrB_2 or HfB_2,[28,29] it is considered to be present as evenly distributed precipitates as shown in Figure 2.4(b). There are some minor peaks on the XRD spectra which could not be indexed with exact match but could be associated with complex oxide or pyrochlore phases.

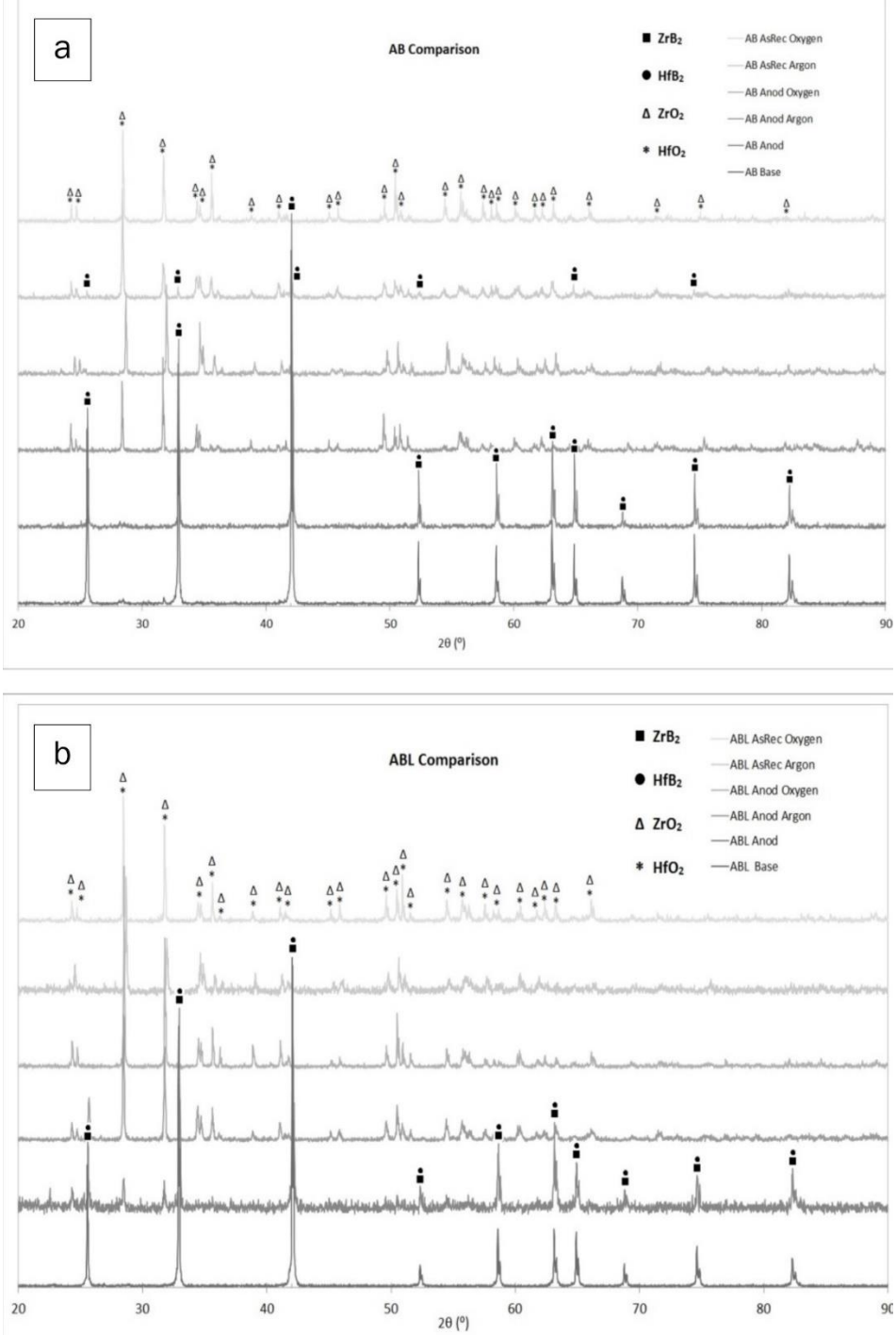

Figure 2.5: XRD results of the high temperature oxidized samples. (a) 1:1 ZrB_2-HfB_2 solid solution (sample AB), and (b) 1:1 ZrB_2-HfB_2 solid solution with 1.8 mol% LaB_6 (sample ABL).

The thermogravimetric data of the all four samples tested during temperature ramping and isothermal conditions are shown in Figure 2.6(a)–(d). The oxidation kinetics of the samples as a function of temperature in oxygen atmosphere (p_{O2} = 0.3 x 10^5 Pa) is shown in Figure 2.6(a). The

decrease in mass until 873 K (600 °C) could be attributed to the evaporation of water and decomposition of carbonaceous matter from the sample. The decrease was not significant compared to the weight gain at high temperatures. When the samples were heated above 873 K (600 °C), the increase in weight was observed in all the samples until about 1573 K (1300 °C), after which a loss in weight was recorded. The temperature at which a decrease in weight was recorded varied with samples depending on their surface preparation and composition. The maximum weight gain observed was 3.2 mg/cm^2 on the as-sintered AB samples at 1573 K (1300 °C). The anodized AB sample showed the lowest weight gain that peaked to a value of 0.65 mg/cm^2 at 1423 K (1150 °C), after which the weight decreased. Both the as-sintered and anodized ABL samples showed similar weight change behaviors until about 1673 K (1400 °C). After reaching 1723 K (1450 °C), the as-sintered ABL sample showed a sharp increase in weight gain. The anodized AB and ABL samples showed weight gain after 1723 K (1450 °C), whereas such behavior was not observed with the as-sintered AB sample. After the change in mass peaked in the temperature range from 1423 K to 1673 K (1150 °C to 1300 °C), the samples started losing weight. This is most likely due to the evaporation of the liquid B_2O_3 layer. The weight gain between 873 K and 1573 K (600 °C and 1300 °C) could be attributed to the oxidation of transition metal borides to their respective oxides as given in the Reaction (1). It should be noted that the rate and the magnitude of weight loss were significant because the boria was not mixed with silica as in other investigations and therefore, the viscosity would have been low. The low weight gain of the anodized AB sample could be attributed to the surface enrichment of the hafnium that provided a better oxidization resistance oxide layer. In case of the ABL samples, Hf enrichment was not observed, and the presence of LaB_6 would have oxidized to La_2O_3 that resulted in glass formation with B_2O_3. Even though the amorphous phase formation did not give as high of an oxidation resistance as the anodized AB sample, the glass phase could seal the pores and hinder oxygen diffusion at temperatures lower than 1773 K (1500 °C).[30]

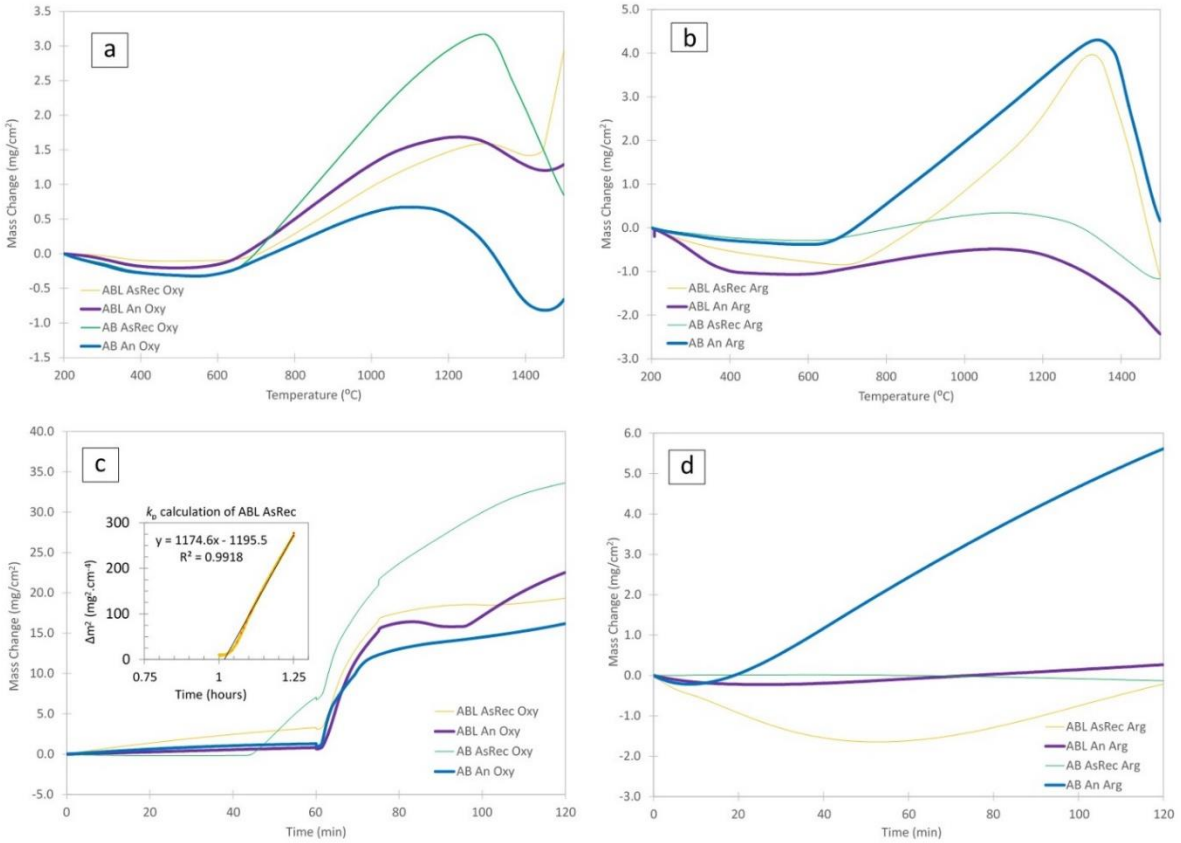

Figure 2.6: Thermogravimetric areal mass change of AB and ABL in anodized and as-received conditions. (a) and (b) Temperature ramp data for oxygen (p_{O2} = 0.3 × 10^5 Pa) and argon (p_{O2} = 0.1 Pa), respectively; (c) and (d) Isothermal condition data at 1773 K (1500 °C) in oxygen and argon, respectively. Oxygen was only introduced after soaking at 1773 K (1500 °C) for 1 hour.

The weight change as a function of time for samples in the argon atmosphere (p_{O2} = 0.1 Pa) is shown in Figure 2.6(b). The oxidation behaviors of the samples were different from that observed in the oxygen atmosphere. In this condition, the anodized AB sample showed the highest weight gain and anodized ABL sample showed almost no weight gain. The next best oxidation resistance was observed with the as-sintered AB sample. The reason for the observed oxidation behavior in low oxygen pressure is not fully understood. Defect structures, pre-existing in the samples prior to high-temperature oxidation studies, could have played a significant role in this behavior. It is well documented that anodic oxide layers contain a significant concentration of oxygen vacancies.[31] The anodized ABL samples also would have a high concentration of oxygen vacancies. These vacancies would not be annihilated when heated to high temperatures in low oxygen partial pressure. On the other hand, the presence of this type of defect structure would help easy diffusion of ions and formation of new phases such as $La_2Zr_2O_7$ or $La_2Hf_2O_7$. The presence of pyrochlores has been reported

to lower the oxygen permeability significantly.[6] The higher resistance to oxidation of the anodized ABL sample could be attributed to the possible in situ formation of pyrochlore phase within the anodic and thermally formed oxide layers.

The isothermal weight change in the samples exposed to oxygen atmosphere at 1773 K (1500 °C) is shown in Figure 2.6(d). It should be noted that the samples were exposed to oxygen only for 15 minutes after 1 hour soaking at the test temperature. In the remaining time, the samples were under argon purging condition. The weight gain of the samples during the 15 minutes of oxidation in oxygen atmosphere (p_{O2} = 0.3 x 10^5 Pa) could be fitted into a parabolic relation:

$$\Delta m^2 = k_p t \tag{17}$$

where Δm = mass change per unit area, k_p = parabolic rate constant, and t = time. Table 2.3 summarizes the parabolic rate constants of different samples. Rate constants were calculated using Equation (17) from data obtained only during the 15-minute window where the oxygen atmosphere (p_{O2} = 0.3 x 10^5 Pa) was admitted into the furnace chamber, as shown in Figure 2.6(c) from time = 60 to 75 minutes. The inset shows the linear relation of Δm^2 vs time. Samples were allowed to come to equilibrium prior to oxygen input for 1 hour at 1773 K (1500 °C) which effectively eliminated any interference in the k_p values from evaporation of B_2O_3. The anodized AB sample showed the lowest rate constant and the as-sintered AB sample showed the highest rate constant for oxidation. It is seen that anodization of the samples helped decrease the oxidation of the samples because of the observed low rate constants. The rate constants determined in this investigation are significantly larger than that reported for single boride material with SiC addition by other researchers.[32,33] However, the values are comparable to the rate constants used by Parthasarathy et al.[22] for their oxidation kinetics model validation of transition metal borides without any additions. This observation indicates that addition of SiC provides better oxidation resistance than the strategies followed in this investigation. However, from electrical conductivity point, which is important for the MHD electrode application, addition of SiC may not be advantageous. In addition, it is likely that the addition of SiC would force the ZrO_2 and HfO_2 oxides to form as porous oxides leading to detrimental oxidation at high temperatures due to the volatilization of the borosilicate glassy layer.

Table 2.3: Parabolic rate constants of the samples exposed to oxygen (p_{O2} = 0.3 × 10^5 Pa) at 1773 K (1500 °C) for 15 minutes.

Sample	*Rate constant, k_p (mg^2/cm^4 h)*	*Log(k_p) (kg^2/m^4 s)*
ABL as-sintered	1174.6	-4.49
ABL anodized	1053.0	-4.53
AB as-sintered	1682.4	-4.33
AB anodized	692.4	-4.72

The isothermal weight change in the samples exposed to argon atmosphere at 1773 K (1500 °C) is shown in Figure 2.6(d). The results observed in argon atmosphere were in contrast to the results observed in the oxygen atmosphere. The anodized AB sample showed the highest weight gain in the argon atmosphere. No significant weight gain was observed in other samples. This could be attributed to a near equilibrium in the competing effects of B_2O_3 volatilization that decreased the weight and formation of transition metal oxides that increased the weight.

Post-thermogravimetric testing SEM side view images of the oxide layers are provided for the as-received and anodized samples in Figure 2.7(a)–(d) and Figure 2.8(a)–(d), respectively, where the presence of thick oxide layers can be observed. The surface composition (metal-based) of the samples is summarized in Table 2.2. In general, enrichment of Zr at the surfaces could be observed on the anodized samples after the high-temperature oxidation. This result was in contrast to the as-anodized condition where Hf enrichment was found on the surface. The significance of Zr enrichment on the oxidation behavior is not very clear due to lack of additional analytical data. The as-sintered samples did not show enrichment of any particular atoms. The summary of the oxide thickness data is given in Table 2.4. The anodized samples showed less oxide layer thickness than their as-sintered counter parts and AB samples had thinner oxide layers than ABL samples.

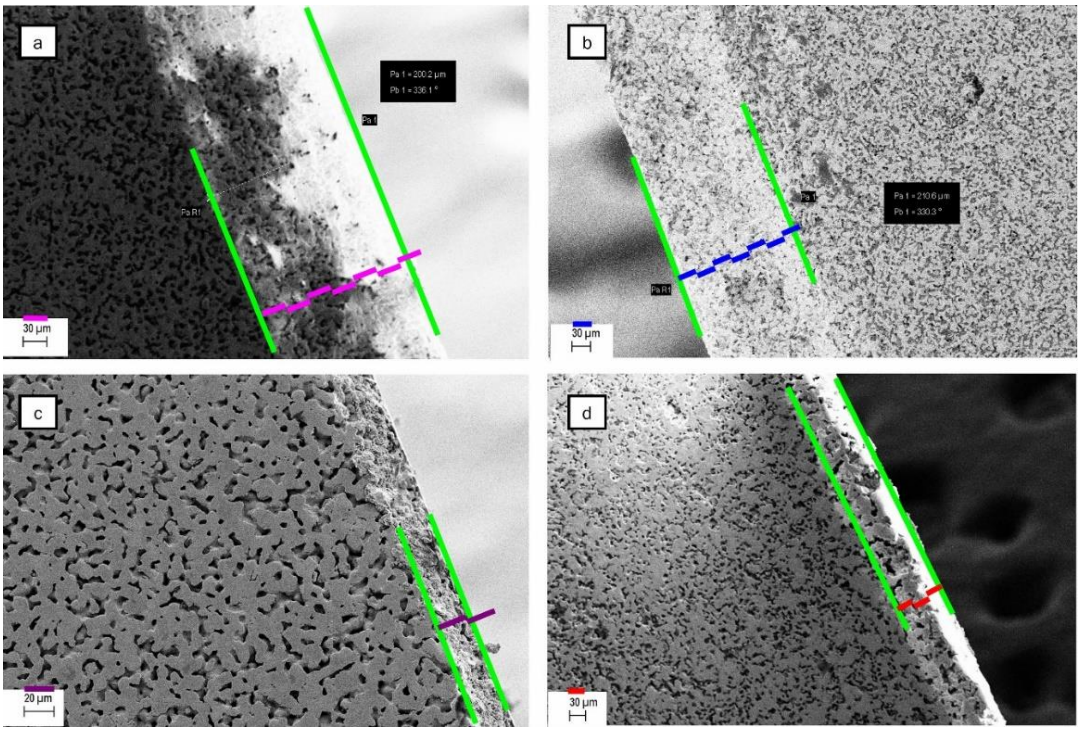

Figure 2.7: Cross-sectional images of the as-sintered samples after high temperature oxidation tests at 1773 K (1500 °C). (a) As-sintered AB oxidized in oxygen; (b) As-sintered ABL oxidized in oxygen; (c) As-sintered AB oxidized in argon; and (d) As-sintered ABL sample oxidized in argon. Metal based comparative oxide compositions are shown in Table 2.2.

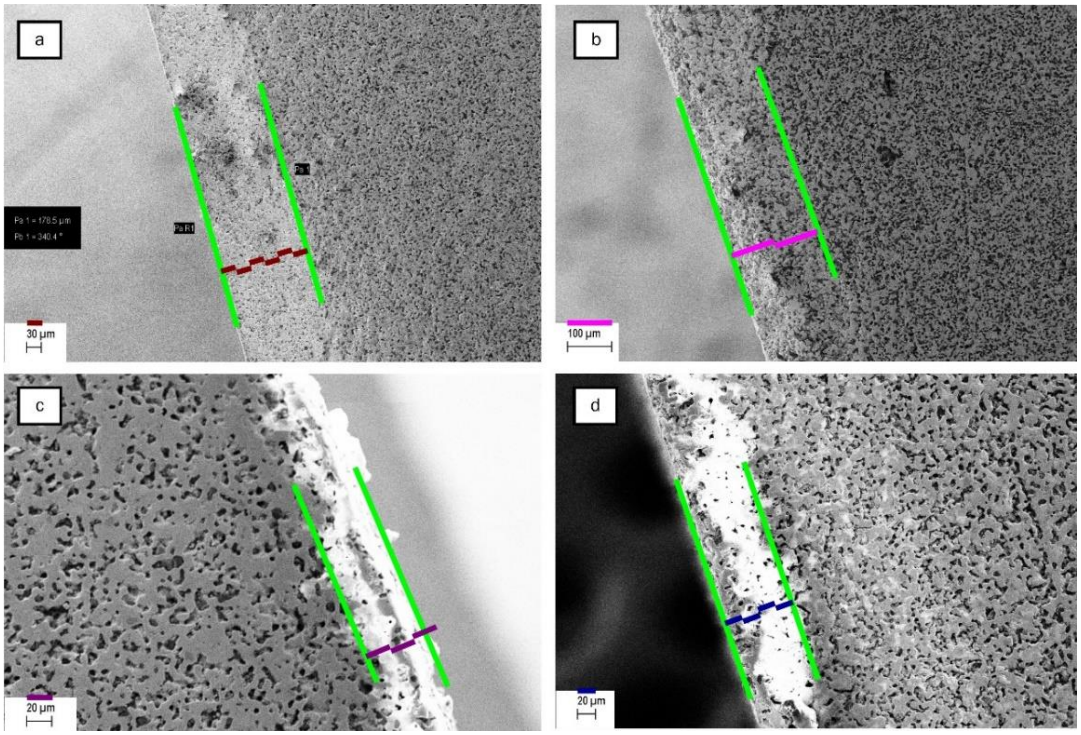

Figure 2.8: Cross-sectional images of the anodized samples after high temperature oxidation tests at 1773 K (1500 °C). (a) Anodized AB oxidized in oxygen; (b) Anodized ABL oxidized in oxygen; (c) Anodized AB oxidized in argon; and (d) Anodized ABL oxidized in argon. Metal based comparative oxide compositions are shown in Table 2.2.

Table 2.4: Summary of oxide thickness data on various samples after oxidation at 1773 K (1500 °C) in different atmospheres compared with anodic oxide.

Sample	*Initial thickness of anodic oxide*	*Oxidized in argon*	*Oxidized in oxygen*
ABL As-sintered (μm)		80	210
ABL Anodized (μm)	20	80	200
AB As-sintered (μm)		20	200
AB Anodized (μm)	20	50	180

2.5 Conclusions

Anodization of ZrB_2-HfB_2 solid solution samples in 0.1 M KOH solution at 10 V showed preferential enrichment of Hf on the surface which helped to enhance the oxidation resistance by about 2.5 times in the oxygen atmosphere at 1773 K (1500 °C). Addition of 1.8 mol% LaB_6 enhanced the oxidation resistance in the as-sintered condition by 30%. The parabolic rate constants of the samples were significantly larger than the values reported for the samples containing SiC, although for the high-temperature MHD application, the addition of SiC would not be advantageous.

2.6 Acknowledgements

The authors gratefully acknowledge the financial support from the National Energy Technology Laboratory, US Department of Energy (Office of Fossil Energy) grant number: DE-FE0022988. Laboratory help from Colin Lunstrum is also gratefully acknowledged.

2.7 Bibliography

[1] J. K. Wright, “The Science of M.H.D. Generators-A Critical Survey,” *Philos. Trans. R. Soc. Lond. Ser. Math. Phys. Sci.*, vol. 261, no. 1123, pp. 347–359, 1967.

[2] D. B. Meadowcroft, “Electronically-Conducting, Refractory Ceramic Electrodes for Open Cycle MHD Power Generation,” *Energy Convers.*, vol. 8, no. 4, pp. 185–190, Dec. 1968.

[3] N. Ram Mohan, K. Thiagarajan, and V. Sivan, “Studies on La(Sr)CrO_3 for Use in a Magnetohydrodynamic Generator,” *Ceram. Int.*, vol. 20, no. 3, pp. 143–146, Jan. 1994.

[4] G. V. Samsonov, B. A. Kovenskaya, and T. I. Serebryakova, “Some Physical Characteristics of the Diborides of Transition Metals of Groups IV and V,” *Sov. Phys. J.*, vol. 14, no. 1, pp. 11–14, Jan. 1971.

[5] R. P. Tye and E. V. Clougherty, “Thermal and Electrical Conductivities of Some Electrically Conducting Compounds.,” *Pp 396-401 Proc. Fifth Symp. Thermophys. Prop. Bonilla C F Ed N. Y. Am. Soc. Mech. Eng. 1970*, Jan. 1970.

[6] M. M. Opeka, I. G. Talmy, and J. A. Zaykoski, “Oxidation-based Materials Selection for 2000°C + Hypersonic Aerosurfaces: Theoretical Considerations and Historical Experience,” *J. Mater. Sci.*, vol. 39, no. 19, pp. 5887–5904, Oct. 2004.

[7] D. D. Jayaseelan, E. Zapata-Solvas, P. Brown, and W. E. Lee, “In-situ Formation of Oxidation Resistant Refractory Coatings on SiC-Reinforced ZrB_2 Ultra High Temperature Ceramics,” *J. Am. Ceram. Soc.*, vol. 95, no. 4, pp. 1247–1254, Apr. 2012.

[8] L. Silvestroni and D. Sciti, “Densification of ZrB_2–$TaSi_2$ and HfB_2–$TaSi_2$ Ultra-High-Temperature Ceramic Composites,” *J. Am. Ceram. Soc.*, vol. 94, no. 6, pp. 1920–1930, Jun. 2011.

[9] E. Opila, S. Levine, and J. Lorincz, “Oxidation of ZrB_2- and HfB_2-based Ultra-High Temperature Ceramics: Effect of Ta Additions,” *J. Mater. Sci.*, vol. 39, no. 19, pp. 5969–5977, Oct. 2004.

[10] X. Zhang, P. Hu, J. Han, L. Xu, and S. Meng, “The Addition of Lanthanum Hexaboride to Zirconium Diboride for Improved Oxidation Resistance,” *Scr. Mater.*, vol. 57, no. 11, pp. 1036–1039, Dec. 2007.

[11] V. A. Lavrenko, V. N. Talash, M. Desmaison-Brut, O. N. Grigor’ev, and Y. B. Rudenko, “Kinetics and Mechanism of the Electrochemical Oxidation of Hafnium Boride,” *Powder Metall. Met. Ceram.*, vol. 48, no. 7–8, pp. 462–465, Nov. 2009.

[12] C. Monticelli, A. Bellosi, and M. Dal Colle, “Electrochemical Behavior of ZrB_2 in Aqueous Solutions,” *J. Electrochem. Soc.*, vol. 151, no. 6, pp. B331–B339, 2004.

[13] Z. Wang, Q. Zhao, L. Jing, Z. Wu, and X. Sun, “Corrosion Behavior of ZrB_2–SiC–Graphite Ceramic in Strong Alkali and Strong Acid Solutions,” *Ceram. Int.*, vol. 42, pp. 2926–2932, Oct. 2015.

[14] Y.-H. Seong and D. K. Kim, “Oxidation Behavior of $ZrB_{2-x}SiC$ Composites at 1500 °C Under Different Oxygen Partial Pressures,” *Ceram. Int.*, vol. 40, no. 9, Part B, pp. 15303–15311, Nov. 2014.

[15] C. M. Carney, P. Mogilvesky, and T. A. Parthasarathy, “Oxidation Behavior of Zirconium Diboride Silicon Carbide Produced by the Spark Plasma Sintering Method,” *J. Am. Ceram. Soc.*, vol. 92, no. 9, pp. 2046–2052, Sep. 2009.

[16] M. M. Opeka, I. G. Talmy, E. J. Wuchina, J. A. Zaykoski, and S. J. Causey, “Mechanical, Thermal, and Oxidation Properties of Refractory Hafnium and Zirconium Compounds,” *J. Eur. Ceram. Soc.*, vol. 19, no. 13–14, pp. 2405–2414, Oct. 1999.

[17] E. J. Opila, J. Smith, S. R. Levine, and M. Reigel, “Oxidation of $TaSi_2$-Containing ZrB_2-SiC Ultra-High Temperature Materials,” *Open Aerosp. Eng. J.*, vol. 3, pp. 41–51, 2010.

[18] D. Sciti, L. Silvestroni, and M. Nygren, “Spark Plasma Sintering of Zr- and Hf-Borides with Decreasing Amounts of $MoSi_2$ as Sintering Aid,” *J. Eur. Ceram. Soc.*, vol. 28, no. 6, pp. 1287–1296, 2008.

[19] J.-G. Song, “Oxidation Behavior of ZrB_2–YAG–Al_2O_3 Ceramics at High Temperature,” *Mater. Manuf. Process.*, vol. 25, no. 8, pp. 724–729, Jul. 2010.

[20] S. Otani, T. Aizawa, and N. Kieda, “Solid Solution Ranges of Zirconium Diboride with Other Refractory Diborides: HfB_2, TiB_2, TaB_2, NbB_2, VB_2 and CrB_2,” *J. Alloys Compd.*, vol. 475, no. 1–2, pp. 273–275, May 2009.

[21] M. Pourbaix, *Atlas of Electrochemical Equilibria in Aqueous Solutions*, 2nd edition. National Association of Corrosion, 1974.

[22] T. A. Parthasarathy, R. A. Rapp, M. Opeka, and R. J. Kerans, “A Model for the Oxidation of ZrB_2, HfB_2 and TiB_2,” *Acta Mater.*, vol. 55, no. 17, pp. 5999–6010, Oct. 2007.

[23] W. C. Tripp, H. H. Davis, and H. C. Graham, “Effect of SiC Addition on Oxidation of ZrB_2,” *Am. Ceram. Soc. Bullitin*, vol. 52, no. 8, pp. 612–616, 1973.

[24] J. B. Berkowitz-Mattuck, “High-Temperature Oxidation,” *J. Electrochem. Soc.*, vol. 113, no. 9, p. 908, 1966.

[25] S. R. Levine, E. J. Opila, M. C. Halbig, J. D. Kiser, M. Singh, and J. A. Salem, “Evaluation of Ultra-High Temperature Ceramics for Aeropropulsion Use,” *J. Eur. Ceram. Soc.*, vol. 22, no. 14–15, pp. 2757–2767, 2002.

[26] J. Li, T. J. Lenosky, C. J. Först, and S. Yip, “Thermochemical and Mechanical Stabilities of the Oxide Scale of ZrB_2+SiC and Oxygen Transport Mechanisms,” *J. Am. Ceram. Soc.*, vol. 91, no. 5, pp. 1475–1480, May 2008.

[27] J. S. Knyrim and H. Huppertz, “High-Pressure Synthesis, Crystal Structure, and Properties of the First Ternary Zirconium Borate β-ZrB_2O_5.,” *Z Naturforsch*, vol. 63b, pp. 707–712, Jan. 2008.

[28] H. Deng, E. C. Dickey, Y. Paderno, V. Paderno, and V. Filippov, “Interface Crystallography and Structure in LaB_6–ZrB_2 Directionally Solidified Eutectics,” *J. Am. Ceram. Soc.*, vol. 90, no. 8, pp. 2603–2609, Aug. 2007.

[29] Y. Paderno, V. Paderno, and V. Filippov, “Some Peculiarities of Eutectic Crystallization of LaB_6–$(Ti,Zr)B_2$ Alloys,” *J. Solid State Chem.*, vol. 154, no. 1, pp. 165–167, Oct. 2000.

[30] W.-M. Guo, J. Vleugels, G.-J. Zhang, P.-L. Wang, and O. Van der Biest, “Effects of Re_2O_3 (Re = La, Nd, Y, and Yb) Addition in Hot-pressed ZrB_2–SiC Ceramics,” *J. Eur. Ceram. Soc.*, vol. 29, no. 14, pp. 3063–3068, Nov. 2009.

[31] S. R. Whitman and K. S. Raja, “Formation and Electrochemical Characterization of Anodic ZrO_2–WO_3 Mixed Oxide Nanotubular Arrays,” *Appl. Surf. Sci.*, vol. 303, pp. 406–418, Jun. 2014.

[32] K. Shugart, B. Patterson, D. Lichtman, S. Liu, and E. Opila, “Mechanisms for Variability of ZrB_2-30 vol% SiC Oxidation Kinetics,” *J. Am. Ceram. Soc.*, vol. 97, no. 7, pp. 2279–2285, Jul. 2014.

[33] M. Miller-Oana and E. L. Corral, “High-Temperature Isothermal Oxidation of Ultra-High Temperature Ceramics Using Thermal Gravimetric Analysis,” *J. Am. Ceram. Soc.*, vol. 99, no. 2, pp. 619–626, Feb. 2016.

CHAPTER 3: Room Temperature Corrosion Behavior of ZrB_2-HfB_2 Solid Solutions in Acidic and Basic Aqueous Environments[2]

3.1 Abstract

Several solid solutions mixtures of ZrB_2 and HfB_2 with and without additives were investigated for corrosion behavior in aqueous solutions in a wide range of pH. The samples were prepared through ball milling followed by spark plasma sintering (SPS). In addition to the single component diborides and mixtures thereof, additives of Hf, Zr, and Ta pure metals as well as LaB_6 and Gd_2O_3 were mixed in to test for corrosion improvements. Several electrochemical methods were employed including potentiostatic polarization, potentiodynamic polarization and electrical impedance spectroscopy (EIS). The results showed that mixed diboride solid solutions had better corrosion resistance than their unmixed counterparts. ZrB_2-rich compositions performed better in the high pH solutions; whereas HfB_2-rich compositions showed better corrosion resistance under acidic conditions. Metal-rich compositions and Ta additions did not show improvements in the corrosion resistance, the addition of LaB6 to the $Hf_{0.5}Zr_{0.5}B_2$ solid solution, however, exhibited enhanced corrosion resistance in non-acidic solutions

3.2 Introduction

Hexagonally structured transition metal diborides such as ZrB_2, HfB_2, TiB_2, etc. are used in high temperature applications where properties such as high melting point, good thermal and electrical conductivity, and thermal shock resistance are required.[1,2] The potential applications included: electrode coatings for direct power extraction from coal fired MHD plants, turbine blades, rocket nozzles, crucibles, thermocouple sheathes, insulating tiles for re-entry space shuttles and protective coating materials in reactor vessels.[3,4] Transition metal diborides could also find applications as protective coating materials at low temperatures. It has been reported that TiB_2, a similar transition metal diboride, exhibited corrosion resistance at low temperature between 25– 65 °C in a 3.5% NaCl solution due to a protective oxide film.[5] Hot pressed ZrB_2 (with the addition of

[2] This chapter has been published and is reproduced with permission from Elsevier as shown in Appendix A: Sitler, S. J., Charit, I., Raja, K. S. "Room Temperature Corrosion Behavior of ZrB_2-HfB_2 Solid Solutions in Acidic and Basic Aqueous Environments" *Electrochimica Acta*. **246**, 173–189 (2017), DOI: 10.1016/j.electacta.2017.06.033.

$2.5_{wt\%}$ Si_3N_4 as a sintering aid) showed passivity in acid chloride and perchlorate aqueous solutions at 45 °C, and active corrosion in acid fluoride solution, it also showed active-passive behavior in acid sulfate and oxalate solutions. [6]

A composite material of ZrB_2-$20v_{ol\%}$ SiC sintered using $25_{wt\%}$ Si_3N_4 as a sintering aid, showed corrosion behavior similar to that of the single component ZrB_2 material in acid chloride solution. No galvanic coupling between ZrB_2 and cathodic SiC phase was reported. A lower corrosion rate was observed in the ZrB_2/SiC composite than that of the monolithic ZrB_2 in acid sulphate solution.[7] Corrosion of ZrB_2 in its particulate form was reported by Lee et al.[8]; these authors investigated the corrosion of ZrB_2 powder during wet processing conditions in static water at different pH conditions (pH 3-11) and the effect of adding Polyethylenimine (PEI) having different molecular weights as a corrosion inhibitor. A thin hydroxide layer of $Zr(OH)_4 \bullet nH_2O$ was observed to form during the corrosion of ZrB_2 powder during ball milling in aqueous environments but the corrosion was not found to be significant. Pressureless sintered composites of ZrB_2-$20_{vol\%}MoSi_2$ showed poor resistance to corrosion attack in 1.8 M H_2SO_4 at 70 °C as well as at lower temperatures.[9] The secondary phase of $MoSi_2$ was found to be more stable than ZrB_2 under the test conditions. Lavrenko et al.[10] investigated the corrosion behavior of ZrB_2-$MoSi_2$ composite specimens in 3% NaCl solution. The samples exhibited potential-independent current densities during anodic polarization above 0.5 $V_{Ag/AgCl}$, which were in the range of 0.1–1 mA/cm^2. ZrB_2 showed a current density of 1 mA/cm^2 that decreased with the $MoSi_2$ content of the specimens down to 0.1 mA/cm^2. Wang et al.[11] investigated the corrosion behavior of ZrB_2-$20v_{ol\%}$SiC-$15_{vol\%}$G (graphite) composite samples in Cl^- and SO_4^{2-} containing alkaline (pH 13) and acidic (pH 1) solutions. Both ZrB_2 and the ZrB_2-SiC-G composite specimens showed better corrosion resistance to acidic chloride attack than to the attack of SO_4^{2-} containing acid and alkaline solutions. The presence of SO_4^{2-} ions caused the formation of soluble $ZrO(SO_4)_2^{2-}$ specimen through the following reaction:[12]

$$ZrO_2 + 2SO_4^{2-} + 2H^+ \rightarrow [ZrO(SO_4)_2]^{2-} + H_2O \quad (1)$$

Monticelli et al.[12] investigated the corrosion behavior of HfB_2 in Cl^- and SO_4^{2-} containing pH 1 and pH 13 solutions. The addition of Si_3N_4 as a sintering aid resulted in the formation of secondary phases such as: 7% BN, 4% Si, HfO_2 and (Hf(C, N, O)) compounds. These secondary phases were subjected to chemical dissolution depending on the pH of the solution. The acid sulfate solution was reported to be more damaging than the alkaline sulfate or acid chloride solutions. The corrosion of

ZrB_2 or HfB_2 was related to the stability of the soluble Zr(IV) or Hf(IV) complexes formed with the anions present in the aqueous solution.[6] The stability of the soluble complexes increased with the trend:

$$[ZrCl_6]^{2-} < [ZrO(SO_4)_2]^{2-} < [Zr(C_2O_4)_3]^{2-} < [ZrF_6]^{2-}$$

Therefore, fluoride ions will be more aggressive than their chloride counterparts. Since $[ZrCl_6]^{2-}$ has lower stability, a continuous ZrO_2 film would form on the surface that would protect the ZrB_2 from further corrosion in chloride containing solution. The formation of a passive layer would follow Reaction (2):[6]

$$ZrB_2 + 8H_20 \rightarrow ZrO_2 + 2H_3BO_3 + 10H^+ + 10e^- \quad (2)$$

Diborides have layered structures and mixed bonding such as metallic bonding between the transition metal atoms, covalent bonding between the boron atoms and ionic bonding between the metal and boron layers.[13] The fraction of ionic bonding is ambiguous. One report suggests that the ionic bonding character as less than 8% and covalent hybridization between (transition metal) TM and B is occurring.[14] On the other hand, Lawson et al.[13] showed no charge localization occurring between Zr-B atoms or across the (TM)/B layers based on their electron localization function (ELF) calculations and therefore considered the bonding between the (TM)/B layers as ionic. The high electrical conductivity[15] and the ability to fusion weld the ZrB_2-HfB_2[16] indicate predominantly metallic behavior. The polished surfaces of the transition metal diborides also have metallic luster. Fahrenholtz et al.[15] assigned formal charges to TM at TM^{2+} and to B as B^-. On the other hand, Lawson et al.[13] performed Bader charge analysis and showed Zr to lose 1.43 electrons and Hf to lose 1.44 electrons making the formal valance state of TM as $TM^{1.43+}$. For simplicity, the valance state of TM for the diborides in this study is considered to TM^{2+}. Most of the available literature on aqueous corrosion of transition metal diborides pertains only to single boride systems such as: ZrB_2, HfB_2, TiB_2, or CrB_2,[17] or composite structures such as: ZrB_2-SiC, ZrB_2-$MoSi_2$, and others. Recently, hydrogen evolution reaction (HER) kinetics of ZrB_2-HfB_2 solid solutions with different compositions and metal-rich diboride compositions were reported.[18,19] The HER catalytic activities of the diboride solid solutions were correlated with the electron density of states at the Fermi level. Metal-rich diborides showed higher density of states, higher current density and lower overpotentials for hydrogen evolution. The density functional theory calculations of unmixed borides such as pure ZrB_2 and HfB_2 indicated the presence of a sharp dip in the density of states (DOS) at the Fermi level which is called

a pseudogap.[13] The clear separation of full, bonding states and empty anti-bonding states with a pseudogap was considered to give the material high cohesive properties and chemical stability. Therefore, if the DOS is high at the Fermi level it could be inferred that the catalytic activity is high although the chemical stability may still be low. On the other hand, available literature indicates that metal-rich diborides show better oxidation resistance.[20]

In order to better understand if the diboride solid solutions showing enhanced HER kinetics also possess a higher corrosion resistance when compared to the single component diboride counterparts, a detailed investigation was carried out. In this study, ten different samples were investigated in three different pH conditions using electrochemical polarization techniques. The main objective was to understand the corrosion behavior of solid solutions of HfB_2-ZrB_2 with different compositions as they form continuous solid solutions because of their similar lattice parameters and crystal structures and compare them to the unmixed diboride specimens. Metal-rich diboride specimens were investigated by adding pure Zr or Hf metals to the HfB_2-ZrB_2 solid solutions. Additions of Ta, LaB_6, and Gd_2O_3 to the 1:1 HfB_2-ZrB_2 solid solutions were carried out to study their effects on aqueous corrosion resistance. Recently, Hilmas et al.[4] reported that the addition of transition metals such as Mo or Nb to ZrB_2 improved the oxidation resistance to 1600 °C. The addition of Ta helps improve the high temperature oxidation resistance when present in the surface oxide as Ta^{5+} by decreasing the concentration of oxygen vacancies based on the following reaction given in standard Kroger-Vink notation:[21]

$$Ta_2O_5 + V_O^{\bullet\bullet} \xrightarrow{2\,TMO_2} 2\,Ta_{TM}^{\bullet} + 5\,O_O \qquad (3)$$

Here, $V_{Ö}$ represents the oxygen vacancy with a +2 charge. Additions of La and Gd in the form of LaB_6 and Gd_2O_3 are also expected to improve the high-temperature oxidation resistance by impeding the outward diffusion of transition metals into the oxide layer by segregated La^{3+} and Gd^{3+} ions pinning the misfit edge dislocations.[22]

3.3 Experimental Section

Commercially available HfB_2 and ZrB_2 powders (15 µm, 99.5% purity) were used individually as well as mixed in 1:1, 1:4 and 4:1 molar ratios. The 1:1 molar ratio solid solution was used as the base composition to which Hf (–325 mesh, 99.6% purity), Zr (–325 mesh, 98.8%), or Ta (–325 mesh, 99.9%) pure metals were added to bring the molar ratio of boron-to-metal down to 1.86 ($MeB_{1.86}$).

In addition, two more samples were created by mixing $1.8_{mol\%}$ of LaB_6 (–325 mesh, and 99.5% purity) or Gd_2O_3 (20–40 nm, 99.99% purity) to the 1:1 molar ratio solid solution. All raw materials were procured from Alfa Aesar. The pure metal additions were carried out inside a glove box in an ultra-high purity (UHP) argon atmosphere (M. Braun Inert Gas-Systeme GmbH).

The 10 different sample powders were ball milled for 3 hours in a zirconia vial using 6.5 mm diameter yttria-stabilized spherical zirconia grinding media (Inframat Advanced Materials LLC, Manchester, CT). A 1:10 powder-to-ball mass ratio was used. This was followed by sintering using a spark plasma sintering machine (Fuji electronics, Japan, model: Dr. Sinter SPS–515 S). A 20.6 mm Isocarb-85 graphite die was used with 5 kN of applied force at 1700 °C for 600 seconds under a 10^{-3} Torr vacuum.

The sintered pellets were cut into pie piece-shapes of about 0.4 cm^2 exposed area. A highly conductive silver epoxy was used to attach copper wires to the back sides of the pie pieces which were then embedded in acrylic to expose only the top surface. The samples were then polished to at least a 1 µm surface finish. The samples were characterized using field emission scanning electron microscope (FESEM) LEO Supra 35VP (Zeiss, Jena, Germany) and Xray diffraction patterns (XRD) were obtained using a D5000 Diffractometer (Siemens AG, Munich, Germany) at a scan rate of 0.02° and a hold time of 5 seconds. Energy dispersive X-ray spectroscopy (EDS) was used to analyze chemical composition of the samples and oxide layers. Spectra were obtained using an accelerating voltage of 20 kV. The density was also measured for each of the sintered pellets using the Archimedes' principle by following the ASTM standard B311-08.

Potentiodynamic polarization studies were carried out using a potentiostat (make: Gamry Instruments, model: Interface 1000) and the samples were anodically polarized by scanning the potential from open circuit potential (OCP) to +5 $V_{Ag/AgCl}$ using a 1 mV/s scan rate in four different electrolytes: 0.1 M H_2SO_4, 0.1 M NaCl, 0.1 M NaOH, and 0.1 M NaOH + 0.1 M NaCl. A platinum counter electrode (3.75 cm^2) was used along with an Ag/AgCl reference electrode immersed in saturated KCl salt bridge (Reference potential: 199 mV vs. SHE). Potentiostatic passivation of the samples was carried out at 0.2 $V_{Ag/AgCl}$ for 1 hour. Electrochemical impedance spectroscopy (EIS) studies were carried out immediately after passivating the samples under potentiostatic control at 0.2 $V_{Ag/AgCl}$ as a standard means of understanding the passivation film characteristics by superimposing an AC voltage of 10 mV and scanning the frequency from 100 kHz to 0.01 Hz in three different electrolytes: 0.1 M H_2SO_4, 0.1 M NaCl, 0.1 M NaOH. All electrochemical tests were carried out at room temperature. The

volume of electrolyte was 150 ml. Neither aeration nor de-aeration of the electrolyte was carried out. The current was normalized with geometric area of the samples to calculate the current densities. The tests were duplicated and in some cases triplicated to verify the reproducibility. The results shown in this manuscript are the best of the 2-3 tests for each sample in each test condition. A Thermo-Scientific DXR dispersive Raman microscope was used to characterize the Raman vibrational modes of the potentiostatically passivated samples. Raman spectra were obtained for individual spots with a diameter of 0.7 µm with four exposures of 8 seconds at 100 X magnification using a 532 nm laser operated at 10 mW

3.4 Results & Discussion

3.4.1 Materials Characterization

Table 3.1 summarizes the sample compositions, sample identifiers, and relative density. These sample identifiers will be used throughout the manuscript.

Table 3.1: Sample identifiers used throughout manuscript and relative densities.

Sample molar contents	*Sample Identifier used*	*Relative Density (% of theoretical density)*
HfB_2	A	91.4
ZrB_2	B	87.2
$Hf_{0.5}Zr_{0.5}B_2$	AB	76.2
$Hf_{0.8}Zr_{0.2}B_2$	4AB	76.5
$Hf_{0.2}Zr_{0.8}B_2$	A4B	82.9
$Hf_{0.5}Zr_{0.5}B_2$ + $1.8_{mol\%}$ Gd_2O_3	ABG	89.5
$Hf_{0.5}Zr_{0.5}B_2$ + Hf (B/Me =1.86)	ABH	96.2
$Hf_{0.5}Zr_{0.5}B_2$ + $1.8_{mol\%}$ LaB_6	ABL	97.2
$Hf_{0.5}Zr_{0.5}B_2$ + Ta (B/Me =1.86)	ABT	94.6
$Hf_{0.5}Zr_{0.5}B_2$ + Zr (B/Me =1.86)	ABZ	94.8

Figure 3.1(a)-(e) shows the FESEM microstructures of the spark plasma sintered HfB_2, ZrB_2 and HfB_2-ZrB_2 solid solutions with ratios of 1:1, 4:1 and 1:4. Figure 3.1(f) shows the XRD results of the samples. Because these borides have hexagonal crystal structures with very similar lattice parameters, when mixed, they form a continuous solid solution with lattice parameters lying between the lattice parameters of the unmixed HfB_2 and ZrB_2. The XRD results confirmed that a complete solid solution formed at different ratios of HfB_2 to ZrB_2, as the peaks of $Hf_xZr_{1-x}B_2$ samples were placed between the corresponding peaks of pure HfB_2 and ZrB_2. These results are similar to the conclusions drawn by Otani et al.,[23] who reported perfect and continuous solid solutionizing

between HfB_2 and ZrB_2. The lattice parameters were calculated from the XRD spectra and are summarized in Table 3.S1 (supporting information). The minor peaks observed in the XRD patterns

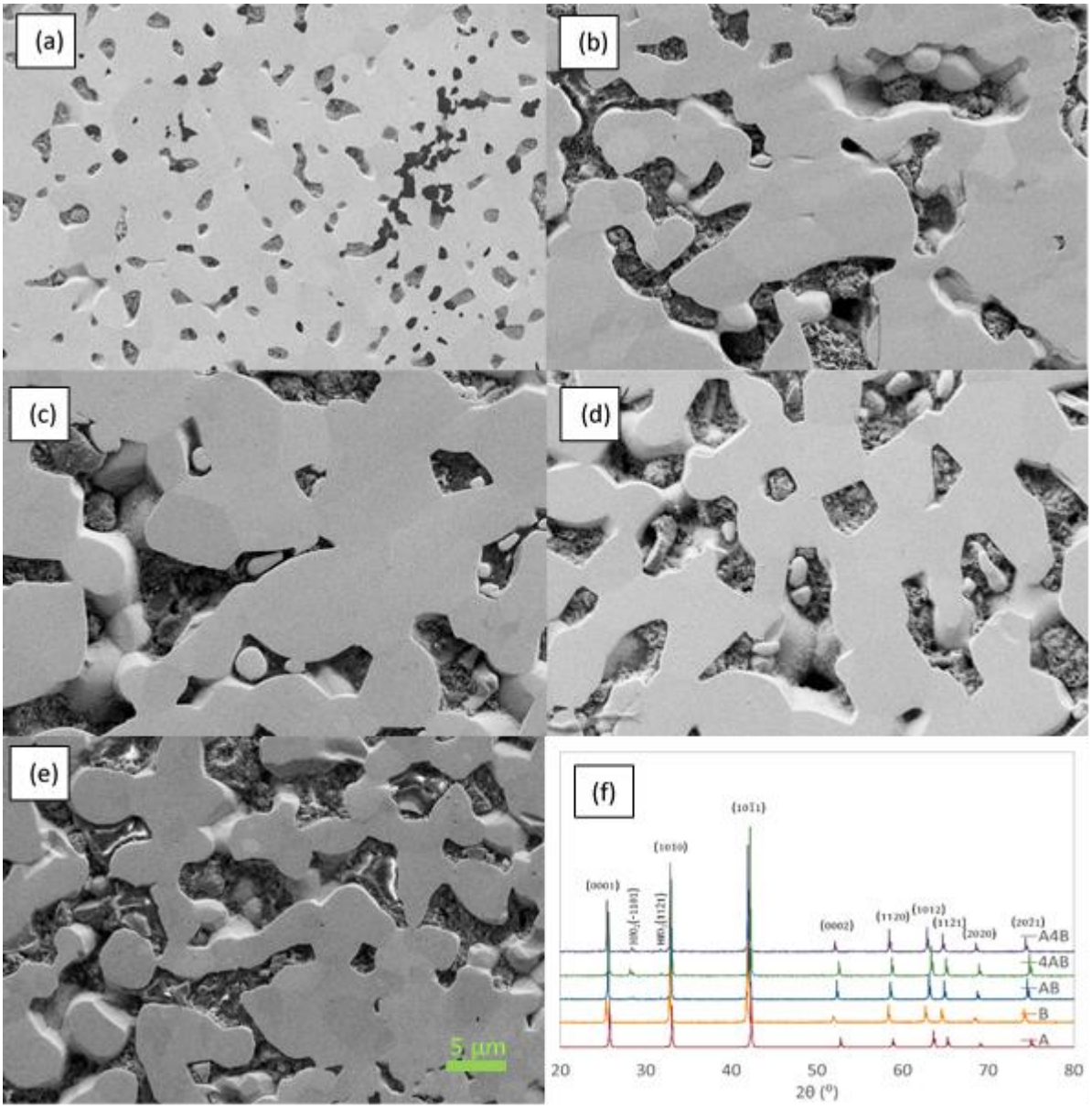

Figure 3.1: SEM micrographs at 2500 X magnification of samples from Table 3.1: A in (a), B in (b), AB in (c), 4AB in (d) and A4B in (e). (f) shows the corresponding XRD spectra for these samples where indices without compound labels are ZrB_2 and HfB_2.

of AB, 4AB and A4B samples between 25 - 30° were identified as monoclinic phases of HfO_2/ZrO_2. These oxides were predominantly present at the porosities. These oxides will have low electrical conductivity. However, the electrical conductivity of the samples was not significantly affected by the presence of the oxide as the measured electrical resistance was less than 0.5 V. A typical result of the

I–*V* plot of samples AB and ABL for measuring the resistance is given in Figure 3.S1 (supporting information). Since the oxide would chemically dissolve during the electrochemical polarization in the test environments, it may not affect the corrosion current values.

Figure 3.S2 (supporting information) shows the energy dispersive X-ray analyses of different locations on the AB sample. The results indicated that the inside of the grain consisted of a solid solution of HfB_2-ZrB_2 whereas, the small particles interlocked between two boride grains showed high oxygen content indicating oxidization of the boride phase. The analyses were carried out on multiple locations over duplicate samples. The results are similar to the ones presented in Figure 3.S2 (supporting information). It should be noted that the EDS analysis was carried out on a sample that was previously electrochemically tested and then metallographically polished. Therefore, the oxidation of diborides could have occurred during sintering, polishing or previous electrochemical testing. Moreover, the quantitative analysis of oxygen and boron using EDS may not be accurate.

Figure 3.2(a)-(e) shows the FESEM microstructures of the 1:1 HfB_2- ZrB_2 solid solutions samples with additions of Hf, Zr, or Ta rendering the samples metal-rich with a boron to metal ratio of 1.86 as well as the samples with the additions of LaB_6 or Gd_2O_3. Figure 3.2(f) shows the XRD results of these 'additive' samples. Like the HfB_2 and ZrB_2 mixtures, the metal-rich borides were also found to be single phase structures based on the XRD results. Only peaks belonging to the hexagonal structure of the 1:1 stoichiometric sample (AB) were observed for all samples except for sample ABG which contained two additional Gd_2O_3 peaks. Since Gd_2O_3 is an oxide with a different crystal structure, solid solutionizing did not occur and the additional two peaks were observed. Interestingly, sample ABL with the addition of $1.8_{mol\%}$ LaB_6 did form a complete solid solution with HfB_2-ZrB_2, since no additional peaks corresponding to LaB_6 were found in the XRD spectra, even though the crystal structures are different. The lattice parameters of the additive samples were calculated and are tabulated in Table 3.S1 (supporting information). The 'metal-rich' borides could also be viewed as 'boron-poor' leading to boron vacancies. Having boron vacancies may alter the electron configurations in the nearest neighbors and therefore, may change the metal-boron (M-B) and boron-boron (B-B) bond lengths. Some of the metal atoms are likely occupying boron vacancy anti-sites, this would lead to the metal-metal (M-M) bond lengths also being modified.[24] Changes to these bond lengths results in a reduction of the lattice parameters and could also modify the density of states and the electron band structures.

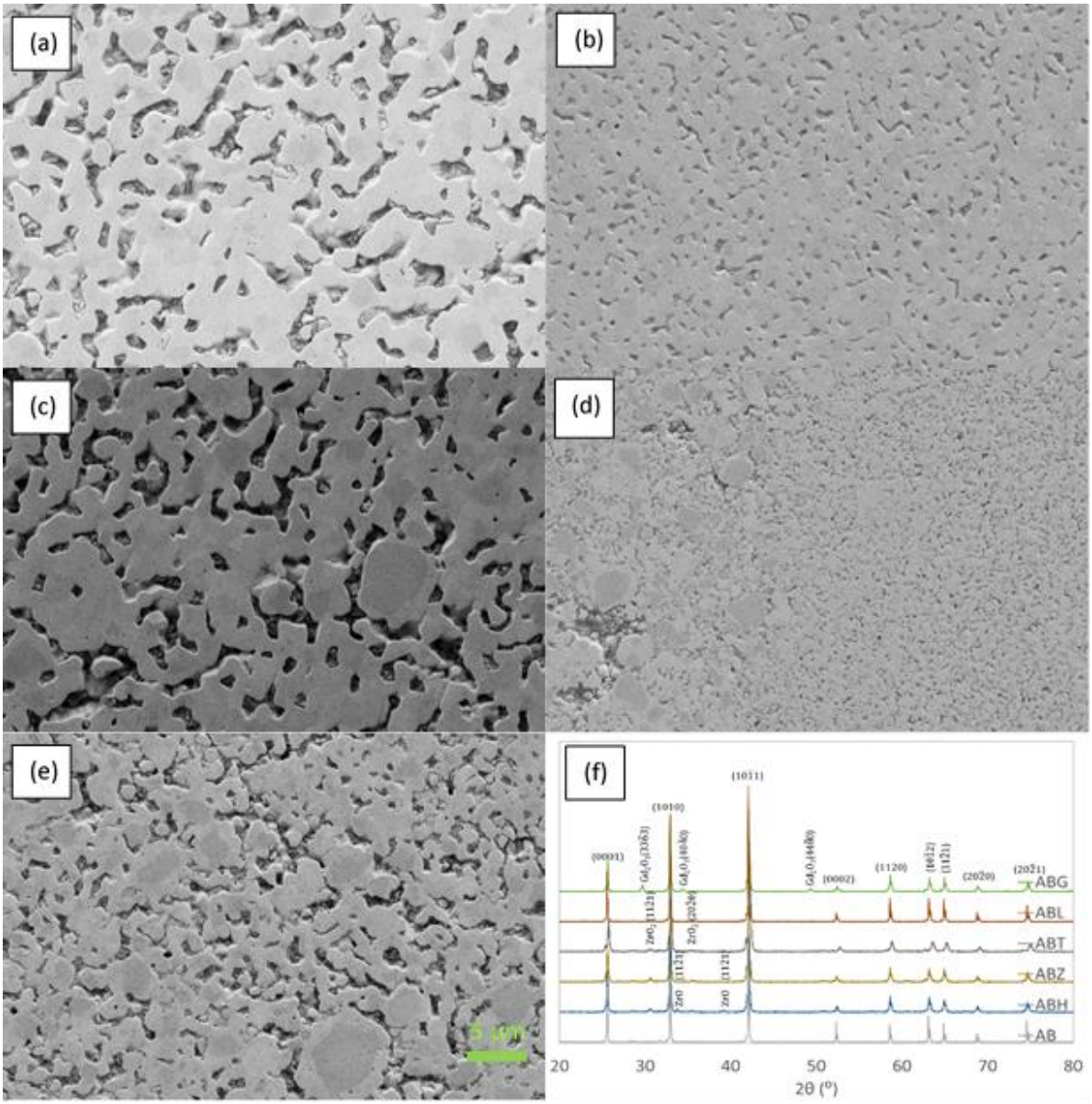

Figure 3.2: SEM micrographs at 2500 X magnification of samples from Table 3.1: ABG in (a), ABH in (b), ABL in (c), ABT in (d) and ABZ in (e). (f) shows the corresponding XRD spectra for these samples where indices without compound labels are ZrB_2 and HfB_2.

3.4.2 Potentiodynamic Polarization

3.4.2.1 Anodic polarization in acidic solution (0.1 M H_2SO_4)

Figure 3.3(a), with a potential up to 1 $V_{Ag/AgCl}$, shows the anodic polarization plots of the unmixed and mixed diboride samples in 0.1 M sulfuric acid solution. The open circuit potential (OCP) of HfB_2 was more active than that of ZrB_2 in 0.1 M H_2SO_4. Samples A and AB showed similar OCPs at

about -0.25 $V_{Ag/AgCl}$ and samples B, 4AB and A4B showed similar OCPs at around 0.05 $V_{Ag/AgCl}$. All the samples revealed a passive-like behavior where the current density was not significantly affected by the applied potential. When polarized only up to 1 $V_{Ag/AgCl}$, which is close to the oxygen evolution potential, the HfB_2-$4ZrB_2$ (A4B) sample showed the lowest current density among all the samples in this group, but the current increased with the increase in the potential from 2 µA/cm^2 to 10 µA/cm^2. Both HfB_2 and ZrB_2 specimens showed similar current density of about 50 µA/cm^2 at 1 $V_{Ag/AgCl}$. Samples 4AB and AB showed relatively high current densities of 200 and 760 µA/cm^2 at 1 $V_{Ag/AgCl}$, respectively. The current densities of samples 4AB and AB were more or less constant, irrespective of the applied potential and therefore mimicked a 'passive-like' behavior. Since the current densities were so high, these samples cannot be considered to have passivated. The higher current densities of the samples AB and 4AB could be related to their low relative density of around 76%.

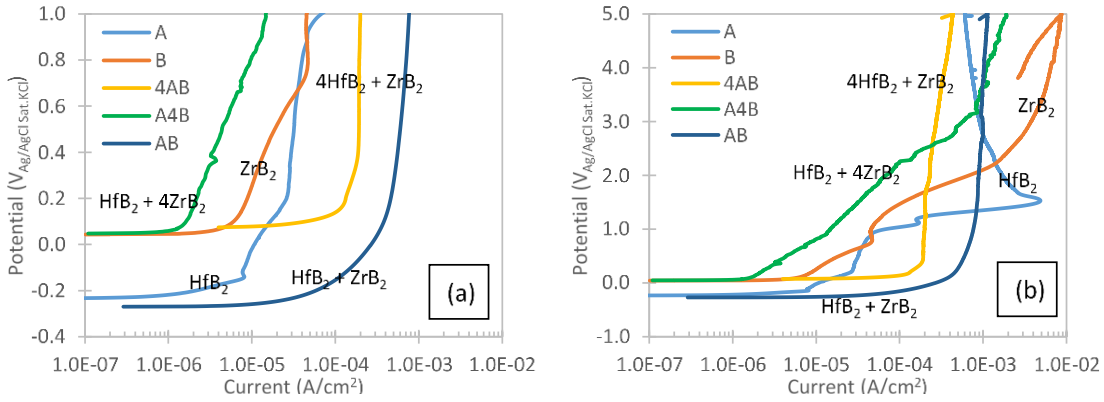

Figure 3.3: Potentiodynamic polarization of the non-additive samples from Figure 3.1 up to 1 $V_{Ag/AgCl}$ in 0.1 M H_2SO_4, (b) up to 5 $V_{Ag/AgCl}$.

Figure 3.3(b) shows the results of these same five samples for anodic polarization in 0.1 M H_2SO_4 up to 5 $V_{Ag/AgCl}$. It should be noted that such high potentials may not represent any practical service environmental condition. However, high potentials may be employed for anodization of the transition metals. Anodization of the diboride samples has been reported[1] earlier and was observed to improve the high-temperature oxidation resistance. Therefore, understanding the electrochemical behavior of the diboride samples at higher potentials will help us understand the formation of surface films and their breakdown character. When the mixed and unmixed ZrB_2 and HfB_2 materials were polarized to 5 $V_{Ag/AgCl}$, very high anodic current densities were observed as seen in Figure 3.3(b). The samples that contained high porosity (or low apparent density) such as 4AB and AB revealed 'passive-like' behavior but with relatively high current densities 0.5 and 1 mA/cm^2, respectively, at 5 $V_{Ag/AgCl}$.

When the potential scan was reversed, the current density decreased indicating that the samples were in a pseudo-passive condition.

Samples A, B, and A4B showed active-passive behavior when polarized to potentials greater than 1 $V_{Ag/AgCl}$. The current density abruptly increased to ~4.43 mA/cm^2 at 1.5 $V_{Ag/AgCl}$ in the case of HfB_2 and started to decrease when the polarization continued to higher potentials. Whereas, the B and A4B samples did not show a threshold current density, like HfB_2 did, before reaching a passive-like condition. The ZrB_2 sample showed the highest current density of 8.4 mA/cm^2 at 5 $V_{Ag/AgCl}$. Considering a formal divalent charge on the transition metals present in the diborides, the anodic current densities could be attributed to the following oxidation reactions:[25]

$$TM \rightarrow TM^{4+} + 4e^- \quad (4)$$

$$TM^{4+} + 2H_2O \rightarrow TMO_2 + 4H^+ \quad (5)$$

$$2B + 6H_2O \rightarrow 2H_3BO_3 + 6H^+ + 6e^- \quad (6)$$

And the overall reaction could be given as:[6]

$$TMB_2 + 8H_2O \rightarrow TMO_2 + 2H_3BO_3 + 10H^+ + 10e^- \quad (7)$$

The presence of sulfate could result in the following reaction:

$$TMO_2 + 2SO_4^{2-} \rightleftharpoons [TMO(SO_4)_2]^{2-} + H_2O \quad (8)$$

Since the solution complex $[TMO(SO_4)_2]^{2-}$ is considered to be highly stable, Reaction (8) proceeds much more favorably in the left-to-right direction in acidic solutions and thus results in dissolving the protective oxide.

Therefore, the high current densities recorded during anodic polarization of the samples could be attributed to the dissolution of the protective oxide film in the form of soluble sulfate complexes. The potential-independent current density recorded which mimics a passivation-like behavior was most likely the result of dissolution and re-precipitation of the sulfate complex on the surface.

Formation of complexes is more likely for Zr(IV) than for Hf(IV) due to the electron configuration of Zr and its relatively small charge density.[26] Table 3.2 shows the stability constants of sulfate and chloride complexes for Zr(IV) and Hf(IV) with an ionic strength of 2.[27]

Table 3.2: Reported stability constants for sulfate and chloride complexes of Zr(IV) and Hf(IV) at ionic strength of 2 (from Ref. 27)

Stability Constant for each step of reaction	*Sulfate*		*Chloride*	
	Zr(IV)	Hf(IV)	Zr(IV)	Hf(IV)
β_1	466	130	0.95	0.95
B_2	3.48×10^3	2.1×10^3	0.12	0.12
β_3	3.92×10^6	3.02×10^6	0.07	0.07
β_4	-	-	0.08	0.08

The complexation reaction involving sulfate can be written as: [27]

$$M^{4+} + nHSO_4^- \rightleftharpoons M(SO_4)_n^{4-2n} + nH^+ \quad (9)$$

The stability constant, β_i, for the i^{th} step is given as:

$$\beta_i = \frac{[M(SO_4)_i^{4-2i}]\,[H^+]^i}{[M^{4+}]\,[HSO_4^-]^i} \quad (10)$$

From Table 3.2, it can be seen that the tendency to form a complex with sulfate ions is significantly higher for the Zr(IV) than for the Hf (IV). Therefore, samples with higher ZrB_2 content showed larger current densities at higher potentials. On the other hand, at low potentials (< 1 $V_{Ag/AgCl}$), samples of AB, 4AB, and A, having higher HfB_2 contents, showed larger current densities. This could be associated with the porosity level of the samples and also the oxidation kinetics. It is noteworthy that complexation is a chemical reaction and requires the transition metal to be in the ionized or oxidized state. The ability of Zr(IV) to, relatively easily, form stable complexes, destabilizes the protective oxide and thereby increases the dissolution current.

Based on the OCP values and the polarization current densities, it can be seen that the hafnium based samples showed a more active condition for oxidation than the zirconium based samples, but at the same time had a lower stability for complexation reactions. Therefore, the current density of HfB_2 was higher at low anodic potentials than that of ZrB_2. When the potential was high, the corrosion rate was not determined by the ionized species of the metal, but by the stability of the sulfate complex.

Figure 3.4(a) shows the polarization plots of HfB_2-ZrB_2 (1:1) solid solution (AB) with additions of Hf, Zr, or Ta, making them $MB_{1.86}$ as well as the additions of LaB_6 and Gd_2O_3. Compared to the base line sample, AB, additions of Hf, LaB_6, and Gd2O3 decreased the current density by about an order of magnitude. It was initially considered that the improved corrosion resistance of the samples ABH, ABL, and ABG should be solely attributed to the lower porosity level when compared to AB. However,

this was incorrect and the improvement cannot be attributed solely to the higher relative density because ABT had a similar porosity level compared to ABH, while the corrosion behavior was very different. This leads to the conclusion that the difference came down to the effect of the additives.

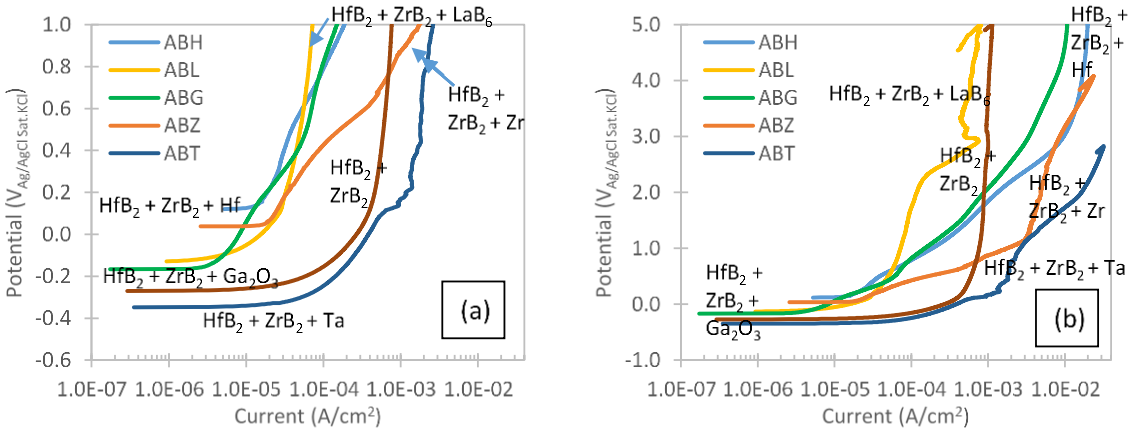

Figure 3.4: (a) Potentiodynamic polarization of the additive samples from Figure 3.2 up to 1 $V_{Ag/AgCl}$ in 0.1 M H_2SO_4, (b) up to 5 $V_{Ag/AgCl}$.

The addition of Ta to the diboride solid solution is considered to result in the following reactions with sulfuric acid:

$$Ta^{2+} \rightarrow Ta^{5+} + 3e^- \quad (11)$$

$$Ta^{5+} + 5H_2O \rightleftharpoons Ta(OH)_5 + 5H^+ \quad (12)$$

$$Ta(OH)_5 + HSO_4^- \rightleftharpoons [Ta(OH)_4(SO_4)]^- + H_2O \quad (13)$$

$$[Ta(OH)_4(SO_4)]^- + HSO_4^- \rightleftharpoons [Ta(OH)_3(SO_4)_2]^{2-} + H_2O \quad (14)$$

$$[Ta(OH)_3(SO_4)_2]^{2-} + HSO_4^- \rightleftharpoons [Ta(OH)_2(SO_4)_3]^{3-} + H_2O \quad (15)$$

Even though Ta ions can exist at Ta^{5+}, Ta^{4+} and Ta^{3+}, the stable state is Ta^{5+}. Tantalum ions are considered to be unstable in aqueous solutions as they are readily hydrolyzed even in very acidic solutions as described in Reaction (12).[28]

In acidic sulfate and chloride solutions, tantalum species form anodic ions by complexing with HSO_4^- and Cl^-. The complexation reactions of Ta are given in reactions (13)–(15). Sulfuric acid is used for extraction of lanthanides from slag by selective leaching at low temperatures (< 80 °C) and relatively low concentrations (0.3–3 M).[29,30] Therefore, preferential dissolution of La and Gd could

be expected under external bias conditions in 0.1 M H_2SO_4 at room temperature. The dissolution reaction can be given as:

$$LaB_6 + 18H_2O \rightarrow La^{3+} + 6H_3BO_3 + 18H^+ + 21e^- \quad (16)$$

It is documented that La^{3+} and Gd^{3+} ions are hydrated with nine equidistantly spaced water molecules in the inner hydration.[25,26] The presence of SO_4^{2-} leads to a stable complex formation with $[La^{3+}\bullet 9H_2O]$ following the reaction:

$$[La(H_2O)_9]^{3+} + nHSO_4^- \rightleftharpoons [La(H_2O)_{9-n}(SO_4)_n]^{3-2n} + nH_2O + nH^+ \quad (17)$$

For Gd_2O_3, a similar dissolution and complexation reaction could be written where Gd^{3+} ions complex with sulfate ions and dissolve. [31] It is reported that Gd^{3+} forms a more stable complex with Cl- and SO_4^{2-} when compared to its La^{3+} counterpart.[32] Therefore, the higher current density observed for ABG compared to ABL can be explained based on the relative stability of the sulfate complexations, in addition to the relatively higher porosity level of the ABG sample. Furthermore, the relative corrosion resistance of the samples can be explained based on their electron densities of states (DOS).

Figure 3.4(b) shows the polarization plots of samples ABG, ABH, ABL, ABT, and ABZ up to 5 $V_{Ag/AgCl}$ in 0.1 M H_2SO_4. Samples ABT, ABZ, and ABH showed active corrosion behavior when the potentials increased above 1 $V_{Ag/AgCl}$. Only the ABL sample showed a potential-independent current behavior. In general, the limiting current behavior could be associated with limited mass transport of cation species from the working electrode surface to the bulk solution.[33] During the anodic polarization, the concentrations of metal cations such as Zr^{4+}, Hf^{4+}, La^{3+}, etc. increase with the increase in the current density near the surface until they reach the saturation limit. Further increase in the concentration of the metal cations causes precipitation of a salt layer in the form of a hydrolyzed species M(OH)*n*, leading to a sulfate complex, $[M(OH)n(SO_4)m]^{-x}$. The presence of a precipitated surface layer on the working electrode which is porous in nature limits the migration of the oxidized metal cations to the electrolyte. This results in a transport limited current density in spite of the increase in the anodic polarization. Even though sample ABL showed limiting current behavior and lower current density than that of sample AB, the corrosion rate of ABL was higher than those of samples A and 4AB at 5 $V_{Ag/AgCl}$. Sample 4AB showed the lowest current density at the highest polarization potential of 5 $V_{Ag/AgCl}$ in 0.1 M H_2SO_4 for this study.

3.4.2.2 Anodic polarization in near-neutral 0.1 M NaCl (pH unadjusted)

Figure 3.5(a) shows the anodic polarization plots of the unmixed and mixed solid solution stoichiometric diboride samples (A, B, AB, A4B, and 4AB) up to 1 $V_{Ag/AgCl}$. All of these samples showed active corrosion behavior as the anodic current increased with the increase in the potential. In this group of samples, sample A (HfB_2) showed the lowest current density of about 35 µA/cm^2 at 1 $V_{Ag/AgCl}$. The rest of the samples showed current densities in the range of 0.3-1.5 mA/cm^2 at 1 $V_{Ag/AgCl}$. Samples A and B showed similar OCPs of about -130 $mV_{Ag/AgCl}$. Other samples showed more active OCPs in the range of -325 to -350 $mV_{Ag/AgCl}$. When the polarization continued above 1 $V_{Ag/AgCl}$, the trend of anodic current was different from that observed at low potentials, below 1 $V_{Ag/AgCl}$. At high potentials, as seen from Figure 3.5(b), sample 4AB showed the lowest current density in this electrolyte, just as in the case of the 0.1 M H_2SO_4 electrolyte. Furthermore, this sample showed a limiting current density of 0.375 mA/cm^2 up to 2.15 $V_{Ag/AgCl}$ and an abrupt increase in the current density above this potential, indicating a passivity breakdown-like behavior. When the potential scan was reversed after reaching a current density of ~13 mA/cm^2, a minor hysteresis was observed in the potential current profile. The crossover potential of the reverse scan current plot was lower than the 'passivity breakdown' potential. On the other hand, other samples did not exhibit a passivity breakdown-like behavior. Even though sample A showed low anodic current density at low potentials, the current density increased steeply at about 1.25 $V_{Ag/AgCl}$ and reached about 3.5 mA/cm^2 near 1.85 $V_{Ag/AgCl}$ and 're-passivated' at about 2 $V_{Ag/AgCl}$ with a current density of 1.3 mA/cm^2. The current increased again after reaching a potential of 2.25 $V_{Ag/AgCl}$. Samples with large amounts of ZrB_2, specifically, B, AB, and A4B showed predominately active corrosion behavior in the near-neutral chloride solution. Predominantly HfB_2 samples showed 'active-passive'-like behavior with limiting current. It should be noted that both Zr and Hf showed similar stability constants for the chloride complex as shown in Table 3.2.

Figure 3.6(a) shows the anodic polarization plots of the metal-rich solid solution samples and the samples with additions of LaB_6 or Gd_2O_3 in 0.1 NaCl at potentials up to 1 $V_{Ag/AgCl}$. These samples all showed a similar polarization trend with increasing current densities in the order: ABL < ABH < ABG < ABZ < ABT.

Interestingly, all the samples showed higher current densities than that of sample AB at 1 $V_{Ag/AgCl}$. Therefore, the metal-rich diborides have lower corrosion resistance in the chloride solution at low polarization conditions.

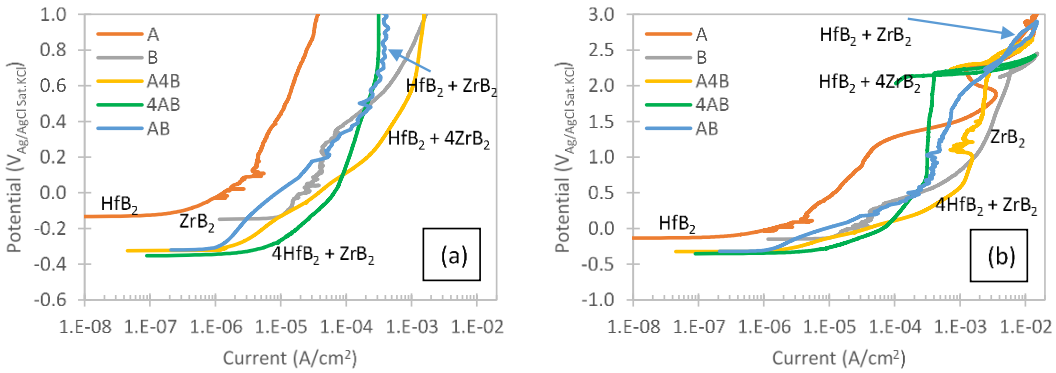

Figure 3.5: (a) Potentiodynamic polarization of the non-additive samples from Figure 3.1 up to 1 $V_{Ag/AgCl}$ in 0.1 M NaCl, (b) up to 3 $V_{Ag/AgCl}$.

Figure 3.6(b) shows the polarization plots at high potentials, up to 3 $V_{Ag/AgCl}$, for the metal-rich solid solution samples and the samples with additions of LaB_6 or Gd_2O_3. Increasing the polarization potential did not alter the ranking of the samples in terms of current densities when compared to Figure 3.6(a). Sample ABL and to some extent sample ABG exhibited a limiting current behavior. Overall, it can be noted that the corrosion resistance in 0.1 M NaCl increased with the increase in the HfB_2 content of the sample. The addition of elemental Hf did not help improve the corrosion behavior of the AB sample because of its high ZrB_2 content.

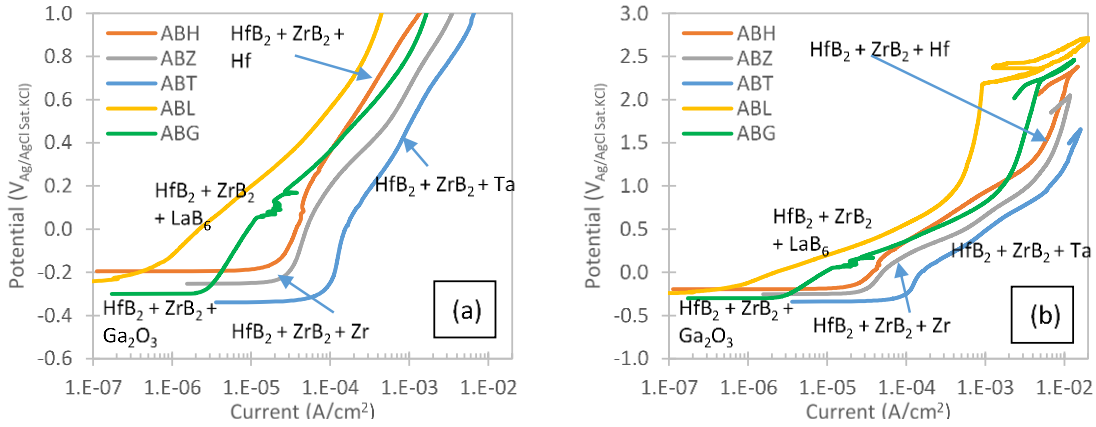

Figure 3.6: (a) Potentiodynamic polarization of the additive samples from Figure 3.2 up to 1 $V_{Ag/AgCl}$ in 0.1 M NaCl, (b) up to 3 $V_{Ag/AgCl}$.

3.4.2.3 Anodic Polarization in basic solution (0.1 M NaOH)

Figure 3.7(a) shows the anodic polarization results of the mixed and unmixed diboride species in 0.1 M NaOH up to 1 $V_{Ag/AgCl}$. In this solution, the oxygen evolution potential is -0.263 $V_{Ag/AgCl}$. A quick look at the polarization plots indicated that oxygen evolution may have only occurred on the

HfB_2 sample. Sample AB showed passivation in the potential range of 0.2-0.7 $V_{Ag/AgCl}$ as the current density was about 6 µA/cm^2. At potentials more than 0.74 $V_{Ag/AgCl}$, the current started to increase. The increase in the anodic current could have two components such as those shown in the following reactions:

$$4OH^- \rightarrow O_{2(g)} + 2H_2O + 4e^- \quad (18)$$

$$TMB_2 + 10OH^- \rightarrow TM(OH)_4 + 2B(OH)_3 + 10e^- \quad (19)$$

$$TM(OH)_4 \rightarrow TMO_2 \bullet 2H_2O \quad (20)$$

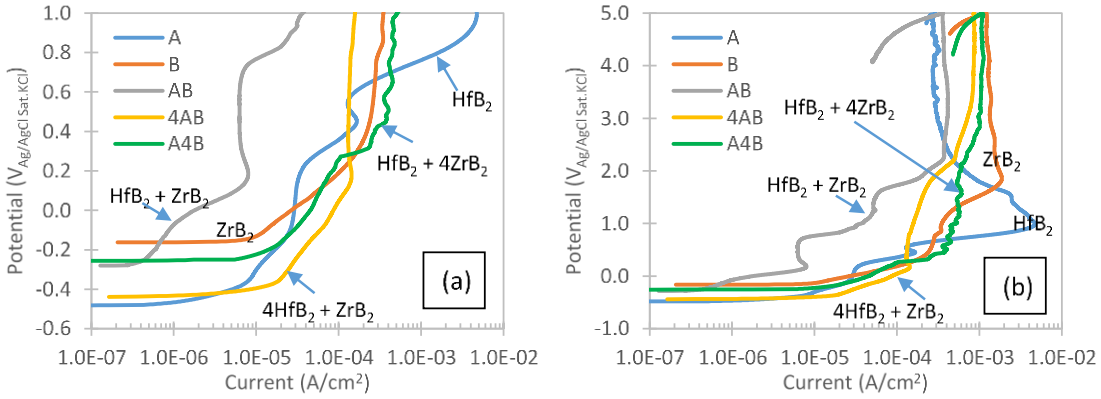

Figure 3.7: (a) Potentiodynamic polarization of the non-additive samples from Figure 3.1 up to 1 $V_{Ag/AgCl}$ in 0.1 M $NaOH_4$, (b) up to 5 $V_{Ag/AgCl}$.

Reaction (20) indicates the presence of hydrated ZrO_2 or HfO_2 on the surface of the sample. The E-pH diagram of Zr-H_2O system indicates that $ZrO_2 \bullet 2H_2O$ will be stable at pH < 13 at all anodic potential conditions. At higher pH conditions, the dissolution product is $HZrO_3^-$ and the stability of $ZrO_2 \bullet 2H_2O$ will increase with the increase in the concentration of $HZrO_3^-$, following reaction:

$$ZrO_2 + H_2O \rightleftharpoons HZrO_3^- + H^+ \quad (21)$$

The $HfO_2 \bullet 2H_2O$ phase is considered to be more stable than $ZrO_2 \bullet 2H_2O$ at high pH conditions based on the E-pH diagram.[25] At pH:13, the stable boron species will be HBO_3^{2-}. The corresponding reaction is given as:

$$B(OH)_3 \rightarrow HBO_3^{2-} + 2H^+ \quad (22)$$

This reaction may decrease the pH locally near the sample surface and disrupt the existing surface layer, as given by the following reactions:

$$TMO_2 + 4H^+ \rightleftharpoons TM^{4+} + 2H_2O \quad (23)$$

$$TM^{4+} + 4H_2O \rightleftharpoons TM(OH)_{4(Aq)} + 4H^+ \quad (24)$$

Therefore, the higher current densities recorded during the anodic polarization could be attributed to the disruption of the surface layer exposing fresh TMB_2 due to local acidification Reactions (22) and (24). However, it should be noted that the solubility product of $TM(OH)_4$ is very small. For example, the solubility product of ZrO_2 is reported as $10^{-62.46}$ by Kobayashi et al.[34] These local acidification, dissolution, and re-precipitation reactions would result in a porous layer on the surface which may not be very protective, especially in the case of B, AB, 4AB, and A4B.

Figure 3.7(b) shows the polarization in 0.1 M NaOH up to 5 $V_{Ag/AgCl}$ of samples A, B, AB, 4AB, and A4B. All of the samples showed limiting current polarization behavior at about 2 $V_{Ag/AgCl}$. Sample A showed active-passive behavior when the polarization continued beyond 1 $V_{Ag/AgCl}$. A maximum current density of 4.6 mA/cm^2 was observed at 1 $V_{Ag/AgCl}$ and the current decreased when the polarization potential continued to increase. A limiting current of 0.28 mA/cm^2 was observed at potentials greater than 3 $V_{Ag/AgCl}$. This limiting current behavior could be described as the diffusion of Hf^{4+} ions limited by the presence of an $HfO_2 \bullet H_2O$ porous film. The porosity of the film was the result of selective leaching of the HBO_3^{2-} ions as described earlier. Sample A showed the lowest current density of 0.27 mA/cm^2 among this group of samples. The highest current density at 5 $V_{Ag/AgCl}$ was recorded for sample B, at 1.23 mA/cm^2. Sample AB showed the second lowest current density of 0.36 mA/cm^2 while the other samples showed current densities between 0.36 and 1.23 mA/cm^2.

Figure 3.8(a) shows the polarization plots for the metal-rich solid solution samples and samples with the additions of LaB_6 or Gd_2O_3 in 0.1 M NaOH at potentials up to 1 $V_{Ag/AgCl}$. Sample A showed the lowest current density in the previous group, as shown in Figure 3.7(a) The polarization results of these samples will be compared with those of AB. As seen in Figure 3.8(a), the current densities of all of those samples were substantially higher than those of AB. The current density of AB at 1 $V_{Ag/AgCl}$ was 36.6 µA/cm^2. Whereas, for the ABL, ABG, and ABH samples, the current densities were 0.137, 0.566, and 0.586 mA/cm^2, respectively, at 1 $V_{Ag/AgCl}$. Sample ABT showed the highest current density of 4.1 mA/cm^2 at 1 $V_{Ag/AgCl}$ among this group of samples. Although this was still slightly lower than that of HfB_2 from Figure 3.7(a), it would be important to point out that sample ABT was

almost constant up to 5 $V_{Ag/AgCl}$ while the current density of sample B dropped by more than an order of magnitude.

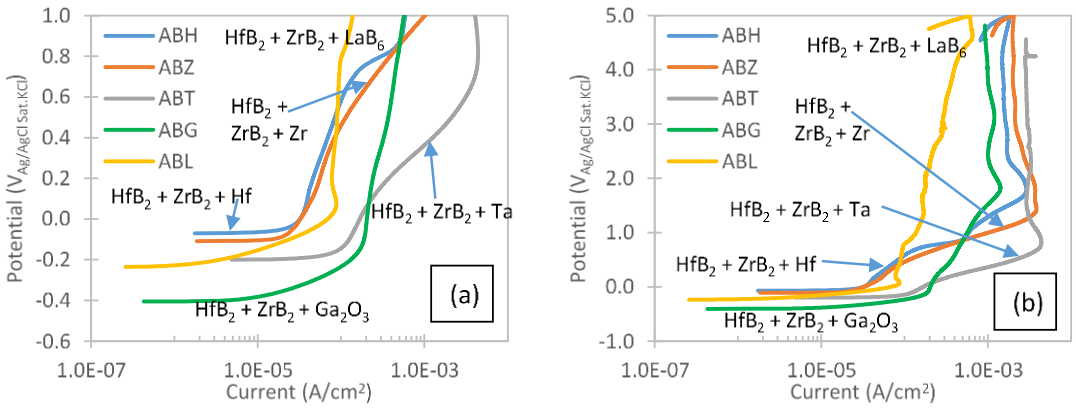

Figure 3.8: (a) Potentiodynamic polarization of the additive samples from Figure 3.2 up to 1 $V_{Ag/AgCl}$ in 0.1 M NaOH, (b) up to 5 $V_{Ag/AgCl}$.

When polarization continued to potentials more than 1 $V_{Ag/AgCl}$, as shown in Figure 3.8(b), a current limiting polarization behavior could be observed for all the samples. The current limiting behavior could be attributed to the presence of a porous hydrated oxide layer as discussed earlier. Reversing the potential scan decreased the current density considerably as seen in Figure 3.8(b). This observation supports the presence of a surface layer. Sample ABL showed the lowest current density of 0.62 mA/cm^2 among this group of samples. However, sample ABL also had a current density about 75% higher than that of sample AB. ABT showed the least corrosion resistance in 0.1 M NaOH when polarized to 5 $V_{Ag/AgCl}$.

3.4.2.4 Anodic polarization in 0.1 M NaOH + 0.1 M NaCl solution

Figure 3.9(a) shows the polarization results of the mixed and unmixed diboride specimens in 0.1 M NaOH + 0.1 M NaCl (pH:13) up to 1 $V_{Ag/AgCl}$. The addition of 0.1 M of chloride to the 0.1 M NaOH solution shifted the OCPs in the negative direction for the sample enriched with HfB_2. Samples A and AB showed active-passive behavior with current densities of 15.7 and 7.6 µA/cm^2 at low potentials. The current densities started to increase at about 0.75 $V_{Ag/AgCl}$ for samples AB and A4B. At 1 $V_{Ag/AgCl}$, the current densities were 0.34, 0.3, 0.074, 0.16, and 0.14 mA/cm^2 for samples A, B, AB, 4AB, and A4B, respectively. These current densities were more or less comparable to those observed in the 0.1 M NaOH solution without the addition of chloride. The addition of the chloride actually decreased the current density for sample A and increased the current density for sample AB. There was no significant effect from the addition of the chloride on the other samples.

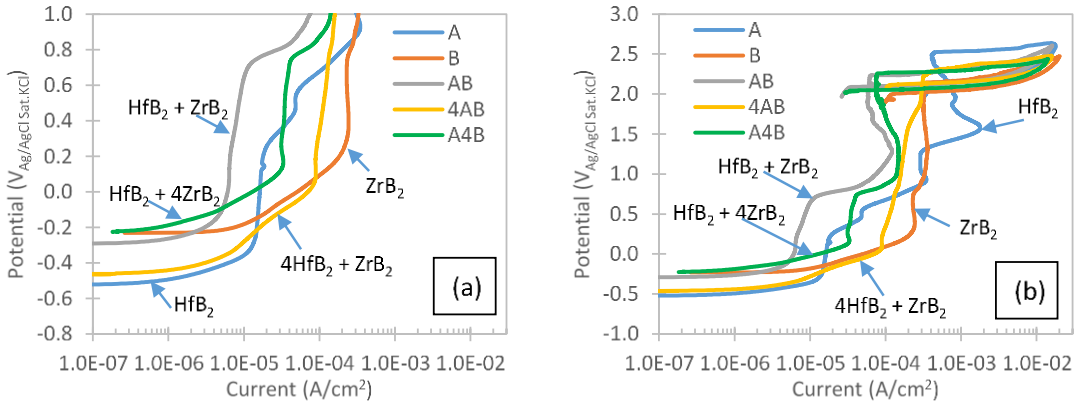

Figure 3.9: (a) Potentiodynamic polarization of the non-additive samples from Figure 3.1 up to 1 $V_{Ag/AgCl}$ in 0.1 M NaCl + 0.1 M NaOH (b) up to 3 $V_{Ag/AgCl}$.

Figure 3.9(b) shows the cyclic polarization behavior for this same set of samples when the potential was increased to 3 $V_{Ag/AgCl}$. An abrupt increase in the current density was observed for all the samples when the potential was increased beyond 2.2 $V_{Ag/AgCl}$. The potential at which the current increased drastically could be considered a type of a 'passivity breakdown' potential. The 'passivity breakdown' of the samples in the pH:13 solutions was very similar to the 'passivity breakdown' in the near-neutral chloride solution. This is interesting because the passivation of the sample was considered to be better in high pH solution and therefore the 'passivity breakdown' potential was expected to be nobler than what was observed in the near-neutral solution. However, if the 'passivity breakdown' potentials were measured with reference to the oxygen evolution potential, then the passivity breakdown potentials would be about 0.4 V more positive in the high pH chloride solution than those of the near-neutral chloride solution. Another noteworthy observation is that the hysteresis observed during the reverse scan in the 0.1 M NaOH + 0.1 M NaCl solution was more significant than the one observed in the near-neutral chloride solution. The area of the hysteresis during the reverse scan of the cyclic polarization plots indicates the extent of localized corrosion or growth of pits. The crossover potential of the reverse scan current profile is considered to be the pitting protection potential. The crossover potential was more or less the same for all of the samples, irrespective of the widely different chemical compositions of the samples. Sample AB exhibited the least limiting current density of 58.5 $\mu A/cm^2$ and a passivity breakdown potential of 2.23 $V_{Ag/AgCl}$. Sample A showed the highest limiting current density of 0.5 mA/cm^2.

Figure 3.10(a) and (b) shows the cyclic polarization behavior of the solid solution diboride samples with the addition of metals, as well as LaB_6 and Gd_2O_3 in the 0.1 M NaOH + 0.1 M NaCl

solution. In this group of samples, ABL showed the lowest current density and ABT showed the highest current density. The limiting current density of ABL was about 90 µA/cm^2, which was about 50% higher than those observed in sample AB. However, the 'passivity breakdown' potential of ABL was about 2.5 $V_{Ag/AgCl}$, which is around 0.3 V higher than what was observed in sample AB. Interestingly, all samples showed similar pitting protection potentials and both ABG and ABZ showed similar cyclic polarization behavior.

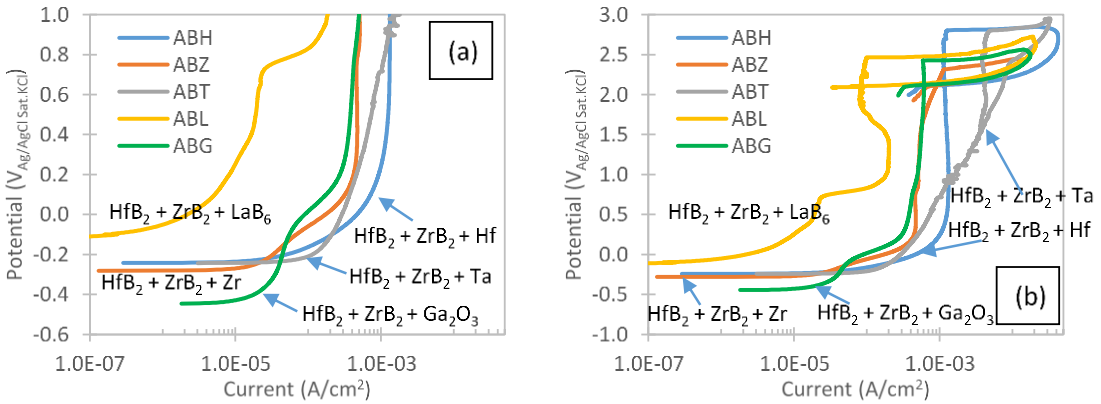

Figure 3.10: (a) Potentiodynamic polarization of the additive samples from Figure 3.2 up to 1 $V_{Ag/AgCl}$ in 0.1 M NaCl + 0.1 M NaOH, (b) up to 3 $V_{Ag/AgCl}$.

3.4.3 Potentiostatic Passivation

The samples were 'passivated' at a constant potential of 0.2 $V_{Ag/AgCl}$ for 2 hours in 0.1 M H_2SO_4, 0.1 M NaCl and 0.1 M NaOH electrolytes. Figure 3.11(a)-(c) shows the *i-t* curves in log-log scale in the different electrolytes. Figure 3.11(a) shows the *log(i)* vs. *log(t)* plot of the samples in 0.1 M H_2SO_4. During the first 10 seconds of applying potential, the current decayed. The slopes of the current decay for all samples ranged between -0.15 for ABL and -0.48 for ABZ. For the other samples, the slopes were around -0.24. Steeper slopes indicate faster kinetics for passivation. However, the current density started to increase after the initial decay behavior and decreased again before reaching a plateau. This plateau behavior was not observed in either of the other two electrolytes, as seen in Figure 3.11(b) and (c).

Figure 3.11(b) shows the *log(i)* vs. *log(t)* plot of the samples in a 0.1 M NaCl when a constant potential 0.2 $V_{Ag/AgCl}$ was applied. Sample 4AB showed the highest current density and sample ABL had the lowest current density. All of the samples in the 0.1 M NaCl solution showed slopes of current decay in the range of -0.15 to -0.38 for the first 10 seconds, although a much steeper slope of -0.63 was observed for sample ABL between 10 and 100 seconds. When comparing the kinetics of surface

passivation between the 0.1 M H_2SO_4 and the 0.1 M NaCl solutions, the somewhat steeper slopes of the *i-t* plots in the 0.1 M H_2SO_4 plots indicate slightly faster kinetics. This could be related to the formation of less stable complexes with chlorides as opposed to more stable complexes with the sulfates. Sample ABH showed a transient behavior after 100 seconds of passivation where the current increased until 400 seconds, after which it started decreasing again. Similar behavior was noted for sample ABZ. This type of behavior indicated the possible formation of a re-precipitated layer after initial dissolution and reaching a threshold current density. A similar phenomenon could have occurred on samples B, A4B, and ABG shown by the slope of the plot abruptly changed to steeper values after 630, 165, and 128 seconds, respectively. Even though these results suggested that decrease in Zr content improved the passivation behavior in 0.1 M NaCl solution, the relation between the composition and passivation was not very clear because sample 4AB showed the highest passivation current.

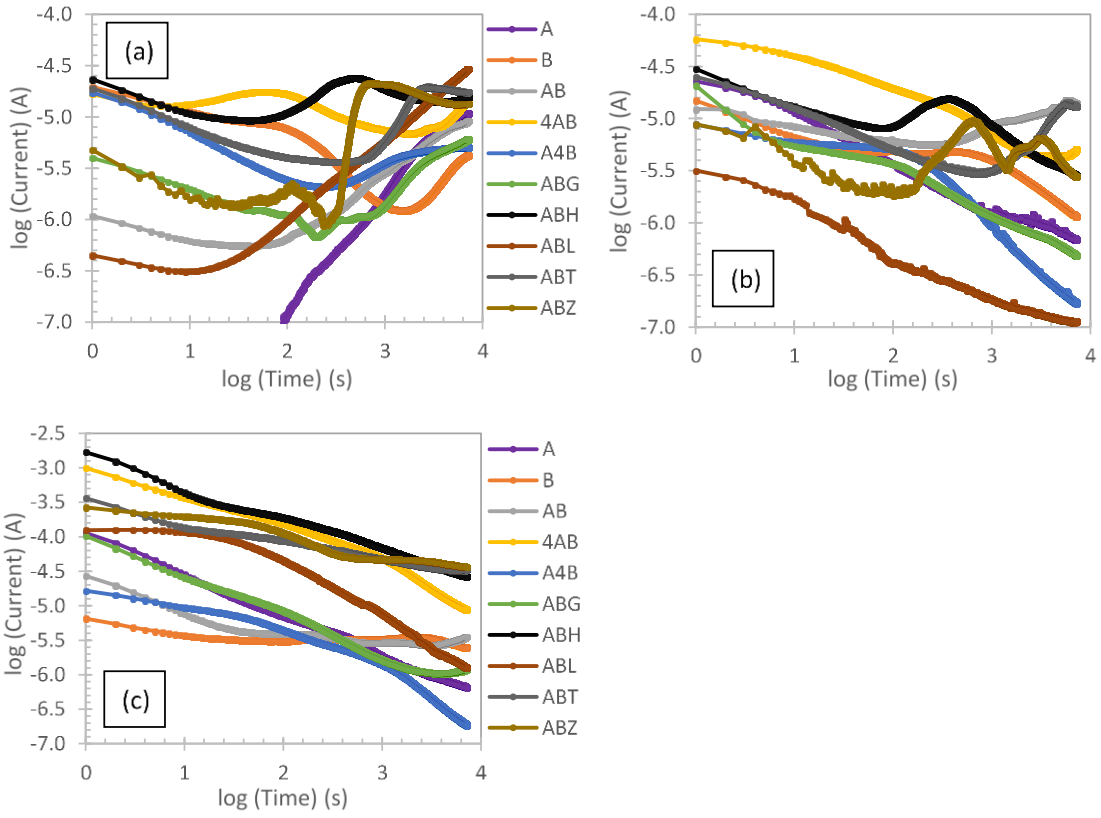

Figure 3.11: Potentiostatic polarization plots in *log(i)* vs. *log(t)* at 0.2 $V_{Ag/AgCl}$ for 2 hours in: (a) 0.1 M H_2SO_4, (b) 0.1 M NaCl, and (c) 0.1 M NaOH of the boride samples from Table 3.1. The legends apply to all plots in this figure.

Figure 3.11(c) shows the *log(i)* vs. *log(t)* plot of the samples in 0.1 M NaOH. The current densities were generally higher in this electrolyte than those recorded in 0.1 M H_2SO_4 or 0.1 M NaCl. The highest current density was recorded for sample ABH and the lowest for sample B. Except for samples B and AB, all samples showed a current decay behavior throughout the potentiostatic test. Samples B and AB showed a current decay behavior for the first 20 seconds after which the current reached a steady state. The steepest slope of the *log(i)* vs. *log(t)* plot for 0.1 M NaOH was about -0.7 for sample ABH and the lowest was -0.24 for sample 4AB. The results pointed out that the passivation behavior improved with increase in the ZrB_2 concentration based on the initial current density values of samples B, A4B, and AB. On the other hand, sample ABZ that had a Zr-rich boron vacancy composition showed higher current density than the AB sample.

Figure 3.12(a)-(e) shows the SEM micrographs of the sample surface after potentiostatic passivation at 0.2 $V_{Ag/AgCl}$ in 0.1 M NaOH for 2 hours. The 4AB sample showed extensive attack on the surface which could be related to the higher anodic current density recorded during the polarization of this sample. Samples 4AB and B showed higher current densities among the stoichiometric boride samples and revealed corrosion attack commensurate with the current densities. The sample ABT also showed the highest current density among the metal-rich boride group of samples and significant corrosion attack on the surface. Samples ABH and ABZ showed the lowest current densities during polarization, and minimal attack on the surface as seen in Figure 3.12(d) and (e). Figure 3.S3(a) and (b) (supporting information) shows the SEM micrographs of the AB and ABH samples after potentiostatic passivation in 0.1 M NaOH solution at 0.2 $V_{Ag/AgCl}$ and EDS analyses results at different locations. The dark etched region in the AB sample was enriched in Zr and slightly depleted in boron, while hafnium was significantly leached out. The surrounding region showed lower concentrations of boron compared to the diboride stoichiometry, and the Zr:Hf ratio was 1:1.25 instead of 1:1. Point 3, on a smaller grain, showed presence of an oxide layer. It should be noted that the EDS analyses of light elements such as boron, and oxygen are only semi-quantitative. Therefore, the analyses presented here should be used only for relative and qualitative comparison between the samples to understand their electrochemical behavior. The point analyses of sample ABH, Figure 3.S3(b) (supporting information), showed wide variations in the composition with Zr enriched regions and Hf enriched regions. The gray etched region in the ABH, point 3, was enriched in Hf, showed presence of oxygen, and a lower amount of boron compared to the stoichiometric portions.

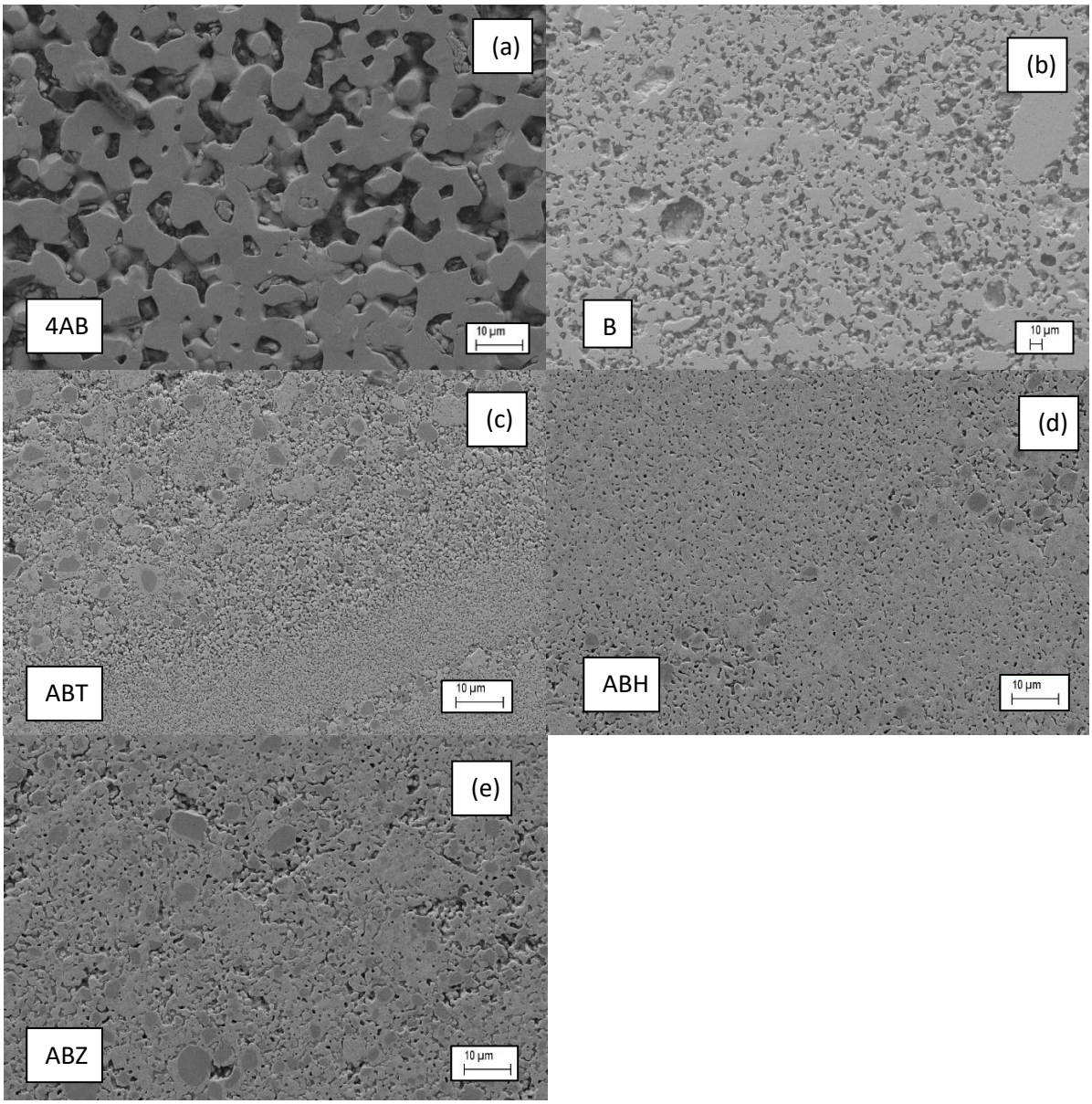

Figure 3.12: SEM micrographs of samples after potentiostatic testing at 0.2 $V_{Ag/AgCl}$, all micrographs were taken after testing in 0.1 M NaOH except for A4B as marked, which was taken after testing in 0.1 M H_2SO_4 (a) 4AB, (b) B shown at 4x lower magnification than other pictures, (c) ABT, (d) ABH, (e) ABZ.

Figures 3.S4 and 3.S5 (supporting information) show the EDS analyses of the passivated ABT and ABG samples in the 0.1 M NaOH solution. The dark etched region (point 2 in Figure 3.S4) showed depletion of Hf and enrichment of Zr. The adjacent region (point 1, Figure 3.S4) showed enrichment of Hf and presence of Ta. More or less a stoichiometric composition of Zr, Hf, and Ta was noted in other regions. Since boron forms soluble corrosion product, the concentration of boron on the surface was lower than the stoichiometric composition. The dark etched Zr-rich region was uniformly

observed throughout the surface after passivation; whereas, the as-polished sample did not show such a wide compositional variation. Similar observations were also made on the AB sample. The dark etched region could be interpreted as the result of outward diffusion of Hf within the grain in the presence of higher valent Ta. However, the reason for such behavior is not clear at this point. More analysis is required to understand the mechanism of formation of the Zr-rich dark etched regions, which is beyond the scope of this work. Sample ABG showed dark and light etched regions as seen in Figure 3.S5 (supporting information). The dark etched region was enriched in Zr and boron, and showed presence of sodium, gadolinium, and oxygen. The light etched regions showed presence of almost equimolar concentrations of Hf and Zr.

Figure 3.S6 (supporting information) shows the EDS analyses results of the ABL sample after passivation in 0.1 M NaOH solution at 0.2 $V_{Ag/AgCl}$. The deterioration of the surface was more significant than that observed in any other sample. The passivation current density of ABL was relatively lower than that of 4AB, ABZ, and ABH, but higher than that of B, A4B, ABG, and ABT. No preferential enrichment or depletion of Zr and Hf was noticed from the compositional analyses of different regions. The analysis did not show lanthanum on the surface indicating that La was possibly in the soluble corrosion product.

The EDS analyses of the A4B sample after passivating in 0.1 M H_2SO_4 solution are given in Figure 3.S7. The composition of original surface would be about 6.67 At% Hf, 26.67 At% Zr, and 66.67 At% B. Most of the points analyzed showed presence of Zr:Hf in the ratio of 3:1 instead of 4:1. The higher concentration of Hf than stoichiometric ratio could be related to the preferential dissolution of Zr by increased complexation with sulfate due to its higher stability constant as seen in Table 3.2. Presence of oxygen and lower concentration of boron were observed which is not unexpected based on Reactions (6) and (7). No significant presence of sulfur was noted on the surface of the sample indicating that the sulfate complexes either dissolved in the electrolyte or were removed from the surface during rinsing. The complexes likely formed on the surface during testing, but did not bond to the surface leading to their disappearance after electrochemical testing.

Figure 3.13(a) shows a typical Raman spectrum obtained on sample B (ZrB_2) after potentiostatic passivation in 0.1 M NaOH for 2 hours at 0.2 $V_{Ag/AgCl}$. Due to its predominantly metallic bonding nature, ZrB_2 is not Raman active.[35] A similar effect is expected for HfB_2 as well. In the passivated sample, the Raman peaks occurred at 146, 263, 321, 463, 604, and 642 cm^{-1}. These peaks correspond to tetragonal phase of the ZrO_2.[36] Formation of crystalline oxide film on Zr is not unusual,

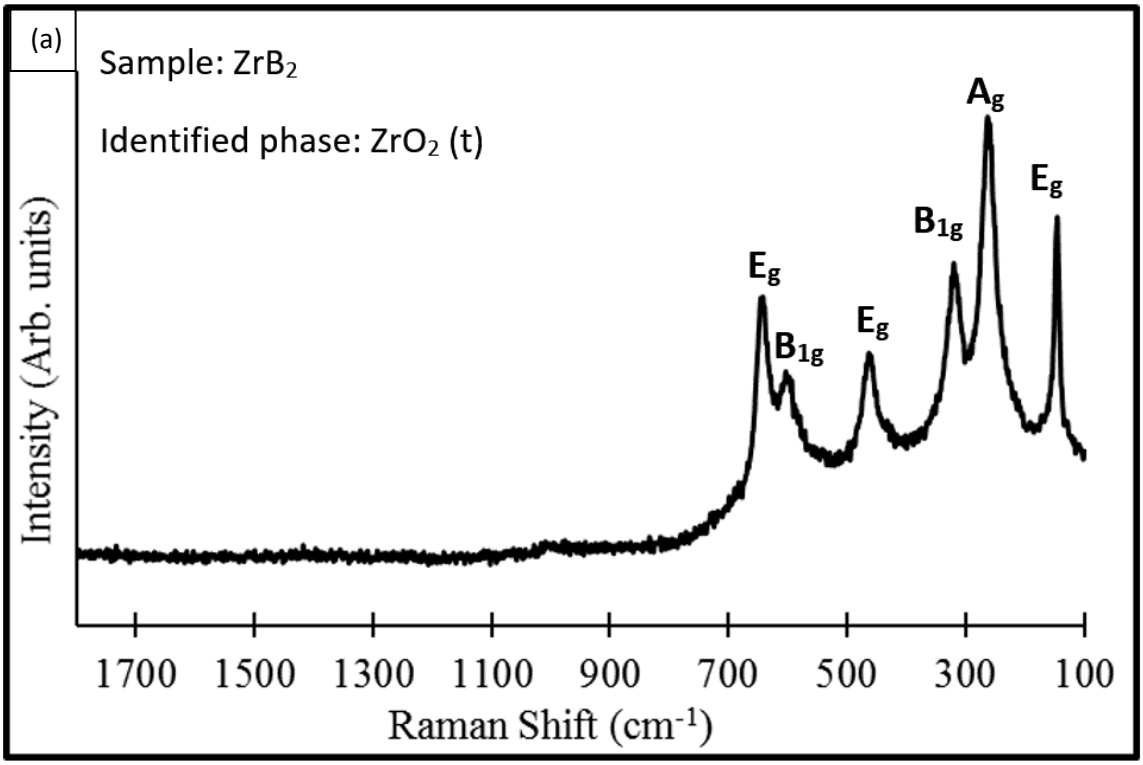

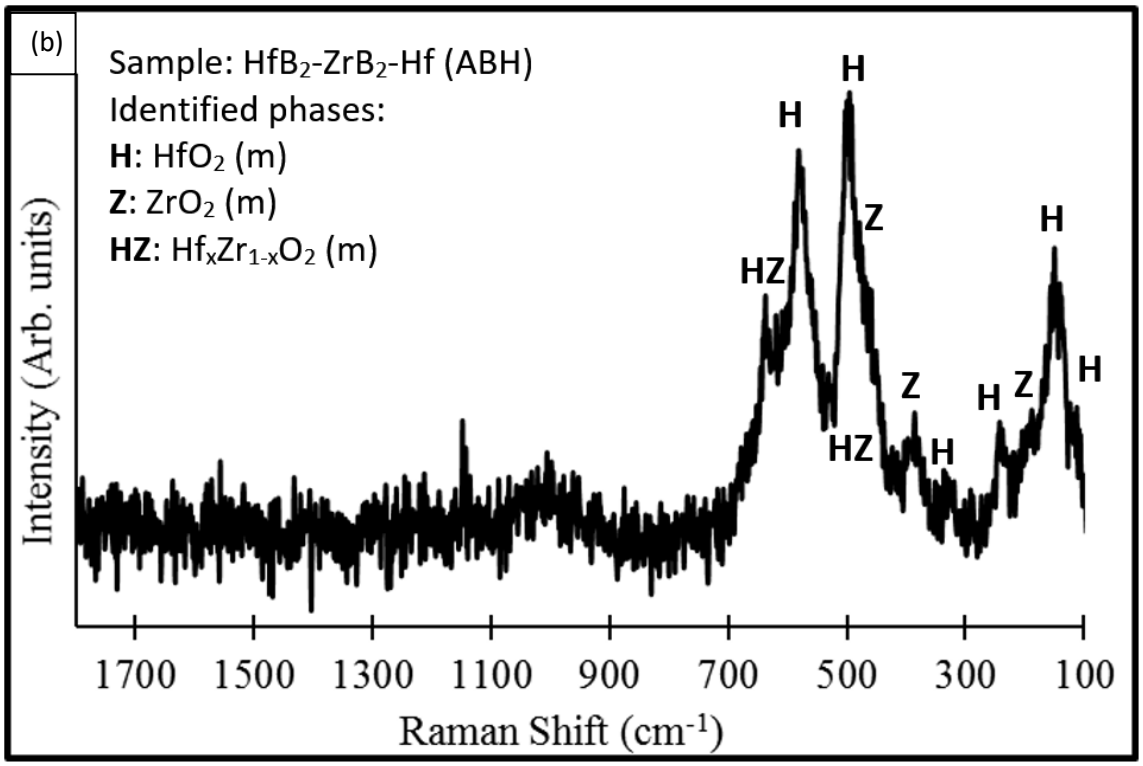

Figure 3.13: Raman spectra of the surface of the samples passivated in 0.1 M NaOH at 0.2 $V_{Ag/AgCl}$ for 2 hours. (a) ZrB_2 and (b) HfB_2-ZrB_2-Hf (ABH).

and different polymorphs of ZrO_2 have been reported during anodization of Zr and Zr-alloys.[37,38] The tetragonal ZrO_2 could have been stabilized by incorporation of B_2O_3 and the presence of inherent oxygen vacancies normally form in the passive oxide film. It is well documented that the addition of lower valent cations typically Y_2O_3 stabilizes the high-temperature tetragonal phase at room temperature in ZrO_2.[39] Figure 3.13(b) shows the Raman spectrum of the ABH sample after potentiostatic passivation in 0.1 M NaOH for 2 hours at 0.2 $V_{Ag/AgCl}$. The major Raman peaks were identified at 110, 149, 192, 241, 332, 384, 496, 580, and 636 cm^{-1}. The peaks match the Raman data reported for monoclinic phases of ZrO_2,[40] HfO_2,[41] and mixed oxide of $Hf_xZr_{1-x}O_2$.[42]

EIS measurements were carried out after 2 hours of potentiostatic conditioning at 0.2 $V_{Ag/AgCl}$. A steady-state condition was assumed after 2 hours of potentiostatic passivation since the *I-t* plot reached a plateau condition. The passive layer of different samples grown under a potentiostatic condition could be compared by evaluating their electrochemical impedance behavior. The EIS results are shown as Bode plots in Figure 3.14(a)-(c). The Nyquist plots are given in the supplemental information in Figure 3.S8 (a)-(c) (supporting information). Figure 3.14(a) shows the Bode plots of the samples at 0.2 $V_{Ag/AgCl}$ in 0.1 M H_2SO_4. The highest impedance modulus at 0.01 Hz was recorded for sample A4B and the lowest was recorded for sample 4AB. The EIS results followed the polarization trend at lower potentials. It should be noted that the trend changes when the applied potentials increase to more than 1 $V_{Ag/AgCl}$. However, the EIS results aid in understanding the physical process occurring at low potentials. The Bode plots indicated that the passivated diborides showed frequency dependent impedance behavior generally referred to as a "Universal Dielectric Response".[43] However, at high frequencies (> 10 kHz) and low frequencies (< 1 Hz), the impedance did not vary significantly. At the intermediate frequencies, the impedance followed a power law, $Z = A(f)^{-\alpha}$, where Z = impedance, f = frequency, and α = exponent in the range of 0.3–1.0, and A is a constant.[44] The EIS data was fitted with an equivalent circuit model as shown in Figure 3.14(d) which consisted of two parallel loops of a resistor and a constant phase element and the loops are connected in series. The constant phase element represents a leaky capacitor. The constant phase element has been described with the unit of admittance, which is the inverse of impedance and is denoted as Y_{top} and $Y_{barrier}$. R_{top} is the charge transfer resistance of the porous salt layer formed. The $R_{barrier}$ and $Y_{barrier}$ terms represent the surface layer formed as given in Reactions (5) or (19) and (20) depending on the electrolyte. The frequency independent impedance observed at the low-frequency region could be due to charge conductance through the percolated path of resistors across the equivalent circuit. At

low frequencies, the resistivity of the constant phase elements was considerably higher than the resistors, and therefore the charge passed through the resistor, exhibiting a plateau behavior in case of the 4AB, ABL, A, and A4B samples. Other samples showed a power law relation even at the low frequencies indicating that the charge flows through both resistors and constant phase elements. At high frequencies, almost all samples, except for ABL, showed a plateau impedance behavior. At high frequencies, the resistivity of the constant phase elements ($Z = (2\pi fY)^{-1}$) would be much lower than the resistor elements in the equivalent circuit. The frequency independent behavior was determined by the resistor connected to the constant phase element. If the conductivity path was due to percolated constant phase elements, then the impedance should decrease with increase in the frequency as observed in sample ABL. Table 3.3 summarizes the equivalent circuit model values that were fitted with the experimental data from the 0.1 M H_2SO_4 solution. Whenever the $R_{barrier}$ was low, the R_{top} was high and vice versa. The R_u term represents the electrolyte resistance. Y_{top} was high for the samples that contained higher amounts of ZrB_2. The addition of metals, LaB_6 and Gd_2O_3 to the diboride solid solution showed increased Y_{top} and $Y_{barrier}$ values when compared to sample AB.

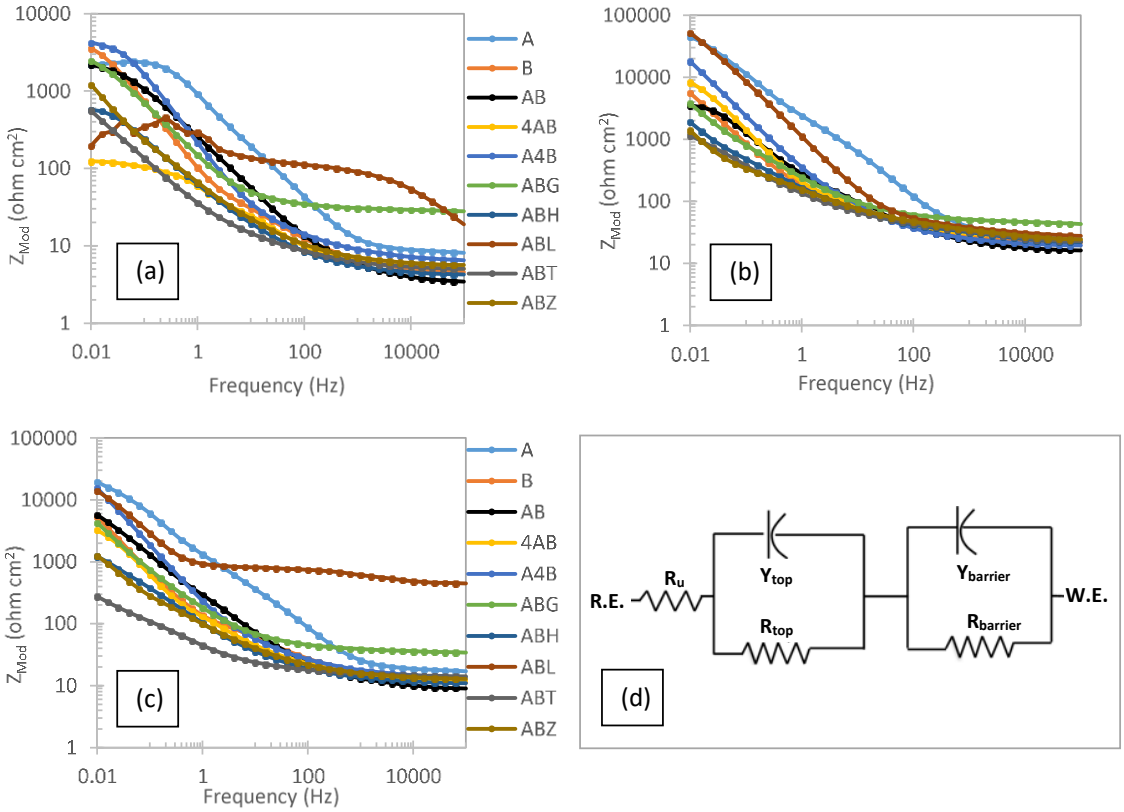

Figure 3.14: EIS results using an applied AC voltage of 10mV and scanning the frequency from 100 kHz to 0.01 Hz shown as Bode plots for (a) 0.1 M H_2SO_4, (b) 0.1 M NaCl, and (c) 0.1 M NaOH of the boride samples from Table 3.1. (d) shows the equivalent circuit model used for fitting the data found in Tables 3.3-3.5. The legends apply to all plots in this figure.

Even though the EDS analyses did not show the presence of sulfate compounds on the surface of the samples, it is believed that the soluble corrosion products were present on the sample surface during polarization based on the current decay behavior during potentiostatic tests (Figure 3.11(a)), and potential independent current behavior during potentiodynamic polarization (Figure 3.3(a) and (b)). The high capacitance values of top layer (Y_{top}) could be attributed to the presence of a re-precipitated layer containing sulfate compounds. Samples 4AB, ABH, ABT, and ABZ showed higher Y_{top} values than the other samples which could be associated with the presence of a thinner porous outer layer with a high dielectric constant. This behavior detrimentally affected the corrosion resistance of the samples in the 0.1 M H_2SO_4 solution.

The capacitance of the barrier film can also be associated with the charge density by the relation:

$$Y_{barrier} = \frac{\partial q}{\partial E} \tag{25}$$

where *q* = charge density and *E* = potential. Alternatively, the capacitance can also be related to the density of states (DOS) of the material.[18]

$$Y_{barrier} = e^2 * DOS \tag{26}$$

where *e* = elementary charge and *DOS* = density of states in $cm^{-2}eV^{-1}$.

The density of states of the samples were estimated based on the density functional theory modeling calculations in our earlier publications.[18,19] The calculations indicated that samples A (HfB_2), and B (ZrB_2) had lower density of states at the Fermi level compared to other samples containing solid solutions of HfB_2 and ZrB_2. The DOS increased significantly in the metal-rich diboride solid solutions. The metal-rich composition could also be viewed as material having boron vacancies. Introducing boron vacancies altered the metal-boron bond length and energy levels of the metal d-orbitals and boron *2p*-orbitals, which resulted in higher DOS at the Fermi level than those normally observed in the stoichiometric $(TM)B_2$ materials. High DOS are considered to increase the catalytic activity of the materials; such as high hydrogen evolution reaction kinetics.[18,19] On the other hand, the high DOS would adversely affect the chemical stability of the material.[45] Our earlier results on the hydrogen evolution reaction kinetics of the diboride samples indicated that samples 4AB, ABH, and ABZ had very high catalytic activities in the sulfuric acid solution. However, when anodically polarized, these samples showed lower corrosion resistance. It should be noted that the DOS,

referred to in Equation (26) pertains to the barrier layer of the samples and not the bulk of the samples as reported in our earlier work.[18,19]

A high resistance value of the $R_{barrier}$ indicates enhanced resistance to the charge transfer across the interface and high $Y_{barrier}$ value indicates high charge carrier density or high DOS. High charge density implies that there is a highly defective barrier film consisting of either oxygen vacancies or cation interstitials assuming that the barrier oxide layer is an n-type semiconductor. The oxide layer complexes with SO_4^{2-} or Cl^-, and preferentially dissolves and re-precipitates as a porous salt layer on the surface of the sample as discussed earlier.

Figure 3.14(b) shows the Bode plots of the samples in 0.1 M NaCl. The highest impedance moduli were observed for samples A and ABL at 0.2 $V_{Ag/AgCl}$. The results followed the same trends as observed in the anodic polarization plots at low potentials. Table 3.4 summarizes the equivalent circuit values that were fitted with the EIS data. The impedance continued to increase with decrease in the frequency, and no plateau-like behavior was observed at low frequencies in contrast to the impedance behavior in the 0.1 M H_2SO_4 solution. This behavior indicated that the charge conductance was through both the resistor and constant phase elements at frequencies lower than 100 Hz. The impedance behavior was not by a percolated resistor at low frequencies. Both samples A and ABL showed similar Y_{top} values. However, the equivalent capacitance of the $Y_{barrier}$ term was an order of magnitude higher for sample ABL than for sample A. Samples ABH and ABZ showed very high Y_{top} and $Y_{barrier}$ values, even though these samples had high R_{top} and $R_{barrier}$ values. The higher capacitance values offset the resistance values, ultimately resulting in relatively lower impedance values and therefore high anodic current density during polarization. Sample 4AB showed the highest current density during potentiostatic current behavior. The R_{top} was the lowest for the sample 4AB, and the exponent 'a' value was closer to 0.5 indicating a diffusion limited Warburg-like behavior of the barrier layer. This observation indicated the presence of a porous top layer that was not protective, resulting in the high observed current density.

Figure 3.14(c) shows the Bode plots of the samples in 0.1 M NaOH. Table 3.5 summarizes the values of the equivalent circuit model components that were fitted with the EIS data. The impedance plateau behavior was observed at high frequencies but not at low frequencies in the 0.1 M NaOH solution. The ABL sample showed relatively high impedance values even at the high frequencies, and the plateau behavior continued until 1 Hz but started to increase with further decrease in the frequency. This could be attributed to the combination of low values of resistor and constant phase

elements. Even though the ABL sample showed the second highest impedance modulus at 10 mHz, the surface of the sample showed significant corrosion as discussed earlier. Sample A showed the highest impedance modulus value and sample ABT showed the lowest. The Y_{top} values were high for all of the mixed boride samples, indicating presence of a porous layer. Samples ABT and ABZ showed very high $Y_{barrier}$ and Y_{top} values and relatively low R_{top} and $R_{barrier}$ values. The high Y_{top} and $Y_{barrier}$ values noted on the samples AB, ABH, and ABT could also be related to the wider compositional variation on the surface due to the distribution of dark and light etched regions. Sample ABH showed the highest current density during the potentiostatic passivation in 0.1 M NaOH solution (Figure 3.11(c)). The Raman spectrum of ABH sample after potentiostatic passivation indicated the presence of both HfO_2 and mixed $Hf_{1-x}Zr_xO_2$ oxide peaks. The dark and light etched regions could be associated with these different oxide phases and constituted percolation paths of capacitors that resulted in high Y_{top} value. ABH showed the lowest R_{top} value which could be associated with a highly porous hydrated oxide layer during the electrochemical testing. The hydrated nature of the oxide was not observed during Raman spectroscopy which could be due to ex-situ nature of the analysis.

Overall, the corrosion behavior of the HfB_2:ZrB_2 solid solutions with additions of Hf, Zr, Ta, LaB_6, and Gd_2O_3 indicated that the corrosion resistance was a function of pH and presence of anions such as Cl^- and SO_4^{2-} in the solution. ZrB_2-rich compositions showed better corrosion resistance in the basic solutions, and HfB_2-rich compositions performed better in the acidic conditions, in general. Mixed borides exhibited better corrosion resistance than their unmixed counterparts at high polarization potentials. The corrosion resistance of metal-rich boride samples was inferior to the stoichiometric boride solid solutions, which is in line with the observation that high electron density of states (DOS) at the Fermi level would have low chemical stability. Addition of Ta did not help improve the corrosion resistance in the aqueous solutions. On the other hand, the addition of LaB_6 was observed to be beneficial which improved the corrosion resistance in non-acidic solutions.

Table 3.3: EIS data fitted into the 2-RC equivalent circuit model found in Figure 3.14(d) of the boride samples after passivation in 0.1 M NaOH at 0.2 $V_{Ag/AgCl}$.

0.1 M NaOH	R_u *(Ohm)*	Y_{top} *($S \cdot s^{\alpha}$)*	α	$R_{barrier}$ *(Ohm)*	$Y_{barrier}$ *($S \cdot s^{\alpha 2}$)*	α_2	R_{top} *(Ohm)*	*Goodness of fit (χ^2)*
A	50.82	57.4×10^{-6}	0.718	57.8×10^{3}	75×10^{-6}	0.828	1.74×10^{3}	1.8×10^{-3}
B	32.68	777×10^{-6}	0.931	0.388×10^{3}	754×10^{-6}	0.480	55.0×10^{3}	0.6×10^{-3}
AB	40.42	1013×10^{-6}	0.451	62.4×10^{3}	246×10^{-6}	0.750	1.39×10^{3}	0.8×10^{-3}
4AB	29.39	1234×10^{-6}	1.000	0.856×10^{3}	1680×10^{-6}	0.453	8.34×10^{3}	1.1×10^{-3}
A4B	35.53	2031×10^{-6}	0.383	233×10^{3}	314×10^{-6}	0.958	0.61×10^{3}	0.4×10^{-3}
ABG	97.79	2451×10^{-6}	0.384	21800×10^{3}	793×10^{-6}	0.797	2.16×10^{3}	0.7×10^{-3}
ABH	29.21	6113×10^{-6}	0.306	6.7×10^{3}	1176×10^{-6}	0.654	0.08×10^{3}	0.2×10^{-3}
ABL	1586	5.3×10^{-6}	0.586	83×10^{3}	158×10^{-6}	0.885	1.44×10^{3}	0.3×10^{-3}
ABT	45.37	3166×10^{-6}	0.576	0.14×10^{3}	3290×10^{-6}	0.413	1.04×10^{3}	2.0×10^{-3}
ABZ	13.22	3081×10^{-6}	0.497	9.78×10^{3}	5368×10^{-6}	0.938	1.08×10^{3}	0.4×10^{-3}

Table 3.4: EIS data fitted into the 2-RC equivalent circuit model found in Figure 3.14(d) of the boride samples after passivation in 0.1 M H_2SO_4 at 0.2 $V_{Ag/AgCl}$.

0.1 M H_2SO_4	R_u *(Ohm)*	Y_{top} *($S \cdot s^{\alpha}$)*	α	$R_{barrier}$ *(Ohm)*	$Y_{barrier}$ *($S \cdot s^{\alpha 2}$)*	α_2	R_{top} *(Ohm)*	*Goodness of fit (χ^2)*
A	24.26	65.9×10^{-6}	0.968	0.648×10^{3}	95.9×10^{-6}	0.731	6.22×10^{3}	2.3×10^{-3}
B	13.54	898×10^{-6}	0.563	19.8×10^{3}	702×10^{-6}	0.892	0.09×10^{3}	1.3×10^{-3}
AB	15.32	226×10^{-6}	0.697	0.007×10^{3}	364×10^{-6}	0.614	13.2×10^{3}	0.4×10^{-3}
4AB	12.88	1344×10^{-6}	0.600	0.185×10^{3}	1991×10^{-6}	0.881	0.08×10^{3}	3.0×10^{-3}
A4B	17.17	323×10^{-6}	0.907	0.047×10^{3}	1887×10^{-6}	0.453	14.2×10^{3}	3.0×10^{-3}
ABG	0.170	693×10^{-6}	0.726	0.102×10^{3}	439×10^{-6}	0.146	16.3×10^{3}	0.9×10^{-3}
ABH	12.21	3341×10^{-6}	0.478	1.49×10^{3}	2666×10^{-6}	0.853	0.58×10^{3}	0.2×10^{-3}
ABL	0.543	9.00×10^{-6}	0.540	0.624×10^{3}	164×10^{-6}	0.983	0.47×10^{3}	22×10^{-3}
ABT	16.00	3790×10^{-6}	0.450	79.6×10^{3}	3228×10^{-6}	0.645	0.02×10^{3}	0.1×10^{-3}
ABZ	13.22	3081×10^{-6}	0.497	9.77×10^{3}	5368×10^{-6}	0.937	1.08×10^{3}	0.4×10^{-3}

Table 3.5: EIS data fitted into the 2-RC equivalent circuit model found in Figure 3.14(d) of the boride samples after passivation in 0.1 M NaCl at 0.2 $V_{Ag/AgCl}$.

0.1 M NaCl	R_u *(Ohm)*	Y_{top} *($S \cdot s^{\alpha}$)*	α	$R_{barrier}$ *(Ohm)*	$Y_{barrier}$ *($S \cdot s^{\alpha 2}$)*	α_2	R_{top} *(Ohm)*	*Goodness of fit (χ^2)*
A	75.81	43.9×10^{-6}	0.828	3.7×10^{3}	38.3×10^{-6}	0.739	172×10^{3}	1.53×10^{-3}
B	62.39	634×10^{-6}	0.875	0.49×10^{3}	692×10^{-6}	0.462	79.0×10^{3}	0.22×10^{-3}
AB	72.06	272×10^{-6}	0.858	1.19×10^{3}	350×10^{-6}	0.488	21.3×10^{3}	1.45×10^{-3}
4AB	61.22	519×10^{-6}	0.545	26.4×10^{3}	451×10^{-6}	0.962	0.30×10^{3}	1.08×10^{-3}
A4B	52.32	236×10^{-6}	0.903	0.54×10^{3}	997×10^{-6}	0.450	448×10^{3}	0.19×10^{-3}
ABG	129.0	2602×10^{-6}	1.000	143×10^{3}	714×10^{-6}	0.503	92.0×10^{6}	1.47×10^{-3}
ABH	51.80	1187×10^{-6}	0.611	2020×10^{3}	3609×10^{-6}	0.231	26.0×10^{9}	1.17×10^{-3}
ABL	91.27	48.6×10^{-6}	0.883	0.12×10^{3}	400×10^{-6}	0.395	490×10^{3}	0.58×10^{-3}
ABT	62.53	1196×10^{-6}	0.568	0.14×10^{3}	1016×10^{-6}	0.326	923×10^{6}	1.29×10^{-3}
ABZ	54.57	1547×10^{-6}	0.364	573×10^{3}	6261×10^{-6}	1.000	2.68×10^{3}	1.45×10^{-3}

3.5 Conclusion

Potentiostatic, potentiodynamic, and EIS investigations were carried out on 10 different mixtures of diboride samples in 0.1 M H_2SO_4, 0.1 M NaOH, and 0.1 M NaCl and additionally 0.1 M

NaOH + 0.1 M NaCl for the potentiodynamic investigation. EIS testing was also performed following the potentiostatic testing.

In both basic solutions sample AB performed better in the potentiodynamic tests than all other mixtures with the exception of sample A in 0.1 M NaOH which was only slightly better at 5 $V_{Ag/AgCl}$. It is noteworthy that ABL also did very well in comparison to the other samples in both of these solutions. In the neutral solution, sample ABL was second best at both high and low voltages, though sample A performed better at low voltages and sample 4AB performed better at high voltages. In the acidic solution, sample A4B did the best at low voltages and sample 4AB did the best at high voltages. Sample ABL also did very well throughout the voltage ranges.

For the potentiostatic testing in the acidic solutions, sample ABH showed the highest current density and sample ABL had the lowest current density. In the neutral solution, sample 4AB showed the highest current density and sample ABL had the lowest current density. In the basic solution, sample ABH showed the highest current density and sample B had the lowest current density.

EIS results in 0.1 M H_2SO_4 showed that the highest impedance modulus at 0.01 Hz was recorded for sample A4B and the lowest was recorded for sample 4AB. In 0.1 M NaCl, the highest impedance modulus at 0.01 Hz was recorded for sample ABL and the lowest was recorded for sample ABT. In 0.1 M NaOH, in 0.1 M H_2SO_4, the highest impedance modulus at 0.01 Hz was recorded for sample A and the lowest was recorded for sample ABT.

As shown throughout the previous section, samples with higher hafnium content had more corrosion resistance in acidic solutions, while samples with higher zirconium content had more corrosion resistance in basic solutions. When comparing the mixed borides to their individual boride (sample AB to sample A or B), the mixed diborides had better corrosion resistance in all tested solutions when considering the full voltage range except in the neutral solution where the final currents of A and AB were very similar. When comparing the mixed diboride sample AB to that of the samples with additives (ABG, ABH, ABL, ABT, ABZ), many of the additives did not increase the corrosion resistance. The addition of lanthanum hexaboride, however, did show the largest corrosion resistance improvement over a broad range of pH even at high voltages.

3.6 Acknowledgments

This work is supported by National Energy Technology Laboratory, US Department of Energy (Office of Fossil Energy) grant number: DE-FE0022988. The authors also gratefully acknowledge Prof.

Dev Chidambaram and Zachery Karmiol of the University of Nevada, Reno, for their help acquiring the Raman spectroscopic data of the samples

3.7 Supporting Information

Supporting information associated with this article can be found in the online version at DOI: 10.1016/j.electacta.2017.06.033 or in Appendix B.

3.8 Bibliography

[1] S. Sitler, C. Hill, K. S. Raja, and I. Charit, "Transition Metal Diborides as Electrode Material for MHD Direct Power Extraction: High-temperature Oxidation of ZrB_2-HfB_2 Solid Solution with LaB_6 Addition," *Metall. Mater. Trans. E*, vol. 3, no. 2, pp. 90–99, Jun. 2016.

[2] R. Telle, L. S. Sigl, and K. Takagi, "Boride-Based Hard Materials," in Handbook of Ceramic Hard Materials, R. Riedel, Ed. *Wiley-VCH Verlag GmbH*, 2000, pp. 802–945.

[3] K. Upadhya, J. M. Yang, and W. P. Hoffman, "Materials for Ultrahigh Temperature Structural Applications," *Am. Ceram. Soc. Bull.*, vol. 76, no. 12, pp. 51–56, Dec. 1997.

[4] M. Kazemzadeh Dehdashti, W. G. Fahrenholtz, and G. E. Hilmas, "Effects of Transition Metals on the Oxidation Behavior of ZrB_2 Ceramics," *Corros. Sci.,* vol. 91, pp. 224–231, Feb. 2015.

[5] C. Monticelli, A. Frignani, A. Bellosi, G. Brunoro, and G. Trabanelli, "The Corrosion Behaviour of Titanium Diboride in Neutral Chloride Solution," *Corros. Sci.,* vol. 43, no. 5, pp. 979–992, May 2001.

[6] C. Monticelli, A. Bellosi, and M. Dal Colle, "Electrochemical Behavior of ZrB_2 in Aqueous Solutions," *J. Electrochem. Soc.*, vol. 151, no. 6, pp. B331–B339, 2004.

[7] C. Monticelli, F. Zucchi, A. Pagnoni, and M. Dal Colle, "Corrosion of a Zirconium Diboride/Silicon Carbide Composite in Aqueous Solutions," *Electrochimica Acta*, vol. 50, no. 16–17, pp. 3461–3469, May 2005.

[8] S.-H. Lee, Y. Sakka, and Y. Kagawa, "Corrosion of ZrB_2 Powder During Wet Processing – Analysis and Control*," J. Am. Ceram. Soc.,* vol. 91, no. 5, pp. 1715–1717, May 2008.

[9] M. Brach, V. Medri, and A. Bellosi, "Corrosion of Pressureless Sintered ZrB_2–$MoSi_2$ Composite in H_2SO_4 Aqueous Solution," *J. Eur. Ceram. Soc.,* vol. 27, no. 2–3, pp. 1357–1360, 2007.

[10] V. A. Lavrenko, V. N. Talash, M. Desmaison-Brut, O. N. Grigor'ev, and Y. B. Rudenko, "Kinetics and Mechanism of the Electrochemical Oxidation of Hafnium Boride," *Powder Metall. Met. Ceram.*, vol. 48, no. 7–8, pp. 462–465, Nov. 2009.

[11] Z. Wang, Q. Zhao, L. Jing, Z. Wu, and X. Sun, "Corrosion Behavior of ZrB_2–SiC–Graphite Ceramic in Strong Alkali and Strong Acid Solutions," *Ceram. Int.,* vol. 42, no. 2, Part B, pp. 2926–2932, Feb. 2016.

[12] C. Monticelli, A. Bellosi, F. Zucchi, and M. Dal Colle, "Corrosion Behaviour of Hafnium Diboride in Aqueous Solutions," *Electrochimica Acta,* vol. 52, no. 24, pp. 6943–6955, Aug. 2007.

[13] J. W. Lawson, C. W. Bauschlicher, M. S. Daw, and W.-Y. Ching, "Ab Initio Computations of Electronic, Mechanical, and Thermal Properties of ZrB_2 and HfB_2," *J. Am. Ceram. Soc.,* vol. 94, no. 10, pp. 3494–3499, Oct. 2011.

[14] P. Vajeeston, P. Ravindran, C. Ravi, and R. Asokamani1, "Electronic Structure, Bonding, and Ground-State Properties of AlB_2-Type Transition-Metal Diborides," *Phys. Rev. B*, vol. 63, no. 4, p. 045115.1-045115.12, Jan. 2001.

[15] W. G. Fahrenholtz, G. E. Hilmas, I. G. Talmy, and J. A. Zaykoski, "Refractory Diborides of Zirconium and Hafnium," *J. Am. Ceram. Soc.,* vol. 90, no. 5, pp. 1347–1364, May 2007.

[16] D. S. King, G. E. Hilmas, and W. G. Fahrenholtz, "Plasma Arc Welding of ZrB_2–20 vol% ZrC Ceramics," *J. Eur. Ceram. Soc*., vol. 34, no. 15, pp. 3549–3557, Dec. 2014.

[17] L. R. Jordan, A. J. Betts, K. L. Dahm, P. A. Dearnley, and G. A. Wright, "Corrosion and Passivation Mechanism of Chromium Diboride Coatings on Stainless Steel," *Corros. Sci.,* vol. 47, no. 5, pp. 1085–1096, May 2005.

[18] S. J. Sitler, K. S. Raja, and I. Charit, "Metal-Rich Transition Metal Diborides as Electrocatalysts for Hydrogen Evolution Reactions in a Wide Range of pH," *J. Electrochem. Soc*., vol. 163, no. 13, pp. H1069–H1075, Jan. 2016.

[19] S. J. Sitler, K. S. Raja, and I. Charit, "ZrB_2-HfB_2 Solid Solutions as Electrode Materials for Hydrogen Reaction in Acidic and Basic Solutions," *Mater. Lett.,* vol. 188, pp. 239–243, Feb. 2017.

[20] L. Kaufman and E. V. Clougherty, "Investigation of Boride Compounds for Very High Temperature Applications, Part II," *Air Force Materials Laboratory*, Technical Documentary Report No. RTD-TDR-63-4096, RTD-TDR-63-4096, Part II, Feb. 1965.

[21] E. Opila, S. Levine, and J. Lorincz, "Oxidation of ZrB_2- and HfB_2-Based Ultra-High Temperature Ceramics: Effect of Ta Additions," *J. Mater. Sci.,* vol. 39, no. 19, pp. 5969–5977, Oct. 2004.

[22] B. Pieraggi and R. A. Rapp, "A Novel Explanation of the 'Reactive Element Effect' in Alloy Oxidation" *J. Phys. IV*, vol. 03, no. C9, pp. C9-275-C9-280, Dec. 1993.

[23] S. Otani, T. Aizawa, and N. Kieda, “Solid Solution Ranges of Zirconium Diboride with Other Refractory Diborides: HfB_2, TiB_2, TaB_2, NbB_2, VB_2 and CrB_2,” *J. Alloys Compd*., vol. 475, no. 1–2, pp. 273–275, May 2009.

[24] M. Dahlqvist, U. Jansson, and J. Rosen, “Influence of Boron Vacancies on Phase Stability, Bonding and Structure of MB_2 (M = Ti, Zr, Hf, V, Nb, Ta, Cr, Mo, W) with AlB_2-Type Structure,” *J. Phys. Condens. Matter*, vol. 27, no. 43, p. 435702, 2015.

[25] M. Pourbaix, Atlas of Electrochemical Equilibria in Aqueous Solutions, 2nd edition. *National Association of Corrosion*, 1974.

[26] L. Y. Wang and M. S. Lee, “A Review on the Aqueous Chemistry of Zr(IV) and Hf(IV) and Their Separation by Solvent Extraction,” J. Ind. Eng. Chem., vol. 39, pp. 1–9, Jul. 2016.

[27] D. I. Ryabchikov, I. N. Marov, A. N. Ermakov, and V. K. Belyaeva, “Stability of Some Inorganic and Organic Complex Compounds of Zirconium and Hafnium,” *J. Inorg. Nucl. Chem*., vol. 26, no. 6, pp. 965–980, Jun. 1964.

[28] Z. Zhu and C. Y. Cheng, “Solvent Extraction Technology for the Separation and Purification of Niobium and Tantalum: A review,” *Hydrometallurgy*, vol. 107, no. 1–2, pp. 1–12, Apr. 2011.

[29] Abhilash, S. Sinha, M. K. Sinha, and B. D. Pandey, “Extraction of Lanthanum and Cerium from Indian Red Mud,” *Int. J. Miner. Process*., vol. 127, pp. 70–73, Mar. 2014.

[30] C.-J. Kim et al., “Leaching Kinetics of Lanthanum in Sulfuric Acid from Rare Earth Element (REE) Slag,” *Hydrometallurgy*, vol. 146, pp. 133–137, May 2014.

[31] R. A. Mayanovic, A. J. Anderson, W. A. Bassett, and I.-M. Chou, “On the Formation and Structure of Rare-Earth Element Complexes in Aqueous Solutions Under Hydrothermal Conditions with New Data on Gadolinium Aqua and Chloro Complexes,” *Chem. Geol*., vol. 239, no. 3–4, pp. 266–283, Apr. 2007.

[32] J. R. Haas, E. L. Shock, and D. C. Sassani, “Rare Earth Elements in Hydrothermal Systems: Estimates of Standard Partial Molal Thermodynamic Properties of Aqueous Complexes of the Rare Earth Elements at High Pressures and Temperatures,” *Geochim. Cosmochim. Acta*, vol. 59, no. 21, pp. 4329–4350, Nov. 1995.

[33] K. Lehovec and J. D’Amico, “Kinetics of Tantalum Corrosion in Aqueous Electrolytes, II,” *J. Electrochem. Soc.*, vol. 114, no. 5, pp. 495–504, May 1967.

[34] T. Kobayashi, T. Sasaki, I. Takagi, and H. Moriyama, “Solubility of Zirconium(IV) Hydrous Oxides,” *J. Nucl. Sci. Technol.,* vol. 44, no. 1, pp. 90–94, Jan. 2007.

[35] J. Watts, G. Hilmas, W. G. Fahrenholtz, D. Brown, and B. Clausen, "Measurement of Thermal Residual Stresses in ZrB_2–SiC Composites," *J. Eur. Ceram. Soc.,* vol. 31, no. 9, pp. 1811–1820, Aug. 2011.

[36] P. Barberis, T. Merle-Méjean, and P. Quintard, "On Raman Spectroscopy of Zirconium Oxide Films," *J. Nucl. Mater.,* vol. 246, no. 2, pp. 232–243, Aug. 1997.

[37] S. R. Whitman and K. S. Raja, "Formation and Electrochemical Characterization of Anodic ZrO_2–WO_3 Mixed Oxide Nanotubular Arrays," *Appl. Surf. Sci.,* vol. 303, pp. 406–418, Jun. 2014.

[38] H. Habazaki et al., "Inter-Relationship Between Structure and Dielectric Properties of Crystalline Anodic Zirconia*," Thin Solid Films*, vol. 479, no. 1–2, pp. 144–151, May 2005.

[39] P. Li, I.-W. Chen, and J. E. Penner-Hahn, "X-ray-Absorption Studies of Zirconia Polymorphs. II. Effect of Y_2O_3 Dopant on ZrO_2 Structure," *Phys. Rev. B*, vol. 48, no. 14, pp. 10074–10081, Oct. 1993.

[40] P. E. Quintard, P. Barbéris, A. P. Mirgorodsky, and T. Merle-Méjean, "Comparative Lattice-Dynamical Study of the Raman Spectra of Monoclinic and Tetragonal Phases of Zirconia and Hafnia," *J. Am. Ceram. Soc.,* vol. 85, no. 7, pp. 1745–1749, Jul. 2002.

[41] A. Aguilar-Castillo et al., "White Light Generation from HfO_2 Films Co-Doped with Eu^{3+} + Tb^{3+} Ions Synthesized by Pulsed Laser Ablation Technique," *Ceram. Int.,* vol. 43, no. 1, Part A, pp. 355–362, Jan. 2017.

[42] R. D. Robinson, J. Tang, M. L. Steigerwald, L. E. Brus, and I. P. Herman, "Raman Scattering in $Hf_xZr_{1-x}O_2$ Nanoparticles," *Phys. Rev. B,* vol. 71, no. 11, p. 115408, Mar. 2005.

[43] A. K. Jonscher, "Physical Basis of Dielectric Loss," *Nature*, vol. 253, no. 5494, pp. 717–719, Feb. 1975.

[44] S. Panteny, R. Stevens, and C. R. Bowen, "The Frequency Dependent Permittivity and AC Conductivity of Random Electrical Networks," *Ferroelectrics*, vol. 319, no. 1, pp. 199–208, Jul. 2005.

[45] D.-C. Tian and X.-B. Wang, "Electronic Structure and Equation of State of TiB_2," *J. Phys. Condens. Matter*, vol. 4, no. 45, pp. 8765–8772, 1992.

CHAPTER 4: Hot Corrosion Behavior of ZrB_2-HfB_2 Solid Solutions in KCl and K_2SO_4 at 1500 °C[3]

4.1 Abstract

Novel electrode coating materials are needed for coal-fired magnetohydrodynamic direct-power extraction power plants. Because of extremely arduous service conditions, these materials must possess certain properties including high-temperature corrosion resistance, high-temperature oxidation resistance, and adequate electrical conductivity. In this work, those very properties of several different compositions of transition metal diborides (HfB_2-ZrB_2) are studied. Two main approaches of oxidation mitigation methods were employed: adding chemical dopants and performing pre-anodization on the samples to create a protective oxide coating. Thermogravimetric experiments were run at different partial pressures of oxygen to determine the high-temperature oxidation resistance of these boride ceramics. In addition, two different salts were applied to the surface of the samples to test their hot corrosion resistance. High-temperature polarization resistance tests were also conducted to measure the electrical resistivity. The addition of lanthanum aided in long term oxidation and corrosion protection, with a K_p = 1.33 x 10^{-5} $kg^2/m^4 \bullet s$, a 40% improvement over the sample without the addition of lanthanum under the same conditions. Anodization, however, proved disadvantageous when combined with either lanthanum or a corrosive environment.

4.2 Introduction

Transition metal diborides, ZrB_2 and HfB_2, are considered ultra-high temperature ceramics (UHTC) because of their (> 3200 °C) and their oxide counterparts' high melting temperatures (2700 - 2800 °C).[1] Below 1100 °C, the borides oxidize following parabolic kinetic behavior.[2] A surface film containing ZrO_2 and B_2O_3 forms during this parabolic oxidation.[3] The melting point of pure B_2O_3 is low at 450 °C. Exposure of diborides to temperatures below 930 °C results in the formation of a continuous B_2O_3 liquid layer on the surface. Diffusion of oxygen is hindered through this liquid layer and therefore a parabolic oxidation behavior is observed.[4]

[3] This chapter is under review for publication: Sitler, S. J., Raja, K. S., Charit, I., "Hot Corrosion Behavior of ZrB_2-HfB_2 Solid Solutions in KCl and K_2SO_4 at 1500 °C" *Ceramics International.* Manuscript number: CERI-D-17-05683.

At higher temperatures in the range of 930 - 1400 °C, B_2O_3 begins to volatilize, but the volatilization rate of B_2O_3 is relatively low, similar to the oxidation rate of boron to B_2O_3, and therefore, the oxidation behavior is described as para-linear.[5] At temperatures higher than 1425 °C, linear oxidation kinetics are reported due to an increased volatilization rate of B_2O_3, leaving a non-protective, porous ZrO_2 layer.[3,4,6] Similar oxidation behavior is to be expected for HfB_2 since the volatilization of the B_2O_3 phase determines the kinetics of oxidation. At around 1700 °C, a phase transition from monoclinic to tetragonal occurs in HfO_2 which increases the oxidation rate sharply.[7] A similar phase transition occurs in ZrO_2 at around 1170 °C. The inadequate oxidation resistance reported for ZrB_2 above 1200 °C could be attributed to both the volatilization of amorphous B_2O_3 and/or the monoclinic-to-tetragonal phase transition.

ZrB_2 and HfB_2 also show high electrical conductivity owing to the metallic bonding in the Zr/Hf planes and metal-like electron configuration with a finite electron density of states at the Fermi level.[8-10] Therefore, these diborides are being considered for use as potential electrode coating material for coal-fired magnetohydrodynamic (MHD) direct-current extraction applications. The operating environment of the coal-fired plasma in the MHD will be highly aggressive due to the presence of impurities such as sulfur, chlorine, and heavy metals in the coal. To increase the conductivity of the plasma, potassium salts will be added. The Cl^- or $SO4^-$ portion of the salts will, in turn, increase the corrosive nature of the environment. Therefore, the electrode coating material needs to be resistant to the hot corrosion conditions induced by the coal plasma. However, there is little information available in literature on the hot corrosion behavior of the ZrB_2 and HfB_2. Zhou et al.[11] reported that a ZrB_2-$20_{vol\%}$SiC-$20_{vol\%}$C composite structure having been tested in molten NaCl at 1000 °C exhibited slight corrosion and observed no noticeable change in the microstructures before and after the 30-minute dipping test. A polymer derived and pulse electric current sintered SiHfCN(O) ceramic material was tested in molten NaCl and Na_2SO_4 salts at 1000 °C for 24 hours.[12] It was reported that no significant weight loss was observed, albeit sodium-induced phase changes, as well as the formation of Na_2SiO_3 as a corrosion product, were reported.

In this study, the hot corrosion behavior of ZrB_2-HfB_2 1:1 solid solution in three different compositional variations is investigated. The compositional variations are:

1. HfB_2-ZrB_2 1:1 mixture showing complete solid solutionizing.
2. HfB_2-ZrB_2 1:1 mixture with additional Hf metal incorporated so that the boron-to-metal ratio was dropped from 1:2 to 1:1.86 ($MeB_{1.86}$). Metal-rich diborides are considered to

render better oxidation resistance.[13] Furthermore, the metal-rich diborides showed better electrocatalytic properties for the hydrogen evolution reaction.[10]

3. HfB_2-ZrB_2 1:1 solid solution with $1.8_{mol\%}$ of LaB_6 added to the powder mixture before spark plasma sintering. LaB_6 was added due to its high electron emissivity and it was postulated that this would improve the electrode kinetics for the MHD applications.[14]

These compositions were selected from a larger group of samples based on their relative aqueous electrochemical corrosion resistance.[15] Furthermore, anodization was carried out to create an oxide surface film that has low boron content in order to minimize the B_2O_3 volatilization at high temperature. Since electrical conductivity is important for effective current extracting electrodes, electrical conductivity measurements were also carried out as a function of temperature.

4.3 Experimental

4.3.1 Materials

Commercial powders of HfB_2 and ZrB_2 (15 µm size, 99.5% purity) were mixed using a ball mill to create the base 1:1 composition (AB). Three powder mixtures were used in this study. In addition to the 1:1 base composition, Hf (44 µm size, 99.6% purity) was added to change the boron-to-metal ratio to 1.86 ($MeB_{1.86}$) (referred to as ABH). Lastly, LaB_6 was added to the ZrB_2:HfB_2 1:1 base composition by mixing $1.8_{mol\%}$ of LaB_6 (44 µm size, and 99.5% purity) to create samples denoted as ABL. All raw materials were procured from Alfa Aesar.

4.3.2 Sample Preparation

The sample powders were mixed using a high-energy ball mill (SPEX Mixer/Mill 8000) with a powder-to-ball weight ratio of 10:1 for 3 hours, utilizing yttria-stabilized zirconia (YSZ) spherical grinding media of 6.5 mm diameter (Inframat Advanced Materials LLC, Manchester, CT). After which they were spark plasma sintered using a spark plasma sintering machine (Fuji Electronics, Japan, model: Dr. Sinter SPS-515 S). No sintering aid was added. An Isocarb-85 graphite die with a 12-mm diameter was used with 5 kN of applied force at 1700 °C for 600 seconds under a ~10^{-3} Torr vacuum.

The sintered pellets were then cut into smaller pie pieces of around 0.5 g. These pellets were polished on all sides to a 0.3 µm surface finish before anodizing, coating with a salt layer, or heating in the furnace.

Electrochemical anodization of the sample surface was accomplished using a Sorenson DC power supply at 12.5 V for 1 hour with a platinum flag counter electrode (3.75 cm^2). Samples were

connected to copper wires using a highly conductive silver epoxy and then placed in an ethylene glycol solution with $6_{wt\%}$ H_2O and 0.14 M NH_4F. After anodization, the samples were washed with distilled water and air dried. For the hot corrosion tests, the top surface of the samples was coated with a salt solution (KCl or K_2SO_4) by using a micropipette and dried. The coating and drying procedure was repeated until 2.5 mg/cm^2 of salt was attained on the top surface, calculated from the volume added and the salt concentration of the solution.

4.3.3 Sample Characterization

4.3.3.1 Conductivity testing

Electrical conductivity measurements were carried out using a potentiostat (Gamry Interface 1000). Samples were heated in a tube furnace in an argon atmosphere containing trace amounts of oxygen (10 ppm), given the flow rate of 2 SCFM and the amount of oxygen, the partial pressure of oxygen (p_{O2}) was around 1 Pa. Platinum leads were clamped to the two faces of the samples using a custom machined clamping device, as seen in Figure 4.S1 (Supporting information), designed to withstand the extreme temperatures. The heating rate was 2.5 °C/min. The electrical resistivity was measured by carrying out several linear polarization experiments using the potentiostat by scanning the potentials from +10 mV to -10 mV at a scan rate of 0.5 mV/s. The inverse slope (*dI/dV*) of the *I-V* plot constructed using the linear polarization data gave the resistivity values. After linear polarization, electrochemical impedance measurements were performed by superimposing an *AC* potential of 10 mV with a *DC* potential of 10 mV on the sample and scanning the frequency from 100 kHz to 10 mHz. Polarization resistance (PR) and electrochemical impedance spectroscopy (EIS) tests were carried out at room temperature and at 100 °C increments starting at 100 °C up to 1000 °C, 1100 °C or 1500 °C.

4.3.3.2 High-temperature exposure testing (1550 °C)

High-temperature tests were conducted in a tube furnace with an argon atmosphere containing trace amounts of oxygen (10 ppm), given the flow rate of 2 SCFM and the amount of oxygen, the partial pressure of oxygen (p_{O2}) was around 1 Pa. Samples were heated and cooled at 2.5 °C/min and held at 1550 °C for 4 hours. The weight change of the three samples (AB, ABH, ABL) was noted after high-temperature exposure in the as-sintered condition (control samples), in the anodized condition, in the salt-coated condition, and in the anodized and salt-coated condition.

4.3.3.3 In situ oxidation and corrosion testing (1500 °C)

Additional high-temperature tests were conducted using a thermogravimetric analyzer (TGA) (Netzsch STA 409). Using a heating and cooling ramp rate of 3 °C/min, the samples were heated to 1500 °C and held for 4 hours under a p_{O2} = 0.1 Pa atmosphere. After 4 hours, oxygen (p_{O2} = 0.3 x 10^5 Pa) was allowed into the system for 15 minutes. The test was continued for another 4 hours (p_{O2} = 0.1 Pa) to understand the oxidation rate differences in the different samples. Two samples were tested using the TGA in four different conditions: AB and ABL were both tested in the as-sintered condition (control samples), in the anodized condition, in the salt-coated condition, and in the anodized and salt-coated condition.

4.3.3.4 Post-test characterization

Post-test characterization of the samples was done through scanning electron microscopy with a field emission scanning electron microscope (FESEM) LEO Supra 35VP (Zeiss, Jena, Germany) and energy-dispersive X-ray spectroscopy (EDS) was used to analyze and quantify the chemical composition of the samples. Spectra were obtained using an accelerating voltage of 20 kV. Linescan data was obtained using a 50-point line scanning at 1 second per point. X-ray diffraction patterns (XRD) were obtained using a D5000 Diffractometer (Siemens AG, Munich, Germany) at a scan rate of 0.02°/hold time with a hold time of 5 s.

4.4 Results & Discussion

4.4.1 High-temperature Oxidation of Samples

4.4.1.1 Samples Soaked for 4 hours at 1550 °C in p_{O2} = 1 Pa without Anodic Oxide Coating

Table 4.1 shows all the weight change results for the samples tested at 1550 °C. The salt coated samples in this table and Table 4.2 will be discussed in section 4.4.2. During these thermal oxidation studies at 1550 °C, a flowing stream of Ar + O_2 gas mixture was used with a partial pressure of oxygen equal to about 1 Pa . The volatility diagram for ZrB_2 at 1800 K (~1525 °C), as reported by Fahrenholtz,[5] indicates that the oxidation of ZrB_2 occurs when the activity of oxygen is greater than 10^{-16}. However, at 1550 °C, significant evaporation of B_2O_3 is expected. Therefore, the net mass change can be expressed as:

$$\Delta m_{net} = \Delta m_{(TM)O_2} - \Delta m_{B_2O_3(g)} \quad (1)$$

$$\Delta m_{(TM)O_2} = m_{(TM)O_2} - m_{(TM)} \quad (2)$$

$$\Delta m_{B_2O_{3(l)}} = m_{B_2O_3} - m_{2B} \quad (3)$$

$$\Delta m_{B_2O_{3(l)}} = \Delta m_{B_2O_{3(g)}} \quad (4)$$

Table 4.1: Weight change after exposure to 1550 °C for 4 hours with a p_{O2} = 1 Pa. KCl salt coating was applied at a rate of 2.5 mg/cm². Anodization was carried out in ethylene glycol with 6$_{wt\%}$ H_2O and 0.14 M NH_4F for 1 hour at 12.5 V.

	Control samples (% weight change)	*Anodized samples (% weight change)*	*KCl-coated as-sintered samples (% weight change)*	*Anodized & KCl-coated samples (% weight change)*
AB	-1.71%	-2.45%	-1.70%	-2.15%
ABH	-3.29%	-3.34%	-2.42%	-3.35%
ABL	0.02%	-1.92%	—	-2.98%

The above relation indicates that during the exposure to 1550 °C, for each ZrB_2 or HfB_2, 2 oxygen atoms are gained in the form of ZrO_2 or HfO_2 and two B atoms are lost in the form of $B_2O_{3(g)}$. Therefore, there should be a net gain of 10.358 g [(2 x 15.99 g) - (2 x 10.81 g)] per molar weight of ZrB_2 or HfB_2 oxidized. The weight gain should be about 6.6% (10.358 g/156.479 g) based on the molar weight.

In contrast, however, the samples exposed to 1550 °C for 4 hours in a flowing gas stream of Ar + O_2 with a p_{O2}=~1 Pa, showed weight losses. The reason for such weight loss is not fully understood at this point but could be due to spallation of the oxide film where small oxide particles are carried away by the gas stream. The higher weight losses of the anodized samples also give evidence that the flowing gas stream is removing the oxide particles from the samples and supports this as the explanation for the observed weight loss. Unfortunately, since the samples only weighed ~0.5 grams, the ~2% loss in mass could not be detected in the exhaust line to prove this theory.

Figure 4.1(a) shows the planar view of the oxidized surface of the control AB sample (without prior anodic oxide coating) and Figure 4.1(b) shows the cross-sectional view of the thermally grown oxide layer of the AB control sample at 1550 °C for 4 hours. The thickness of the oxide layer was 90 - 105 µm. Table 4.2 summarizes the results of the EDS analysis carried out on the top surface of the samples, as mentioned before, the salt coated samples in this table will be discussed in section 4.4.2 The top surface indicated enrichment of Hf in the AB control sample. The concentration of Hf was about 45% higher than the concentration of Zr. The oxide layer was observed to be continuous and no connected pores were observed.

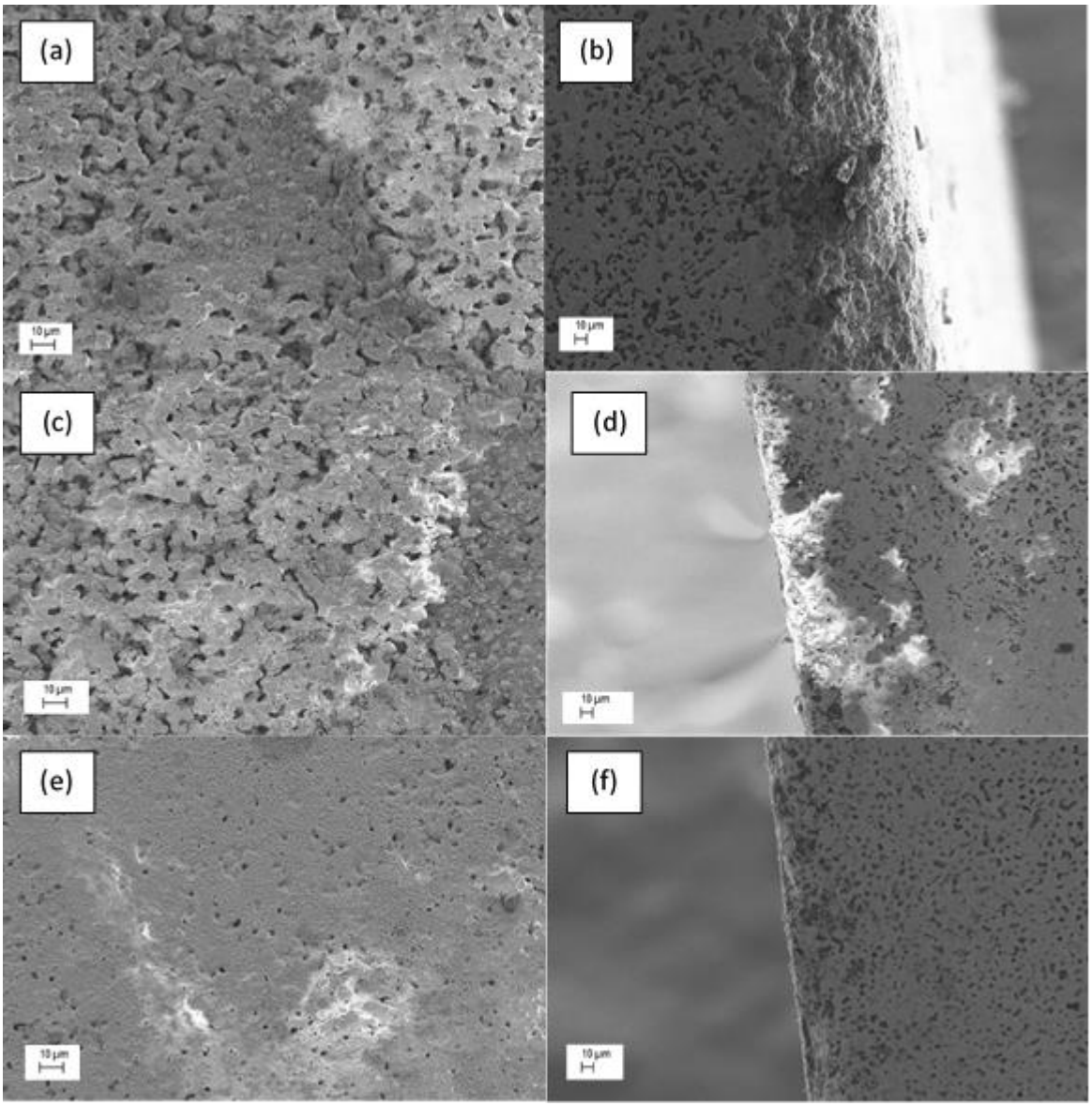

Figure 4.1: SEM images of un-anodized samples after heating in tube furnace for 4 hours at 1550 °C with p_{O2} ~ 1 Pa. (a) top view of sample AB at 500 X, (b) cross-sectional view of sample AB at 250 X, (c) top view of sample ABL at 500 X, (d) cross-sectional view of sample ABL at 250 X, (e) top view of sample ABH at 500 X, (f) cross-sectional view of sample ABH at 250 X.

Figures 4.1(c) and (d) show the top surface morphology and cross-sectional view of the oxide layer formed on the ABL control sample after exposure to 1550 °C for 4 hours. Unlike the AB control sample (Figure 4.1(b)), the ABL control sample showed non-uniform thickness/growth of oxide layer (Figure 4.1(d)) as the thickness of the oxide layer varied from 42 - 105 µm on sample ABL. The variation in the oxide layer thickness could possibly be attributed to the non-uniform distribution of La at the substrate-oxide interface. Previous work has shown that the presence of La helps improve

the oxidation resistance by pinning the misfit dislocation which leads to preventing the movement of the transition metal (TM) which otherwise would diffuse outward and oxidize.[16] Increased growth of oxide might have occurred at the locations where the interfacial misfit dislocations were not pinned by La. Furthermore, the top surface of the oxide of the ABL control sample appeared to be more porous than that of AB control sample. This sample showed a weight gain after the high-temperature testing at 1550 °C in contrast to the other samples. The EDS analysis of the top surface indicated significantly higher Hf concentrations than those recorded for other samples. No lanthanum was present on the top surface which supports the hypothesis that La could be enriched at the substrate/oxide interface and therefore, inhibited the outward diffusion of the transition metal. The EDS results suggest that La potentially pinned the diffusion of Zr, but not Hf.

Table 4.2: EDS analysis of the top surface of samples after exposure to 1550 °C for 4 hours in a p_{O2} = 1 Pa atmosphere.

Control samples (without anodic oxide or salt coatings)					
Sample	*Boron (at%)*	*Oxygen (at%)*	*Zirconium (at%)*	*Hafnium (at%)*	*Lanthanum (at%)*
AB	4.94	73.61	8.65	12.79	—
ABH	0	64.08	20.18	15.73	—
ABL	13.13	51.97	11.63	23.27	0
Anodized samples					
AB	15.96	65.03	13.54	5.47	—
ABH	16.35	61.64	14.24	7.77	—
ABL	22.05	57.88	7.47	4.46	8.14
As-sintered samples coated with KCl salt layer					
AB	15.34	34.79	24.7	25.17	—
ABH	21.07	40.06	14.49	24.38	—
ABL	21.07	54.39	6.9	9.13	8.51
Anodized samples coated with KCl salt layer					
AB	14.69	56.23	17.42	11.65	—
ABH	17.09	59.67	13.44	9.81	—
ABL	49.45	31.61	11.99	6.83	0.13

Figure 4.1(e) and (f) illustrated the surface morphology and cross-sectional view of the ABH control sample. (Hf-rich $HfB_{1.86}$) after oxidation at 1550 °C for 4 hours. The oxide layer was continuous and only discrete porosity could be observed. In this sample, the oxide layer thickness was also non-uniform and varied from 10 - 63 µm. The weight change recorded was the highest for this sample. The EDS analysis (Table 4.2) of the oxide surface showed enrichment of Hf having even a higher content than the AB oxide surface layer as expected after the addition of the pure Hf metal.

4.4.1.2 Samples Soaked for 4 hours at 1550 °C in p_{O2} = 1 Pa with Anodic Oxide Coating

4.4.1.2.1 Anodic oxide formation

During anodization, both transition metals (Zr and Hf) and boron oxidized to higher valent ions. The important consideration is the valent state of the transition metals in the diborides. The diborides have layered structures and different bonding conditions exist between the metal and boron layers. Metallic bonding occurs between the transition metal atoms, covalent bonding is considered to take place between the boron atoms and ionic bonding exists between the metal and boron layers.[8] The fraction of ionic bonding is not well defined. One report suggests that the ionic bonding character is less than 8% and covalent hybridization is considered to occur between TM and B atoms.[17] On the other hand, Lawson et al. showed no charge localization occurring between Zr-B atoms or across the TM/B layers based on their first principle calculations and therefore considered the bonding between the TM/B layers as ionic.

Fahrenholtz et al.[2] assigned formal charges to TM at TM^{2+} and to B as B^{-}. On the other hand, Lawson et al.[8] reported the formal valance state of TM as $TM^{+1.43}$ based on Bader charge analysis calculations. For simplicity, the valance state of TM in the diborides in this study is considered to be TM^{2+}. Therefore, during anodization in fluoride containing organic electrolyte the following reactions are expected to take place. Overall, the anodic oxide formation is given as:

$$(TM)B_2 + 8H_2O \rightarrow (TM)O_2 + 2H_3BO_3 + 5H_2 \quad (5)$$

The anodic reactions are:

$$2H_2O \rightarrow 4H^+ + O_2 + 4e^- \quad (6)$$

$$TM^{2+} \rightarrow TM^{4+} + 2e^- \quad (7)$$

$$2B^- \rightarrow 2B^{3+} + 8e^- \quad (8)$$

The fluoride present in the organic electrolyte solution limited the amount of water available to react with TM^{4+} through the following reaction:

$$TM^{4+} + 6F^- \rightarrow [TMF_6]^{2-} \quad (9)$$

Furthermore, the boron species will also react with the fluoride ions through the following reactions:

$$B^{3+} + H_2O \rightleftharpoons H_3BO_3 + 3H^+ \quad (10)$$

$$H_3BO_3 + 4F^- + 4H^+ \rightarrow H_3OBF_4 + 2H_2O \quad (11)$$

$$B^{3+} + 3F^- \rightarrow BF_3 \quad (12)$$

$$4BF_3 + 3H_2O \rightarrow 3HBF_4 + H_3BO_3 \quad (13)$$

Fluoroboric acid, boric acid, and boron trifluoride are soluble in water. Therefore, during anodization, the boron is considered to oxide, react with the fluoride ion, and be preferentially leached out.

Because the enthalpy of formation of ZrF_4 is low at -1911 KJ/mol and the enthalpy of formation of both BF_4^- and $(NH_4)_2ZrF_6$ are higher at 1574.9 KJ/mol and -697.5 Kcal/mol, respectively, the fluorides will preferentially attach to Zr^{4+}. Furthermore, the reactions of ethylene glycol with $(TM)B_2$ could be given by the following reactions:

$$(TM)B_2 + 2(CH_2OH)_2 + 2H_2O \rightarrow TM\text{-}(COOH\text{-}CH_2OH) + 2B\text{-}(COOH\text{-}CH_2OH) + 8H^+ + 8e^- \quad (14)$$

$$COOH\text{-}CH_2OH \rightarrow (R\text{-}COO)^- + H^+ + e^- \quad (15)$$

$$TM + 4(R\text{-}COO)^- \rightarrow (RCOO)_4TM + 4e^- \quad (16)$$

$$(R\text{-}COO)_4(TM) \rightarrow (TM)O_2 + CO_2 + nH^+ + ne^- \quad (17)$$

However, during the anodization process, boron species in the form of borates were also expected to reprecipitate on the sample surface after being preferentially leached out. This may explain why more boron is present on the surface of the anodized samples as shown in Table 4.2. The reprecipitation species were likely HfB_2O_5 or ZrB_2O_5 as discussed in a study by Knyrim and Huppertz,[18] or possibly other oxo borate species as discussed in their publication.

4.4.1.2.2 Morphological and compositional analysis of the anodic oxide coated samples

Figure 4.S2(a-c) (Supporting information) shows the surface morphology of the AB, ABH, and ABL samples after anodization. The compositional analysis of sample AB, using SEM-EDS, of the top surface and the concentration profile of the elements using a linescan are given in Figure 4.S3(a) and (b) (Supporting information). The anodic oxide layer surface was enriched with hafnium. The linescan

across the thickness of the AB sample showed similar concentrations of both Zr and Hf, and no preferential enrichment of either one of the transition metals was observed.

The anodic oxide layer of all the samples showed the presence of a significant amount of carbon which could be associated with the ethylene glycol used as the anodization electrolyte base. The surface morphology anodized ABH anodic oxide is shown in Figure 4.S2(b) (Supporting information). The compositional analysis of the top surface by EDS and the EDS linescan across the thickness of the ABH sample are given in Figure 4.S4(a) and (b) (Supporting information). The EDS top scan revealed that the surface layer was enriched in hafnium. The EDS linescan also indicated enrichment of hafnium on the surface.

Figure 4.S5(a) and (b) (Supporting information) shows the compositional analysis of the top surface and the linescan EDS analyses results of the as-anodized ABL sample. The sub-surface region showed enrichment of lanthanum. The Hf concentration was higher than that of Zr at the oxide surface and sub-surface layer. Boron concentration was low at the regions where Hf and La were high. The oxygen concentration increased across the oxide layer as a function of distance from the substrate/oxide interface towards the oxide/air interface. It should be noted that the concentrations of oxygen and especially boron and carbon determined from the EDS analyses will not be accurate and the discussion is based on a qualitative comparison between the samples.

4.4.1.2.3 High-temperature oxidation of anodized samples

The anodic oxide coated samples were further exposed to high temperature at 1550 °C for 4 hours. Figure 4.2(a) and (b) shows the top morphology and side view of the anodized AB sample's oxide layer after high-temperature exposure. A two-layered structure could be seen on the AB-anodized sample after high-temperature exposure. The oxide layer thickness varied from 16 - 75 µm, which was thinner than oxide layer on the AB control sample without prior anodic oxide coating. The weight loss recorded in Table 4.1 for this sample was about 2.45% which was larger than the weight loss recorded for the un-anodized AB control sample. The increased weight loss points to the idea that the anodic oxide possibly contained more of the B_2O_3 phase that evaporated during the exposure to 1550 °C. On the other hand, the EDS analysis (Table 4.2) showed the presence of larger amounts of boron on the surface of the anodized AB sample than the un-anodized AB control sample after 1550 °C exposure. The anodized AB sample showed enrichment of Zr after high-temperature exposure as opposed to the un-anodized AB control sample, which showed enrichment of Hf on the surface.

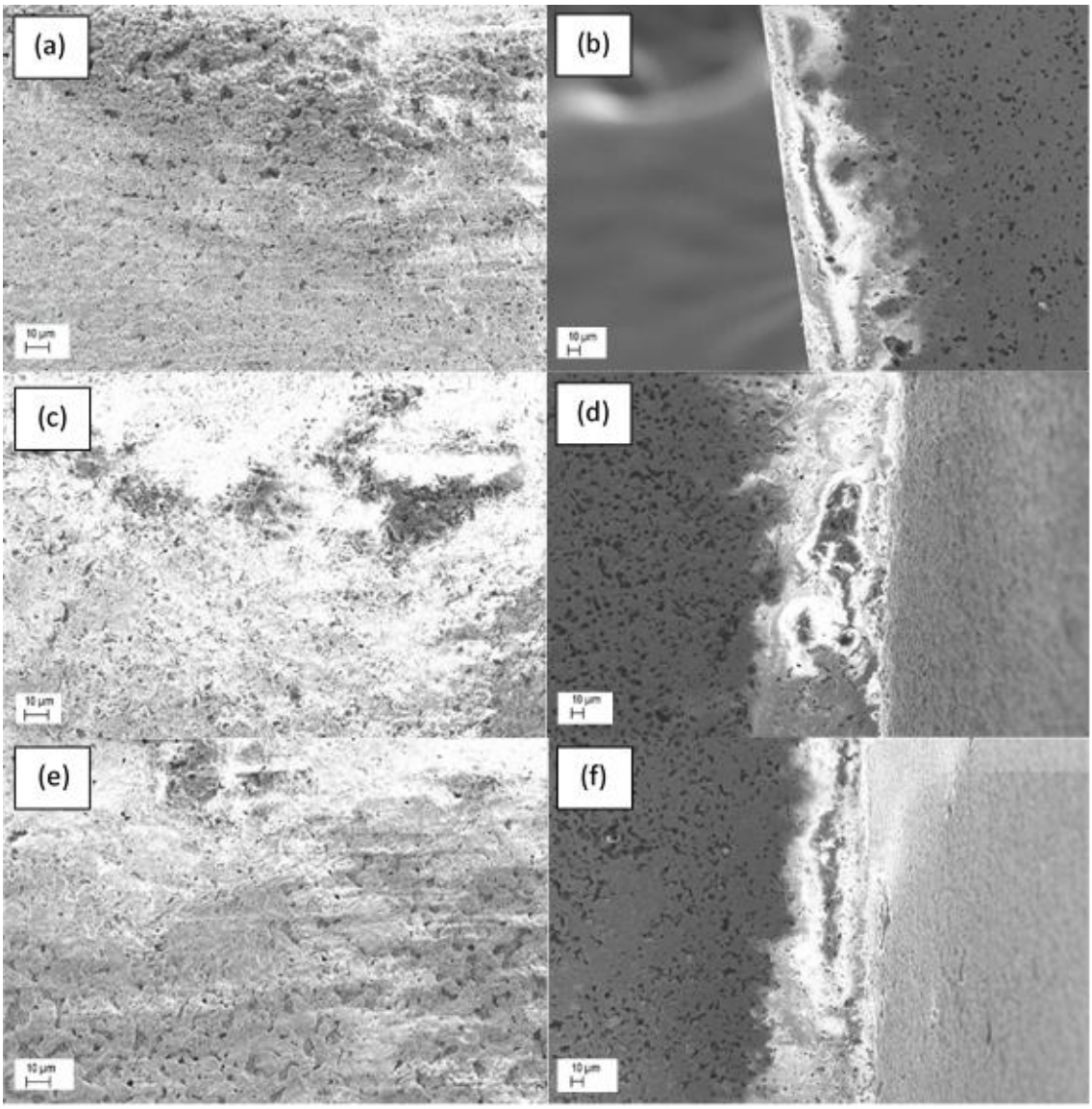

Figure 4.2: SEM images of anodized samples after heating in tube furnace for 4 hours at 1550 °C with p_{O2} ~ 1 Pa. (a) top view of sample AB at 500 X, (b) cross-sectional view of sample AB at 250 X, (c) top view of sample ABL at 500 X, (d) cross-sectional view of sample ABL at 250 X, (e) top view of sample ABH at 500 X, (f) cross-sectional view of sample ABH at 250 X.

Figure 4.2(c) and (d) shows the oxide morphology of the ABL anodized sample after high-temperature exposure. A two-layered structure could be observed in this sample also, but the top oxide layer was less porous than that observed in the anodized AB sample. The total oxide layer thickness was about 110 µm. The Zr content was higher than Hf on the top surface. The Zr-enrichment was lower than that observed on the anodized AB sample after high-temperature exposure. Interestingly, the anodized ABL sample showed a large amount of La on the surface. It

should be noted that the un-anodized ABL sample did not show any presence of La on the surface. The ABL-anodized sample showed the lowest weight loss among the anodized samples.

Figure 4.2(e) and (f) are the SEM images of the anodized ABH sample after high-temperature oxidation at 1550 °C for 4 hours. The top surface clearly shows a double layered oxide structure. Seong et al.[19] reported that irrespective of the oxygen partial pressure, oxidation of ZrB_2 occurred by inward diffusion of oxygen through ZrB_2 grain boundaries and ZrO_2 grain boundaries and that the new oxide formed at the interface between the oxidized layer and unreacted layer. Furthermore, gaseous diffusion of oxygen through the liquid B_2O_3 has been considered as the mechanism of ZrB_2 oxidation by many investigations.[2,5,20] Based on these literature reports, it can be proposed that the oxide formation during the 1550 °C exposure occurred at the interface of the anodic oxide/$(TM)B_2$ substrate. The outer layer observed on the anodized ABH (also other anodized samples) was the anodic oxide and the layer beneath the top surface was the thermally grown oxide layer. The thickness of the oxide layer varied from 17 - 86 µm. The anodized ABH sample showed the highest weight loss among the anodized and un-anodized samples. The EDS analysis (Table 4.2) of the top surface indicated the surface was enriched in Zr despite having additional Hf in the original composition. The EDS of all the anodized samples indicated that the presence of the anodic oxide promoted outward diffusion of Zr but not Hf during the 1550 °C exposure.

4.4.1.3 TGA Results of Anodized and Un-Anodized Control Samples at 1500 °C in p_{O2} = 0.1 Pa and p_{O2} = 0.3 x 10^5 Pa

Figure 4.3 shows the mass change of 8 samples (AB-(as-sintered, un-anodized)), AB-anodized, (ABL-(as-sintered, un-anodized)), and ABL-anodized) all with and without K_2SO_4 salt coating during the heating cycle to 1500 °C in a p_{O2} = 0.1 Pa atmosphere. The anodized samples of AB and ABL showed initial mass loss until the temperature reached a value of ~680 °C. The initial mass loss at these low temperatures could be associated with decomposition of carbonaceous materials incorporated in the anodic oxide layer from the anodization electrolyte. The un-anodized AB and ABL samples showed a mass gain at a slower rate at temperatures below 650 °C. A sharp increase in the rate of mass gain was observed above 670 °C for sample AB and above 700 °C for sample ABL. The mass gain rate was lower for the anodized samples as noted in Figure 4.3. The mass gain of the ABL un-anodized and anodized samples continued until about 1300 °C and then plateaued. When the temperature increase beyond 1360 °C, a mass-loss was recorded until the final test temperature was reached. In the case of the AB-anodized sample, the mass gain continued until 1415 °C and a further

increase in the temperature caused a mass loss. The mass loss on the samples could be associated with the vaporization of $B_2O_{3(l)}$ to $B_2O_{3(g)}$.

Figure 4.3: TGA results during ramping up to 1500 °C in p_{O2} = 0.1 Pa for samples AB and ABL in the un-anodized, anodized, salted, and anodized & salted conditions. Sample weights were set to zero after three hours to adjust for sample moisture variations.

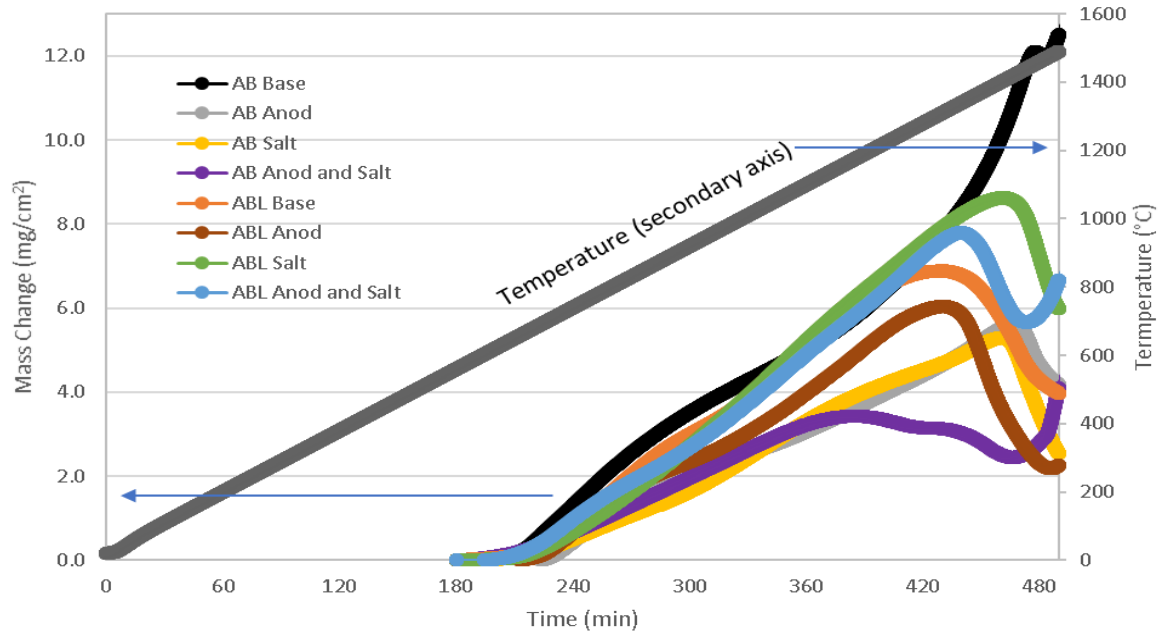

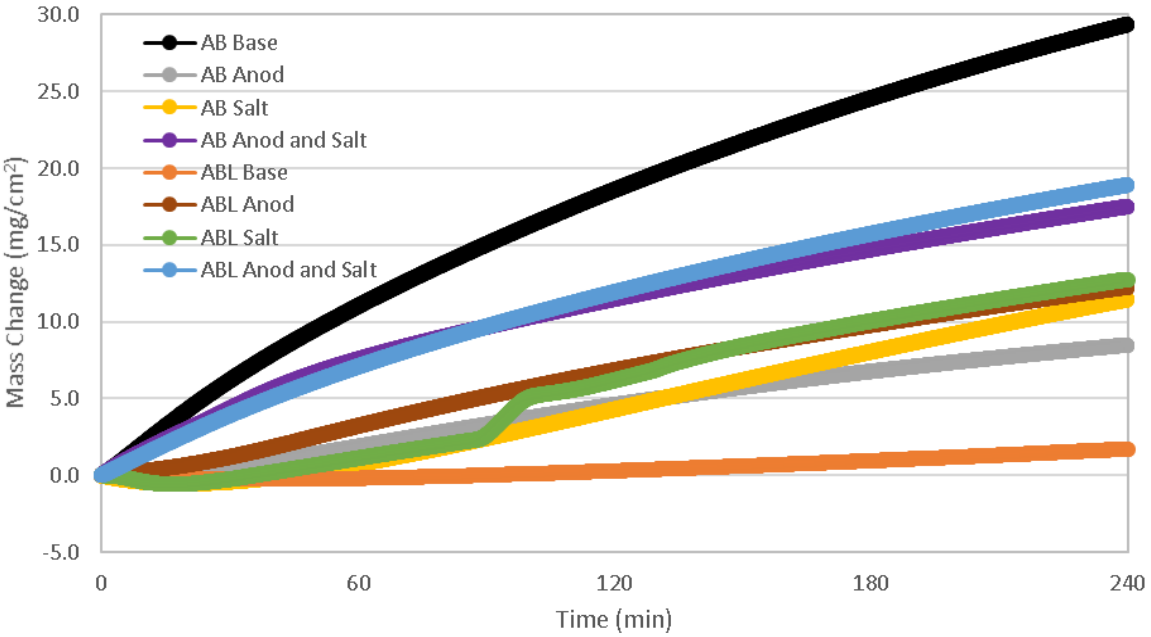

Figure 4.4: Isothermal TGA results at 1500 °C in p_{O2} = 0.1 Pa for samples AB and ABL in the un-anodized, anodized, salted, and anodized & salted conditions. Samples weights were set to zero at 1500 °C for comparison.

After reaching 1500 °C, the samples were soaked at this temperature for 4 hours and the weight change was monitored. Figure 4.4 shows the weight change of the samples at 1500 °C as a function of time in the low oxygen atmosphere of p_{O2} = 0.1 Pa. For simplicity, the initial weight of all the samples was tared to zero when the 1500 °C soaking started. It should be noted that there were significant weight change differences during the ramping up to 1500 °C between the samples. The mass change vs. time data plots were analyzed using logarithmic and parabolic relations. When the data was plotted in log-log scale, the mass gain was linear during the first 10 minutes of isothermal oxidation at 1500 °C as seen in Figure 4.S6 (log(Δm) vs. log(t)) (Supporting information). For samples AB un-anodized and ABL anodized, the later stages of isothermal oxidation of the samples followed a parabolic relation. Table 4.3 summarizes the parabolic rate constants (K_p) calculated based on the mass gain data at 1500 °C at p_{O2} = 0.1 Pa. The transitions in the oxidation behaviors of ZrB_2 and pure Zr have been reported by other researchers. Dollins[21] and Yoo et al.[22] both observed parabolic oxidation behavior of Zr-alloy during the initial period, which transitioned into cubic oxidation behavior and finally showed linear oxidation behavior. According to the Deal-Grove model,[23] the linear oxidation kinetics is controlled by the surface reaction and the oxide film is very thin where the concentration of oxidant is assumed constant throughout the system. The parabolic oxidation kinetics indicates that there is a thicker film and the oxide growth is controlled by the diffusion of oxidant. The cubic oxidation kinetics is associated with the growth of an inner protective layer controlled by oxygen grain boundary transport.[24] Hauffe and Kefstad[25] observed cubic rate law data during the oxidation of Cu_2O at 600-1000 °C and attributed field assisted transport of ions through the CuO layer to cubic growth.

Table 4.3: Parabolic rate constants determined from TGA data for samples without salt addition during the later portion of soaking time at 1500 °C in p_{O2} = 0.1 Pa and during the injection of oxygen equal to p_{O2} = 0.3 x 10^5 Pa for 15 minutes.

Condition	*Sample*	K_p $(mg^2/cm^4 \cdot min)$	K_p $(mg^2/cm^4 \cdot hr)$	K_p $(kg^2/m^4 \cdot s)$	$log\ (K_p)$
p_{O2} = 0.1 Pa	AB Base	4.16	249.36	6.93 x 10^{-6}	-5.16
p_{O2} = 0.1 Pa	AB Anod	0.39	23.12	6.42 x 10^{-7}	-6.19
p_{O2} = 0.1 Pa	ABL Base	0.01	0.816	2.27 x 10^{-8}	-7.64
p_{O2} = 0.1 Pa	ABL Anod	0.78	46.61	1.29 x 10^{-6}	-5.89
p_{O2} = 0.3 x 10^5 Pa	AB Base	5.43	325.79	0.91 x 10^{-5}	-5.04
p_{O2} = 0.3 x 10^5 Pa	AB Anod	4.99	299.67	0.83 x 10^{-5}	-5.08
p_{O2} = 0.3 x 10^5 Pa	ABL Base	17.25	1035.18	2.88 x 10^{-5}	-4.54
p_{O2} = 0.3 x 10^5 Pa	ABL Anod	14.93	895.86	2.49 x 10^{-5}	-4.60

Monteverde and Bellosi[26] proposed a para-linear model for oxidation of monolithic ZrB_2. Tu et al.[27] investigated high-temperature oxidation of ZrB_2-SiC composites at different oxygen partial pressures and temperatures. The authors of the present work observed that the parabolic rate constant (K_p) increased with lower p_{O2}, possibly due a lesser amount of glass layer being formed on the composite surface. At 1773 K, Tu et al. reported K_p values on the order of 0.7×10^{-6} $kg^2/m^4 \bullet s$. This value is similar to the K_p value of the AB-anodized sample in the $p_{O2} = 0.1$ Pa atmosphere.

This observation indicated that the anodization of the samples gave them a protective effect similar to when SiC is added to ZrB_2. The parabolic rate constants of AB un-anodized was an order of magnitude higher than that of the AB anodized. The ABL un-anodized samples showed the lowest K_p value among the samples tested. The better oxidation resistance of the ABL samples could be attributed to the addition of La which possible hindered the diffusion of ions. The anodization of ABL was observed not to increase the oxidation resistance. The higher K_p value of the anodized ABL, when compared to the un-anodized ABL, could be related to porosity developed on the anodic oxide due to decomposition of the carbonaceous material. It should also be noted that the anodized samples of both AB and ABL showed the same order of magnitudes of K_p values. In fact, the AB-anodized sample showed better oxidation resistance than the ABL-anodized sample. Incorporation of La^{3+} into the anodic oxide layer was probably detrimental as it could introduce more oxygen vacancies.

After 4 hours of isothermal oxidation at a $p_{O2} = 0.1$ Pa, the test continued by increasing the oxygen partial pressure to 0.3×10^5 Pa for 15 minutes. After this 15-minutes inlet of oxygen, the oxygen partial pressure was returned to the 0.1 Pa and the oxidation continued for another 4 hours. During the oxygen partial pressure change, the temperature was held constant at 1500 °C. Figure 4.5 shows the mass change of the samples as a function of time under isothermal conditions for this p_{O2} change and the following 4 hours. During the introduction of the $p_{O2} = 0.3 \times 10^5$ Pa, the mass gain data plotted in log-log scale showed a slope of about 0.75. This behavior is in-between linear and parabolic growth kinetics.

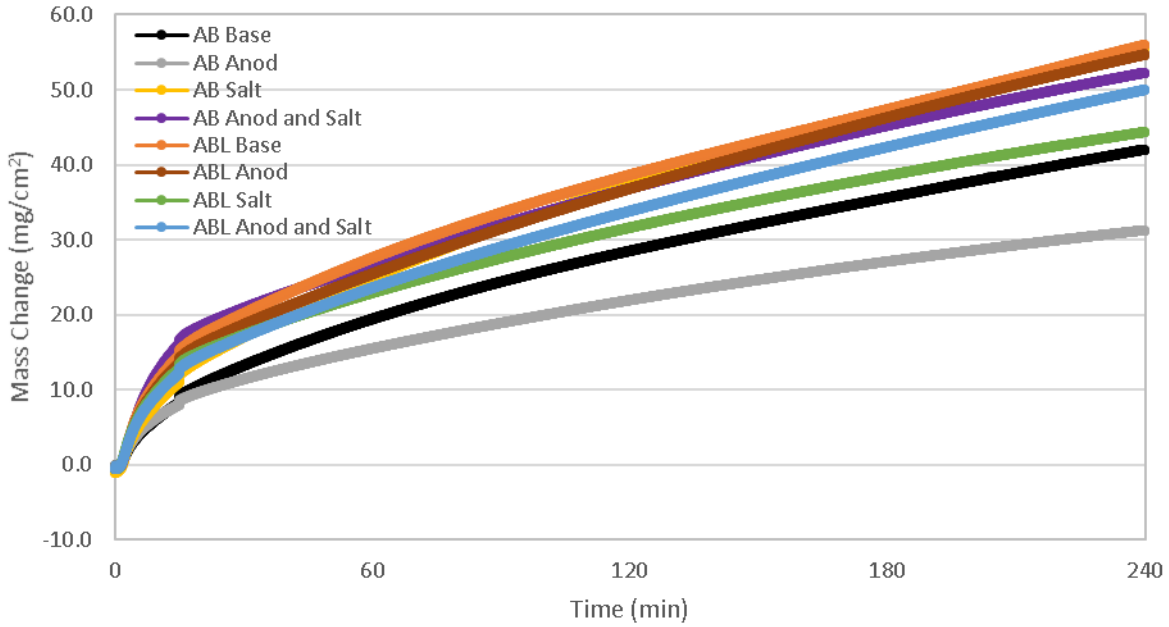

Figure 4.5: Isothermal TGA results at 1500 °C in p_{O2} = 0.3 x 10^5 Pa for samples AB and ABL in the un-anodized, anodized, salted, and anodized & salted conditions. Sample weights were set to zero at the start of the oxygen introduction for comparison.

After the introduction of the higher oxygen partial pressure, the oxidation continued at low partial pressure during which time the oxygen present in the tube furnace was consumed. It was during this time that the oxidation kinetics transitioned to a parabolic growth rate as the slope of the log (Δm) and log (t) was ~0.5. Table 4.3 also summarizes the parabolic rate constants of the samples in high oxygen concentrations at 1500 °C. The anodized AB sample showed the lowest K_p value and the un-anodized ABL showed the highest K_p value among the unsalted samples tested. Anodization was found to help control the oxidation of the AB samples.

Seong et al.[28] reported very high K_p values (125,442 $\mu m^2/h$) for oxidation of monolithic ZrB_2 without SiC addition in air at 1500 °C without any SiC addition. If ZrO_2 has a density of 5.68 g/cm^3 and assuming that the oxide layer is non-porous, the K_p value reported by Seong et al.[28] could be calculated as 1.12 x 10^{-3} $Kg^2/m^4 \bullet s$. The K_p value of our AB sample was more than two orders of magnitude lower than the K_p value reported for unmixed ZrB_2 in air at 1500 °C. Additionally, anodization of the AB sample decreased the oxidation kinetics by about 10-20% as compared to the un-anodized AB control sample. Unfortunately, the data available in literature is quite limited on pure ZrB_2 or HfB_2 systems without the addition of SiC or other sintering aids.

The SEM images in Figure 4.6(a-d) show the morphology of the oxidized surface after high-temperature oxidation. The EDS linescan analysis on these four samples, shown in Figures 4.S7-4.S10

(Supporting information), revealed that the AB control sample had hafnium enrichment at the oxide/substrate interface, but that throughout the oxide layer there was a higher concentration of zirconium. This oxide layer enrichment of zirconium was enhanced even further by the anodization process. The zirconium concentration near the surface increased for all samples. In the ABL control sample, the concentration of hafnium was also lower throughout the oxide layer when compared to the AB control sample. Although the anodization process did not enhance this pattern as in the AB sample, it did create a lanthanum enriched layer about 50 µm below the surface whereas the ABL control sample showed no lanthanum enriched layer.

4.4.2 Hot Corrosion of Samples

4.4.2.1 TGA Results of Anodized and Un-Anodized Samples at 1500 °C in p_{O2} = 0.1 Pa and p_{O2} = 0.3 x 10^5 Pa Using a K_2SO_4 Salt Coating

The weight change plots of samples that were coated with K_2SO_4 and exposed to 1500 °C under a low oxygen partial pressure of 0.1 Pa are shown in Figure 4.4. Higher weight gain was observed, in general, for the salt corrosion samples than for those samples without salt. After reaching temperatures in the range of 1300 °C, a decrease in weight was observed in all the samples coated with K_2SO_4 salt. During isothermal oxidation at 1500 °C with an oxygen partial pressure of 0.1 Pa, a linear oxidation kinetics was observed for anodized AB and anodized ABL. The linear kinetics indicated that the oxidation occurred by surface reactions with adsorbed oxygen gas molecules at the sites where salt molecules were not present. These sites were most likely available due to inevitable problems with complete wetting of the surface with the K_2SO_4 salt which is liquid at these temperatures. The oxides nucleated by surface reactions grew by surface diffusion as well as diffusion through the salt coating and the entire surface was covered with a thin surface oxide layer. At this point, the linear kinetics transitioned to parabolic kinetics. The parabolic rate constants of the K_2SO_4 salt coated samples are summarized in Table 4.4. The K_p value for the un-anodized AB salt sample was lower than the K_p value for the un-anodized AB sample without salt shown in Table 4.3.

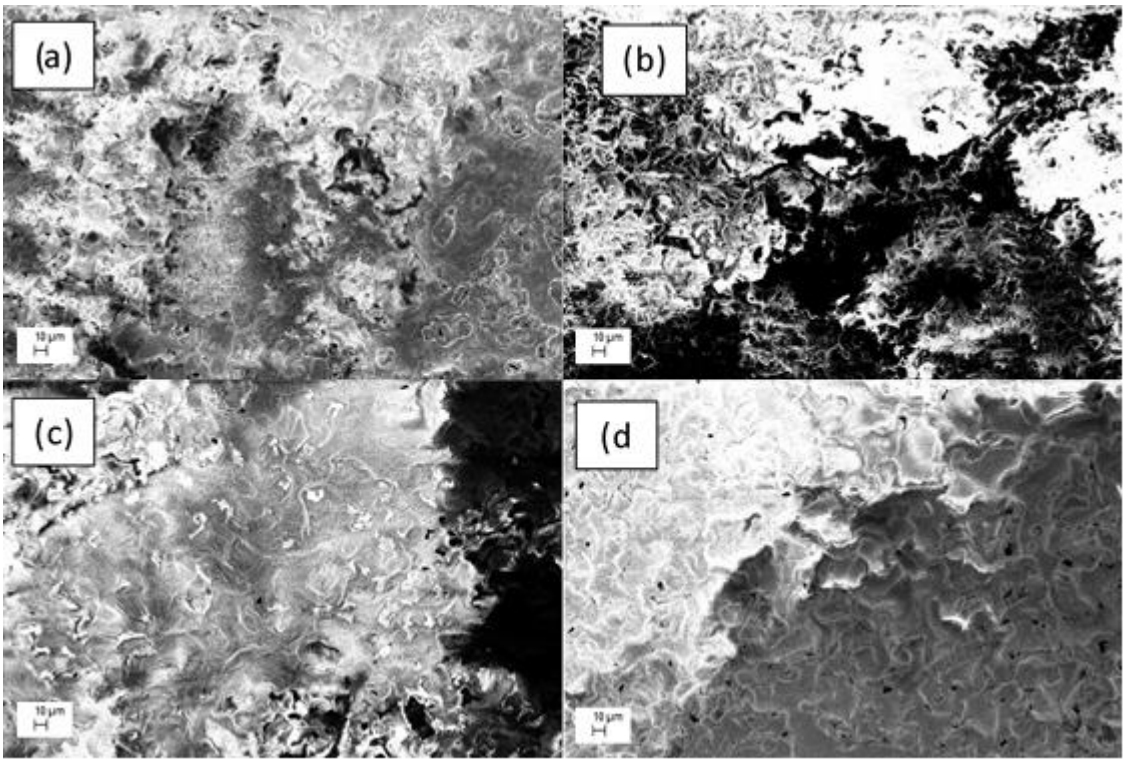

Figure 4.6: Post-TGA SEM images at 250 X showing the morphology of the oxidized surface for the samples witho addition. (a) Sample AB, (b) anodized sample AB, (c) sample ABL, (d) anodized sample ABL.

Table 4.4: 4.4 Parabolic rate constants determined from TGA data for samples with K_2SO_4 salt addition applied at a rate of 2.5 mg/cm², at 1500 °C in a p_{O2} = 0.1 Pa and during the injection of oxygen equal to p_{O2} = 0.3 x 10^5 Pa for 15 minutes.

Condition	*Sample*	K_p *(mg²/cm⁴•min)*	K_p *(mg²/cm⁴•hr)*	K_p *(kg²/m⁴•s)*	*log (K_p)*
p_{O2} = 0.1 Pa	AB Salt	0.70	42.21	1.17 x 10^{-6}	-5.93
p_{O2} = 0.1 Pa	AB Anod & Salt	1.38	82.83	2.30 x 10^{-6}	-5.64
p_{O2} = 0.1 Pa	ABL Salt	1.01	60.77	1.69 x 10^{-6}	-5.77
p_{O2} = 0.1 Pa	ABL Anod & Salt	1.71	102.66	2.85 x 10^{-6}	-5.54
p_{O2} = 0.3 x 10^5 Pa	AB Salt	9.90	593.81	1.65 x 10^{-5}	-4.78
p_{O2} = 0.3 x 10^5 Pa	AB Anod & Salt	22.06	1323.72	3.68 x 10^{-5}	-4.43
p_{O2} = 0.3 x 10^5 Pa	ABL Salt	13.14	788.52	2.19 x 10^{-5}	-4.66
p_{O2} = 0.3 x 10^5 Pa	ABL Anod & Salt	11.99	719.58	2.00 x 10^{-5}	-4.70

On the other hand, the K_p values increased in the salt containing atmosphere for all other samples. The K_p values were in the range of 1.17 x 10^{-6} – 2.85 x 10^{-6} Kg^2/m^4•s for all the samples with the addition of the salt at 1500 °C with a partial pressure of oxygen of 0.1 Pa. When the oxygen partial pressure was increased to 0.3 x 10^5 Pa, the parabolic rate constants increased by an order of magnitude as shown in Tables 4.3 and 4.4. It should be noted that the presence of an anodic oxide layer (anodized samples) was not advantageous with regards to decreasing the oxidation kinetics in

both the low and high partial pressures of oxygen. For the ABL samples, the presence of a salt coating was observed to decrease the oxidation kinetics in both the anodized and un-anodized conditions. On the other hand, AB samples showed enhanced oxidation kinetics in the presence of the K_2SO_4 salt. Anodization, as mentioned before, was not beneficial when K_2SO_4 was present, in fact, it adversely affected the oxidation resistance of the AB sample. The surface morphology of the four samples tested with salt can be seen in Figure 4.7(a-d). The EDS linescan analysis, shown in Figures 4.S11-4.S14 (Supporting information) supports the theory that the B_2O_3 has evaporated from the top surface of the samples as all the samples had either none or very low boron content at the surface. For the un-anodized AB sample, the hafnium concentration decreased as the linescan approached the surface and ended with a spike of zirconium at the surface. It was also noted that boron was depleted just below the oxide/substrate interface for both un-anodized samples. The boron content, in general, reached a peak concentration at or near the middle of the oxide layer and decreased rapidly toward the sample surface. For the anodized AB sample, the oxide layer contained a higher concentration of zirconium than hafnium. Both anodized samples showed no indication of a boron depleted zone below the oxide/subsurface interface. For the anodized ABL sample lanthanum was enriched on the surface of the sample, this was in opposition to the un-anodized ABL sample which showed no change in lanthanum concentration across the oxide layer. The XRD analysis was used to compare the anodized AB sample to the salted AB sample as shown in Figure 4.8. Anodization increased the relative intensity of several oxide peaks (25°, 49°, 72°) and also a boride peak at 58°. The oxide peaks were identified as monoclinic oxide peaks. No additional salt peaks were noted on the sample coated with 2.5 mg/cm^2 K_2SO_4 after the 8 hour TGA furnace run at 1500 °C.

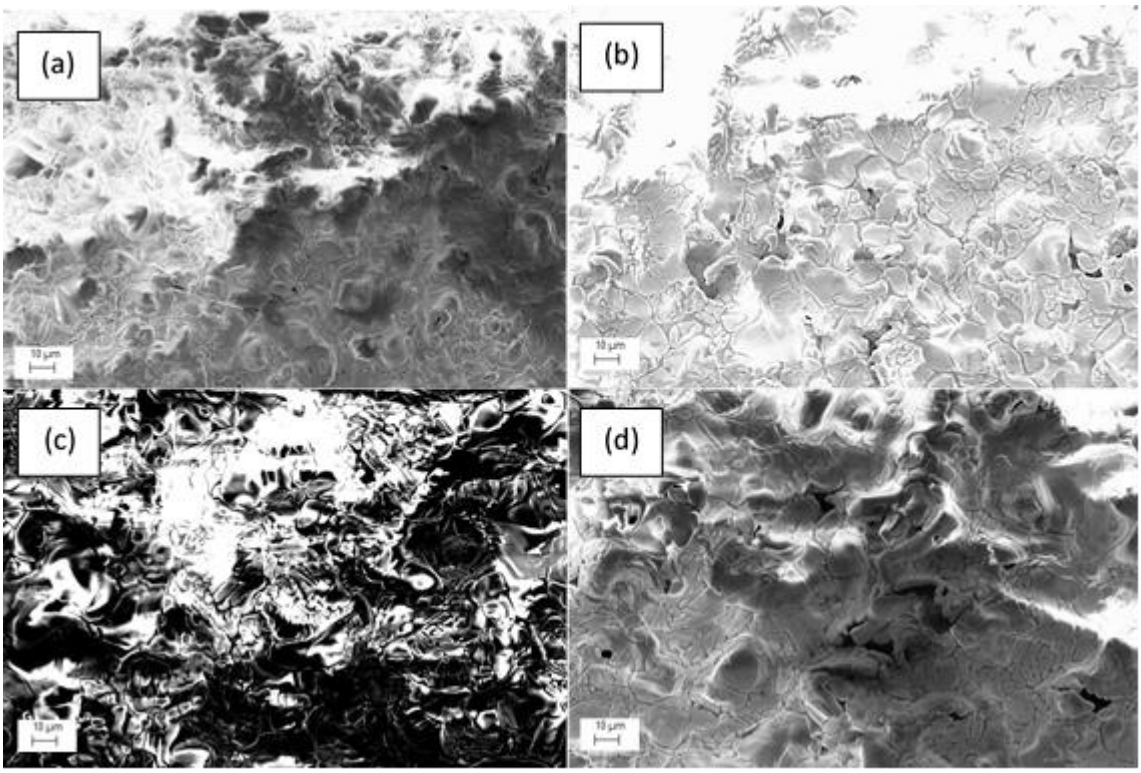

Figure 4.7: Post-TGA SEM images at 500 X showing the morphology of the oxidized surface for the samples with K_2SO_4 salt applied at a rate of 2.5 mg/cm². (a) Sample AB salted, (b) anodized sample AB salted, (c) sample ABL salted, (d) anodized sample ABL salted.

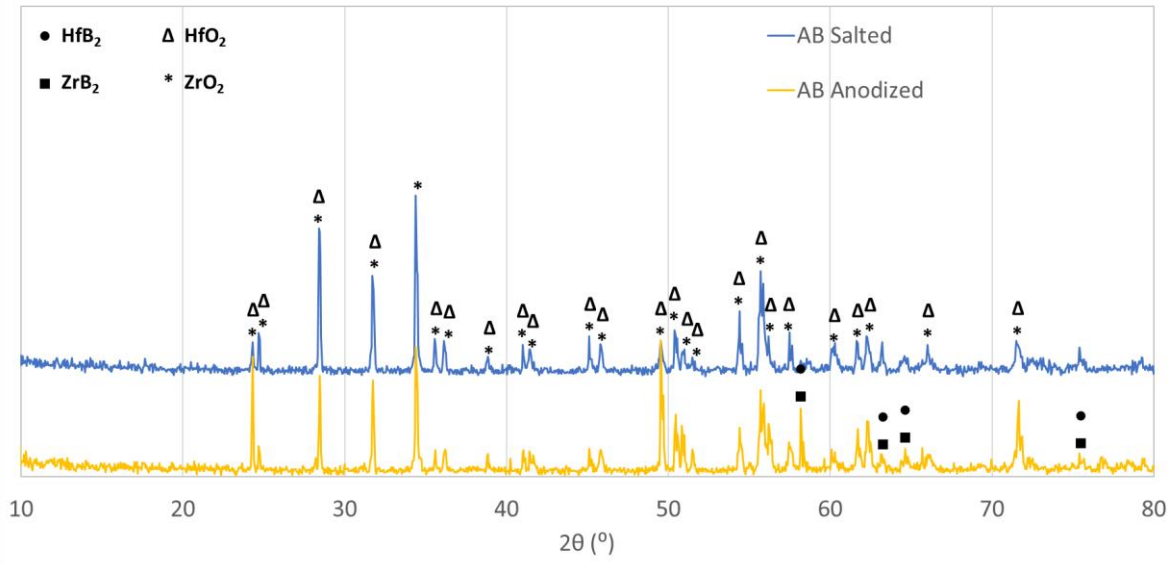

Figure 4.8: Post-TGA XRD analysis of AB samples comparing surface analysis of anodized sample to sample coated with 2.5 mg/cm² K_2SO_4 salt.

4.4.2.2 Hot Corrosion of Samples Soaked for 4 hours at 1550 °C in p_{O2} = 1 Pa without Anodic Oxide Coating

Figure 4.9(a) and (b) illustrate the surface attack on the AB un-anodized sample coated with KCl and exposed to 1550 °C for 4 hours. It should be noted that the melting point of KCl is 770 °C and the boiling point is 1420 °C. The possible reactions of $(TM)B_2$ with KCl in the presence of oxygen could be given as:

$$(TM)B_2 + 2KCl + 3/2\ O_2 \rightarrow K_2(TM)O_3 + Cl_2 \quad (17)$$

$$(TM)O_2 + 2KCl \rightarrow (TM)OCl_2 + K_2O \quad (18)$$

The other possible reaction products are $ZrCl_4$, $HfCl_4$ BCl_3 K_2ZrCl_6, K_2HfCl_6, Etc., however, the tetra-chloride of transition metals and BCl_3 are possible only through the following carbothermal reactions where (TM) represents any of the available transition metals:

$$B_2O_3 + 3C + 3Cl_2 \rightarrow 2BCl_3 + 3CO \quad (19)$$

$$(TM)O_2 + 2C + 2Cl_2 \rightarrow (TM)Cl_4 + 2CO \quad (20)$$

In the absence of sufficient carbon, the formation of tetra or tri-chlorides is not expected in this study. The top morphology shows the presence of a discontinuous layer and the cross-sectional view does not indicate the presence of a thick corrosion layer. Weight loss was recorded on this sample as -1.7% which was similar to the weight loss recorded without KCl. The EDS analysis shown in Table 4.2 indicated that the amounts of Zr and Hf present on the top surface were almost equal. The boron content was also low on the surface.

Figure 4.9(c) and (d) show the surface and cross-sectional views of the ABL sample that was exposed to KCl at 1550 °C for 4 hours. The top surface showed the formation of a continuous layer but the thickness of the corrosion product layer was not clearly discernable. The maximum depth of attack at discrete locations was estimated to be about 30 µm. The exact weight change of this sample could not be determined due to breaking the sample upon removal from the furnace. The EDS analysis (Table 4.2) indicated that lower amounts of Zr and Hf and higher amounts of B were present when compared to the AB sample under the same conditions. As a reminder, the concentrations of O and especially B and C determined from the EDS are not reliable and useful only for qualitative comparison.

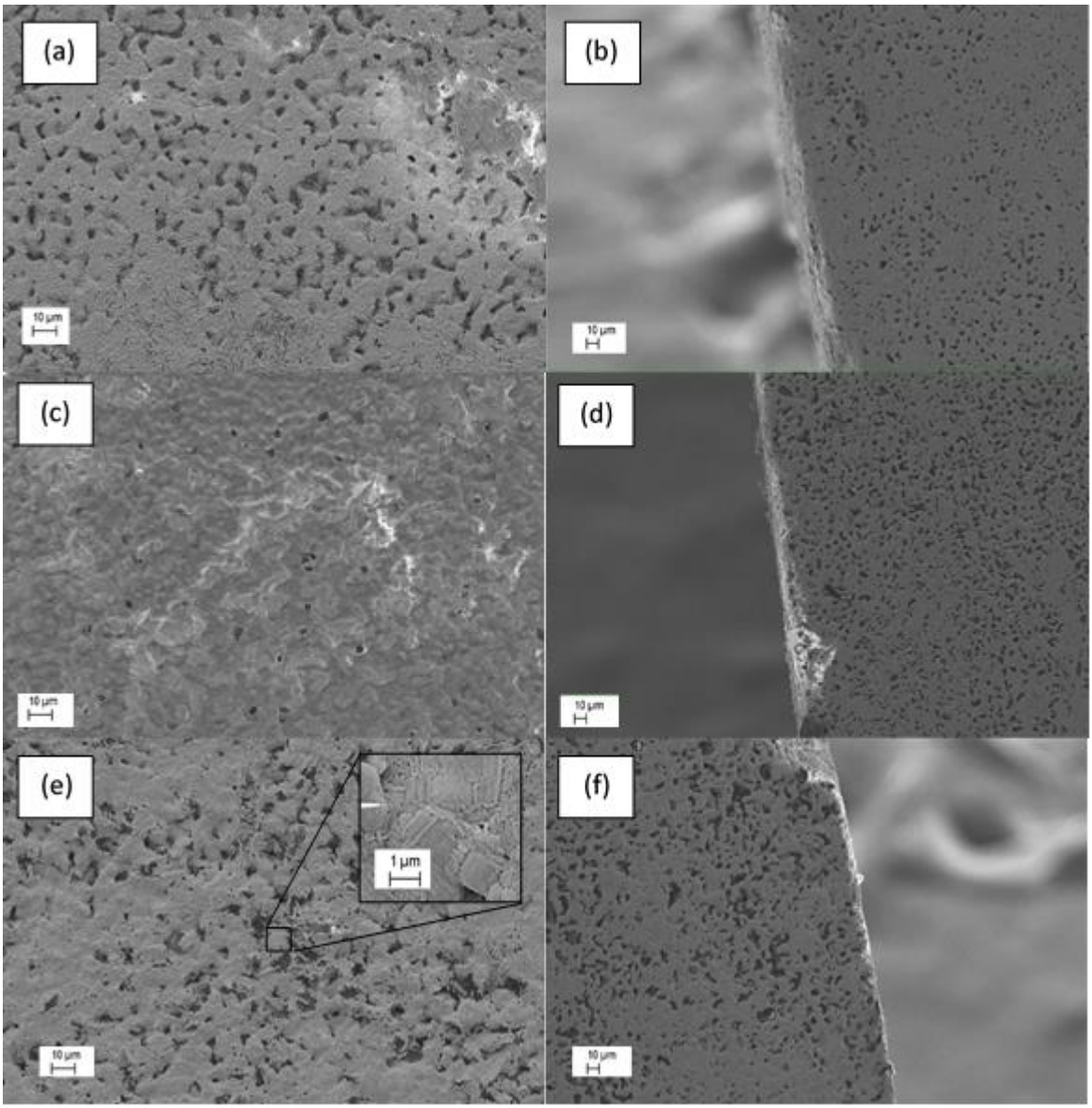

Figure 4.9: SEM images of un-anodized samples coated with KCl at a rate of 2.5 mg/cm² after heating in tube furnace for 4 hours at 1550 °C with p_{O2} ~ 1 Pa. (a) top view of sample AB at 500 X, (b) cross-sectional view of sample AB at 250 X, (c) top view of sample ABL at 500 X, (d) cross-sectional view of sample ABL at 250 X, (e) top view of sample ABH at 500 X with magnified inset at 5K X, (f) cross-sectional view of sample ABH at 250 X.

Figure 4.9(e) and (f) show the images of the ABH sample surface exposed to the chloride salt at 1550 °C for 4 hours. A dual layered structure, similar to the one observed for the AB control sample, was observed. The cross-sectional image shows a uniform attack depth of 10 µm with deeper attacks at discrete locations with a depth of ~150 µm. The weight loss of the ABH sample was larger than that of AB. This result was similar to the trend observed in the weight loss during thermal oxidation.

The EDS analysis (Table 4.2) showed that the top surface was enriched in Hf and the boron content was higher than in sample AB.

4.4.2.3 Hot Corrosion of Samples Soaked for 4 hours at 1550 °C in p_{O2} = 1 Pa with Anodic Oxide Coating

The hot corrosion tests with KCl coating on the anodized samples (Figure 4.10(a-f)) indicated that the weight loss characteristics are similar to the un-anodized sample. In fact, the anodized samples showed higher weight losses than those observed on the un-anodized samples. The EDS analysis indicated that the compositions of the top layer of the anodized samples exposed to KCl had similar trends to the anodized samples without KCl salt exposure. All samples showed higher Zr content than Hf. However, the La content of the ABL sample was low, as compared to the ABL sample not coated with KCl. The top surface morphologies after KCl corrosion were similar to the surface morphologies exposed to high temperatures without a KCl coating. The cross-sectional SEM images indicated deeper corrosion penetration with the anodized samples than that of the un-anodized samples as can be seen in Figure 4.10(b), (d), and (f) when compared to Figure 4.9(b), (d) and (f). The XRD analysis of the two KCl-salted ABH samples, one anodized one as-received, showed that the anodized sample significantly reduced the amount of diboride on the surface. All oxide peaks were identified as monoclinic oxide. The additional or intensified peaks at 26°, 33°, 42°, 52°, 58°, 63°, 65°, 68°, and 75° are all associated with hafnium and zirconium diboride. These peaks are either not present or much less intense in the anodized & salted ABH sample as can be seen in Figure 4.11.

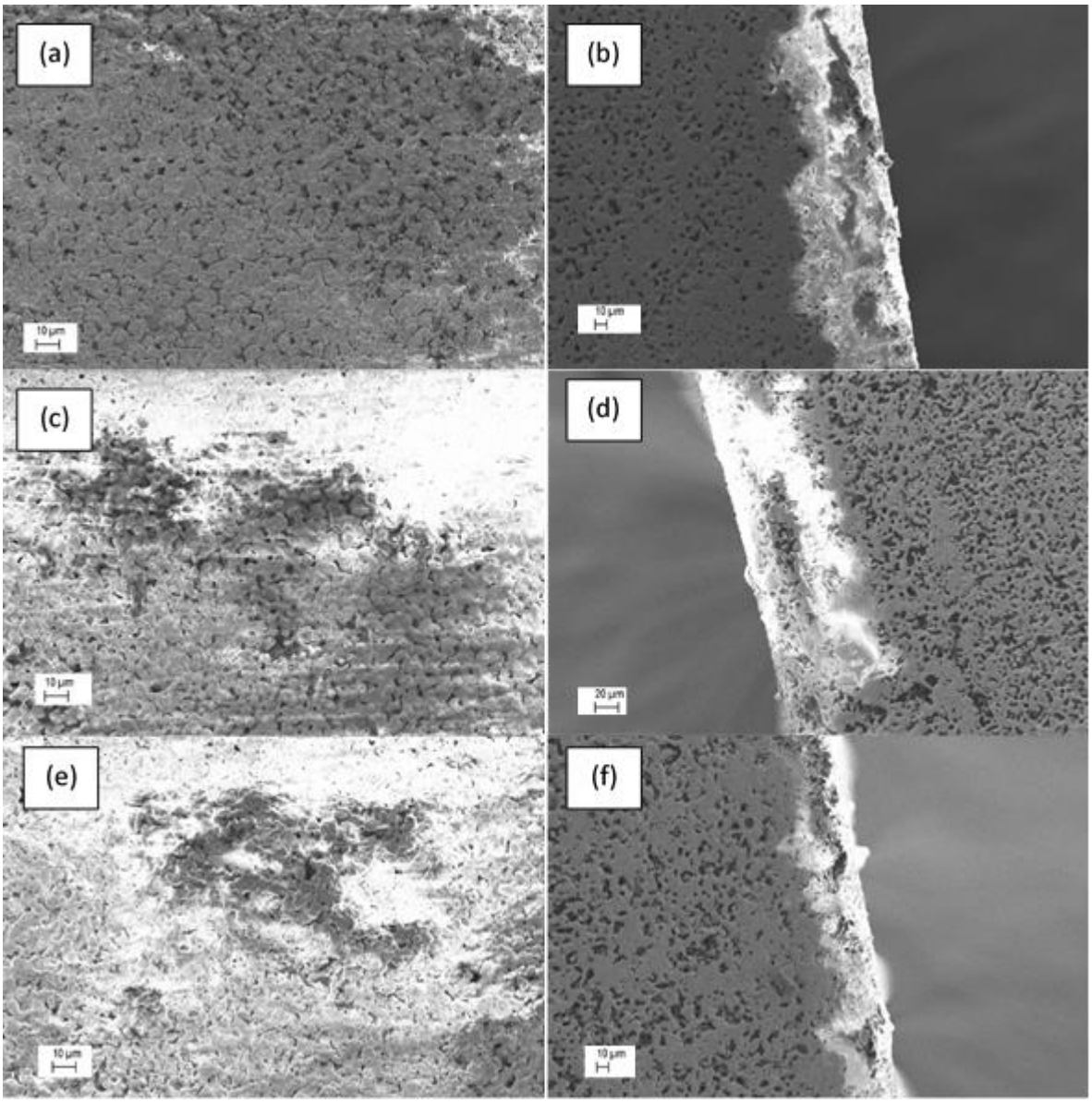

Figure 4.10: SEM images of anodized samples coated with KCl at a rate of 2.5 mg/cm^2 after heating in tube furnace for 4 hours at 1550 °C with p_{O2} ~ 1 Pa. (a) top view of sample AB at 500 X, (b) cross-sectional view of sample AB at 250 X, (c) top view of sample ABL at 500 X, (d) cross-sectional view of sample ABL at 250 X, (e) top view of sample ABH at 500 X with magnified inset at 5K X, (f) cross-sectional view of sample ABH at 250 X.

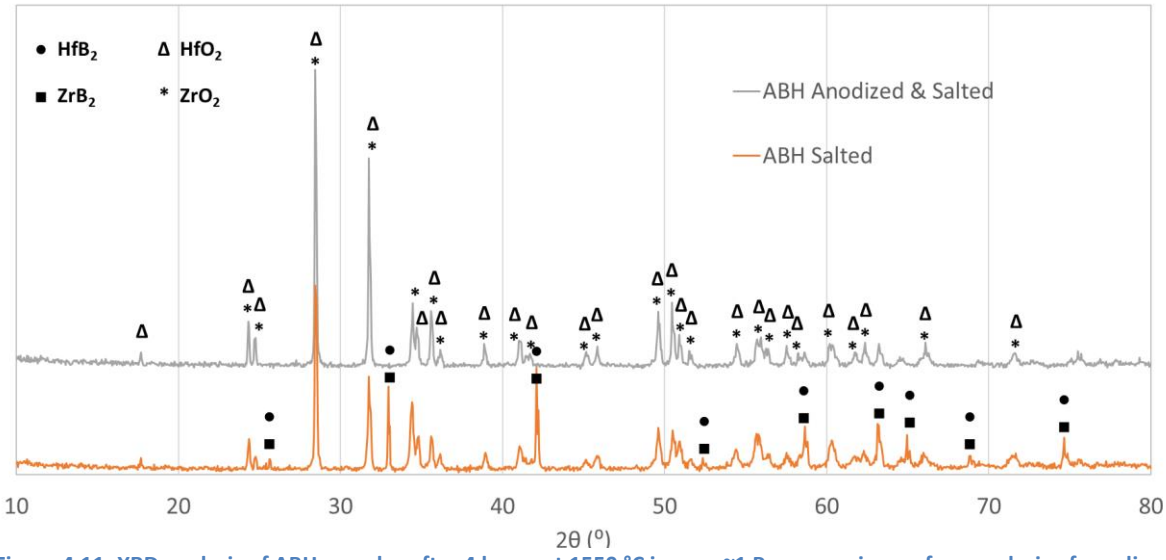

Figure 4.11: XRD analysis of ABH samples after 4 hours at 1550 °C in p_{O2} =~1 Pa comparing surface analysis of anodized & salted ABH sample to un-anodized salted ABH sample both coated with 2.5 mg/cm² KCl salt.

4.4.3 High-Temperature Conductivity

4.4.3.1 Electrical Resistivity

Figure 4.12 shows the electrical resistivity of the as-sintered AB, anodized AB, and as-sintered ABL samples as a function of temperature. Sample ABL showed the highest resistivity and the anodized AB sample showed the lowest resistivity as a function of temperature. The increase in resistivity for the AB sample was 3.8 mΩ-cm/°C and for the ABL sample it was about 15% higher than that of AB at 4.4 mΩ-cm/°C. The anodized AB sample showed an increase in resistivity at the rate of 2.43 mΩ-cm/°C. The ABL sample showed higher resistivity than both as-sintered AB sample and the anodized AB sample, which was counter intuitive to our expectations as La was expected to improve conductivity. This could possibly be attributed to the increased electron scattering by La which also showed higher density of states at the Fermi level.[10]

4.4.3.2 Electrochemical Impedance Spectroscopy and Equivalent Circuit Modeling

To understand the conductivity behavior further, electrochemical impedance spectroscopy (EIS) results were analyzed. Figure 4.S15(a-c) (Supporting information) shows the Nyquist plots of the as-sintered AB, anodized AB, and as-sintered ABL samples at different temperatures. The Bode plots are given in Figure 4.S16(a-c) (Supporting information) for the as-sintered AB, anodized AB, and as-sintered ABL samples, respectively. The EIS data were fitted with different electrical circuits consisting of resistors, capacitors, and inductors. The electrical equivalent circuit, shown in Figure

4.S17 (Supporting information), fit the EIS data well with a goodness of fit (χ^2) less than 10^{-5}. The equivalent circuit model consists of an inductor and a capacitor connected in parallel forming an 'LC' loop which was connected in series with a resistor. Here the inductor could be associated with adsorbed gaseous molecules from the stream of argon. The commercial purity argon contained 10 ppm of oxygen. It is reported that the inductor behavior in EIS is often related to the adsorption species on the surface of the sample.[29] The capacitance behavior could be attributed to the formation of a thin oxide layer by adsorption of trace oxygen from the argon at low temperatures. At high temperatures, a capacitor-like behavior is possible because of the formation of the B_2O_3 liquid phase. When temperatures increase above 1200 °C, the thickness of the liquid layer decreased because of volatilization leading to the capacitance of inductance values changing as the temperatures increase beyond this temperature.

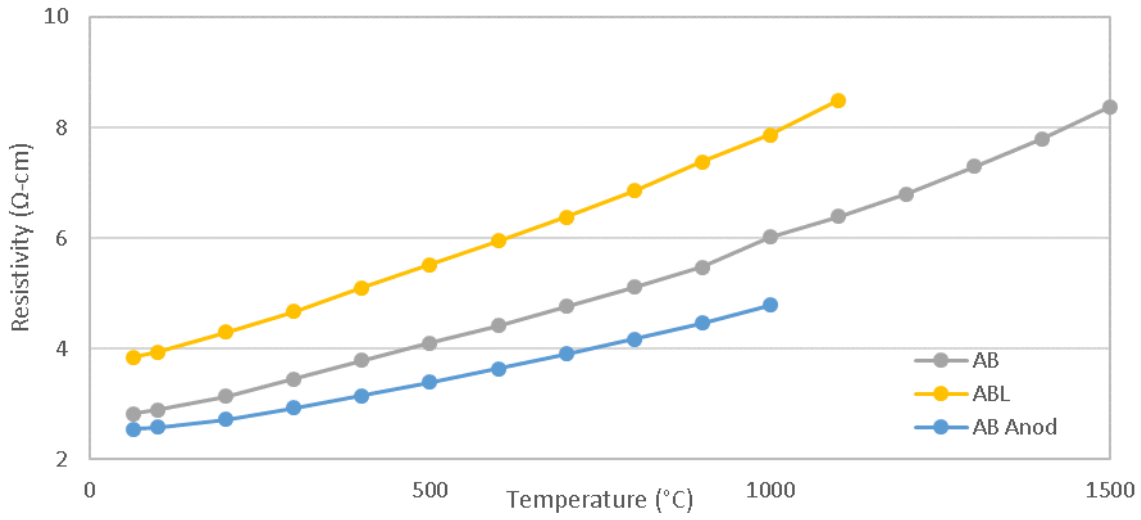

Figure 4.12: Electrical resistivity of sample AB, sample AB after being anodized, and sample ABL. All samples were tested using the clamping system in Figure 4.S1 at 100 °C intervals with a ramp rate of 8 °C/min in a p_{O2} ~ 1 Pa atmosphere.

Tables 4.5-4.7 summarize the values of the components of the electrical equivalent circuit shown in Figure 4.S17 (Supporting information), for the as-sintered AB, anodized AB, and as-sintered ABL samples, respectively. The R_1 term, representing the bulk resistance of the sample, increased with the increase in temperature. These values matched well with the values determined by linear polarization measurements. The resistivity values (shown in Figure 4.12) were determined from the linear polarization measurements after accounting for the cross-sectional area and the thickness using the relation $\rho = R*A/L$, where ρ is resistivity in Ω-cm, R = resistivity in Ω and equals the measured

slope of the linear polarization, *A* = cross-sectional area of the sample, and *L* = the thickness of the sample.

The value of the inductor of the AB sample was around 945 x 10^{-9} Ω-s or Henry, around 9.86 x 10^{-9} Ω-s or Henry for the anodized AB sample, and for the ABL sample, the inductor value was about 1.37 x 10^{-6} Ω-s or Henry. The inductor values were very stable across the temperature changes. The ABL sample showed a ~35% higher inductance which could be attributed to the increased number of unpaired electrons on the surface due to La incorporation. The capacitance values of all three samples were of the same order of magnitude. The capacitance values decreased with an increase in the temperature, in general. If the capacitor value is related to the space charge layer of the surface layer of the sample at low temperatures, and interfacial capacitance due to liquid B_2O_3 film at intermediate temperatures, then increasing the space charge layer width or increasing the thickness of the liquid film would results in the decrease of capacitance following the simple relation $C = \varepsilon\varepsilon_0/d$, where ε = dielectric constant (assumed to be invariant with temperature), ε_0 = permittivity in vacuum, and d = thickness of liquid film or space charge layer. At high temperatures, the B_2O_3 liquid film evaporates leaving a porous surface which results in an increase in the 'd' value and a decrease the 'ε' value as well. Therefore, the significant reduction in the capacitor values at temperatures >900 °C in the case of ABL, >1000 °C for anodized AB, and >1100 °C in the case of AB could be related to the loss of B_2O_3.

Table 4.5: Equivalent circuit model parameters fit into model shown in Figure 4.S17 (Supporting information) for sample AB up to 1500 °C.

Temp (°C)	*R_1 (Ω)*	*C_2 (Farad)*	*L_3 (Henry)*	*Goodness of fit (χ^2)*
RT	0.477	4.40 x 10^{-8}	9.37 x 10^{-7}	3.10 x 10^{-5}
100	0.492	4.30 x 10^{-8}	9.38 x 10^{-7}	3.54 x 10^{-5}
200	0.533	4.25 x 10^{-8}	9.41 x 10^{-7}	3.20 x 10^{-5}
300	0.586	3.73 x 10^{-8}	9.41 x 10^{-7}	2.98 x 10^{-5}
400	0.642	3.55 x 10^{-8}	9.42 x 10^{-7}	2.89 x 10^{-5}
500	0.695	3.40 x 10^{-8}	9.43 x 10^{-7}	2.70 x 10^{-5}
600	0.749	2.89 x 10^{-8}	9.43 x 10^{-7}	2.60 x 10^{-5}
700	0.807	2.82 x 10^{-8}	9.43 x 10^{-7}	2.67 x 10^{-5}
800	0.865	2.53 x 10^{-8}	9.42 x 10^{-7}	2.61 x 10^{-5}
900	0.926	2.35 x 10^{-8}	9.44 x 10^{-7}	2.48 x 10^{-5}
1000	1.007	3.35 x 10^{-8}	9.52 x 10^{-7}	4.13 x 10^{-5}
1100	1.083	2.77 x 10^{-8}	9.48 x 10^{-7}	2.50 x 10^{-5}
1200	1.148	1.97 x 10^{-8}	9.42 x 10^{-7}	2.59 x 10^{-5}
1300	1.234	2.10 x 10^{-8}	9.48 x 10^{-7}	2.51 x 10^{-5}
1400	1.317	1.43 x 10^{-8}	9.50 x 10^{-7}	2.56 x 10^{-5}
1500	1.411	1.39 x 10^{-8}	9.54 x 10^{-7}	2.67 x 10^{-5}

Table 4.6: Equivalent circuit model parameters fit into model shown in Figure 4.S17 (Supporting information) for the anodized AB sample up to 1000 °C.

Temp (°C)	*R_1 (Ω)*	*C_2 (Farad)*	*L_3 (Henry)*	*Goodness of fit (χ^2)*
RT	0.471	5.59×10^{-8}	0.982×10^{-6}	4.08×10^{-5}
100	0.480	5.20×10^{-8}	0.981×10^{-6}	3.99×10^{-5}
200	0.505	4.96×10^{-8}	0.982×10^{-6}	3.84×10^{-5}
300	0.546	4.67×10^{-8}	0.983×10^{-6}	3.49×10^{-5}
400	0.586	4.49×10^{-8}	0.985×10^{-6}	3.43×10^{-5}
500	0.640	4.07×10^{-8}	0.986×10^{-6}	3.30×10^{-5}
600	0.677	4.06×10^{-8}	0.987×10^{-6}	3.21×10^{-5}
700	0.724	3.91×10^{-8}	0.989×10^{-6}	3.12×10^{-5}
800	0.773	3.61×10^{-8}	0.990×10^{-6}	2.89×10^{-5}
900	0.829	3.37×10^{-8}	0.990×10^{-6}	2.88×10^{-5}
1000	0.894	2.44×10^{-8}	0.984×10^{-6}	5.31×10^{-5}

Table 4.7: Equivalent circuit model parameters fit into model shown in Figure 4.S17 (Supporting information) for sample ABL up to 1100 °C.

Temp (°C)	*R_1 (Ω)*	*C_2 (Farad)*	*L_3 (Henry)*	*Goodness of fit (χ^2)*
RT	0.4595	5.86×10^{-8}	1.38×10^{-6}	8.30×10^{-5}
100	0.472	5.54×10^{-8}	1.38×10^{-6}	7.36×10^{-5}
200	0.5133	5.24×10^{-8}	1.38×10^{-6}	6.78×10^{-5}
300	0.5588	5.08×10^{-8}	1.38×10^{-6}	5.90×10^{-5}
400	0.6166	4.82×10^{-8}	1.39×10^{-6}	6.15×10^{-5}
500	0.6618	4.44×10^{-8}	1.39×10^{-6}	5.28×10^{-5}
600	0.7134	3.64×10^{-8}	1.37×10^{-6}	3.17×10^{-5}
700	0.765	3.50×10^{-8}	1.37×10^{-6}	2.70×10^{-5}
800	0.821	3.23×10^{-8}	1.37×10^{-6}	3.32×10^{-5}
900	8876	1.46×10^{-12}	1.36×10^{-6}	4.37×10^{-5}
1000	0.9448	2.11×10^{-14}	1.35×10^{-6}	3.94×10^{-5}
1100	1.018	1.071×10^{-13}	1.35×10^{-6}	3.67×10^{-5}

4.5 Conclusions

In summary, an evaluation of the oxidation resistance, hot corrosion resistance, and electrical resistivity of three diboride compositions has been completed. Anodization was found to aid in the oxidation resistance of sample AB but not for samples with the addition of lanthanum. Anodization was also found to have a distinct disadvantage for sample AB when the sample was exposed to the hot K_2SO_4 corrosive environment and to have no advantage for sample ABL. If a hot corrosive environment is to be used, the un-anodized ABL sample ($K_p = 1.33 \times 10^{-5}$ $kg^2/m^4 \bullet s$, TGA, post O_2 introduction) had the least amount of oxidation and corrosion and would be recommended for further research. The electrical resistivity measurements showed that the anodized AB sample had the highest conductivity and the ABL sample had the lowest conductivity at high temperatures. The diboride coating materials showed some promise for being able to withstand the extreme

environments of a plasma direct-power extraction chamber and would be good candidates for study in realistic prototype applications.

4.6 Acknowledgments

This work is supported by National Energy Technology Laboratory, US Department of Energy (Office of Fossil Energy) grant number: DEFE0022988.

4.7 Supporting Information

Supporting information associated with this article can be found in the online version at doi:10.1016/j.matlet.2016.10.122 or in Appendix C.

4.8 Bibliography

[1] D. L. Poerschke, M. D. Novak, N. Abdul-Jabbar, S. Krämer, and C. G. Levi, "Selective Active Oxidation in Hafnium Boride-Silicon Carbide Composites above 2000 °C," *J. Eur. Ceram. Soc.,* vol. 36, no. 15, pp. 3697–3707, Nov. 2016.

[2] W. G. Fahrenholtz, G. E. Hilmas, I. G. Talmy, and J. A. Zaykoski, "Refractory Diborides of Zirconium and Hafnium," *J. Am. Ceram. Soc.,* vol. 90, no. 5, pp. 1347–1364, May 2007.

[3] W. C. Tripp and H. C. Graham, "Thermogravimetric Study of the Oxidation of ZrB_2 in the Temperature Range of 800° to 1500°C," *J. Electrochem. Soc.,* vol. 118, no. 7, pp. 1195–1199, Jul. 1971.

[4] A. K. Kuriakose and J. L. Margrave, "The Oxidation Kinetics of Zirconium Diboride and Zirconium Carbide at High Temperatures," *J. Electrochem. Soc*., vol. 111, no. 7, pp. 827–831, Jul. 1964.

[5] W. G. Fahrenholtz, "The ZrB_2 Volatility Diagram," *J. Am. Ceram. Soc*., vol. 88, no. 12, pp. 3509–3512, Dec. 2005.

[6] W. C. Tripp, H. H. Davis, and H. C. Graham, "Effect of SiC Addition on Oxidation of ZrB_2," *Am. Ceram. Soc. Bullitin*, vol. 52, no. 8, pp. 612–616, 1973.

[7] J. B. Berkowitz-Mattuck, "High-Temperature Oxidation," *J. Electrochem. Soc*., vol. 113, no. 9, p. 908, 1966.

[8] J. W. Lawson, C. W. Bauschlicher, and M. S. Daw, "Ab Initio Computations of Electronic, Mechanical, and Thermal Properties of ZrB_2 and HfB_2," *J. Am. Ceram. Soc.,* vol. 94, no. 10, pp. 3494–3499, Oct. 2011.

[9] S. J. Sitler, K. S. Raja, and I. Charit, "ZrB_2-HfB_2 Solid Solutions as Electrode Materials for Hydrogen Reaction in Acidic and Basic Solutions," *Mater. Lett*., vol. 188, pp. 239–243, Feb. 2017.

[10] S. J. Sitler, K. S. Raja, and I. Charit, "Metal-Rich Transition Metal Diborides as Electrocatalysts for Hydrogen Evolution Reactions in a Wide Range of pH," *J. Electrochem. Soc.,* vol. 163, no. 13, pp. H1069–H1075, Jan. 2016.

[11] S. B. Zhou, J. X. Gao, P. Hu, Y. H. Cheng, and P. Wang, "Hot Corrosion Resistance of ZrB_2-based Ceramic Composites Against NaCl Molten Salt," *Mater. Res. Innov.*, vol. 19, no. sup1, pp. S1–347–S1–349, Apr. 2015.

[12] S. Jothi, S. Ravindran, L. Neelakantan, and R. Kumar, "Corrosion Behavior of Polymer-Derived SiHfCN(O) Ceramics in Salt and Acid Environments," *Ceram. Int.,* vol. 41, no. 9, Part A, pp. 10659–10669, Nov. 2015.

[13] L. Kaufman and E. V. Clougherty, "Investigation of Boride Compounds for Very High Temperature Applications, Part I," *Air Force Materials Laboratory*, RTD-TDR-63-4096, Part I, 1963.

[14] C. Oshima, E. Bannai, T. Tanaka, and S. Kawai, "Thermionic Work Function of LaB_6 Single Crystals and Their Surfaces," *J. Appl. Phys.,* vol. 48, no. 9, pp. 3925–3927, Sep. 1977.

[15] S. J. Sitler, I. Charit, and K. S. Raja, "Room Temperature Corrosion Behavior of ZrB_2-HfB_2 Solid Solutions in Acidic and Basic Aqueous Environments," *Electrochimica Acta,* vol. 246, pp. 173–189, Aug. 2017.

[16] B. Pieraggi and R. A. Rapp, "A Novel Explanation of the 'Reactive Element Effect' in Alloy Oxidation," *J. Phys. IV*, vol. 03, no. C9, pp. C9–275–C9–280, Dec. 1993.

[17] P. Vajeeston, P. Ravindran, C. Ravi, and R. Asokamani1, "Electronic Structure, Bonding, and Ground-State Properties of AlB_2-type Transition-Metal Diborides," *Phys. Rev. B*, vol. 63, no. 4, pp. 045115.1–045115.12, Jan. 2001.

[18] J. S. Knyrim and H. Huppertz, "High-pressure Synthesis, Crystal Structure, and Properties of the First Ternary Zirconium Borate β-ZrB2O5.," *Z Naturforsch*, vol. 63b, pp. 707–712, Jan. 2008.

[19] Y.-H. Seong, S. J. Lee, and D. K. Kim, "TEM Study of the High-Temperature Oxidation Behavior of Hot-Pressed ZrB_2–SiC Composites," *J. Am. Ceram. Soc.*, vol. 96, no. 5, pp. 1570–1576, May 2013.

[20] M. M. Opeka, I. G. Talmy, E. J. Wuchina, J. A. Zaykoski, and S. J. Causey, "Mechanical, Thermal, and Oxidation Properties of Refractory Hafnium and Zirconium Compounds," *J. Eur. Ceram. Soc.,* vol. 19, no. 13–14, pp. 2405–2414, Oct. 1999.

[21] C. C. Dollins and M. Jursich, "A Model for the Oxidation of Zirconium-Based Alloys," *J. Nucl. Mater.,* vol. 113, no. 1, pp. 19–24, Jan. 1983.

[22] H.-I. Yoo, B.-J. Koo, J.-O. Hong, I.-S. Hwang, and Y.-H. Jeong, "A Working Hypothesis on Oxidation Kinetics of Zircaloy," *J. Nucl. Mater.,* vol. 299, no. 3, pp. 235–241, Dec. 2001.

[23] B. E. Deal and A. S. Grove, "General Relationship for the Thermal Oxidation of Silicon," *J. Appl. Phys.*, vol. 36, no. 12, pp. 3770–3778, Dec. 1965.

[24] X. H. Wang and Y. C. Zhou, "High-Temperature Oxidation Behavior of Ti_2AlC in Air," *Oxid. Met.,* vol. 59, no. 3–4, pp. 303–320, Apr. 2003.

[25] K. Hauffe and P. Kofstad, "Über den Mechanismus der Oxydation von Cu_2O bei hohen Temperaturen," *Z. Für Elektrochem. Berichte Bunsenges. Für Phys. Chem*., vol. 59, no. 5, pp. 399–404, Jul. 1955.

[26] F. Monteverde and A. Bellosi, "Oxidation of ZrB_2-Based Ceramics in Dry Air," *J. Electrochem. Soc.,* vol. 150, no. 11, pp. B552–B559, Nov. 2003.

[27] R. Tu et al., "Oxidation Behavior of ZrB_2–SiC Composites at Low Pressures," *J. Am. Ceram. Soc.,* vol. 98, no. 1, pp. 214–222, Jan. 2015.

[28] Y.-H. Seong and D. K. Kim, "Oxidation Behavior of $ZrB_{2-x}SiC$ Composites at 1500 °C under Different Oxygen Partial Pressures," *Ceram. Int.,* vol. 40, no. 9, Part B, pp. 15303–15311, Nov. 2014.

[29] M. E. Orazem and B. Tribollet, Electrochemical Impedance Spectroscopy, 1st ed. Hoboken, N.J: *Wiley-Interscience*, 2008.

CHAPTER 5: ZrB_2-HfB_2 Solid Solutions as Electrode Materials for Hydrogen Reaction in Acidic and Basic Solutions[4]

5.1 Abstract

Spark plasma sintered transition metal diborides such as HfB_2, ZrB_2 and their solid solutions were investigated as electrode materials for electrochemical hydrogen evolutions reactions (HER) in 1 M H_2SO_4 and 1 M NaOH electrolytes. HfB_2 and ZrB_2 formed complete solid solutions when mixed in 1:1, 1:4, and 4:1 ratios and they were stable in both electrolytes. The HER kinetics of the diborides were slower in the basic solution than in the acidic solutions. The Tafel slopes in 1 M H_2SO_4 were in the range of 0.15–0.18 V/decade except for pure HfB_2 which showed a Tafel slope of 0.38 V/decade. In 1 M NaOH the Tafel slopes were in the range of 0.12–0.27 V/decade. The composition of $Hf_xZr_{1-x}B_2$ solid solutions with x=0.2–0.8, influenced the exchange current densities, overpotentials and Tafel slopes of the HER. The EIS data were fitted with a porous film equivalent circuit model in order to better understand the HER behavior. In addition, modeling calculations, using density functional theory approach, were carried out to estimate the density of states and band structure of the boride solid solutions.

5.2 Introduction

Earth abundant electrocatalysts for hydrogen evolutions reactions (HER) are being actively investigated as low cost alternatives for platinum group materials.[1] Transition metal based chalcogenides, carbides, nitrides, phosphides, and borides are the candidate materials for HER catalysts. Molybdenum boride (MoB) showed an overpotential of 220 mV in pH 14 and 210 mV in pH 0 solutions at current densities of 10 mA/cm^2 with Tafel slopes in the range of 55–59 mV/decade.[2] Amorphous cobalt boride in the form of Co-B[3] and Co_2B[4] was observed to be highly active for HER. Amorphous nickel boride was reported to be a stable HER catalyst in both acidic and alkaline electrolytes with high activity.[5.6] The high electrocatalytic activity of the amorphous transition metal borides (TMB_x, with x < 2) was attributed to their electronic structure that transferred electrons from

[4] This chapter has been published and is reproduced with permission from Elsevier as shown in Appendix A: Sitler, S. J., Raja, K. S., Charit, I. "ZrB_2-HfB_2 Solid Solutions as Electrode Materials for Hydrogen Reaction in Acidic and Basic Solutions" *Materials Letters*. 188, 239-243 (2016), DOI: 10.1016/j.matlet.2016.10.122.

boron to *d*-orbitals of the transition metals.[7] The electron rich *d*-orbitals of metal atoms are considered to be highly active for HER.

Recently, Lim et al.[8] investigated electrochemical behavior of layered TiB_2 modified by sodium naphthalenide and butylithium in order to exfoliate the TiB_2. The unmodified TiB_2 required an overpotential of 1.1 V for HER activity of -10 mA/cm^2 and the exfoliated TiB_2 required 1.0 V for -10 mA/cm^2. Transition metal diborides are considered for ultra-high temperature applications due to their high melting point and stability in extreme conditions. High electrical conductivity and enhanced chemical resistance render the diborides a great candidate material for HER electrocatalysts with enhanced stability in a wide pH range of electrolyte. The HER catalytic behavior of solid solutions of two transition metal diborides mixtures has not been reported to the best of the authors' knowledge. In this investigation, HfB_2 and ZrB_2 are investigated as individual borides as well as solid solutions of $Hf_xZr_{1-x}B_2$ with x varying between 0.2 and 0.8. Samples were prepared through high energy ball milling followed by spark plasma sintering.

5.3 Experimental

Commercially available HfB_2 and ZrB_2 powders (Alfa-Aesar, -325 mesh) were mixed at different ratios to achieve stoichiometries of $Hf_xZr_{1-x}B_2$ with x in the range of 0.2–0.8. The mixed powders were ball milled for 3 h in a zirconia vial with 6.5 mm diameter spherical zirconia grinding material using a powder-to-ball mass ratio of 1:10. The ball milled powder mixtures were sintered using a spark plasma sinter machine (Fuji electronics, Japan, model: Dr. Sinter SPS-515 S) using a 20.6 mm graphite die with 5 kN force at 1700 °C for 600 s under 10^{-3} Torr vacuum.

The ~4 mm thick sintered pellets were sectioned to yield small coupons of about 0.4 cm^2 exposed area. After attaching copper wires to the back side of the coupons using highly conductive silver epoxy, the coupons were masked using an acrylic mold exposing only the top surface. The exposed surface was metallographically polished to at least 1 µm surface finish. Table 5.1 shows the naming schemes used hereafter.

Table 5.1: Sample nomenclature and density data.

Identifier used	*Sample molar contents*	*Theoretical Density (g/cm²)*	*Relative Density (%)*	
A	(HfB_2)	9.594	91.4	Figures and Tables with an "S" in the numbering can be found in the Supporting information.
B	(ZrB_2)	5.308	87.2	
AB	($Hf_{0.5}Zr_{0.5}B_2$)	6.346	76.2	
4AB	($Hf_{0.8}Zr_{0.2}B_2$)	7.377	76.5	
A4B	($Hf_{0.2}Zr_{0.8}B_2$)	5.796	82.9	

Electrochemical experiments were carried out in 1 M H_2SO_4 and 1 M NaOH electrolytes. Initially, samples were activated by carrying out 10 cycles of cyclic voltammetry from open circuit potential to -1 V_{RHE} at a scan rate of 100 mV/s. A platinum flag (3.75 cm^2) was used as a counter electrode and Ag/AgCl immersed in saturated KCL was used as the reference electrode (199 mV vs. SHE), the potentials were converted to RHE scale using the relation $V_{RHE}=V_{Ag/AgCl}$ +0.199+(0.059 • pH).

After the initial activation, cathodic polarization to -1 V_{RHE} at a scan rate of 5 mV/s was initiated to record the *I-V* plot. Potentiostatic tests were carried out at two different potentials followed by electrochemical impedance spectroscopy (EIS) at two potentials; -0.2 and -0.5 V_{RHE} in pH 14 and -0.4 and -0.6 V_{RHE} in pH 0.

The samples were characterized using SEM and XRD. Density measurements were carried out on the sintered pellets using the Archimedes' principle following the ASTM standard B962-08. The details of the density functional calculations are given in the Supporting information.

5.4 Results and Discussion

Figure 5.1(a)–(e) shows the FESEM results of the spark plasma sintered samples. Theoretical density and relative density of the samples are given in Table 5.1. The relative densities of the samples varied from 76.1% to 91.4% of their respective theoretical densities. AB and 4AB showed higher porosity levels at about 24% more than other samples. The surface morphology as observed from the FESEM images was not the real representation of the porosity level due to grain pull-outs during polishing. The grain sizes were in the range of 1.5–3.0 µm. Figure 5.1(f) shows the XRD patterns of the samples. The XRD results indicated that a complete solid solution formed at different ratios of HfB_2 to ZrB_2, as the peaks of $Hf_xZr_{1-x}B_2$ samples were placed between the corresponding peaks of pure HfB_2 and ZrB_2. These results are similar to the conclusions drawn by Otani et al.,[9] who reported perfect and continuous solid solutionizing between HfB_2 and ZrB_2. The lattice parameters calculated from the XRD spectra are summarized in Table 5.S1.

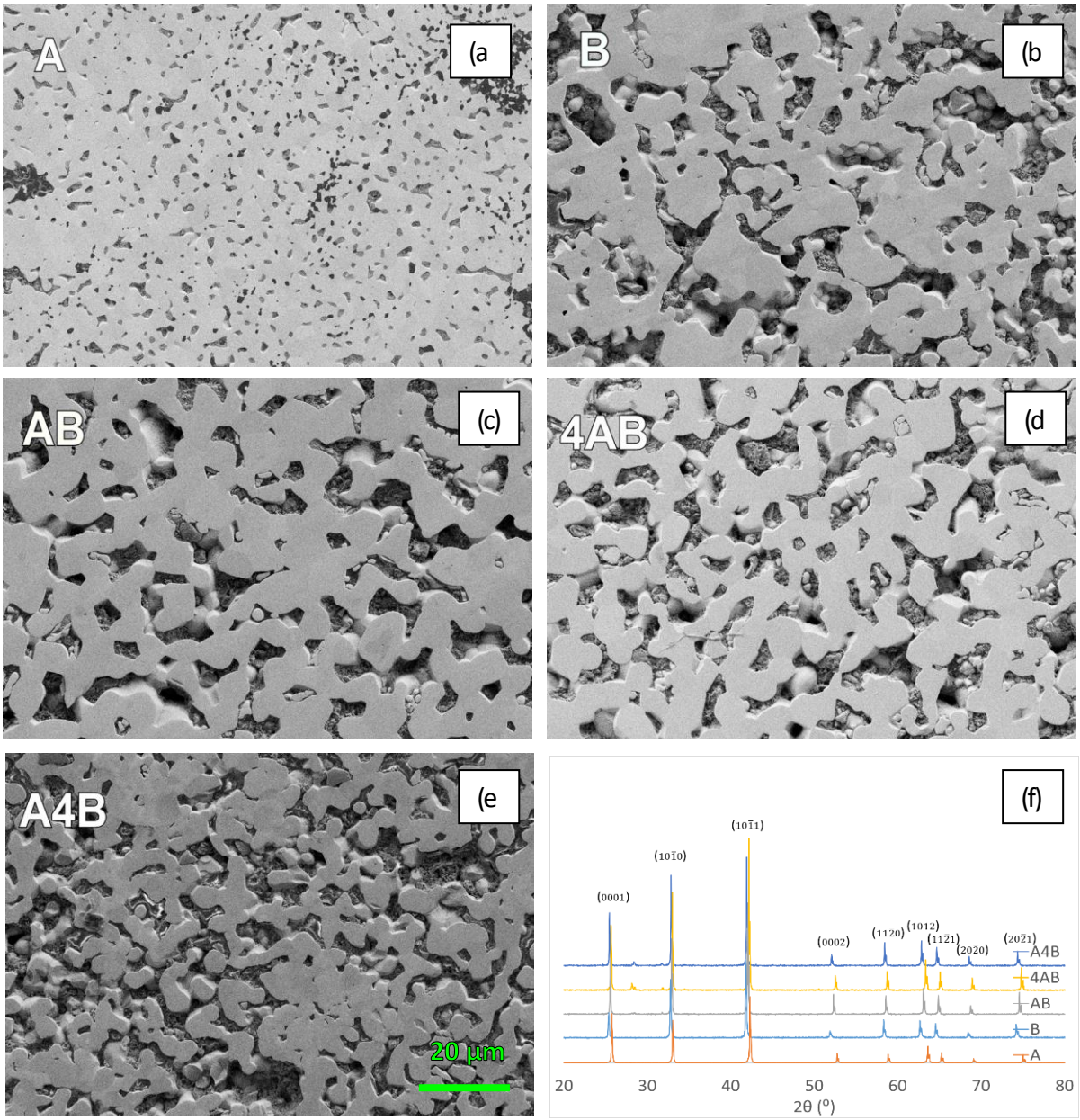

Figure 5.1: FESEM and XRD characterization of HfB_2-ZrB_2 samples. FESEM surface morphology at 1000X of the spark plasma sintered diboride samples (a) HfB_2, (b) ZrB_2, (c) $Hf_{0.5}Zr_{0.5}B_2$, (d) $Hf_{0.8}Zr_{0.2}B_2$, (e) $Hf_{0.2}Zr_{0.8}B_2$, and (f) XRD patterns of the $Hf_xZr_{1-x}B_2$ samples.

Figure 5.2(a)–(d) shows the electrochemical hydrogen evolution behavior of the HfB_2-ZrB_2 solid solutions in two different pH conditions. Figure 5.2(a) illustrates the *I-V* characteristics of the diborides in 1 M H_2SO_4. The Tafel slopes were in the range of 150–380 mV/decade illustrating a volcano type trend with the stoichiometry of the solid solutions as shown by Zeng and Li[1] in Figure 2 of their paper. Sample A exhibited the highest Tafel slope of 380 mV/decade and, 4AB and AB

showed the lowest Tafel slopes of about 150 mV/decade. The Tafel slopes, exchange current densities, and the overpotentials for 10 mA/cm^2 are listed in Table 5.S2.

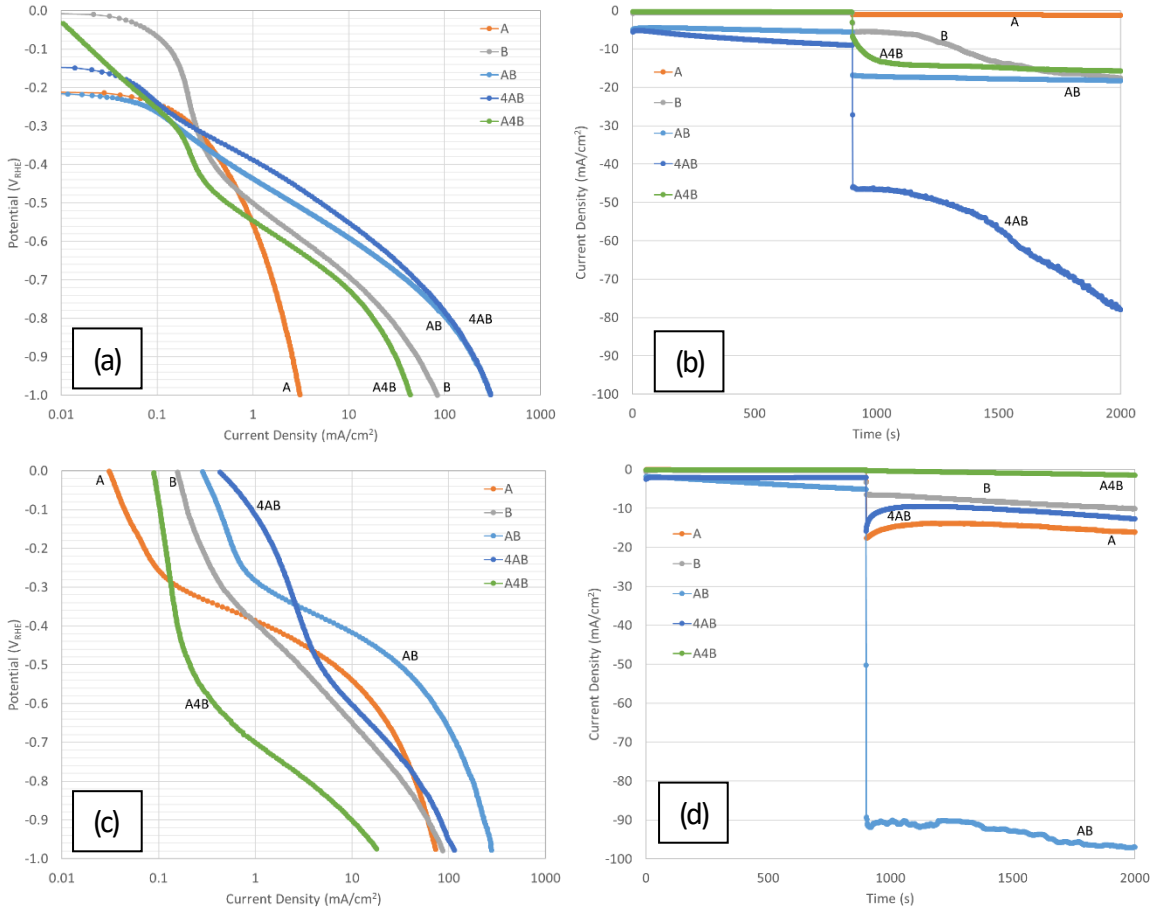

Figure 5.2: Electrochemical hydrogen evolution characteristics of HfB_2-$ZrfB_2$ solid solutions. (a) *I-V* plots in 1 M H_2SO_4, (b) *I-t* plots at -0.4 V_{RHE} and changing to -0.6 V_{RHE} at 900 seconds in 1 M H_2SO_4 (c) *I-V* plots in 1 M NaOH, and (d) *I-t* plots at -0.2 V_{RHE} and changing to -0.5 V_{RHE} at 900 seconds in 1 M NaOH.

It is noted that the Tafel slopes of the diborides are higher than the reported values for the mono-borides of nickel and cobalt.[3,4] However, Tafel slopes of 146–158 mV/decade were reported for TiB_2.[8] If the rate determining step of HER is a Volmer reaction ($H_3O^+ + e^- + M \rightarrow M\text{-}H + H_2O$), a Tafel slope of 120 mV/decade is usually observed.[10] The steeper Tafel slopes indicated the possibility of high coverage of adsorbed hydrogen atoms and the formation of a hydride layer on the surface as the open circuit potential shifted to more negative potentials. Similar observations were noted on amorphous nickel boride electrodes.[5]

Figure 5.2(b) illustrates the *I-t* plots of the diborides in the 1 M H_2SO_4 at -0.4 V_{RHE} and -0.6 V_{RHE}. At -0.4 V_{RHE}, the current densities were about 0.5 mA/cm^2 for A, B, and A4B. AB and 4AB showed current densities of 5.6 and 4 mV/cm^2 at -0.4 V_{RHE}. The current densities showed an increasing trend

with time. Switching to a higher potential of -0.6 V_{RHE} increased the current densities significantly as noted from both the *I-V* and *I-t* plots. B and AB showed similar current densities of around 18.5 mA/cm^2 at -0.6 V_{RHE} and A4B showed slightly lower current density of 15.5 mA/cm^2. The highest current density of 77.7 mA/cm^2 was observed with 4AB. It should be noted that both AB and 4AB had similar porosity levels. 4AB showed the shallowest Tafel slope and highest current density among all samples investigated in 1 M H_2SO_4.

Figure 5.2(c) shows the *I-V* plots in 1 M NaOH. Sample A showed the lowest Tafel slope of 100 mV/decade indicating that the Volmer step is the operating mechanism of HER in sample A. Other samples showed much higher Tafel slopes and relatively high exchange current densities. The higher exchange current densities of AB and 4AB could be attributed to their higher porosity levels. Figure 5.2(d) shows the *I-t* plots in 1 M NaOH at -0.2 V_{RHE} and -0.5 V_{RHE}. 4AB showed 2 and 12.8 mA/cm^2 at -0.2 and -0.5 V_{RHE} respectively. The current values increased initially with time under the potentiostatic condition and plateaued after about 1 h of polarization. No visible corrosion was noticed. Therefore, the observed high current densities were not attributed to the corrosion current. Crystalline boron is considered to be resistant to acid and concentrated alkaline solutions.[11] Since alkaline zirconates are not soluble and therefore form a protective film in alkaline solutions, preferential dissolutions of zirconium could be ruled out.[12] Similarly, hafnium is also stable in alkaline solutions. Interestingly, sample AB showed the highest current density of 97 mA/cm^2 at -0.5 V_{RHE}. Overall, the HER tests indicated the superiority of AB in both acidic and alkaline electrolytes.

In order to further understand the HER behavior, electrochemical impedance spectroscopy (EIS) and density functional theory (DFT) analyses were carried out. Figure 5.3(a) shows the bode plots of EIS in 1 M H_2SO_4 obtained at -0.6 V_{RHE}. Samples A and B showed no significant variation of the impedance at low frequencies and thus exhibited more of a resistor-like behavior which could be associated with low porosity levels in these samples. The solid solution samples showed a decrease in impedance at low frequencies. This implies a mass transfer controlled redox reaction because of the relatively higher porosity levels in these samples. The EIS data were fitted with an equivalent circuit as shown in Figure 5.S1 and the values of the electrical circuit components are summarized in Table 5.S3. The EIS data fit well with the porous film equivalent circuit model commonly reported by other investigators.[10,13] R_f is associated with the charge transfer resistance, R_p is attributed to the mass transfer resistance due to porosity and the adsorption intermediates. Y_f and Y_p are constant

phase elements due to distributed time constants because of surface roughness and associated with double layer capacitance and pseudo capacitance respectively.

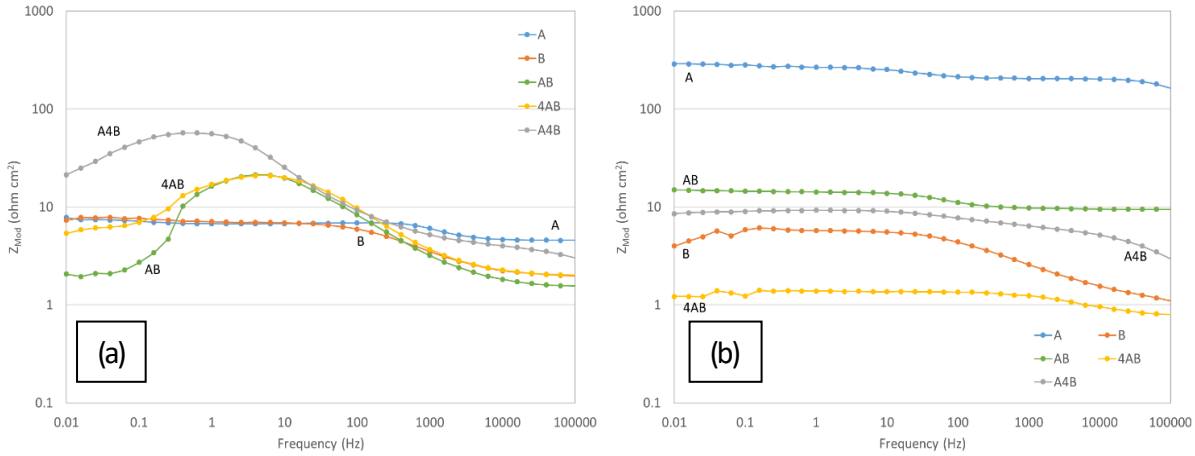

Figure 5.3: EIS bode plots of (a) 1 M H_2SO_4 at -0.6 V_{RHE} and (b) 1 M NaOH at -0.5 V_{RHE}.

Sample A showed the highest charge transfer and mass transfer resistance values, and samples AB, and 4AB showed the lowest values. The EIS behavior of the samples could be directly correlated to the HER performance. The values of the constant phase elements are given in the unit of admittance as $S \bullet s^n$. When n is unity, the behavior is purely capacitive, but when n is ½, it acts as a Warburg element. Because of high porosity levels, samples AB and 4AB exhibited pure capacitance behavior while others showed leaky capacitance.

Figure 5.3(b) shows the EIS results of the samples in 1 M NaOH at -0.5 V_{RHE}. Interestingly, the redox reaction was not significantly mass transfer controlled in the alkaline solution in contrast to that observed in acidic solution. Sample A showed the highest impedance spectrum while sample 4AB showed the lowest impedance spectrum. It is interesting to note that in spite of exhibiting higher impedance spectrum, sample AB possessed the best HER catalytic properties in 1 M NaOH. The EIS data were fitted into a porous film equivalent circuit model as described previously and the results are summarized in Table 5.S4 and 5.S5 for -0.2 V_{RHE} and -0.5 V_{RHE}, respectively.

Electron Density of States (DOS) calculations were carried out using DFT based on the CASTEP method using Materials Studio® software. The calculation details are given in Supporting information. Table 5.S6 and Figure 5.S2(a) and (b) show the band structure and DOS of a unit cell of HfB_2. The lines at 0 eV indicate the Fermi level of the material. The overlapping of the valance and conduction bands indicates metallic conductivity of HfB_2. Finite level DOS were observed at the Fermi

level. A valley region (a sharp drop in DOS near Fermi level) is observed in the DOS plot which is called a pseudogap.[14]

Ionic character and hybridization effects are attributed to pseudogaps. In hexagonal diborides, the pseudogap is due to TM-*d* and B-*2p* orbital hybridization and also the resonance of the *d*-orbital.[15] If the minimum of the pseudogap aligns with the Fermi level, then the stability of the compound is considered to be better in terms of melting point and chemical inertness. It should be noted that the pseudogap minimum of HfB_2 occurs at its Femi level, indicating a high melting point and high chemical inertness. On the other hand, the low DOS at the Fermi level could adversely affect the catalytic properties. Therefore, the limited HER electrocatalytic activity of HfB_2 could be associated with its electronic structure.

The band structure and DOS of ZrB_2 are illustrated in Figure 5.S3(a) and (b) respectively. The results are similar to HfB_2 and match values reported in literature.[16] However, no reports are available on the electronic structure of the solid solutions of HfB_2-ZrB_2. The density of states of AB, 4AB, and A4B are illustrated in Figure 5.S4(a)–(c).

The 1:1 HfB_2-ZrB_2 solid solution shifted the valley of the pseudogap to more negative energy levels. The DOS peak near -10 eV is attributed to the s-electrons of boron. The peak around -5 eV is associated with degenerate *d*-orbitals of Hf and Zr and the *2p*-orbitals of boron. The antibonding states at higher energy levels are attributed to the *d*-states of Hf and Zr.[16] Geometry optimization of the lattice of the HfB_2-ZrB_2 solid solutions indicated contraction of the cell volume for AB and A4B and very little expansion of 4AB as compared to B. The change in the cell volume modified the bond lengths of the TM-TM and TM-B bonds which altered the electronic structure. The electron density at the Fermi level of the solid solutions of HfB_2-ZrB_2 was higher than that of the unmixed borides. The extension of the DOS over the Fermi level suggests higher reactivity of the material.[17] The higher HER activity of the solid solution samples could be attributed to their anti-bonding electron structure and relatively higher electron density at the Fermi Level. HfB_2 showed high HER activity in alkaline solution, which could be attributed to the chemical stability under the alkaline experimental conditions. The modeling of DOS in A4B and AB samples showed higher electron densities at the Fermi level than the 4AB. The HER activity of A4B was lower than that of 4AB, which could be due to the relatively lower chemical stability of the Zr in both acidic and alkaline condition than that of Hf. It is believed that HfB_2 will be more stable than ZrB_2 because *5d*-orbitals of Hf are delocalized more than the *4d*-orbitals of Zr and undergo strong covalent bonding with boron.[18]

5.5 Conclusions

HfB_2 showed high electrocatalytic behavior in 1 M NaOH for hydrogen evolution reactions where the Tafel slope was 100 mV/decade and the overpotential 540 mV for HER at 10 mA/cm^2. In 1 M H_2SO_4, the performance of HfB_2 was poor.

ZrB_2 showed Tafel slopes of 270 mV/decade and 180 mV/decade in 1 M NaOH and 1 M H_2SO_4, respectively. The overpotentials were 650 and 690 mV at 10 mA/cm^2 in the electrolytes, respectively.

Among the HfB_2-ZrB_2 solid solutions samples, AB showed the best results. The Tafel slopes and overpotentials of AB at 10 mA/cm^2, were 120 and 150 mV/decade and 420 and 590 mV in 1 M NaOH and 1 M H_2SO_4 respectively. The HER catalytic activities can be directly related to the DOS at the Fermi level.

5.6 Acknowledgements

This work is supported by National Energy Technology Laboratory, US Department of Energy (Office of Fossil Energy) grant number: DEFE0022988. Dr. Jason Hissam is the program manager.

5.7 Supporting Information

Supporting information associated with this article can be found in the online version at doi:10.1016/j.matlet.2016.10.122 or in Appendix D.

5.8 Bibliography

[1] M. Zeng and Y. Li, “Recent Advances in Heterogeneous Electrocatalysts for the Hydrogen Evolution Reaction,” *J. Mater. Chem. A*, vol. 3, no. 29, pp. 14942–14962, Jul. 2015.

[2] H. Vrubel and X. Hu, “Molybdenum Boride and Carbide Catalyze Hydrogen Evolution in Both Acidic and Basic Solutions,” *Angew. Chem. Int. Ed.*, vol. 51, no. 51, pp. 12703–12706, Dec. 2012.

[3] S. Gupta, N. Patel, A. Miotello, and D. C. Kothari, “Cobalt-Boride: An Efficient and Robust Electrocatalyst for Hydrogen Evolution Reaction,” *J. Power Sources*, vol. 279, pp. 620–625, Apr. 2015.

[4] J. Masa *et al.*, “Amorphous Cobalt Boride (Co_2B) as a Highly Efficient Nonprecious Catalyst for Electrochemical Water Splitting: Oxygen and Hydrogen Evolution,” *Adv. Energy Mater.*, vol. 6, no. 6, pp. 1502313–1502323, Mar. 2016.

[5] P. Los and A. Lasia, “Electrocatalytic Properties of Amorphous Nickel Boride Electrodes for Hydrogen Evolution Reaction in Alkaline Solution,” *J. Electroanal. Chem.*, vol. 333, no. 1, pp. 115–125, Jul. 1992.

[6] M. Zeng *et al.*, “Nanostructured Amorphous Nickel Boride for High-Efficiency Electrocatalytic Hydrogen Evolution Over a Broad pH Range,” *ChemCatChem*, vol. 8, no. 4, pp. 708–712, Feb. 2016.

[7] S. Carenco, D. Portehault, C. Boissière, N. Mézailles, and C. Sanchez, “Nanoscaled Metal Borides and Phosphides: Recent Developments and Perspectives,” *Chem. Rev.*, vol. 113, no. 10, pp. 7981–8065, Oct. 2013.

[8] C. S. Lim, Z. Sofer, V. Mazánek, and M. Pumera, “Layered Titanium Diboride: Towards Exfoliation and Electrochemical Applications,” *Nanoscale*, vol. 7, no. 29, pp. 12527–12534, Jul. 2015.

[9] S. Otani, T. Aizawa, and N. Kieda, “Solid Solution Ranges of Zirconium Diboride with Other Refractory Diborides: HfB_2, TiB_2, TaB_2, NbB_2, VB_2 and CrB_2,” *J. Alloys Compd.*, vol. 475, no. 1–2, pp. 273–275, May 2009.

[10] N. Krstajić, M. Popović, B. Grgur, M. Vojnović, and D. Šepa, “On the Kinetics of the Hydrogen Evolution Reaction on Nickel in Alkaline Solution: Part I. The Mechanism,” *J. Electroanal. Chem.*, vol. 512, no. 1–2, pp. 16–26, Oct. 2001.

[11] M. Pourbaix, *Atlas of Electrochemical Equilibria in Aqueous Solutions*, 2nd edition. National Association of Corrosion, 1974, p. 165.

[12] M. Pourbaix, *Atlas of Electrochemical Equilibria in Aqueous Solutions*, 2nd edition. National Association of Corrosion, 1974, p. 228.

[13] R. D. Armstrong and M. Henderson, “Impedance Plane Display of a Reaction with an Adsorbed Intermediate,” *J. Electroanal. Chem. Interfacial Electrochem.*, vol. 39, no. 1, pp. 81–90, Sep. 1972.

[14] J.-H. Xu and A. J. Freeman, “Phase Stability and Electronic Structure of $ScAl_3$ and $ZrAl_3$ and of Sc-Stabilized Cubic $ZrAl_3$ Precipitates,” *Phys. Rev. B*, vol. 41, no. 18, pp. 12553–12561, Jun. 1990.

[15] D.-C. Tian and X.-B. Wang, “Electronic Structure and Equation of State of TiB_2,” *J. Phys. Condens. Matter*, vol. 4, no. 45, pp. 8765–8772, 1992.

[16] J. W. Lawson, C. W. Bauschlicher, M. S. Daw, and W.-Y. Ching, “Ab Initio Computations of Electronic, Mechanical, and Thermal Properties of ZrB_2 and HfB_2,” *J. Am. Ceram. Soc.*, vol. 94, no. 10, pp. 3494–3499, Oct. 2011.

[17] L. M. C. Pinto and G. Maia, “Selected Properties of Pt(111) Modified Surfaces: A DFT Study,” *Electrochem. Commun.*, vol. 60, pp. 135–138, Nov. 2015.

[18] P. Vajeeston, P. Ravindran, C. Ravi, and R. Asokamani1, “Electronic Structure, Bonding, and Ground-state Properties of AlB_2-Type Transition-metal Diborides,” *Phys. Rev. B*, vol. 63, no. 4, p. 045115.1-045115.12, Jan. 2001.

CHAPTER 6: Metal-rich Transition Metal Diborides as Electrocatalysts for Hydrogen Evolution Reactions in a Wide Range of pH[5]

6.1 Abstract

Solid solutions of HfB_2-ZrB_2 mixtures were prepared by high-energy ball milling of diboride and additive powders followed by spark plasma sintering (SPS). A mixture of stoichiometric 1:1 HfB_2-ZrB_2 borides was the base composition to which Hf, Zr, Ta, LaB_6 or Gd_2O_3 was added. Hf, Zr, and Ta were added in order to bring the boron-to-metal ratio down to 1.86, rendering the boride as MeB1.86. In the case of LaB_6 and Gd_2O_3, 1.8 mol% was added. Electroanalytical behavior of hydrogen evolution reactions was evaluated in 1 M H_2SO_4 and 1 M NaOH solutions. The LaB_6 additive material showed Tafel slopes of 125 and 90 mV/decade in acidic and alkaline solutions respectively. The Hf and Zr rich samples showed Tafel slopes of about 120 mV/decade in both electrolytes. The overpotentials of hydrogen evolution reactions (at 10 mA/cm^2) in the alkaline solution were about 100 mV lower than those in acidic solution. The metal-rich diborides and addition of LaB_6 showed better hydrogen evolution reaction (HER) activities than the base 1:1 HfB_2-ZrB_2 stoichiometric diboride solid solution. The higher activity of metal-rich borides could be attributed to the increased electron population at the *d*-orbitals of the metal shown by band structure modeling calculations using the Density Functional Theory (DFT) approach.

6.2 Introduction

The electrochemical hydrogen evolution reaction (HER) pathways on a metal surface are given by Volmer-Heyrovsky-Tafel mechanisms as follows:[1]

$$M + H_3O^+ + e^- \rightarrow MH + H_2O \qquad \text{Volmer} \qquad (1)$$

$$M + H_2O + e^- \rightarrow MH + OH^- \qquad \text{Volmer} \qquad (2)$$

[5] This chapter has been published and is used under creative commons license https://creativecommons.org/licenses/by-nc-nd/4.0/ : Sitler, S. J., Raja, K. S., Charit, I. "Metal Rich Transition Metal Diborides as Electrocatalysts for Hydrogen Evolution Reactions in a Wide Range of pH" *J. Electrochem. Soc.* **163**, H1069–H1075 (2016), DOI: 10.1149/2.0201613jes.

$MH + H_3O^+ + e^- \rightarrow M + H_2O + H_2$	Heyrovsky	(3)
$MH + H_2O + e^- \rightarrow M + OH^- + H_2$	Heyrovsky	(4)
$MH + MH \rightarrow 2\ M + H_2$	Tafel	(5)

The Volmer reactions are considered to be the discharge or adsorption reactions, Heyrovsky reactions are the charge or desorption reactions, and Tafel's is a recombination reaction with Tafel slopes of 118, 39, 29.5 mV/decade, respectively for the Volmer, Heyrovsky, and Tafel equations.[2] Since HER involves successive steps of adsorption and desorption of hydrogen atoms, the electrode material should have optimal binding energy for hydrogen for enhanced electrocatalysts. Platinum groups metals have the highest catalytic properties for HER. However, several earth abundant low-cost alternative materials for HER are being investigated.[3] Metal borides, such as MoB,[4,5] Co_2B,[6] CoB,[7] and NiB[8,9] are reported as potential electrocatalysts for HER.

The high catalytic activity of metal mono-borides is attributed to the electron transfer from boron to metal in the amorphous state that enriches the *d*-band electron density.[7] The stability of the monoborides is attributed to the ability of boron to prevent the metal from oxidizing by donating electrons to stabilize the valance state and reductively remove surface oxides.[4,9] Furthermore, the lattice strains involved in the process of boron incorporation in the metal lattice is believed to lower the energy barrier for catalytic reactions.[6]

Only limited investigations have been reported on metal diborides as electrocatalysts for HER. Layered titanium diborides with and without exfoliation were investigated[10] and a significantly high overpotential of >1 V_{RHE} was reported for a HER current density of -10 mA/cm^2. Lavrenko et al.[11] investigated HER activity of ZrB_2 in 1 M H_2SO_4 and reported that it was lower than that of other borides such as NbB_2 and TaB_2. Other layered inorganic materials such as $Ca_3Co_4O_9$ have been reported to show a Tafel slope of 87 mV/decade for HER.[12]

Metal-rich borides are reported to have a much higher resistance to oxidation at high temperatures than that of their stoichiometric counterparts.[13] Therefore, in this investigation, metal-rich solid solutions of HfB_2-ZrB_2 with the addition of Hf, Zr, Ta, LaB_6 or Gd_2O_3 were investigated as hydrogen evolution catalysts.

6.3 Experimental

Commercial HfB_2 and ZrB_2 powders (15 µm, 99.5% purity) were mixed in a 1:1 molar ratio. This solid solution was the base composition to which Hf (-325 mesh, 99.6% purity), Zr (-325 mesh, 98.8%), or Ta (-325 mesh, 99.9%) pure metals were added to bring the molar ratio of boron-to-metal down to 1.86 ($MeB_{1.86}$). Additionally, two more samples were created by mixing 1.8 mol% of LaB_6 (-325 mesh, and 99.5% purity) or Gd_2O_3 (20–40 nm, 99.99% purity) to the base HfB_2-ZrB_2 solid solution. All the raw materials were procured from Alfa Aesar. The pure metal additions were carried out inside a dry glove box filled with ultra-high purity (UHP) argon (M. Braun Inert Gas-Systeme GmbH).

The mixed powders were ball milled for 3 hours in a zirconia vial with 6.5 mm diameter spherical yttria-stabilized zirconia grinding material (Inframat Advanced Materials LLC, Manchester, CT) using a powder-to-ball mass ratio of 1:10. The ball milled powder mixtures were sintered using a spark plasma sinter machine (Fuji electronics, Japan, model: Dr. Sinter SPS-515 S) with a 20.6 mm Isocarb-85 graphite die at 5 kN applied force at 1700 °C for 600 seconds under 10^{-3} Torr vacuum.[14]

The sintered pellets were partitioned into small coupons of about 0.4 cm^2 exposed area. Copper wires were attached to the back sides of the coupons using a highly conductive silver epoxy, the coupons were then embedded in acrylic molds exposing only the top surface. The exposed surface was metallographically polished to at least 1 µm surface finish. Table 6.1 shows the sample identifiers used hereafter. The samples were characterized using FESEM and XRD. Additionally, density was measured for each of the sintered pellets with the Archimedes' principle using the ASTM standard B962-08.

Samples were electrochemically tested in both acidic and basic solutions (1 M H_2SO_4 and 1 M NaOH). The samples were activated prior to this study by carrying out 20 cycles of cyclic voltammetry from open circuit potential to -1 V_{RHE} at a scan rate of 100 mV/s. A platinum counter electrode (3.75 cm^2) was used along with an Ag/AgCl immersed in saturated KCL reference electrode (199 mV vs. SHE). The potentials were converted to the RHE scale using the relation $V_{RHE} = V_{Ag/AgCl} + 0.199 + (0.059 \bullet pH)$.

Cathodic polarization to -1 V_{RHE} at a scan rate of 5 mV/s was then carried out in order to record the *I-V* plot. Potentiostatic tests were carried out at two different potentials followed by electrochemical impedance spectroscopy (EIS) at these two potentials; -0.2 and -0.5 V_{RHE} in pH 14 and -0.4 and -0.6 V_{RHE} in pH 0.

The Density Functional Theory (DFT) calculations of HfB_2-ZrB_2 solid solutions with additives were performed under the framework of DFT as implemented in the CASTEP module of Materials Studio™ software package. Initially, the geometry of the unit cell was optimized using Generalized Gradient Approximation (GGA) using a Perdew-Burke-Ernzerhof (PBE) functional.[15] The wave functions are expanded in a plane-wave basis set with an energy cutoff of 420 eV. The *k*-points in the Brillouin Zone (BZ) of the primitive unit cell were sampled on a 12 × 12 × 12 mesh. The geometry was optimized for the convergence tolerance of energy = 0.5×10^{-6} eV/atom, Eigen energy convergence tolerance: 0.125×10^{-6} eV, Gaussian smearing scheme with a smearing width of 0.1 eV, and Fermi energy convergence tolerance of 0.125×10^{-7} eV. Electron–ion interactions were described by the norm-conserving pseudopotentials. 2 × 2 × 2 super cells were considered when introducing boron vacancies by deleting boron atoms.

6.4 Results and Discussion

6.4.1 Material Characterization

Figure 6.1(a)–(f) shows the FESEM microstructures of the samples after metallographically polishing to ~1 µm surface finish without any etching. The base composition of $Hf_{0.5}Zr_{0.5}B_2$ showed higher porosity than other samples. The density of the samples was measured using Archimedes' principle and the values are given in terms of % fraction of theoretical density. The Hf-rich sample (ABH) and the sample with LaB_6 addition showed relatively high densities. The grain size of all the samples was in the range of 0.5–7 µm. Samples enriched with Hf or Ta showed finer grain size in the range of 0.5–1.1 µm. ABL had larger grains between 2–7 µm, while the other samples showed grain sizes in the intermediate range of 1–4 µm. The high sintered density could be related to the finer grain size of the samples except in the case of ABL.

Figure 6.2 shows the XRD patterns of the samples. Both the HfB_2 and ZrB_2 have hexagonal crystal structure with very similar lattice parameters. Therefore, these borides, when mixed, formed a continues solid solution with the lattice parameters lying between the lattice parameters of the unmixed HfB_2 and ZrB_2. Metal-rich borides were found to be single phase structures based on the XRD results. Only peaks corresponding to hexagonal structure of AB type were observed for all samples except for ABG which contained the addition of Gd_2O_3. Since Gd_2O_3 has a cubic structure, no solid solution was formed and additional peaks associated with Gd_2O_3 were observed. It was observed that the addition of 1.8 mol% of LaB_6 formed a complete solid solution with HfB_2-ZrB_2. Since no additional peaks corresponding to LaB_6 were noticed in the XRD patterns.

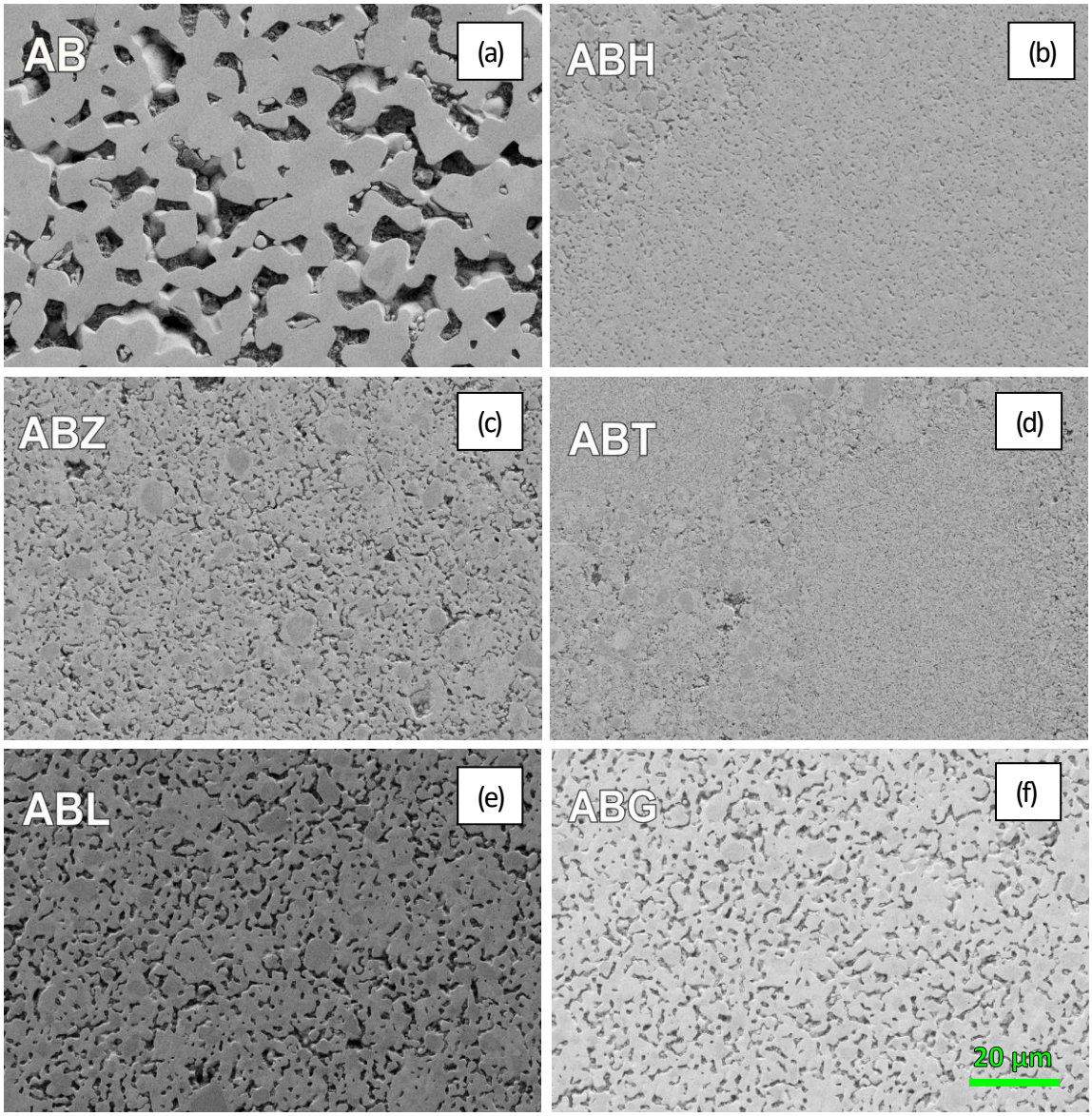

Figure 6.1: FESEM micrographs of HfB_2-ZrB_2 samples. FESEM surface morphology at 1000 X of the spark plasma sintered diboride samples (a) $Hf_{0.5}Zr_{0.5}B_2$, (b) $Hf_{0.5}Zr_{0.5}B_2$ + Hf, (c)$Hf_{0.5}Zr_{0.5}B_2$ + Zr, (d) $Hf_{0.5}Zr_{0.5}B_2$ + Ta, (e) $Hf_{0.5}Zr_{0.5}B_2$ + LaB_6, and (f) $Hf_{0.5}Zr_{0.5}B_2$ + Gd_2O_3.

The lattice parameters of the samples are summarized in Table 6.1. It can be seen that addition of Hf, Zr, and Ta shrunk the lattice parameters and unit cell volume as compared to those of AB. The metal-rich borides can be considered, hypothetically, to have born vacancies given by the formula AB_{2-x}, where x is the fraction of vacancy, in this case x = 0.14. The presence of boron vacancies could alter the electron configurations in the nearest neighbors and therefore may alter the Metal-Boron (M-B) and Boron-Boron (B-B) bond lengths. If some of the metals' atoms are occupying the boron vacancy anti-sites, the Metal-Metal (M-M) bond length could also be modified.[16] These

changes in bond lengths manifest into a reduction of the lattice parameters and possibly into modifications to the electron band structures and density of states.

Table 6.1: Sample identifiers used throughout manuscript and physical properties data.

Sample	*Label*	*Relative Density (% of theoretical density)*	*Lattice Parameters*		*Volume of unit cell (nm^3)*
			a (nm)	*c (nm)*	
$Hf_{0.5}Zr_{0.5}B_2$	AB	76.2	0.314642	0.348757	0.02990
$Hf_{0.5}Zr_{0.5}B_2$ + Hf (B/Me =1.86)	ABH	96.2	0.314505	0.348643	0.02987
$Hf_{0.5}Zr_{0.5}B_2$ + Zr (B/Me =1.86)	ABZ	94.8	0.314497	0.348437	0.02985
$Hf_{0.5}Zr_{0.5}B_2$ + Ta (B/Me =1.86)	ABT	94.6	0.313599	0.346095	0.02948
$Hf_{0.5}Zr_{0.5}B_2$ + 1.8 mol% LaB_6	ABL	97.2	0.314645	0.348767	0.02990
$Hf_{0.5}Zr_{0.5}B_2$ + 1.8 mol% Gd_2O_3	ABG	89.5	0.314435	0.348180	0.02981

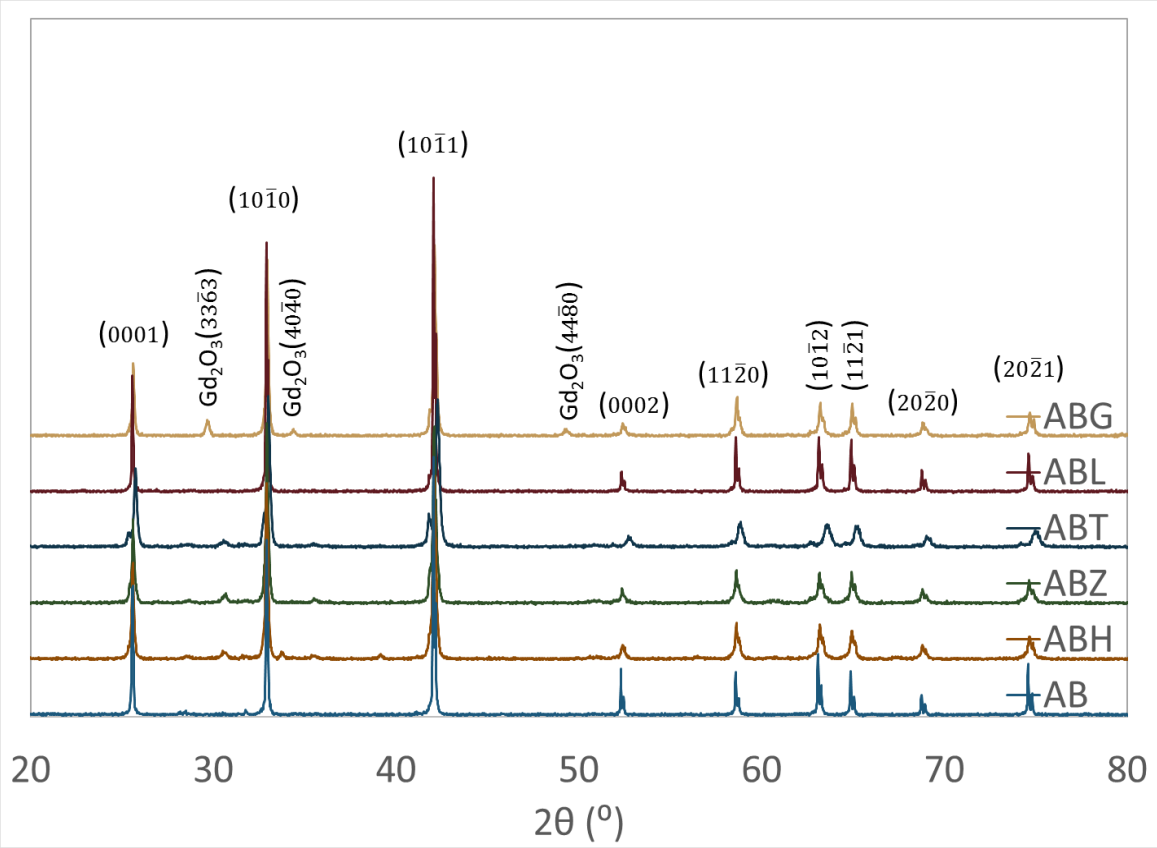

Figure 6.2: XRD patterns of the AB and AB with additives samples with indexed peaks. Except for ABG, all other additives were in the solid solution.

Table 6.2: Theoretically calculated lattice parameters using Density Functional Theory.

Sample	*Calculated 'a' (nm)*	*Calculated 'c' (nm)*	*Calculated volume (nm^3)*
AB	0.29869	0.33648	0.025997
ABH	0.30850	0.31743	0.026163
ABZ	0.29174	0.33890	0.024980
ABT	0.30523	0.31724	0.025596
ABL	0.29845	0.33696	0.025993

6.4.2 Estimation of Density of States

In order to understand the electronic behavior, Density Functional Theory modeling was carried out using the CASTEP module in Materials Studio software package. In order to simulate the metal rich boride composition, boron vacancies of 6.25% and 12.5% were investigated in the calculations.

Table 6.2 summarizes the calculated lattice parameters of the samples based on the DFT model. Compared to the lattice parameters derived from the XRD data, these values were 12.4–16% smaller. An overall decreasing trend of the lattice parameters of the metal enriched borides with B/Me ratio = 1.86, was observed in the modeling results, except in the case of ABH.

Recently, Dahlqvist et al.[16] calculated variations in the lattice parameters of ZrB_2 and HfB_2 with the introduction of boron vacancies and observed that the unit cell volume does not change significantly for up to 50% boron vacancies, even though the lattice parameters "a" increased and "c" decreased with an increase in the boron vacancy. In this investigation, solid solution of $Hf_{0.5}Zr_{0.5}B_2$, $Hf_{0.6}Zr_{0.4}B_2$, $Hf_{0.4}Zr_{0.6}B_2$, $Hf_{0.45}Zr_{0.45}Ta_{0.1}B_2$, and $Zr_{0.49}Hf_{0.49}La_{0.02}B_2$ were considered in the calculations. In the solid solutions, the introduction of boron vacancies also generally increased the '*a*' values and decreased the '*c*' values (these results are included in Table 6.3) when compared to the lattice parameters of their respective stoichiometric composition. However, there are some exceptions, especially with Zr and Ta-enriched compositions. It should be noted that increases in the '*a*' values in the hexagonal diborides will result in increases in the in-plane M-M bond length and possible increases in the B-B bond length. The decrease in the '*c*' parameter will lead to out-of-plane MM bond length decrease as well as a decrease in the M-B bond length. Hexagonal diborides are layered structures having six coordinated metal planes and three coordinated boron planes. The electrons in the metal planes are not localized and results in metallic bonding, while the bonding between boron atoms is considered to be covalent.[17] Since boron is electron deficient, a finite charge transfer from

metal to boron is considered to occur that results in a substantial ionic contribution to the M-B bonding.[18]

Table 6.3: Lattice parameters of select solid solution samples with and without boron vacancies.

Composition	*Boron vacancy (%)*	*a (nm)*	*c (nm)*
$Hf_{0.5}Zr_{0.5}B_2$	0	0.29870	0.33648
	6.25	0.30484	0.31575
	12.5	0.30360	0.31002
$Hf_{0.6}Zr_{0.4}B_2$	0	0.30823	0.32348
	6.25	0.30850	0.31743
$Hf_{0.4}Zr_{06}B_2$	0	0.28839	0.35530
	6.25	0.29175	0.33890
$Hf_{0.45}Zr_{0.45}Ta_{0.1}B_2$	0	0.30507	0.32355
	6.25	0.30523	0.31725

Therefore, M-B bonding has a strong ionic character and a weak covalent character. This charge transfer from metal to boron is considered to be a function of boron concentrations that affects the electrocatalytic properties. As mentioned in the introduction, metal-rich borides are expected to have a much higher resistance to oxidation at high temperatures.[13] This is due to the electron transfer from boron to metal in the metal-rich borides (MB_x, $x < 2$).[19] In this condition, the *d*-electrons in the metal are oppositely polarized and thus have increased concentrations in the *d*-orbitals.[19] This will be reflected in the density of states where higher electron populations will be observed at the Fermi level (i.e. (number of states at the Fermi level ($N(E_F)$) will be higher).

Figures 6.S1(a)–(c) shows the calculated electron density of states for the $Hf_{0.5}Zr_{0.5}B_2$ 1× 1× 1 unit formula cell with no boron vacancies and the 2 × 2 × 2 super cell with 6.25% and 12.5% boron vacancies, respectively. The peak observed at -40 eV is associated with the core electrons of the metals which is not the focus of this investigation. The peak at -10 eV is attributed to the localized '*s*' electrons of boron.[17] The TM-*d* and B-*p* degenerate states could be observed from the peak at ∼-5 eV. Such degenerate states may not result in hybridization because of the spatial separation between transition metal (TM) and boron (B) and therefore a charge transfer effect could be considered.[18] A sharp valley observed near the Fermi level (at 0 eV) is considered, what is called, a pseudogap. If the minimum of the valley aligns with the Fermi level, then the material is considered to be very stable and to have a high melting point.[20] However, since the electron density of the Fermi level is low at this condition, the catalytic activity of the material will also be low.

Pinto and Maia[21] pointed out that the extension of TM-*d* band further from the Fermi level improved the catalytic behavior of Mo/Pt structure. Typically, higher $N(E_F)$ enhances the catalytic activity. Following this pattern, it was observed that the density of states at the Fermi level increased for the $Hf_{0.5}Zr_{0.5}B_2$ system with an increase in the boron vacancies and a decrease in the antibonding states as observed from Figure 6.S1(b) and (c).

Figure 6.S2(a) and (b) show the calculated DOS of $Hf_{0.6}Zr_{0.4}B_2$ with and without boron vacancies. These calculations, especially Figure 6.S2(b), simulate the ABH sample condition. It can be seen that there is a local maximum in the DOS at the Fermi level, possibly indicating high catalytic activity. At the same time, it should be noted that with the high $N(E_F)$, lower chemical stability of the material is expected. Figure 6.S3(a) and (b) shows the DOS of $Hf_{0.4}Zr_{0.6}B_2$ with and without boron vacancies. The E_F was aligned with a local minimum of the DOS, as in case of the stoichiometric composition. Whereas, an introduction of 6.25% boron vacancy, that simulates the ABZ condition, showed E_F aligning with a DOS peak. It was observed that the introduction of the boron vacancies marginally increased the $N(E_F)$. Similar observations were reported for unmixed ZrB_2 and HfB_2 with boron vacancies by Dahlqvist et al.[16] Figure 6.S4(a) and (b) show the calculated DOS plots for ABT with and without boron vacancies. It was observed that the introduction of boron vacancies decreased the electron states at the Fermi level compared to the DOS of the stoichiometric composition (AB). Therefore, Ta-enriched compositions may not yield favorable electrocatalytic properties. On the other hand, the addition of 1.8 mol% of La ($Hf_{0.49}Zr_{0.49}La_{0.02}B_2$) was observed to result in a high $N(E_F)$ which may give favorable electrocatalytic properties.

In summary, the DFT based calculations indicated that the introduction of boron vacancies to the solid solutions of transition metal diborides increased the lattice parameter '*a*' and decreased the lattice parameter '*c*' and showed changes in the DOS and $N(E_F)$. The electron density at the Fermi level increased in general with the introduction of boron vacancies, possibly indicating high catalytic activity. However, the chemical stability is considered to be adversely affected. The addition of Ta was found to be not favorable, while the addition of lanthanum showed some promise. In the following sections, the theoretical predictions will be compared with the experimental results.

6.4.3 Hydrogen Evolution Reaction Results

Figure 6.3(a)–(d) shows the results of hydrogen evolution reaction behavior of the samples. Figure 6.3(a) shows the *I-V* characteristics in 1 M H_2SO_4 under cathodic polarization. The results are summarized in Table 6.4. Sample AB showed a Tafel slope of 160 mV/decade and all of the other

samples showed slopes of ~125 mV/decade except for ABT which showed a Tafel slop of 400 mV/decade. Except for AB and ABT, the values were lower than the value reported for TiB_2[10] (146–158 mV/decade). The higher Tafel slopes observed in AB and especially ABT could be attributed to an effect of high porosity, specifically, the possibility of having unreduced oxide in the subsurface pores of the porosity. The exchange current density for the HER was in the range of 1.2×10^{-4}–1.2×10^{-3} mA/cm^2, except for ABT which had an exchange current density of 5.5×10^{-2} mA/cm^2. These values are more or less on the same order of magnitude as the exchange current densities reported for the monoborides which were in the range of 1–2 µA/cm^2.[22]

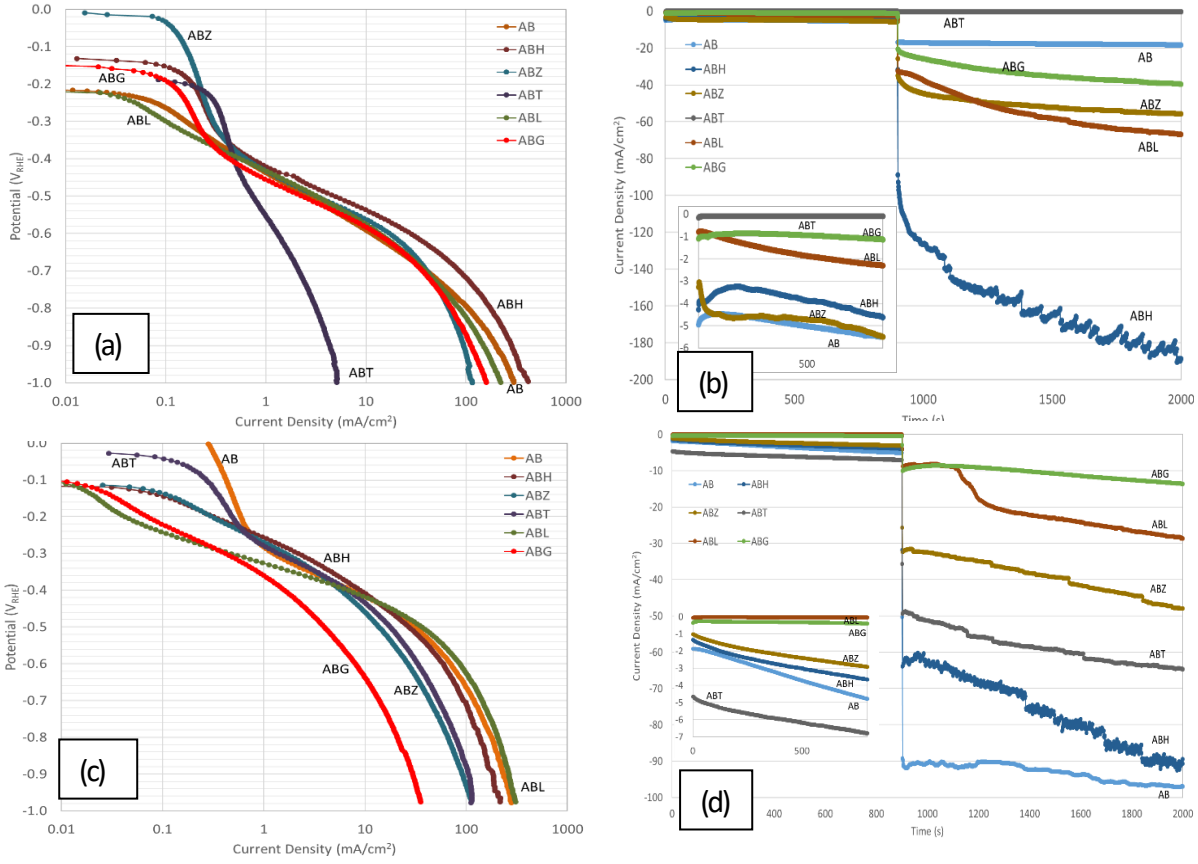

Figure 6.3: Electrochemical hydrogen evolution characteristics of HfB_2-$ZrfB_2$ solid solutions with additives, identifiers are shown in Table 6.1. (a) *I-V* plots in 1 M H_2SO_4, (b) *I-t* plots in 1 M H_2SO_4 at -0.4 and -0.6 V_{RHE} (c) *I-V* plots in 1 M NaOH, and (d) *I-t* plots in 1 M NaOH at -0.2 and -0.5 V_{RHE}.

Table 6.4: Summary of HER behavior of the HfB_2-ZrB_2 solid solutions in both 1 M H_2SO_4 and 1 M NaOH.

	1 M H_2SO_4				
Sample	Tafel slope, b (mV/dec)	Overpotential, η at 10 mA/cm^2 (V_{RHE})	Exchange current density, I_o	Quasi-steady state current density, I at -0.4 V_{RHE} (mA/cm^2)	Quasi-steady state current density, I at -0.6 V_{RHE}
AB	160	0.53	1.2 x 10^{-3}	-5.57	-18.5
ABG	125	0.58	1.2 x 10^{-4}	-1.16	-42.6
ABH	120	0.54	2.5 x 10^{-4}	-4.76	-199
ABL	125	0.56	2.5 x 10^{-4}	-2.36	-70.0
ABT	400	>1.0	5.5 x 10^{-2}	-0.09	-0.30
ABZ	125	0.56	5.0 x 10^{-4}	-5.68	-57.9
	1 M NaOH				
Sample	Tafel slope, b (mV/dec)	Overpotential, η at 10 mA/cm^2 (V_{RHE})	Exchange current density, I_o	Quasi-steady state current density, I at -0.2 V_{RHE} (mA/cm^2)	Quasi-steady state current density, I at -0.5 V_{RHE}
AB	115	0.42	2.5 x 10^{-3}	-0.331	-97.0
ABG	120	0.64	1.0 x 10^{-3}	-0.426	-13.6
ABH	115	0.41	5.0 x 10^{-3}	-3.860	-92.4
ABL	90	0.42	1.0 x 10^{-4}	-0.045	-28.5
ABT	125	0.44	6.0 x 10^{-3}	-7.020	-64.8
ABZ	130	0.46	7.1 x 10^{-3}	-3.082	-48.1

Overpotentials are considered to be an important criterion for comparing different electrocatalysts. The overpotentials of the samples for 10 mA/cm^2 current density were in the range of 0.53–0.58 V_{RHE} with the exception of ABT which showed an overpotential of greater than 1.0 V_{RHE}. There was no particular trend observed from the materials chemistry point of view of the *I-V* characteristics of the samples. However, Figure 6.3(b) illustrates the *I-t* characteristics of the samples at two different potentiostatic conditions that showed the effects of materials chemistry. At the low overpotential of -0.4 V_{RHE}, AB, ABH, and ABZ showed current densities of about 5 mA/cm^2, while ABT showed very low current density. At the high overpotential of -0.6 V_{RHE}, the highest current density of 199 mA/cm^2 was observed in ABH. The next highest current density was 70 mA/cm^2 which was observed in ABL. ABZ, ABG, and AB showed 58, 42.6 and 18.5 mA/cm^2 at -0.6 V_{RHE}. All the samples showed increasing HER activity with time, and as polarization continued, the current densities

reached a quasi-steady state condition after about an hour. It should be noted that modeling calculations showed higher electron density at the Fermi levels for the simulated ABL, ABZ, and ABH conditions than that of AB. The experimentally recorded higher HER current density of the metal-rich borides could be correlated to the higher DOS than that of stoichiometric diboride solid solution sample, AB.

Figure 6.3(c) shows the *I-V* plots in 1 M NaOH. ABZ showed the highest Tafel slope of 130 mV/decade, although this was very similar to all of the other slopes ranging from 115–125 mV/decade, except for ABL which had the lowest Tafel slope of 90 mV/decade. The exchange current densities were an order of magnitude higher in the alkaline solutions than in the acid solution. ABL showed the lowest exchange current density of 1.0×10^{-4} mA/cm^2 even though the Tafel slope was favorable. The overpotentials for 10 mA/cm^2 were in the range of 0.41–0.46 V_{RHE} for the metal-rich boride samples, ABH, ABZ, ABT as well as samples ABL and AB. ABG, however, showed a much higher overpotential of 0.64 V_{RHE} for 10 mA/cm^2.

Figure 6.3(d) shows the *I-t* plots in 1 M NaOH at -0.2 V_{RHE}. ABT, ABH, and ABZ showed current densities of about 7, 4, and 3 mA/cm^2 at -0.2 V_{RHE}, respectively. Other samples showed less than 1 mA/cm^2 at the lower overpotential. Increasing the overpotential to -0.5 V_{RHE} increased the HER current density significantly. The current density observed in ABH was 92.4 mA/cm^2. ABT, ABZ, ABL and ABG yielded current densities of about 65, 48, 28.5, and 13.6 mA/cm^2 at -0.5 V_{RHE}, respectively. AB showed the highest cathodic current density of 97 mA/cm^2. In the alkaline solution, the HER current density increased (in the negative direction) with time and leveled off after about an hour of polarization. No corrosion attack on the surface of the samples was noted and the electrolyte remained colorless after the electrochemical tests. Therefore, the recorded current is attributed only to the hydrogen reduction reactions.

6.4.4 Electrochemical Impedance Spectroscopy Results

Figure 6.4(a) shows the Bode plots of the samples in 1 M H_2SO_4 at -0.6 $V_{RHE.}$ It should be noted that the EIS measurements were carried out under quasi-steady state conditions, and therefore the results were used for comparison between different samples tested under identical conditions. The Hf-enriched sample showed the lowest impedance modulus values at all frequencies and the system behaved more like a resistor. The sample with Ta addition showed the highest impedance modulus at frequencies below 1 KHz. AB showed higher impedance values than ABG, ABH, ABZ, and ABL. The EIS data were fitted with an equivalent circuit as shown in Figure 6.S6 and the circuit parameters are

summarized in Table 6.S1 for samples in 1 M H_2SO_4 at -0.6 V_{RHE}. The R_s in the electrical circuit pertains to the solution resistance, R_f is associated with charge transfer resistance for the reduction reaction, and Y_f corresponds to the capacitance associated with the electrode/electrolyte interface. The R_p and Y_p components are associated with the porous nature of the electrode and mass transfer controlled reactions. Similar models have been used by other researchers.[23,24]

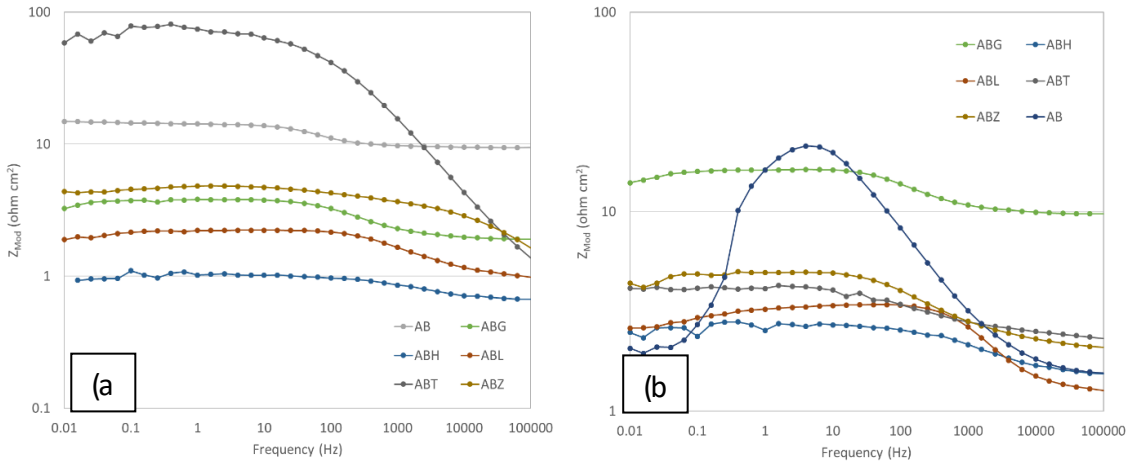

Figure 6.4: EIS bode plots of (a) 1 M H_2SO_4 at -0.6 V_{RHE} and (b) 1 M NaOH at -0.5 V_{RHE}.

As seen from Table 6.S1, ABT showed the highest charge transfer resistance, which is associated with the lowest HER performance observed in 1 M H_2SO_4. The capacitance values are given as admittance values for leaky capacitors or constant phase elements. ABH, which performed well as a HER catalyst based on the *I-V* and *I-t* plots, showed very low resistance to charge and mass transfer. The Y_f of ABH behaved like an ideal capacitor. Overall, the higher HER activity in 1 M H_2SO_4 could be correlated to the low resistance values for charge transfer and mass transfer.

Figure 6.4(b) shows the Bode plots in 1 M NaOH at -0.5 V_{RHE}. All samples showed similar impedance spectrums, except for the sample AB. The decrease in the impedance at low frequencies could be related to the mass transfer controlled redox reaction occurring on the surface of sample AB. It should be noted that this sample had the lowest apparent density and therefore high porosity level. The highest impedance values were also recorded for AB. At low frequencies the impedance values followed the order AB > ABG > ABT > ABZ > ABL > ABH. Overall, ABH showed the lowest impedance values at all frequencies. Except for ABL, all samples showed phase angles between 0° and -13°, exhibiting predominantly resistor-like behavior in the HER conditions tested.

The Bode plots of the EIS data at -0.2 V_{RHE} (not shown here) indicated that the ABL sample showed the highest impedance modulus values and had a capacitor controlled rate determining

reaction step at frequencies in between 10–100 Hz. The phase angle at these frequencies was about -64°. ABH, ABL, and ABT behaved more like resistors as the phase angles varied from 0° to -17°. The phase angle of ABG was in the range of 0° to -23.4°.

Table 6.S2 summarizes the values of model parameters fitted with the porous film equivalent circuit. The applied potential, -0.2 V_{RHE}, corresponds to the start of a linear region of the *I-V* plot in semi-log. At this potential, only partial coverage of hydrogen atoms is expected. Therefore, the high resistance values of R_p and R_f of the ABG and ABZ samples could be attributed to partially oxidized species, such as $HZrO^{3-}$ and $Gd(OH)_3$, possibly existing on the samples' surface. The 'true' capacitance (*C*) values of the constant phase element Y_f or Y_p can be estimated using a simplified relation:

$$C = \frac{(Y_f \times R_f)^{1/m}}{R_f} \quad (6)$$

Based on the arguments that the constant phase element represents a distributed time constants and that it can be represented as:[25]

$$R_f \times Y_f = \tau^m \quad (7)$$

And the time constant (τ) of real capacitance can be given as:

$$R_f \times C = \tau \quad (8)$$

Where τ = time constant and m = a parameter representing distributed time constant for surface reactions of surface heterogeneity. The averaged 'true' capacitance value can, in turn, be related to the density of states (DOS) of the material using another relation:[26]

$$C = q^2 \times DOS \quad (9)$$

Where q = elementary charge in coulombs and DOS = density of states in $cm^{-2} \bullet eV^{-1}$. From Table 6.S2, it can be seen that ABT showed the highest current density at -0.2 V_{RHE} and also showed the lowest value of $R_p + R_f$. The Y_f value of 1.3×10^{-3} $S \bullet s^{0.551}$ could be converted to the capacitance of 10.4 µF at the interface. ABZ showed an interfacial capacitance of 447 µF and ABH was estimated at 133 µF. These capacitance values can be correlated to the DOS of the samples and their high exchange current densities.

Table 6.S3 summarizes the model parameters of the porous film equivalent circuit used for fitting the EIS data in 1 M NaOH at -0.5 V_{RHE}. The lowest value of $R_p + R_f$ was observed for ABH which showed a high current density of -92.4 mA/cm^2 at -0.5 V_{RHE}. The estimated 'true' capacitance of the interface was 22 µF. The 'true' interfacial capacitance values of the samples based on Y_f, varied from 15 µF to 51 µF, corresponding to ABL and ABG respectively. The estimated 'true' capacitance based on the Y_p values was at least an order of magnitude higher for all samples. This capacitance is associated with the faradaic reactions and considered to be a pseudo-capacitance. However, the pseudo-capacitance values were not directly proportional to the HER kinetics. For examples, the pseudo-capacitance of ABH was estimated as 155 µF, which was the lowest among the measured values, but showed the highest HER current density at -0.5 V_{RHE}. On the other hand, sample AB showed the highest estimated pseudo-capacitance (39 mF) but the lowest current density. Therefore, the Y_p values were inversely proportional to the HER kinetics.

6.5 Conclusions

Electrochemical hydrogen evolution reaction kinetics of solid solutions of HfB_2-ZrB_2 with additions of Hf, Zr, Ta, LaB_6, and Gd_2O_3 were investigated in 1 M H_2SO_4 and 1 M NaOH electrolytes at room temperature. The electronic structures of the diboride mixtures were calculated using the Density Functional Theory approach. Based on the theoretical calculations, microstructural characterizations, and electrochemical characterizations, the following conclusions can be drawn:

- XRD results showed formation of complete solid solutions when additional Hf, Zr, and Ta metal were added to the 1:1 mixture of HfB_2-ZrB_2 rendering the final product as $MeB_{1.86}$.
- Introduction of boron vacancies to the solid solutions of transition metal diborides (to simulate the $MeB_{1.86}$ condition) increased the hexagonal lattice parameter '*a*' and decreased the lattice parameter '*c*' according to the modeling calculations. The experimental XRD data supported the trend observed in the theoretical estimation.
- The electron density at the Fermi level increased in general with the introduction of boron vacancies, or metal-rich conditions, possibly indicating high catalytic activity.
- The Hf-enriched boride sample (ABH) showed better performance in 1 M H_2SO_4 with a Tafel slope of 120 mV/decade, exchange current density of 0.25 µA/cm^2, and ~0.2 A/cm^2 HER current density at an overpotential of 0.6 V_{RHE}.

- Addition of 1.8 mol% LaB_6 to the 1:1 HfB_2-ZrB_2 solid solution exhibited better performance in 1 M NaOH with a Tafel slope of 90 mV/decade, exchange current density of 0.1 μA/cm^2, and an overpotential of 0.42 V_{RHE} for a HER current density of 10 mA/cm^2.
- The metal-rich diboride solid solutions showed better HER catalytic activities than that of stoichiometric diborides, which could be due to the high electron densities available at their Fermi level.

6.6 Acknowledgments

This work is supported by National Energy Technology Laboratory, US Department of Energy (Office of Fossil Energy) grant number: DE-FE0022988. Dr. Jason Hissam is the program manager

6.7 Supporting Information

Supporting information associated with this article can be found in the online version at DOI:10.1149/2.0201613jes or in Appendix E.

6.8 Bibliography

[1] L. Chen and A. Lasia, "Study of the Kinetics of Hydrogen Evolution Reaction on Nickel-Zinc Alloy Electrodes," *J. Electrochem. Soc.*, vol. 138, no. 11, pp. 3321–3328, 1991.

[2] E. Gileadi, *Physical Electrochemistry*, 1st ed. Weinheim: Wiley-VCH, 2011.

[3] J. K. Nørskov *et al.*, "Trends in the Exchange Current for Hydrogen Evolution," *J. Electrochem. Soc.*, vol. 152, no. 3, pp. J23–J26, Mar. 2005.

[4] H. Vrubel and X. Hu, "Molybdenum Boride and Carbide Catalyze Hydrogen Evolution in Both Acidic and Basic Solutions," *Angew. Chem. Int. Ed.*, vol. 51, no. 51, pp. 12703–12706, Dec. 2012.

[5] M. D. Scanlon *et al.*, "Low-cost Industrially Available Molybdenum Boride and Carbide as 'Platinum-Like' Catalysts for the Hydrogen Evolution Reaction in Biphasic Liquid Systems," *Phys. Chem. Chem. Phys.*, vol. 15, no. 8, pp. 2847–2857, Jan. 2013.

[6] J. Masa *et al.*, "Amorphous Cobalt Boride (Co_2B) as a Highly Efficient Nonprecious Catalyst for Electrochemical Water Splitting: Oxygen and Hydrogen Evolution," *Adv. Energy Mater.*, vol. 6, no. 6, pp. 1502313–1502323, Mar. 2016.

[7] S. Gupta, N. Patel, A. Miotello, and D. C. Kothari, "Cobalt-boride: An Efficient and Robust Electrocatalyst for Hydrogen Evolution Reaction," *J. Power Sources*, vol. 279, pp. 620–625, Apr. 2015.

[8] P. Los and A. Lasia, “Electrocatalytic Properties of Amorphous Nickel Boride Electrodes for Hydrogen Evolution Reaction in Alkaline Solution,” *J. Electroanal. Chem.*, vol. 333, no. 1, pp. 115–125, Jul. 1992.

[9] M. Zeng *et al.*, “Nanostructured Amorphous Nickel Boride for High-Efficiency Electrocatalytic Hydrogen Evolution Over a Broad pH Range,” *ChemCatChem*, vol. 8, no. 4, pp. 708–712, Feb. 2016.

[10] C. S. Lim, Z. Sofer, V. Mazánek, and M. Pumera, “Layered Titanium Diboride: Towards Exfoliation and Electrochemical Applications,” *Nanoscale*, vol. 7, no. 29, pp. 12527–12534, Jul. 2015.

[11] V. A. Lavrenko, L. N. Yagupolskaya, L. I. Kuznetsova, L. K. Doroshenko, and E. S. Lugovskaya, “The Oxidation of ZrB_2, TaB_2, NbB_2, and W_2B_5 in Atomic Oxygen and by Anodic Polarization,” *Oxid. Met.*, vol. 8, no. 3, pp. 131–137, Jun. 1974.

[12] C. S. Lim, C. K. Chua, Z. Sofer, O. Jankovský, and M. Pumera, “Alternating Misfit Layered Transition/Alkaline Earth Metal Chalcogenide $Ca_3Co_4O_9$ as a New Class of Chalcogenide Materials for Hydrogen Evolution,” *Chem. Mater.*, vol. 26, no. 14, pp. 4130–4136, Jul. 2014.

[13] L. Kaufman and E. V. Clougherty, “Investigation of Boride Compounds for Very High Temperature Applications, Part I,” Air Force Materials Laboratory, RTD-TDR-63-4096, Part I, 1963.

[14] S. Sitler, C. Hill, K. S. Raja, and I. Charit, “Transition Metal Diborides as Electrode Material for MHD Direct Power Extraction: High-temperature Oxidation of ZrB_2-HfB_2 Solid Solution with LaB_6 Addition,” *Metall. Mater. Trans. E*, vol. 3, no. 2, pp. 90–99, Jun. 2016.

[15] J. P. Perdew, K. Burke, and M. Ernzerhof, “Generalized Gradient Approximation Made Simple,” *Phys. Rev. Lett.*, vol. 77, no. 18, pp. 3865–3868, Oct. 1996.

[16] M. Dahlqvist, U. Jansson, and J. Rosen, “Influence of Boron Vacancies on Phase Stability, Bonding and Structure of MB_2 (M = Ti, Zr, Hf, V, Nb, Ta, Cr, Mo, W) with AlB_2-type Structure,” *J. Phys. Condens. Matter*, vol. 27, no. 43, p. 435702, 2015.

[17] J. W. Lawson, C. W. Bauschlicher, M. S. Daw, and W.-Y. Ching, “Ab Initio Computations of Electronic, Mechanical, and Thermal Properties of ZrB_2 and HfB_2,” *J. Am. Ceram. Soc.*, vol. 94, no. 10, pp. 3494–3499, Oct. 2011.

[18] P. Vajeeston, P. Ravindran, C. Ravi, and R. Asokamani1, “Electronic Structure, Bonding, and Ground-State Properties of AlB_2-type Transition-metal Diborides,” *Phys. Rev. B*, vol. 63, no. 4, p. 045115.1-045115.12, Jan. 2001.

[19] S. Carenco, D. Portehault, C. Boissière, N. Mézailles, and C. Sanchez, “Nanoscaled Metal Borides and Phosphides: Recent Developments and Perspectives,” *Chem. Rev.*, vol. 113, no. 10, pp. 7981–8065, Oct. 2013.

[20] D.-C. Tian and X.-B. Wang, “Electronic Structure and Equation of State of TiB_2,” *J. Phys. Condens. Matter*, vol. 4, no. 45, pp. 8765–8772, 1992.

[21] L. M. C. Pinto and G. Maia, “Selected Properties of Pt(111) Modified Surfaces: A DFT Study,” *Electrochem. Commun.*, vol. 60, pp. 135–138, Nov. 2015.

[22] M. Zeng and Y. Li, “Recent Advances in Heterogeneous Electrocatalysts for the Hydrogen Evolution Reaction,” *J. Mater. Chem. A*, vol. 3, no. 29, pp. 14942–14962, Jul. 2015.

[23] N. Krstajić, M. Popović, B. Grgur, M. Vojnović, and D. Šepa, “On the Kinetics of the Hydrogen Evolution Reaction on Nickel in Alkaline Solution: Part I. The Mechanism,” *J. Electroanal. Chem.*, vol. 512, no. 1–2, pp. 16–26, Oct. 2001.

[24] R. D. Armstrong and M. Henderson, “Impedance Plane Display of a Reaction with an Adsorbed Intermediate,” *J. Electroanal. Chem. Interfacial Electrochem.*, vol. 39, no. 1, pp. 81–90, Sep. 1972.

[25] M. E. Orazem and B. Tribollet, *Electrochemical Impedance Spectroscopy*, 1st edition. Hoboken, N.J: Wiley-Interscience, 2008.

[26] B. Klahr, S. Gimenez, F. Fabregat-Santiago, T. Hamann, and J. Bisquert, “Water Oxidation at Hematite Photoelectrodes: The Role of Surface States,” *J. Am. Chem. Soc.*, vol. 134, no. 9, pp. 4294–4302, Mar. 2012.

CHAPTER 7: Conclusions and Future Work

7.1 Conclusions

Chapter 2 showed that the pre-anodization process, even in the unoptimized form, enhanced the oxidation resistance by 2.5 times compared to the un-anodized sample at 1500 °C after an injection of oxygen with a p_{O2} = 0.3 x 10^5 Pa. This chapter also showed how the addition of 1.8 mol% LaB_6 as a chemical dopant enhanced the oxidation resistance by 30% when compared to the un-anodized AB sample. These two conclusions led to the decision that both of these methods of oxidation mitigation were worth pursuing more in-depth.

One of the motives behind the work in Chapter 3 was to draw a comparison between aqueous corrosion resistance and high-temperature corrosion resistance. The conclusions drawn in Chapter 3 showed that at room temperature in basic solutions, sample AB surprisingly outperformed all the additive samples and most of the other samples except for pure HfB_2 and that was only minimally better. Another conclusion that was drawn was the consistency of sample ABL, although it did not always perform the best, it was consistently in the top ranking few samples. No other sample performed better with regards to corrosion resistance across all pH solutions tested. It was from these conclusions that samples AB and ABL were chosen for further testing in Chapter 4.

The work in Chapters 5 and 6 was also done to aid in the selection process for the samples which would be further tested in Chapter 4. Hafnium diboride performed well with regards to the hydrogen evolution reaction in basic solution, in acidic solution however it did quite poorly. Sample AB barely underperformed sample A in the basic solution but also did very well in the acidic solution. It was also for this reason that Sample AB was chosen for further testing in Chapter 4. After comparing the DFT calculations and the experimental data it was found that a direct correlation could be made between the HER catalytic activity and the DOS at the Fermi level. Boron vacancy modeling also showed that an increase in boron vacancies caused an increase in the DOS at the Fermi level which directly correlates to HER catalytic activity. It was for this reason along with the performance of sample ABH in the acidic solution that it was chosen for further testing in Chapter 4. Sample ABL also performed well in the basic solution and this was another reason that it was chosen for further testing in Chapter 4.

Several important conclusions were drawn from the data in Chapter 4. With regards to the electrical resistivity of three diboride samples tested, ABL, unexpectedly, performed the worst, even worse than an anodized AB sample. The newly optimized pre-anodization process also gave some unexpected results. It performed as expected to improve oxidation resistance for sample AB, but when coupled with the addition of LaB_6, it did not improve the oxidation resistance. When anodized AB and anodized ABL samples were tested in a corrosive environment, they actually performed worse than samples with no pre-anodization. In the presence of oxygen and a corrosive environment, the ABL sample without pre-anodization performed the best. The diboride coating materials showed some promise for being able to withstand the extreme environments of a plasma direct-power extraction chamber and would be good candidates for study in realistic prototype applications.

7.2 Future Work

7.2.1 Dopants

There are two main areas that would be very interesting to see researched. They correspond to the two main methods of oxidation mitigation studied in this dissertation. The first area would be to perform a much more comprehensive study on the oxidation resistance of the ZrB_2:HfB_2 mixture with varying amounts of LaB_6 and/or Gd_2O_3. Gd_2O_3 did not give high enough corrosion resistance data from Chapter 3 to merit additional testing in Chapter 4. The high-temperature oxidation and corrosion resistance study may give an alternative conclusion. It would be important to continue the research into both LaB_6 and Gd_2O_3 as dopants with higher percentages as this may reveal even better oxidation resistance performance than found in Chapter 4.

7.2.2 Anodization

The second area that would be very interesting to see researched would be to adhere a solid transition metal layer on the samples through an electron beam physical vapor deposition (EBPVD) process. There would be many barriers to this concept, but if successful, this procedure would allow a subsequent anodization on that pure metal surface which may alleviate the concerns with the volatilization of B_2O_3 leaving behind a porous, non-protective oxide layer. Another option to research would be the use a zirconium or hafnium oxide target as opposed to a pure metal target to deposit a thin film of metal oxide onto the samples, which may accomplish the same thing as anodization of the pure metal layer.

APPENDIX A: Copyright Licenses

SPRINGER LICENSE

TERMS AND CONDITIONS

Apr 25, 2017

This Agreement between Steven Sitler ("You") and Springer ("Springer") consists of your license details and the terms and conditions provided by Springer and Copyright Clearance Center.

License Number 4095990336456

License date Apr 25, 2017

Licensed Content Publisher Springer

Licensed Content Publication Metallurgical and Materials Transactions E

Licensed Content Title	Transition Metal Diborides as Electrode Material for MHD Direct Power Extraction: High-temperature Oxidation of ZrB_2-HfB_2 Solid Solution with LaB_6 Addition
Licensed Content Author	Steven Sitler
Licensed Content Date	Jan 1, 2016
Licensed Content Volume	3
Licensed Content Issue	2
Type of Use	Thesis/Dissertation
Portion	Full text
Number of copies	1
Author of this Springer article	Yes and you are a contributor of the new work

Order reference number

Title of your thesis /dissertation Electrochemical and High Temperature Characterizations of Hafnium and Zirconium Diboride Solid Solutions with Different Additives

Expected completion date May 2017

Estimated size(pages) 150

Requestor Location Steven Sitler
875 Perimeter Dr.
MS 3024
MOSCOW, ID 83844
United States
Attn: Steven Sitler

Billing Type Invoice

Billing Address Steven Sitler
875 Perimeter Dr.
MS 3024
MOSCOW, ID 83844
United States
Attn: Steven Sitler

Total 0.00 USD

Terms and Conditions

Introduction

The publisher for this copyrighted material is Springer. By clicking "accept" in connection with completing this licensing transaction, you agree that the following terms and conditions apply to this transaction (along with the Billing and Payment terms and conditions established by Copyright Clearance Center, Inc. ("CCC"), at the time that you opened your Rightslink account and that are available at any time at http://myaccount.copyright.com).

Limited License

With reference to your request to reuse material on which Springer controls the copyright, permission is granted for the use indicated in your enquiry under the following conditions:

- Licenses are for one-time use only with a maximum distribution equal to the number stated in your request.

- Springer material represents original material which does not carry references to other sources. If the material in question appears with a credit to another source, this permission is not valid and authorization has to be obtained from the original copyright holder.

- This permission

• is non-exclusive

• is only valid if no personal rights, trademarks, or competitive products are infringed.

• explicitly excludes the right for derivatives.

- Springer does not supply original artwork or content.

- According to the format which you have selected, the following conditions apply accordingly:

• **Print and Electronic:** This License include use in electronic form provided it is password protected, on intranet, or CD-Rom/DVD or E-book/E-journal. It may not be republished in electronic open

access.

• **Print:** This License excludes use in electronic form.

• **Electronic:** This License only pertains to use in electronic form provided it is password protected, on intranet, or CD-Rom/DVD or E-book/E-journal. It may not be republished in electronic open access.

For any electronic use not mentioned, please contact Springer at permissions.springer@spiglobal.com.

- Although Springer controls the copyright to the material and is entitled to negotiate on rights, this license is only valid subject to courtesy information to the author (address is given in the article/chapter).

- If you are an STM Signatory or your work will be published by an STM Signatory and you are requesting to reuse figures/tables/illustrations or single text extracts, permission is granted according to STM Permissions Guidelines: http://www.stm-assoc.org/permissionsguidelines/ For any electronic use not mentioned in the Guidelines, please contact Springer at permissions.springer@spi-global.com. If you request to reuse more content than stipulated in the STM Permissions Guidelines, you will be charged a permission fee for the excess content. Permission is valid upon payment of the fee as indicated in the licensing process. If permission is granted free of charge on this occasion, that does not prejudice any rights we might have to charge for reproduction of our copyrighted material in the future.

-If your request is for reuse in a Thesis, permission is granted free of charge under the following conditions:

This license is valid for one-time use only for the purpose of defending your thesis and with a maximum of 100 extra copies in paper. If the thesis is going to be published, permission needs to be reobtained.

- includes use in an electronic form, provided it is an author-created version of the thesis on his/her own website and his/her university's repository, including UMI (according to the definition on the Sherpa website: http://www.sherpa.ac.uk/romeo/);

- is subject to courtesy information to the co-author or corresponding author.

Geographic Rights: Scope

Licenses may be exercised anywhere in the world.

Indemnity

You hereby indemnify and agree to hold harmless Springer and CCC, and their respective officers, directors, employees and agents, from and against any and all claims arising out of your use of the licensed material other than as specifically authorized pursuant to this license.

No Transfer of License

This license is personal to you and may not be sublicensed, assigned, or transferred by you without Springer's written permission.

No Amendment Except in Writing

This license may not be amended except in a writing signed by both parties (or, in the case of Springer, by CCC on Springer's behalf).

Objection to Contrary Terms

Springer hereby objects to any terms contained in any purchase order, acknowledgment, check endorsement or other writing prepared by you, which terms are inconsistent with these terms and conditions or CCC's Billing and Payment terms and conditions. These terms and conditions, together with CCC's Billing and Payment terms and conditions (which are incorporated herein), comprise the entire agreement between you and Springer (and CCC) concerning this licensing transaction. In the event of any conflict between your obligations established by these terms and conditions and those established by CCC's Billing and Payment terms and conditions, these terms and conditions shall control.

Jurisdiction

All disputes that may arise in connection with this present License, or the breach thereof, shall be settled exclusively by arbitration, to be held in the Federal Republic of Germany, in accordance with German law.

Other conditions:

V 12AUG2015

Questions? customercare@copyright.com or +1-855-239-3415 (toll free in the US) or +1-978-646-2777.

ELSEVIER LICENSE

TERMS AND CONDITIONS

Apr 25, 2017

This Agreement between Steven Sitler ("You") and Elsevier ("Elsevier") consists of your license details and the terms and conditions provided by Elsevier and Copyright Clearance Center.

License Number 4095951087845

License date Apr 25, 2017

Licensed Content Publisher Elsevier

Licensed Content Publication Materials Letters

Licensed Content Title	ZrB_2-HfB_2 solid solutions as electrode materials for hydrogen reaction in acidic and basic solutions
Licensed Content Author	Steven J. Sitler, Krishnan S. Raja, Indrajit Charit
Licensed Content Date	1 February 2017
Licensed Content Volume	188
Licensed Content Issue	n/a
Licensed Content Pages	5
Start Page	239
End Page	243
Type of Use	reuse in a thesis/dissertation
Portion	full article
Format	both print and electronic

Are you the author of this Elsevier article? Yes

Will you be translating? No

Order reference number

Title of your thesis/dissertation Electrochemical and High Temperature Characterizations of Hafnium and Zirconium Diboride Solid Solutions with Different Additives

Expected completion date May 2017

Estimated size (number of pages) 150

Elsevier VAT number GB 494 6272 12

Requestor Location Steven Sitler
875 Perimeter Dr.
MS 3024

MOSCOW, ID 83844
United States
Attn: Steven Sitler

Publisher Tax ID 98-0397604

Total 0.00 USD

Terms and Conditions

INTRODUCTION

1. The publisher for this copyrighted material is Elsevier. By clicking "accept" in connection with completing this licensing transaction, you agree that the following terms and conditions apply to this transaction (along with the Billing and Payment terms and conditions established by Copyright Clearance Center, Inc. ("CCC"), at the time that you opened your Rightslink account and that are available at any time at http://myaccount.copyright.com).

GENERAL TERMS

2. Elsevier hereby grants you permission to reproduce the aforementioned material subject to the terms and conditions indicated.

3. Acknowledgement: If any part of the material to be used (for example, figures) has appeared in our publication with credit or acknowledgement to another source, permission must also be sought from that source. If such permission is not obtained then that material may not be included in your publication/copies. Suitable acknowledgement to the source must be made, either as a footnote or in a reference list at the end of your publication, as follows:

"Reprinted from Publication title, Vol /edition number, Author(s), Title of article / title of chapter, Pages No., Copyright (Year), with permission from Elsevier [OR APPLICABLE SOCIETY COPYRIGHT OWNER]." Also Lancet special credit - "Reprinted from The Lancet, Vol. number, Author(s), Title of article, Pages No., Copyright (Year), with permission from Elsevier."

4. Reproduction of this material is confined to the purpose and/or media for which permission is hereby given.

5. Altering/Modifying Material: Not Permitted. However figures and illustrations may be altered/adapted minimally to serve your work. Any other abbreviations, additions, deletions and/or any other alterations shall be made only with prior written authorization of Elsevier Ltd. (Please

contact Elsevier at permissions@elsevier.com). No modifications can be made to any Lancet figures/tables and they must be reproduced in full.

6. If the permission fee for the requested use of our material is waived in this instance, please be advised that your future requests for Elsevier materials may attract a fee.

7. Reservation of Rights: Publisher reserves all rights not specifically granted in the combination of (i) the license details provided by you and accepted in the course of this licensing transaction, (ii) these terms and conditions and (iii) CCC's Billing and Payment terms and conditions.

8. License Contingent Upon Payment: While you may exercise the rights licensed immediately upon issuance of the license at the end of the licensing process for the transaction, provided that you have disclosed complete and accurate details of your proposed use, no license is finally effective unless and until full payment is received from you (either by publisher or by CCC) as provided in CCC's Billing and Payment terms and conditions. If full payment is not received on a timely basis, then any license preliminarily granted shall be deemed automatically revoked and shall be void as if never granted. Further, in the event that you breach any of these terms and conditions or any of CCC's Billing and Payment terms and conditions, the license is automatically revoked and shall be void as if never granted. Use of materials as described in a revoked license, as well as any use of the materials beyond the scope of an unrevoked license, may constitute copyright infringement and publisher reserves the right to take any and all action to protect its copyright in the materials.

9. Warranties: Publisher makes no representations or warranties with respect to the licensed material.

10. Indemnity: You hereby indemnify and agree to hold harmless publisher and CCC, and their respective officers, directors, employees and agents, from and against any and all claims arising out of your use of the licensed material other than as specifically authorized pursuant to this license.

11. No Transfer of License: This license is personal to you and may not be sublicensed, assigned, or transferred by you to any other person without publisher's written permission.

12. No Amendment Except in Writing: This license may not be amended except in a writing signed by both parties (or, in the case of publisher, by CCC on publisher's behalf).

13. Objection to Contrary Terms: Publisher hereby objects to any terms contained in any purchase order, acknowledgment, check endorsement or other writing prepared by you, which terms are inconsistent with these terms and conditions or CCC's Billing and Payment terms and conditions. These terms and conditions, together with CCC's Billing and Payment terms and conditions (which

are incorporated herein), comprise the entire agreement between you and publisher (and CCC) concerning this licensing transaction. In the event of any conflict between your obligations established by these terms and conditions and those established by CCC's Billing and Payment terms and conditions, these terms and conditions shall control.

14. Revocation: Elsevier or Copyright Clearance Center may deny the permissions described in this License at their sole discretion, for any reason or no reason, with a full refund payable to you. Notice of such denial will be made using the contact information provided by you. Failure to receive such notice will not alter or invalidate the denial. In no event will Elsevier or Copyright Clearance Center be responsible or liable for any costs, expenses or damage incurred by you as a result of a denial of your permission request, other than a refund of the amount(s) paid by you to Elsevier and/or Copyright Clearance Center for denied permissions.

LIMITED LICENSE

The following terms and conditions apply only to specific license types:

15. **Translation:** This permission is granted for non-exclusive world **English** rights only unless your license was granted for translation rights. If you licensed translation rights you may only translate this content into the languages you requested. A professional translator must perform all translations and reproduce the content word for word preserving the integrity of the article.

16. **Posting licensed content on any Website:** The following terms and conditions apply as follows: Licensing material from an Elsevier journal: All content posted to the web site must maintain the copyright information line on the bottom of each image; A hyper-text must be included to the Homepage of the journal from which you are licensing at http://www.sciencedirect.com/science/journal/xxxxx or the Elsevier homepage for books at http://www.elsevier.com; Central Storage: This license does not include permission for a scanned version of the material to be stored in a central repository such as that provided by Heron/XanEdu. Licensing material from an Elsevier book: A hyper-text link must be included to the Elsevier homepage at http://www.elsevier.com. All content posted to the web site must maintain the copyright information line on the bottom of each image.

Posting licensed content on Electronic reserve: In addition to the above the following clauses are applicable: The web site must be password-protected and made available only to bona fide students registered on a relevant course. This permission is granted for 1 year only. You may obtain a new license for future website posting.

17. **For journal authors:** the following clauses are applicable in addition to the above:

Preprints:

A preprint is an author's own write-up of research results and analysis, it has not been peer-reviewed, nor has it had any other value added to it by a publisher (such as formatting, copyright, technical enhancement etc.).

Authors can share their preprints anywhere at any time. Preprints should not be added to or enhanced in any way in order to appear more like, or to substitute for, the final versions of articles however authors can update their preprints on arXiv or RePEc with their Accepted Author Manuscript (see below).

If accepted for publication, we encourage authors to link from the preprint to their formal publication via its DOI. Millions of researchers have access to the formal publications on ScienceDirect, and so links will help users to find, access, cite and use the best available version. Please note that Cell Press, The Lancet and some society-owned have different preprint policies. Information on these policies is available on the journal homepage.

Accepted Author Manuscripts: An accepted author manuscript is the manuscript of an article that has been accepted for publication and which typically includes author incorporated changes suggested during submission, peer review and editor-author communications. Authors can share their accepted author manuscript:

- immediately
    - via their non-commercial person homepage or blog
    - by updating a preprint in arXiv or RePEc with the accepted manuscript
    - via their research institute or institutional repository for internal institutional uses or as part of an invitation-only research collaboration work-group
    - directly by providing copies to their students or to research collaborators for their personal use
    - for private scholarly sharing as part of an invitation-only work group on commercial sites with which Elsevier has an agreement
- After the embargo period
    - via non-commercial hosting platforms such as their institutional repository
    - via commercial sites with which Elsevier has an agreement

In all cases accepted manuscripts should:

- link to the formal publication via its DOI
- bear a CC-BY-NC-ND license - this is easy to do
- if aggregated with other manuscripts, for example in a repository or other site, be shared in alignment with our hosting policy not be added to or enhanced in any way to appear more like, or to substitute for, the published journal article.

Published journal article (JPA): A published journal article (PJA) is the definitive final record of published research that appears or will appear in the journal and embodies all value-adding publishing activities including peer review co-ordination, copy-editing, formatting, (if relevant) pagination and online enrichment.

Policies for sharing publishing journal articles differ for subscription and gold open access articles:

Subscription Articles: If you are an author, please share a link to your article rather than the full-text. Millions of researchers have access to the formal publications on ScienceDirect, and so links will help your users to find, access, cite, and use the best available version. Theses and dissertations which contain embedded PJAs as part of the formal submission can be posted publicly by the awarding institution with DOI links back to the formal publications on ScienceDirect. If you are affiliated with a library that subscribes to ScienceDirect you have additional private sharing rights for others' research accessed under that agreement. This includes use for classroom teaching and internal training at the institution (including use in course packs and courseware programs), and inclusion of the article for grant funding purposes.

Gold Open Access Articles: May be shared according to the author-selected end-user license and should contain a CrossMark logo, the end user license, and a DOI link to the formal publication on ScienceDirect. Please refer to Elsevier's posting policy for further information.

18. **For book authors** the following clauses are applicable in addition to the above:

Authors are permitted to place a brief summary of their work online only. You are not allowed to download and post the published electronic version of your chapter, nor may you scan the printed edition to create an electronic version. **Posting to a repository:** Authors are permitted to post a summary of their chapter only in their institution's repository.

19. **Thesis/Dissertation:** If your license is for use in a thesis/dissertation your thesis may be submitted to your institution in either print or electronic form. Should your thesis be published commercially, please reapply for permission. These requirements include permission for the Library and Archives of Canada to supply single copies, on demand, of the complete thesis and include permission for

Proquest/UMI to supply single copies, on demand, of the complete thesis. Should your thesis be published commercially, please reapply for permission. Theses and dissertations which contain embedded PJAs as part of the formal submission can be posted publicly by the awarding institution with DOI links back to the formal publications on ScienceDirect.

ELSEVIER LICENSE

TERMS AND CONDITIONS

Jul 19, 2017

This Agreement between Steven Sitler ("You") and Elsevier ("Elsevier") consists of your license details and the terms and conditions provided by Elsevier and Copyright Clearance Center.

License Number 4152740140779

License date Jul 19, 2017

Licensed Content Publisher Elsevier

Licensed Content Publication Electrochimica Acta

Licensed Content Title	Room Temperature Corrosion Behavior of ZrB_2-HfB_2 Solid Solutions in Acidic and Basic Aqueous Environments
Licensed Content Author	Steven J. Sitler, Indrajit Charit, Krishnan S. Raja
Licensed Content Date	Aug 20, 2017
Licensed Content Volume	246
Licensed Content Issue	n/a
Licensed Content Pages	17
Start Page	173
End Page	189
Type of Use	reuse in a thesis/dissertation
Portion	full article
Format	both print and electronic

Are you the author of this Elsevier article? Yes

Will you be translating? No

Order reference number

Title of your thesis/dissertation Electrochemical and High Temperature Characterizations of Hafnium and Zirconium Diboride Solid Solutions with Different Additives

Expected completion date May 2017

Estimated size (number of pages)150

Elsevier VAT number GB 494 6272 12

Requestor Location Steven Sitler
875 Perimeter Dr.
MS 3024

MOSCOW, ID 83844
United States
Attn: Steven Sitler

Publisher Tax ID 98-0397604

Total 0.00 USD

Terms and Conditions

INTRODUCTION

1. The publisher for this copyrighted material is Elsevier. By clicking "accept" in connection with completing this licensing transaction, you agree that the following terms and conditions apply to this transaction (along with the Billing and Payment terms and conditions established by Copyright Clearance Center, Inc. ("CCC"), at the time that you opened your Rightslink account and that are available at any time at http://myaccount.copyright.com).

GENERAL TERMS

2. Elsevier hereby grants you permission to reproduce the aforementioned material subject to the terms and conditions indicated.

3. Acknowledgement: If any part of the material to be used (for example, figures) has appeared in our publication with credit or acknowledgement to another source, permission must also be sought from that source. If such permission is not obtained then that material may not be included in your publication/copies. Suitable acknowledgement to the source must be made, either as a footnote or in a reference list at the end of your publication, as follows:

"Reprinted from Publication title, Vol /edition number, Author(s), Title of article / title of chapter, Pages No., Copyright (Year), with permission from Elsevier [OR APPLICABLE SOCIETY COPYRIGHT OWNER]." Also Lancet special credit - "Reprinted from The Lancet, Vol. number, Author(s), Title of article, Pages No., Copyright (Year), with permission from Elsevier."

4. Reproduction of this material is confined to the purpose and/or media for which permission is hereby given.

5. Altering/Modifying Material: Not Permitted. However figures and illustrations may be altered/adapted minimally to serve your work. Any other abbreviations, additions, deletions and/or any other alterations shall be made only with prior written authorization of Elsevier Ltd. (Please

contact Elsevier at permissions@elsevier.com). No modifications can be made to any Lancet figures/tables and they must be reproduced in full.

6. If the permission fee for the requested use of our material is waived in this instance, please be advised that your future requests for Elsevier materials may attract a fee.

7. Reservation of Rights: Publisher reserves all rights not specifically granted in the combination of (i) the license details provided by you and accepted in the course of this licensing transaction, (ii) these terms and conditions and (iii) CCC's Billing and Payment terms and conditions.

8. License Contingent Upon Payment: While you may exercise the rights licensed immediately upon issuance of the license at the end of the licensing process for the transaction, provided that you have disclosed complete and accurate details of your proposed use, no license is finally effective unless and until full payment is received from you (either by publisher or by CCC) as provided in CCC's Billing and Payment terms and conditions. If full payment is not received on a timely basis, then any license preliminarily granted shall be deemed automatically revoked and shall be void as if never granted. Further, in the event that you breach any of these terms and conditions or any of CCC's Billing and Payment terms and conditions, the license is automatically revoked and shall be void as if never granted. Use of materials as described in a revoked license, as well as any use of the materials beyond the scope of an unrevoked license, may constitute copyright infringement and publisher reserves the right to take any and all action to protect its copyright in the materials.

9. Warranties: Publisher makes no representations or warranties with respect to the licensed material.

10. Indemnity: You hereby indemnify and agree to hold harmless publisher and CCC, and their respective officers, directors, employees and agents, from and against any and all claims arising out of your use of the licensed material other than as specifically authorized pursuant to this license.

11. No Transfer of License: This license is personal to you and may not be sublicensed, assigned, or transferred by you to any other person without publisher's written permission.

12. No Amendment Except in Writing: This license may not be amended except in a writing signed by both parties (or, in the case of publisher, by CCC on publisher's behalf).

13. Objection to Contrary Terms: Publisher hereby objects to any terms contained in any purchase order, acknowledgment, check endorsement or other writing prepared by you, which terms are inconsistent with these terms and conditions or CCC's Billing and Payment terms and conditions. These terms and conditions, together with CCC's Billing and Payment terms and conditions (which

are incorporated herein), comprise the entire agreement between you and publisher (and CCC) concerning this licensing transaction. In the event of any conflict between your obligations established by these terms and conditions and those established by CCC's Billing and Payment terms and conditions, these terms and conditions shall control.

14. Revocation: Elsevier or Copyright Clearance Center may deny the permissions described in this License at their sole discretion, for any reason or no reason, with a full refund payable to you. Notice of such denial will be made using the contact information provided by you. Failure to receive such notice will not alter or invalidate the denial. In no event will Elsevier or Copyright Clearance Center be responsible or liable for any costs, expenses or damage incurred by you as a result of a denial of your permission request, other than a refund of the amount(s) paid by you to Elsevier and/or Copyright Clearance Center for denied permissions.

LIMITED LICENSE

The following terms and conditions apply only to specific license types:

15. **Translation:** This permission is granted for non-exclusive world **English** rights only unless your license was granted for translation rights. If you licensed translation rights you may only translate this content into the languages you requested. A professional translator must perform all translations and reproduce the content word for word preserving the integrity of the article.

16. **Posting licensed content on any Website:** The following terms and conditions apply as follows: Licensing material from an Elsevier journal: All content posted to the web site must maintain the copyright information line on the bottom of each image; A hyper-text must be included to the Homepage of the journal from which you are licensing at http://www.sciencedirect.com/science/journal/xxxxx or the Elsevier homepage for books at http://www.elsevier.com; Central Storage: This license does not include permission for a scanned version of the material to be stored in a central repository such as that provided by Heron/XanEdu. Licensing material from an Elsevier book: A hyper-text link must be included to the Elsevier homepage at http://www.elsevier.com . All content posted to the web site must maintain the copyright information line on the bottom of each image.

Posting licensed content on Electronic reserve: In addition to the above the following clauses are applicable: The web site must be password-protected and made available only to bona fide students registered on a relevant course. This permission is granted for 1 year only. You may obtain a new license for future website posting.

17. **For journal authors:** the following clauses are applicable in addition to the above:

Preprints:

A preprint is an author's own write-up of research results and analysis, it has not been peerreviewed, nor has it had any other value added to it by a publisher (such as formatting, copyright, technical enhancement etc.).

Authors can share their preprints anywhere at any time. Preprints should not be added to or enhanced in any way in order to appear more like, or to substitute for, the final versions of articles however authors can update their preprints on arXiv or RePEc with their Accepted Author Manuscript (see below).

If accepted for publication, we encourage authors to link from the preprint to their formal publication via its DOI. Millions of researchers have access to the formal publications on ScienceDirect, and so links will help users to find, access, cite and use the best available version. Please note that Cell Press, The Lancet and some society-owned have different preprint policies. Information on these policies is available on the journal homepage.

Accepted Author Manuscripts: An accepted author manuscript is the manuscript of an article that has been accepted for publication and which typically includes author incorporated changes suggested during submission, peer review and editor-author communications. Authors can share their accepted author manuscript:

- immediately
    - via their non-commercial person homepage or blog
    - by updating a preprint in arXiv or RePEc with the accepted manuscript
    - via their research institute or institutional repository for internal institutional uses or as part of an invitation-only research collaboration work-group
    - directly by providing copies to their students or to research collaborators for their personal use
    - for private scholarly sharing as part of an invitation-only work group on commercial sites with which Elsevier has an agreement.
- After the embargo period
    - via non-commercial hosting platforms such as their institutional repository
    - via commercial sites with which Elsevier has an agreement.

In all cases accepted manuscripts should:

- link to the formal publication via its DOI
- bear a CC-BY-NC-ND license - this is easy to do
- if aggregated with other manuscripts, for example in a repository or other site, be shared in alignment with our hosting policy not be added to or enhanced in any way to appear more like, or to substitute for, the published journal article.

Published journal article (JPA): A published journal article (PJA) is the definitive final record of published research that appears or will appear in the journal and embodies all value-adding publishing activities including peer review co-ordination, copy-editing, formatting, (if relevant) pagination and online enrichment. Policies for sharing publishing journal articles differ for subscription and gold open access articles:

Subscription Articles: If you are an author, please share a link to your article rather than the full-text. Millions of researchers have access to the formal publications on ScienceDirect, and so links will help your users to find, access, cite, and use the best available version. Theses and dissertations which contain embedded PJAs as part of the formal submission can be posted publicly by the awarding institution with DOI links back to the formal publications on ScienceDirect. If you are affiliated with a library that subscribes to ScienceDirect you have additional private sharing rights for others' research accessed under that agreement. This includes use for classroom teaching and internal training at the institution (including use in course packs and courseware programs), and inclusion of the article for grant funding purposes.

Gold Open Access Articles: May be shared according to the author-selected end-user license and should contain a CrossMark logo, the end user license, and a DOI link to the formal publication on ScienceDirect. Please refer to Elsevier's posting policy for further information.

18. **For book authors** the following clauses are applicable in addition to the above: Authors are permitted to place a brief summary of their work online only. You are not allowed to download and post the published electronic version of your chapter, nor may you scan the printed edition to create an electronic version. **Posting to a repository:** Authors are permitted to post a summary of their chapter only in their institution's repository.

19. **Thesis/Dissertation:** If your license is for use in a thesis/dissertation your thesis may be submitted to your institution in either print or electronic form. Should your thesis be published commercially, please reapply for permission. These requirements include permission for the Library and Archives of Canada to supply single copies, on demand, of the complete thesis and include permission for

Proquest/UMI to supply single copies, on demand, of the complete thesis. Should your thesis be published commercially, please reapply for permission. Theses and dissertations which contain embedded PJAs as part of the formal submission can be posted publicly by the awarding institution with DOI links back to the formal publications on ScienceDirect.

APPENDIX B: Supporting Information for Chapter 3

Room Temperature Corrosion Behavior of ZrB_2-HfB_2 Solid Solutions in Acidic and Basic Aqueous Environments

Steven J. Sitler[a†], Indrajit Charit[a], Krishnan S. Raja[a]

[†]Corresponding author: sitl1428@vandals.uidaho.edu; University of Idaho, 875 Perimeter Dr. MS3024 Moscow, ID 83844.

[a]Department of Chemical and Materials Engineering, University of Idaho, Moscow, Idaho 83844

Table 3.S1: Lattice parameters of boride samples from XRD data.

		Lattice Parameters		
		a	*c*	*Volume of unit cell*
Sample	*Identifier*	(nm)	(nm)	(nm^3)
HfB_2	A	0.313250	0.346146	0.029415
ZrB_2	B	0.315917	0.351421	0.030372
$Hf_{0.5}Zr_{0.5}B_2$	AB	0.314642	0.348757	0.029901
$Hf_{0.8}Zr_{0.2}B_2$	4AB	0.315361	0.350250	0.030166
$Hf_{0.2}Zr_{0.8}B_2$	A4B	0.313929	0.347482	0.029657
$Hf_{0.5}Zr_{0.5}B_2$ + 1.8 mol% Gd_2O_3	ABG	0.314435	0.348180	0.029812
$Hf_{0.5}Zr_{0.5}B_2$ + Hf (B/Me =1.86)	ABH	0.314505	0.348643	0.029865
$Hf_{0.5}Zr_{0.5}B_2$ + 1.8 mol% LaB_6	ABL	0.314645	0.348767	0.029902
$Hf_{0.5}Zr_{0.5}B_2$ + Ta (B/Me =1.86)	ABT	0.313599	0.346095	0.029476
$Hf_{0.5}Zr_{0.5}B_2$ + Zr (B/Me =1.86)	ABZ	0.314497	0.348437	0.029846

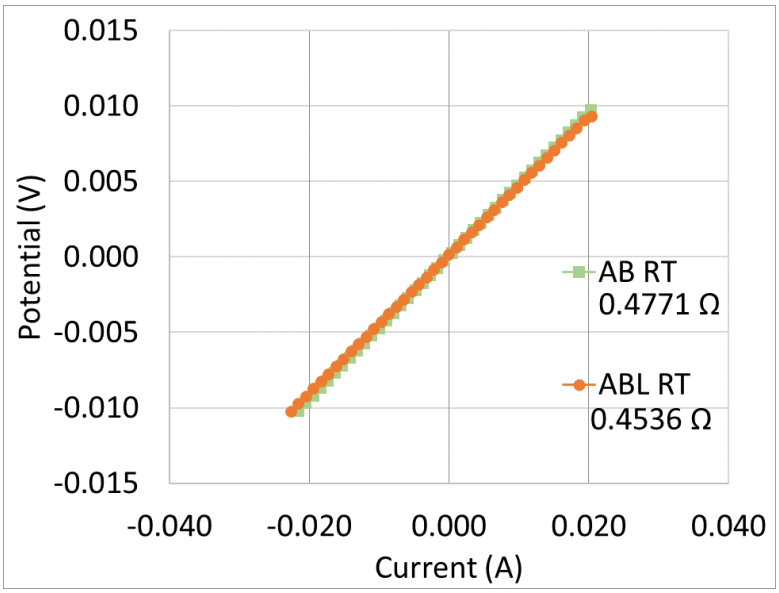

Figure 3.S1: *I-V* plot of the AB (1:1 HfB_2:ZrB_2) and ABL (1:1 HfB_2:ZrB_2 + 1.8 mol% LaB_6) samples to measure the electrical resistance at room temperature.

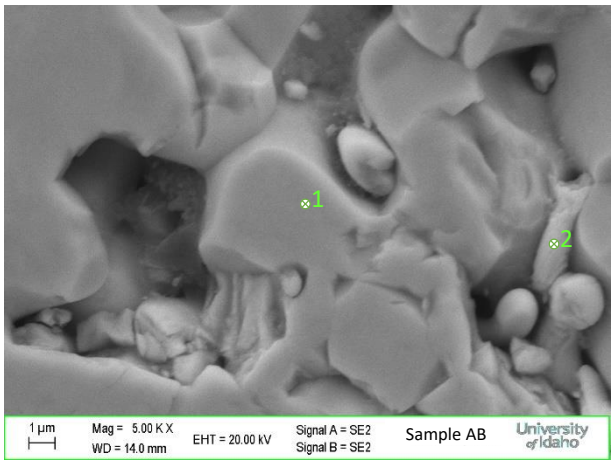

AB Point 1				
Element	Wt. %	Wt.% Error	At. %	At. % Error
B	8.5	±0.9	52.7	±5.5
Zr	35.6	±0.8	26.3	±0.6
Hf	55.9	±2.6	21.1	±1.0

AB Point 2				
Element	Wt. %	Wt.% Error	At. %	At. % Error
B	0.3	±0.6	1.6	±12.6
O	17.2	±0.6	63.8	±2.3
Zr	22.8	±0.7	14.8	±0.5
Hf	59.7	±2.6	19.8	±0.9

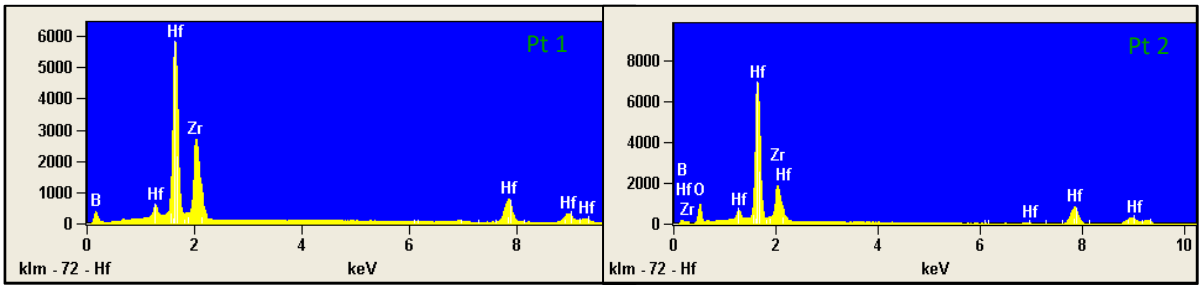

Figure 3.S2: EDS analysis of samples AB for secondary phases on polished sample.

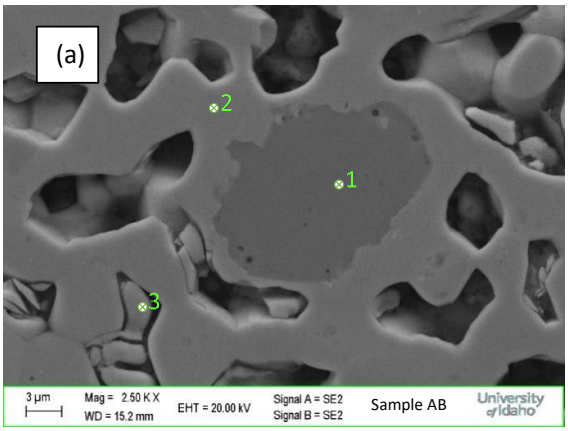

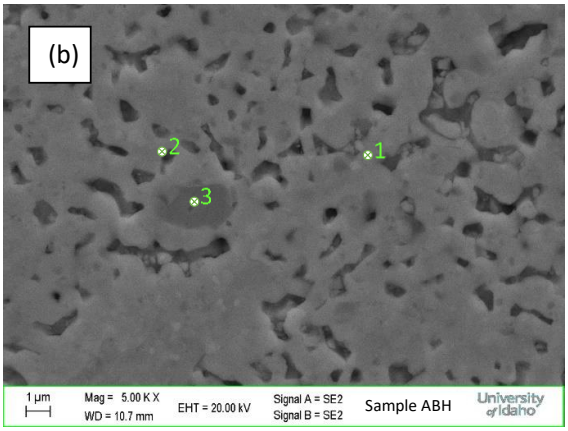

AB Point 1				
Element	Wt. %	Wt.% Error	At. %	At. % Error
B	13.4	±0.7	56.9	±2.8
Zr	84.0	±0.9	42.4	±0.5
Hf	2.7	±0.9	0.7	±0.2

AB Point 2				
Element	Wt. %	Wt.% Error	At. %	At. % Error
B	8.8	±0.9	53.8	±5.4
Zr	35.6	±0.8	25.7	±0.6
Hf	55.6	±2.7	20.5	±1.0

AB Point 3				
Element	Wt. %	Wt.% Error	At. %	At. % Error
B	4.4	±0.6	23.4	±3.1
O	12.0	±0.5	43.5	±1.8
Zr	20.0	±0.7	12.6	±0.5
Hf	63.6	±2.7	20.5	±0.9

ABH Point 1				
Element	Wt. %	Wt.% Error	At. %	At. % Error
B	15.7	±1.0	63.5	±4.1
O	0.4	±0.3	1.0	±0.9
Zr	64.1	±0.8	30.6	±0.4
Hf	19.8	±1.8	4.9	±0.5

ABH Point 2				
Element	Wt. %	Wt.% Error	At. %	At. % Error
B	4.5	±1.8	34.3	±13.3
O	2.4	±0.3	12.3	±1.5
Zr	3.9	±0.8	21.5	±0.7
Hf	69.2	±2.6	31.9	±1.2

ABH Point 3				
Element	Wt. %	Wt.% Error	At. %	At. % Error
B	3.5	±1.9	22.2	±12.2
O	8.4	±0.4	36.0	±1.6
Zr	5.7	±0.7	11.7	±0.5
Hf	1.7	±2.7	27.5	±1.0

Figure 3.S3: EDS analysis of samples (a) AB and (b) ABH for secondary phases after potentiostatic and EIS testing in 0.1 M NaOH at 0.2 $V_{Ag/AgCl}$.

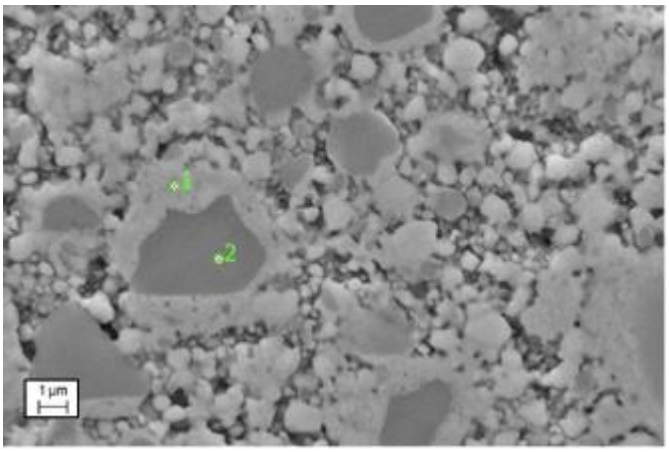

ABT Point 1				
Element	Wt. %	Wt.% Error	At. %	At. % Error
B	8.8	±1.7	56.4	±10.5
O	0.7	±0.2	3.2	±1.0
Zr	14.6	±0.7	11.1	±0.5
Hf	62.2	±2.9	24.1	±1.1
Ta	13.7	±2.5	5.2	±1.0
ABT Point 2				
Element	Wt. %	Wt.% Error	At. %	At. % Error
B	16.6	±0.8	63.2	±2.9
Zr	79.2	±0.9	35.8	±0.4
Hf	4.2	±1.6	1.0	±0.4

Figure 3.S4: EDS analysis of sample ABT after potentiostatic and EIS testing in 0.1 M NaOH at 0.2 $V_{Ag/AgCl}$.

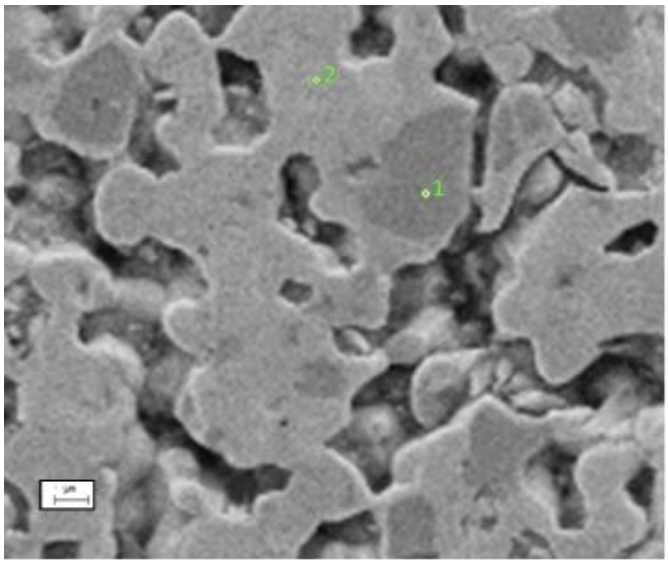

ABG Point 1				
Element	Wt. %	Wt.% Error	At. %	At. % Error
B	13.2	±1.2	55.0	±4.9
O	3.1	±0.6	8.6	±1.6
Zr	63.6	±0.8	31.3	±0.4
Hf	19.8	±1.9	5.0	±0.5
Gd	0.3	±0.4	0.1	±0.1
ABG Point 2				
Element	Wt. %	Wt.% Error	At. %	At. % Error
B	3.6	±2.1	26.5	±15.5
O	3.6	±0.4	18.1	±1.8
Zr	33.0	±0.9	28.7	±0.8
Hf	59.0	±3.0	26.3	±1.3
Gd	0.8	±0.6	0.4	±0.3

Figure 3.S5: EDS analysis of sample ABG after potentiostatic and EIS testing in 0.1 M NaOH at 0.2 $V_{Ag/AgCl}$.

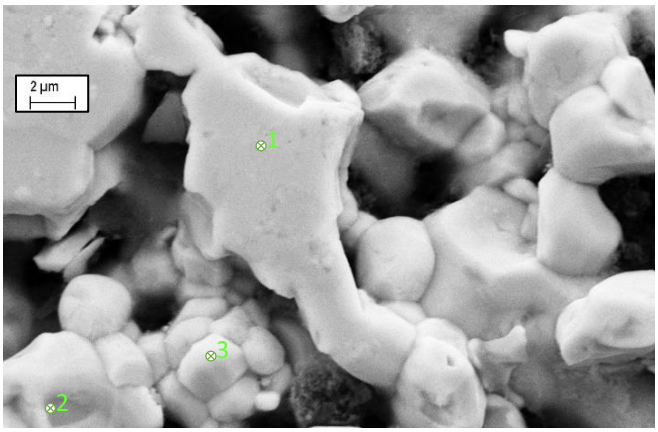

ABL Point 1				
Element	Wt. %	Wt.% Error	At. %	At. % Error
B	7.3	±1.4	50.1	±9.3
Zr	28.8	±0.7	23.4	±0.6
Hf	63.9	±2.8	26.5	±1.2
La	0	±0.0	0	---

ABL Point 2				
Element	Wt. %	Wt.% Error	At. %	At. % Error
B	6.4	±0.8	46.8	±5.8
O	0.4	±0.2	1.9	±1.0
Zr	24.5	±0.7	21.1	±0.6
Hf	68.6	±3.0	30.2	±1.3
La	0	±0.0	0	---

ABL Point 3				
Element	Wt. %	Wt.% Error	At. %	At. % Error
B	4.8	±1.4	36.2	±10.7
O	1.6	±0.2	8.3	±1.2
Zr	28.3	±0.7	25.5	±0.6
Hf	65.3	±2.8	30.0	±1.3
La	0	±0.0	0	---

Figure 3.S6: EDS analysis of sample ABL after potentiostatic and EIS testing in 0.1 M NaOH at 0.2 $V_{Ag/AgCl}$.

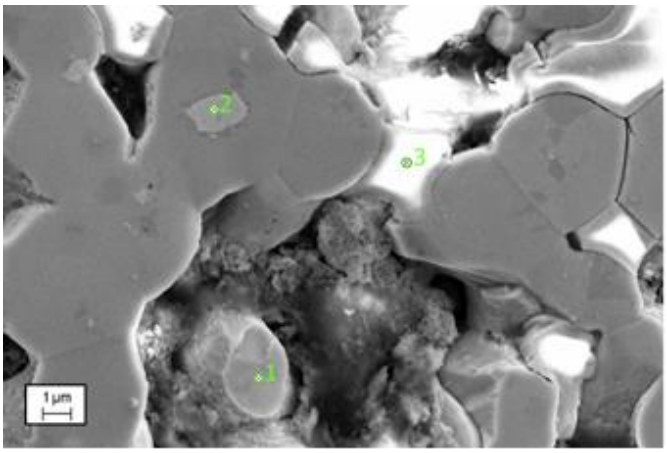

A4B Point 1				
Element	Wt. %	Wt.% Error	At. %	At. % Error
B	0	±0.0	0	---
O	13.8	±0.5	53.8	±1.9
Zr	48.0	±0.8	32.8	±0.6
Hf	38.2	±2.3	13.4	±0.8

A4B Point 2				
Element	Wt. %	Wt.% Error	At. %	At. % Error
B	8.2	±0.8	41.4	±4.1
O	4.7	±0.6	16.1	±1.9
Zr	54.1	±0.8	32.5	±0.5
Hf	33.0	±2.2	10.1	±0.7

A4B Point 3				
Element	Wt. %	Wt.% Error	At. %	At. % Error
B	10.0	±1.7	41.5	±7.2
O	9.5	±0.6	26.8	±1.8
Zr	47.4	±0.8	23.4	±0.4
Hf	33.1	±2.1	8.3	±0.5

Figure 3.S7: EDS analysis of sample A4B after potentiostatic and EIS testing in 0.1 M H_2SO_4 at 0.2 $V_{Ag/AgCl}$.

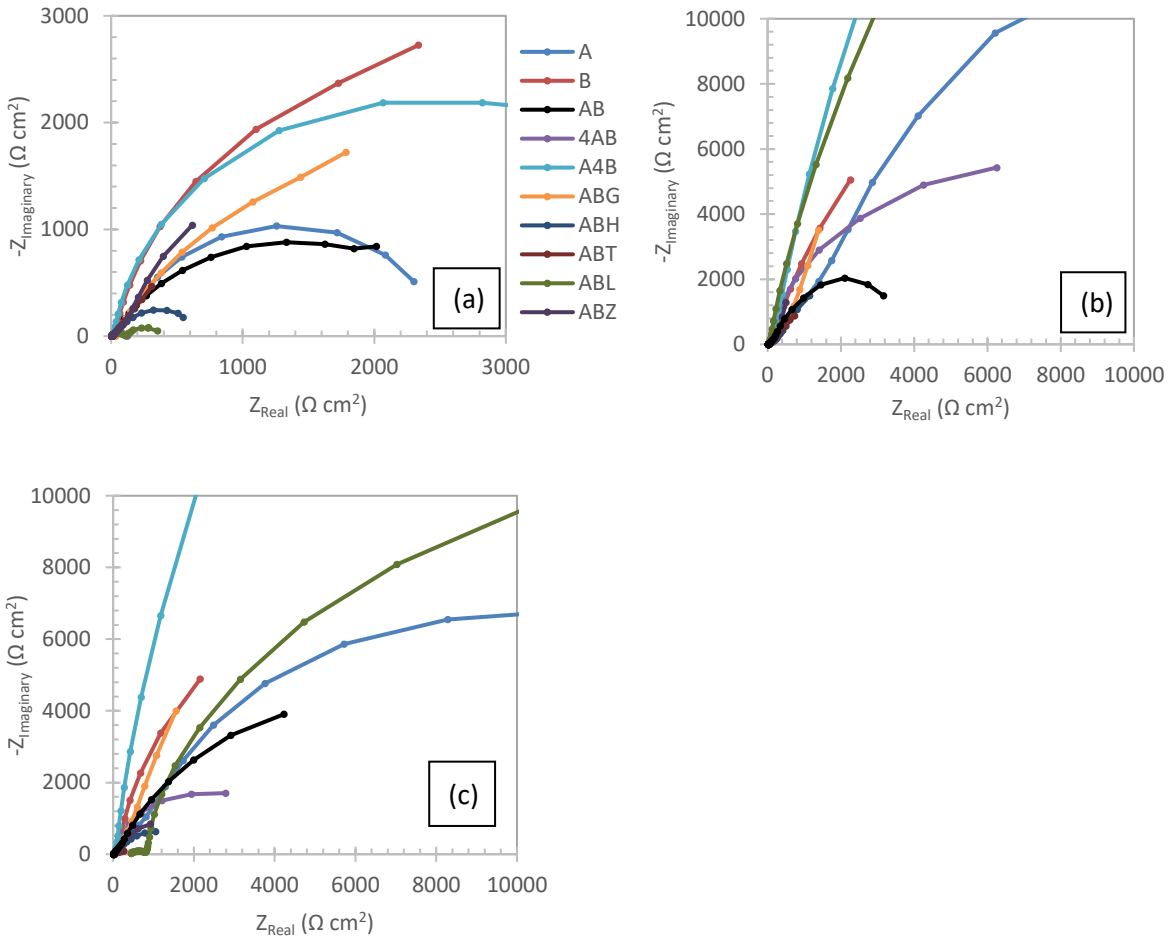

Figure 3.S8: EIS results using an applied AC voltage of 10 mV and scanning the frequency from 100 kHz to 0.01 Hz shown as Nyquist plots of the boride samples for (a) 0.1 M H_2SO_4, (b) 0.1 M NaCl, and (c) 0.1 M NaOH. The legend is valid for all graphs in this figure.

APPENDIX C: Supporting Information for Chapter 4

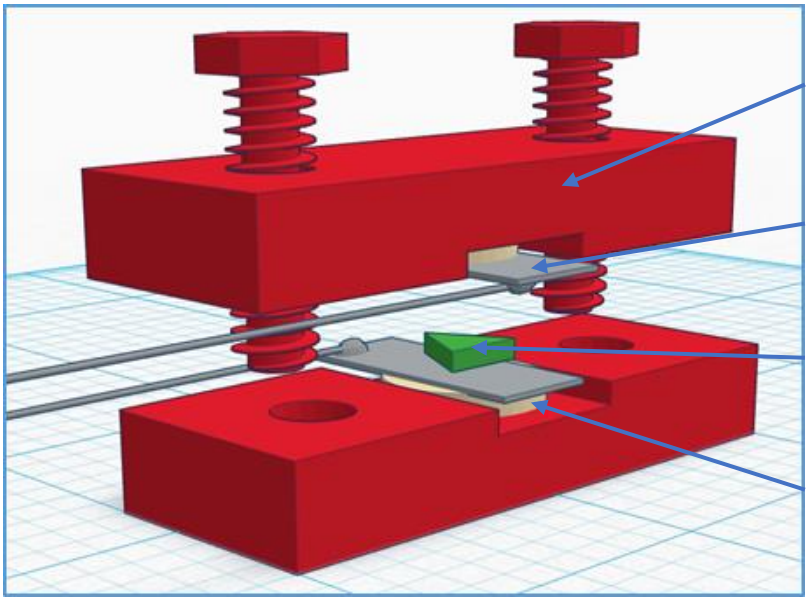

Figure 4.S1: Custom clamp used for measuring high temperature electrical conductivity inside of the tube furnace.

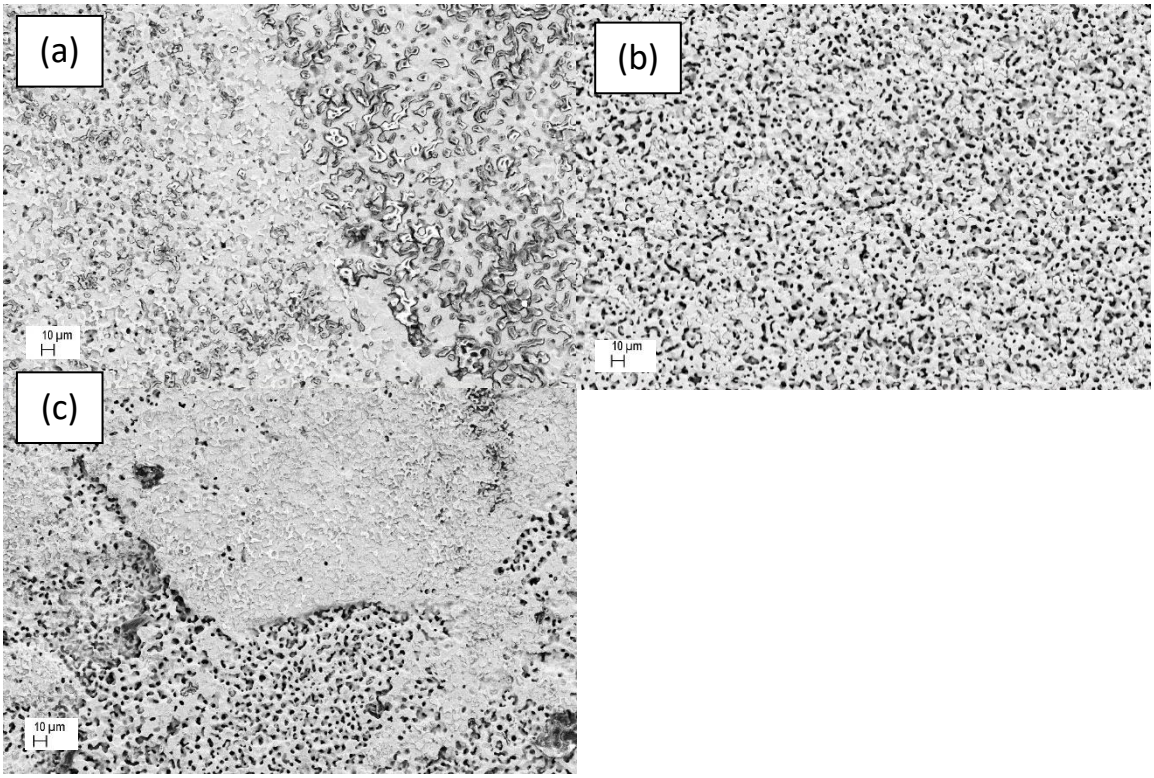

Figure 4.S2: Surface morphology of samples after anodization process, before heating in TGA or tube furnace. (a) Sample AB, (b) sample ABH, (c) sample ABL.

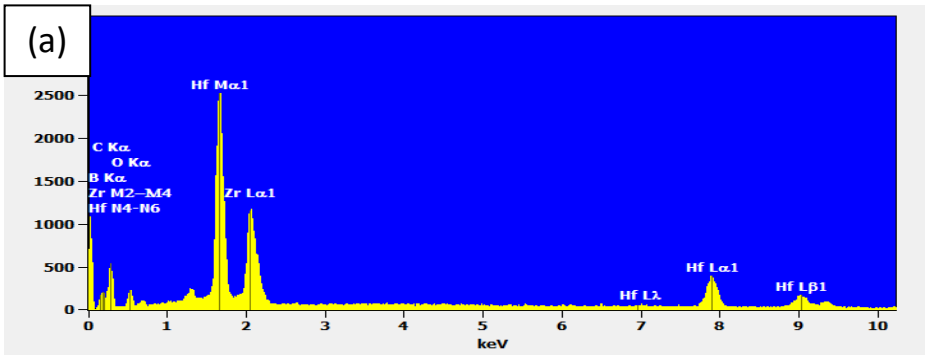

Quantitative Results for: AB top

Element Line	Net Counts	Net Counts Error	Weight %	Weight % Error	Atom %	Atom % Error
B K	0	± 133	0.00	---	0.00	± 0.00
O K	307	± 78	3.63	± 0.92	23.85	± 6.06
Zr L	15991	± 344	34.44	± 0.74	39.68	± 0.85
Hf L	9974	± 336	61.93	± 2.09	36.47	± 1.23
Total			100.00		100.00	

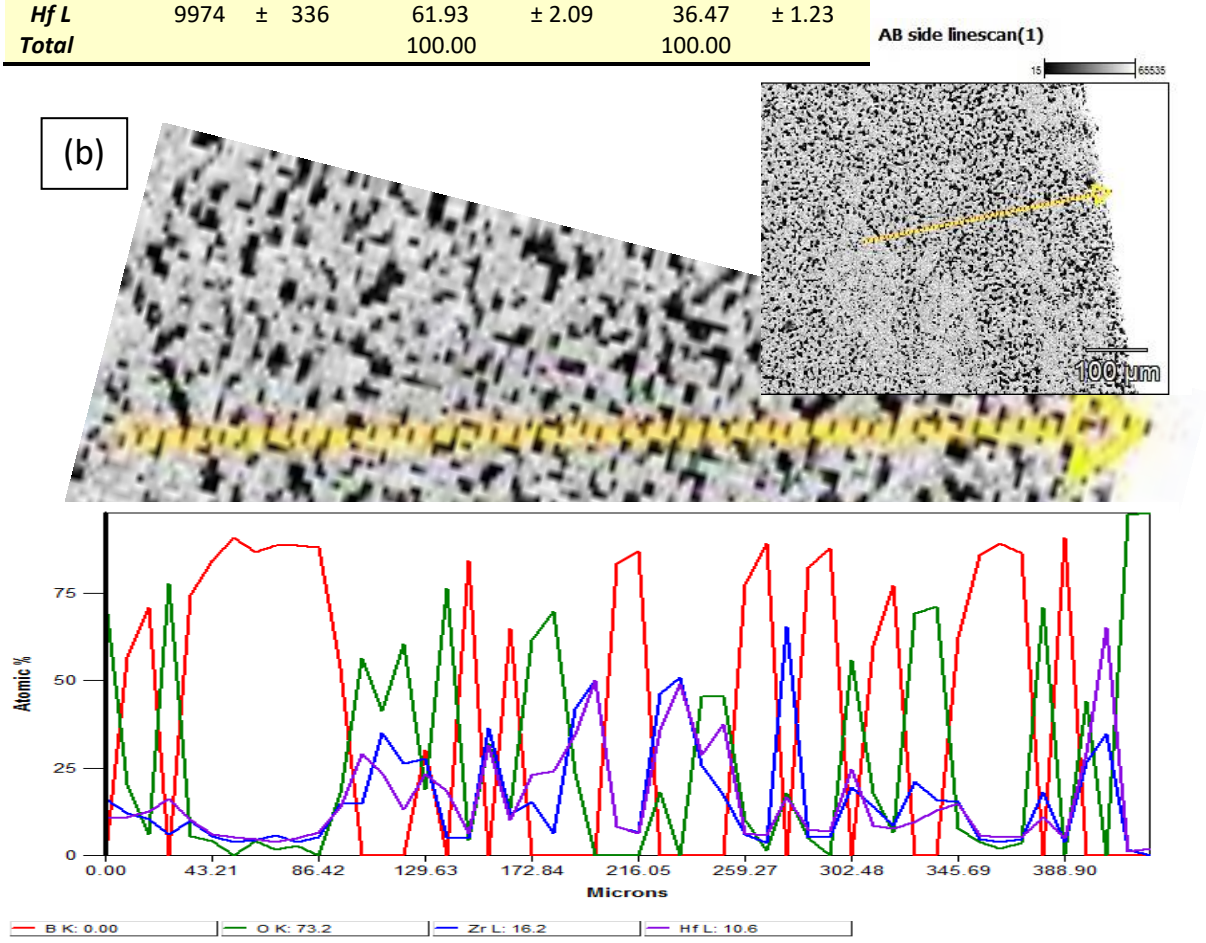

Figure 4.S3: EDS analysis of anodized sample AB prior to TGA testing, (a) top surface (b) cross-sectional linescan. Carbon was removed from the quantitative analysis.

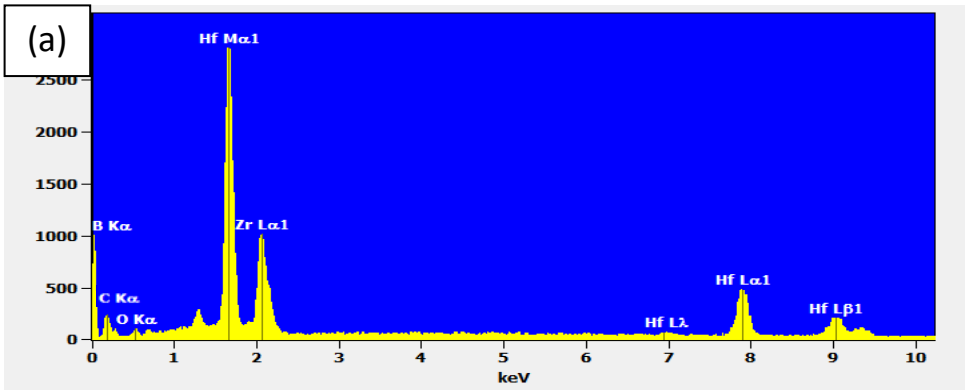

Quantitative Results for: ABH top

Element Line	Net Counts	Net Counts Error	Weight %	Weight % Error	Atom %	Atom % Error
B K	798	± 39	40.76	± 1.99	87.82	± 4.29
O K	350	± 38	2.08	± 0.23	3.03	± 0.33
Zr L	13771	± 330	13.51	± 0.32	3.45	± 0.08
Hf L	12736	± 375	43.65	± 1.29	5.70	± 0.17
Total			100.00		100.00	

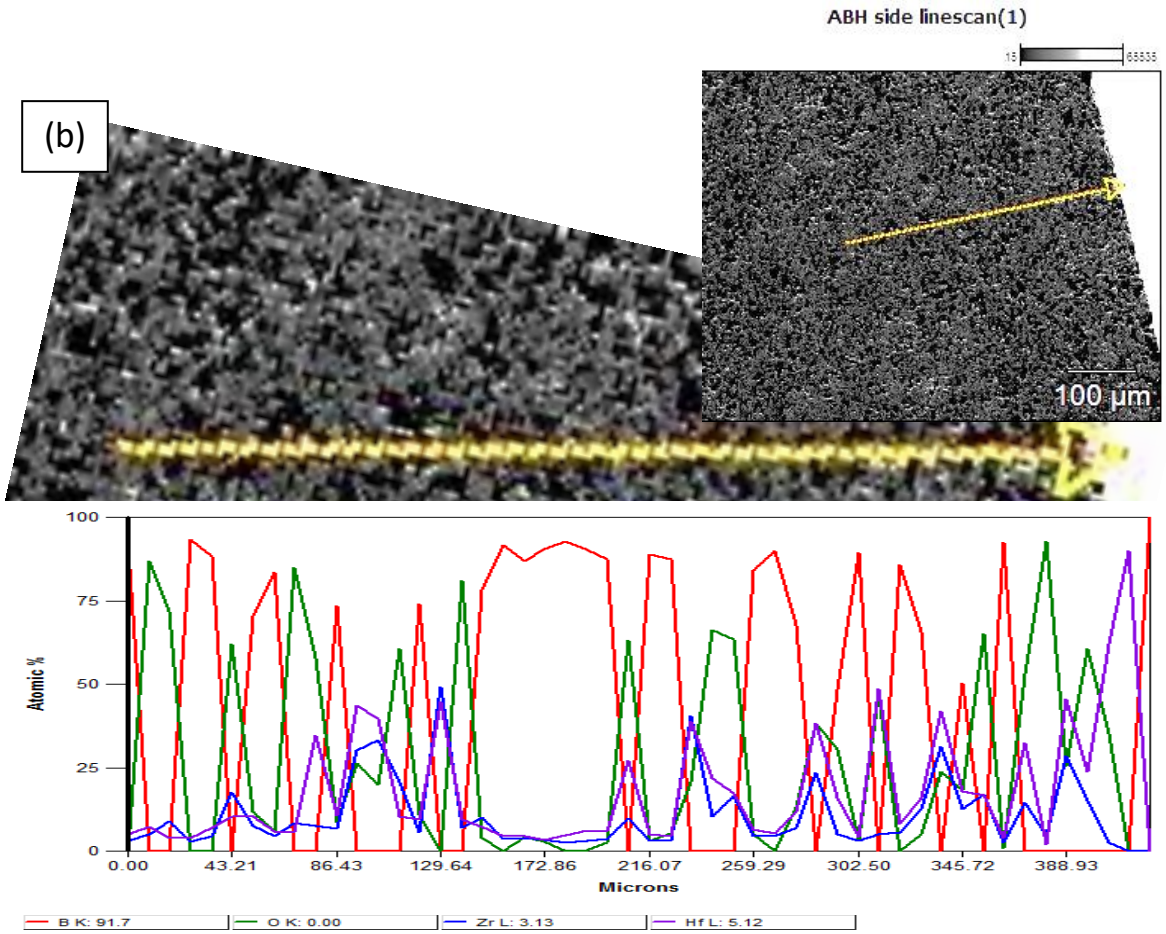

Figure 4.S4: EDS analysis of anodized sample ABH prior to TGA testing, (a) top surface (b) cross-sectional linescan. Carbon was removed from the quantitative analysis.

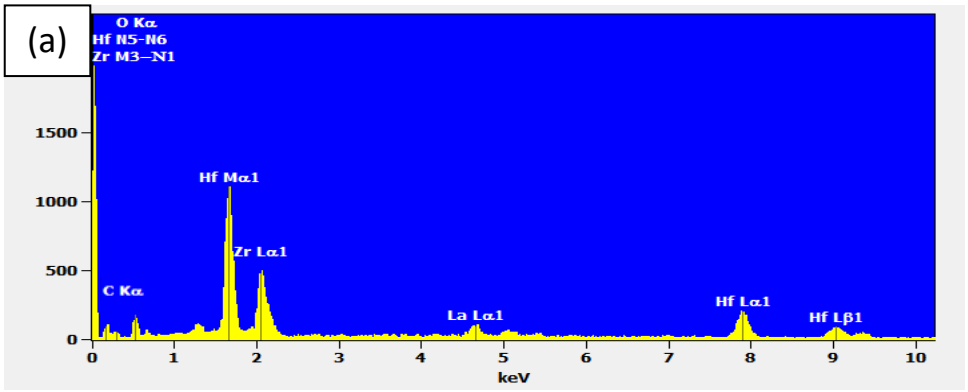

Quantitative Results for: ABL top

Element Line	Net Counts	Net Counts Error	Weight %	Weight % Error	Atom %	Atom % Error
B K	0	± 35	0.00	---	0.00	± 0.00
O K	1068	± 39	15.48	± 0.57	61.66	± 2.25
Zr L	6482	± 225	21.27	± 0.74	14.86	± 0.52
La L	1946	± 171	8.87	± 0.78	4.07	± 0.36
Hf L	5704	± 248	54.38	± 2.36	19.41	± 0.84
Total			100.00		100.00	

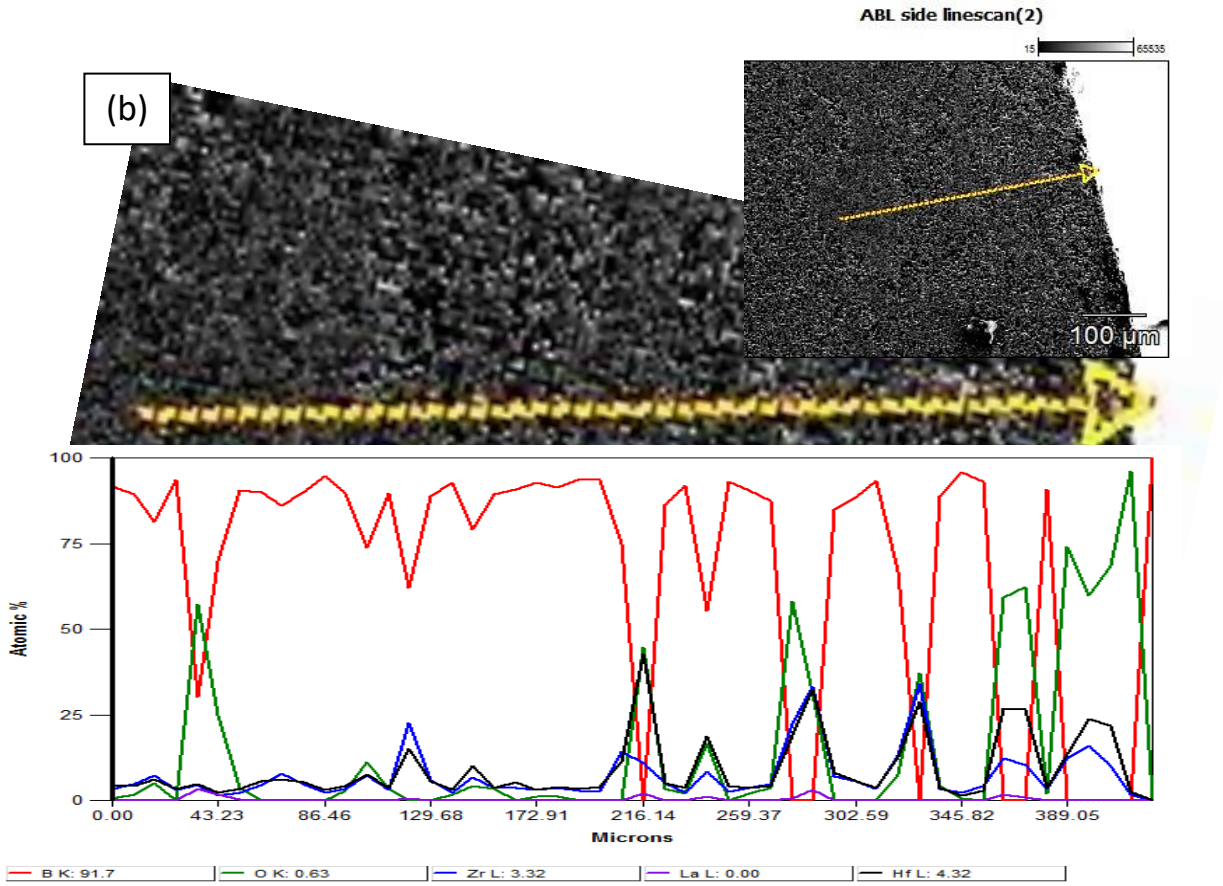

Figure 4.S5: EDS analysis of anodized sample ABL prior to TGA testing, (a) top surface (b) cross-sectional linescan. Carbon was removed from the quantitative analysis.

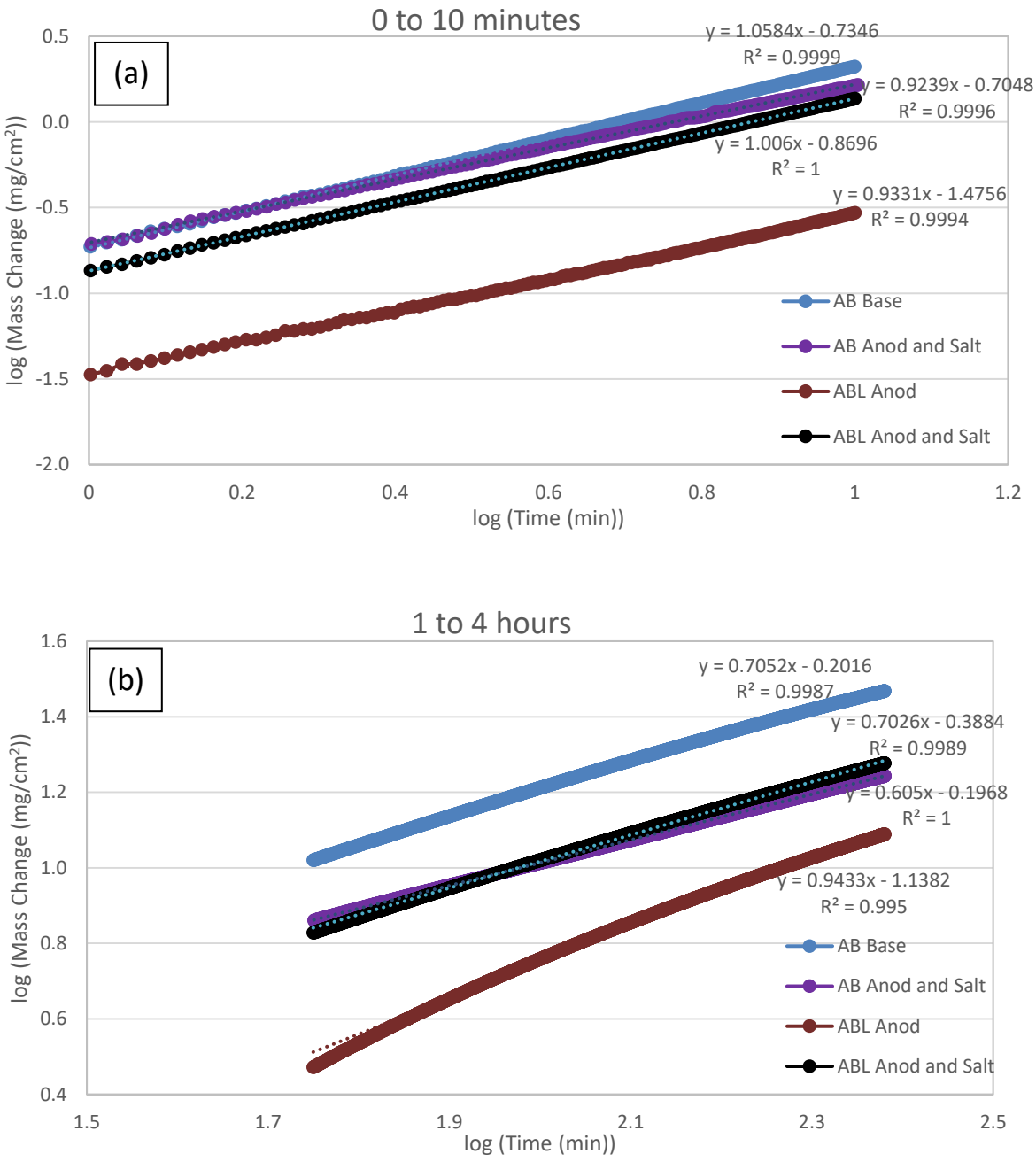

Figure 4.S6: TGA data plotted in the log-log scale to determine kinetics type and rate constants. (a) 0-10 minutes in p_{O2} = 0.1 Pa, (b) 1 to 4 hours in p_{O2} = 0.1 Pa.

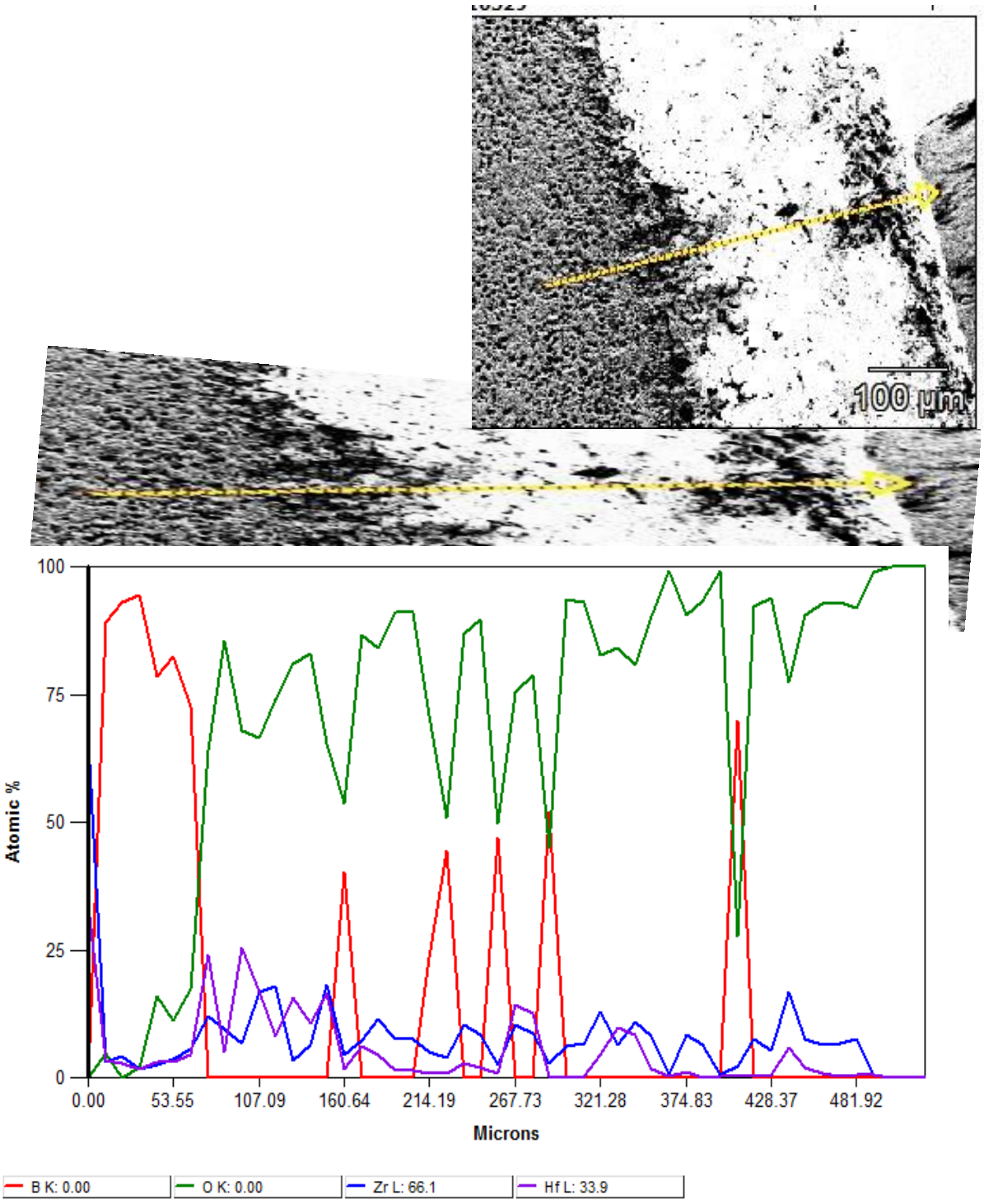

Figure 4.S7: EDS linescan of AB control sample after 8 hour TGA run at 1500 °C.

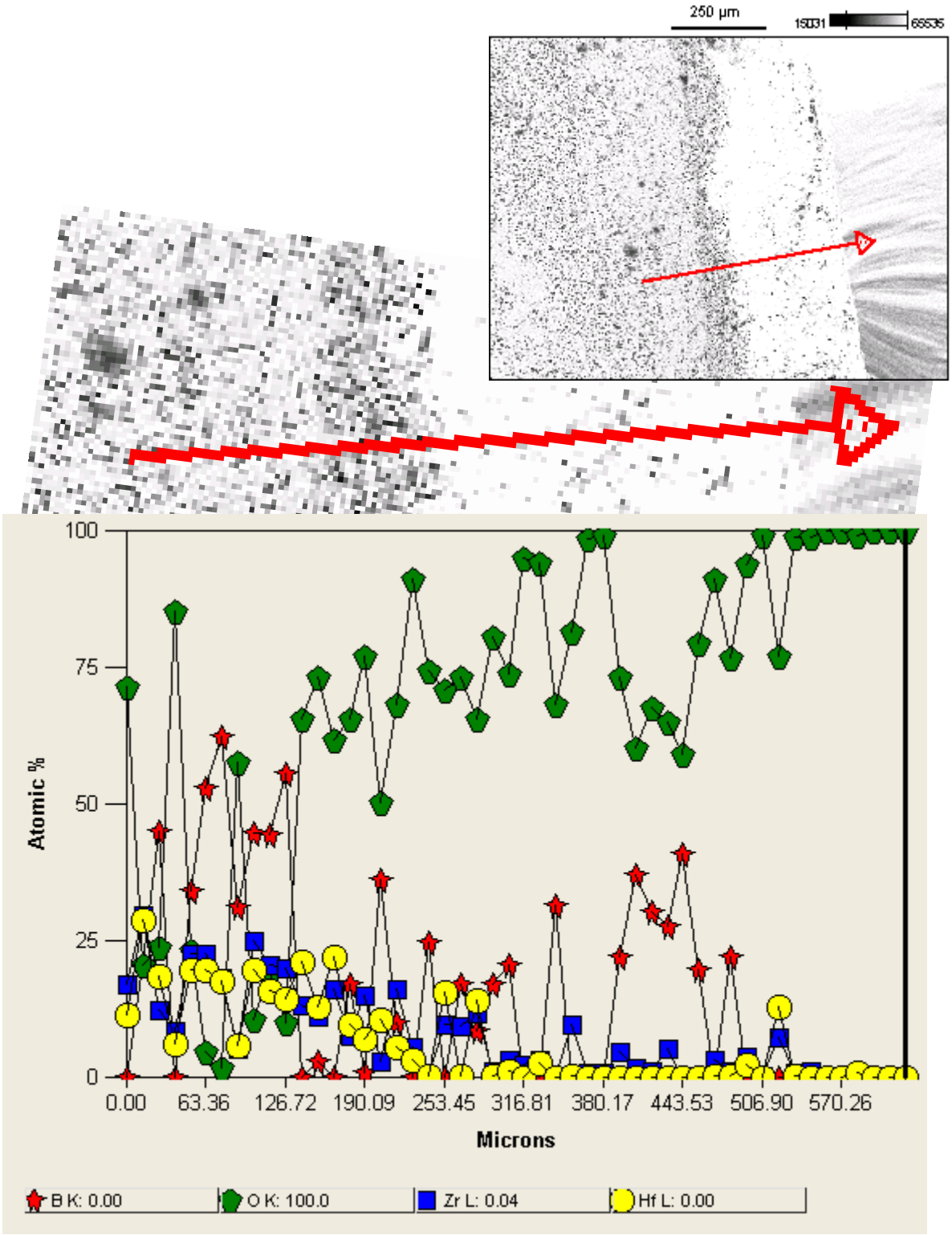

Figure 4.S8: EDS linescan of anodized AB sample after 8 hour TGA run at 1500 °C.

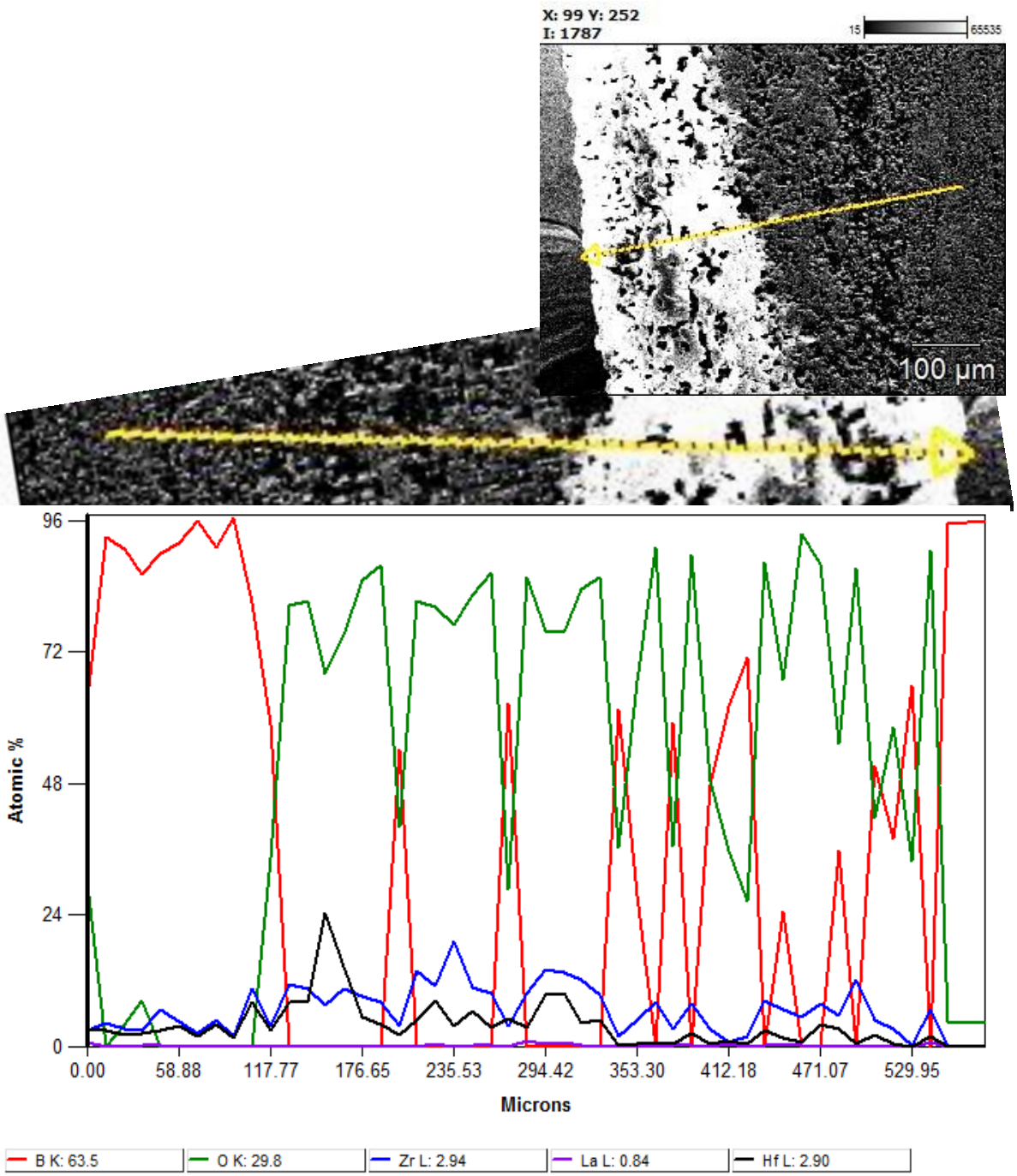

Figure 4.S9: EDS linescan of ABL control sample after 8 hour TGA run at 1500 °C.

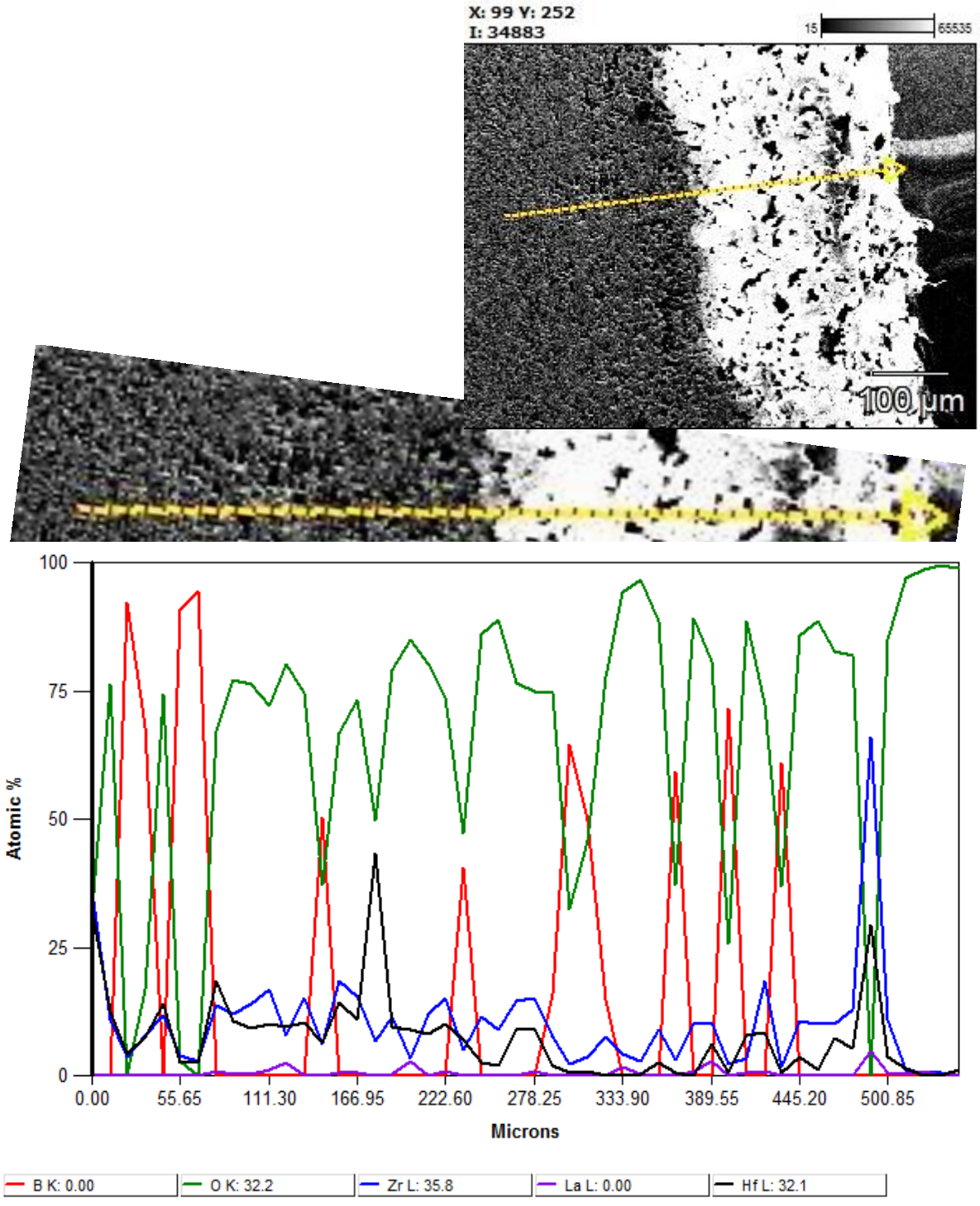

Figure 4.S10: EDS linescan of anodized ABL sample after 8 hour TGA run at 1500 °C.

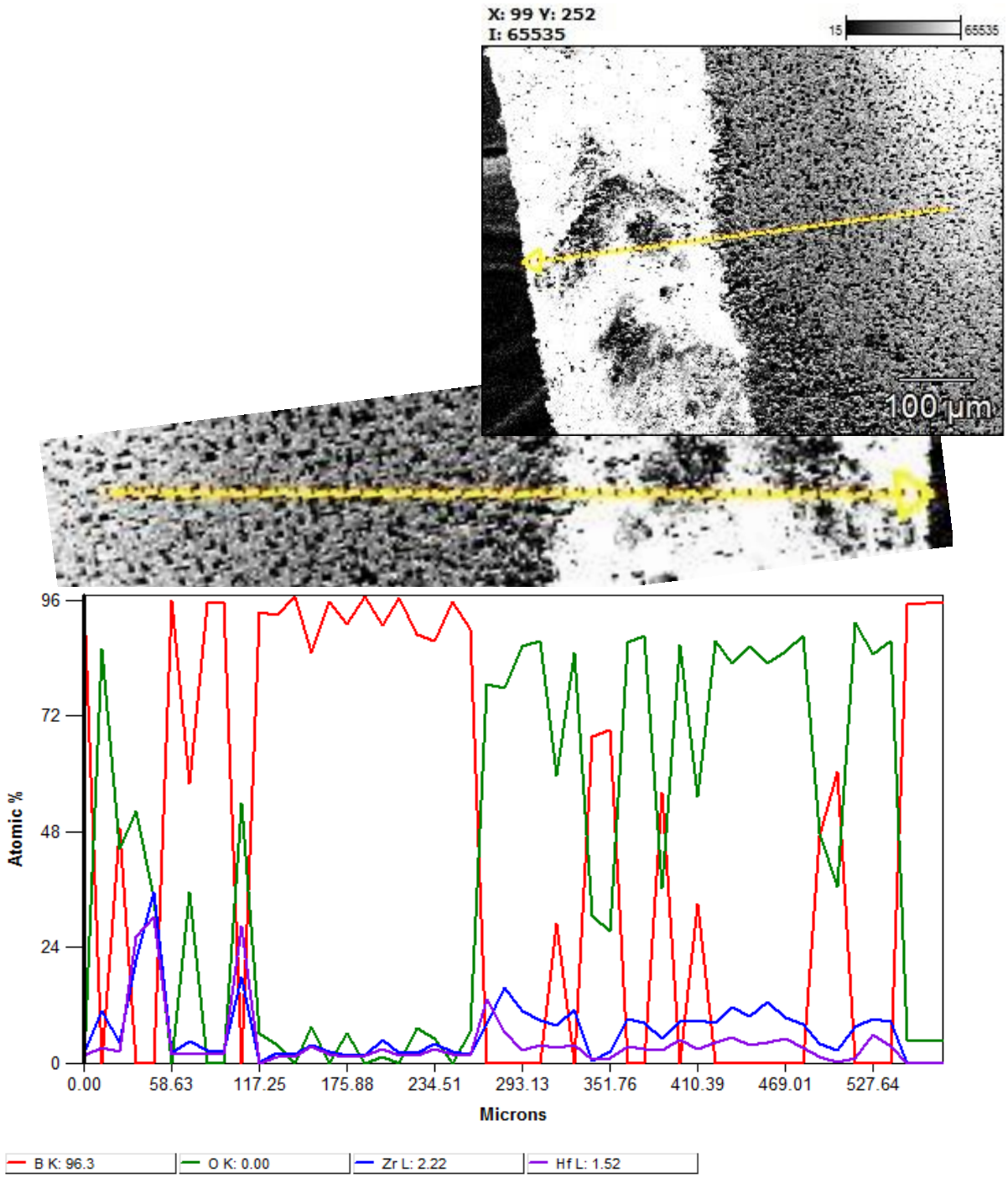

Figure 4.S11: EDS linescan of the AB sample coated with 2.5 mg/cm^2 K_2SO_4 salt after 8 hour TGA run at 1500 °C.

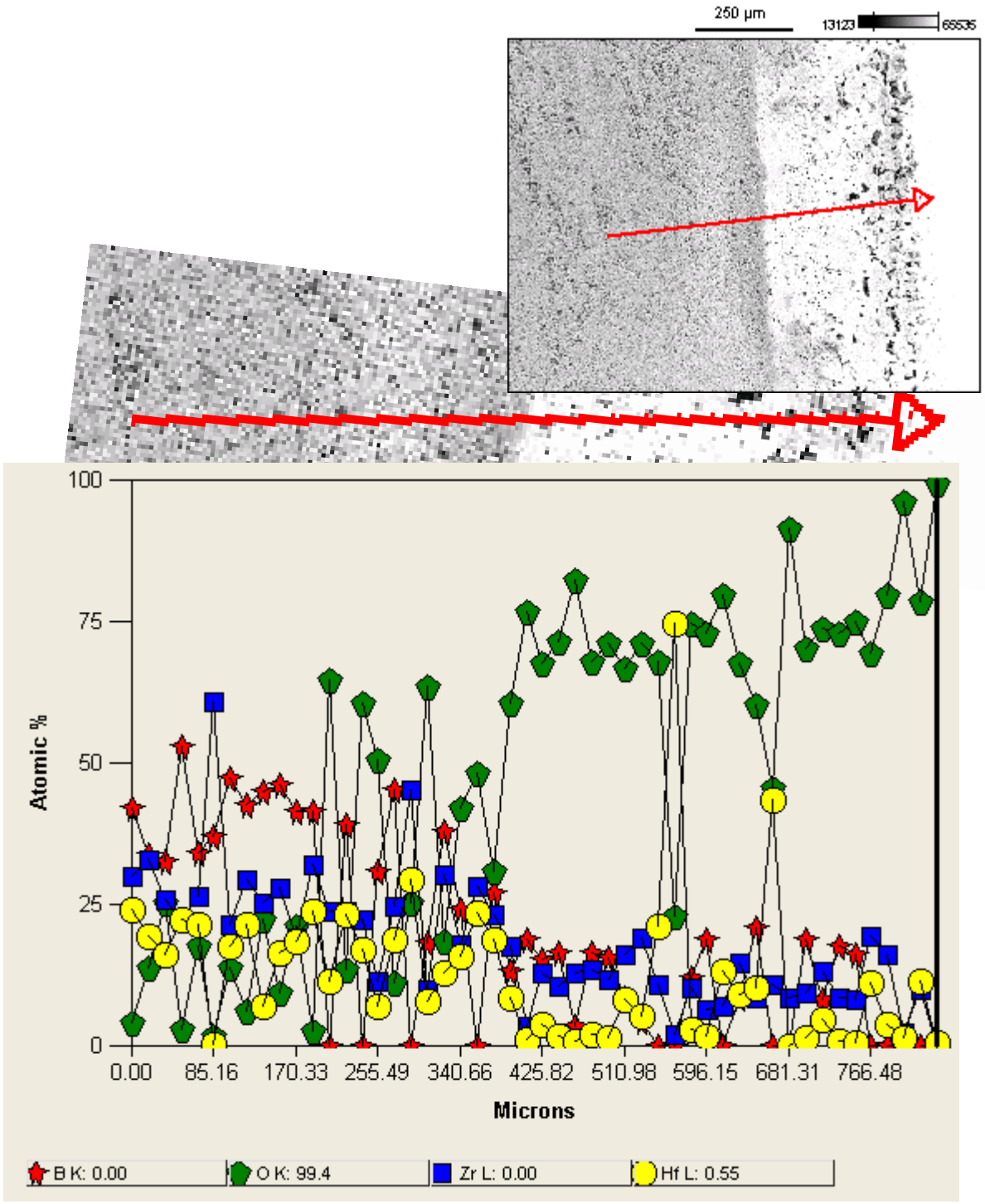

Figure 4.S12: EDS linescan of the anodized AB sample coated with 2.5 mg/cm^2 K_2SO_4 salt after 8 hour TGA run at 1500 °C.

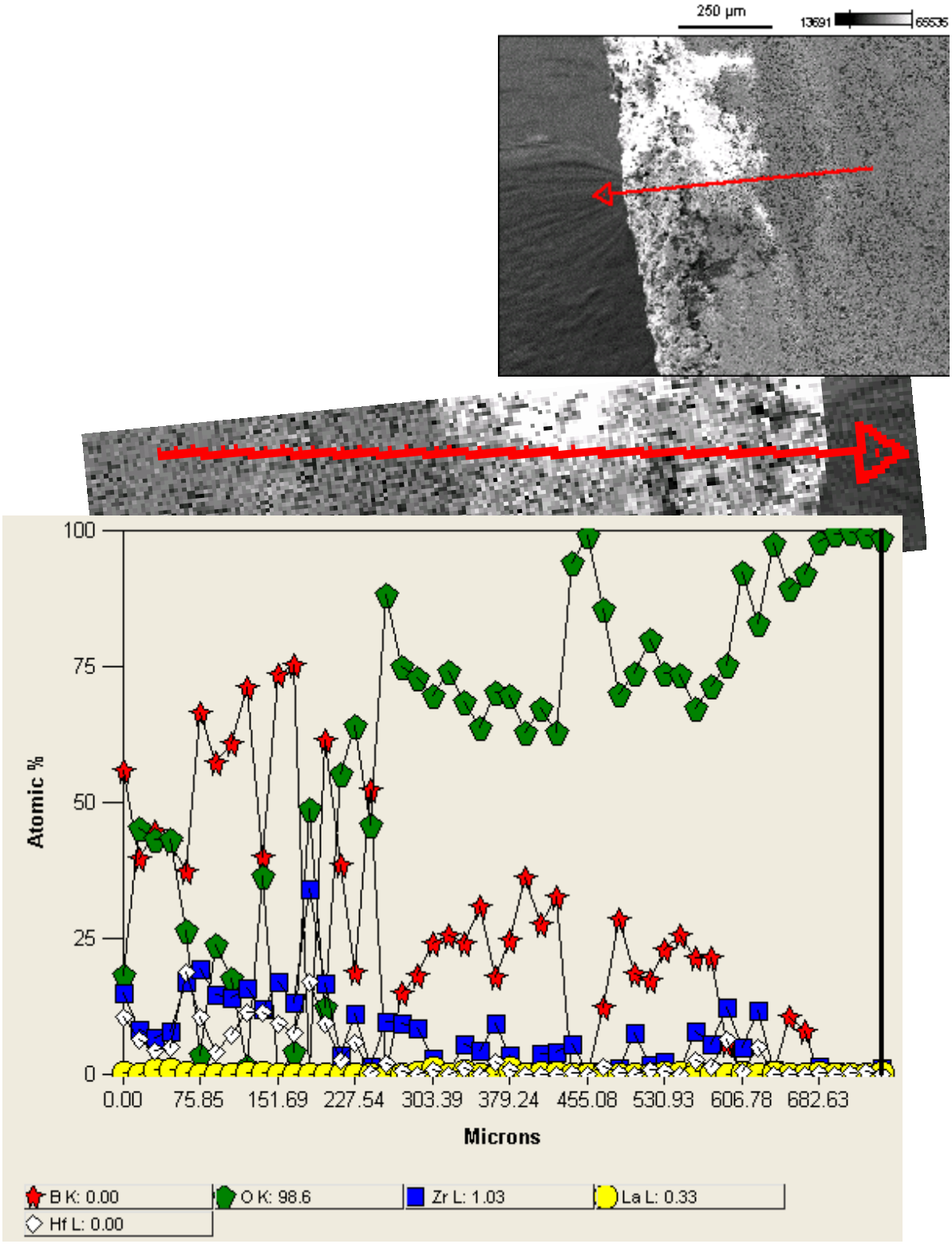

Figure 4.S13: EDS linescan of the ABL sample coated with 2.5 mg/cm^2 K_2SO_4 salt after 8 hour TGA run at 1500 °C.

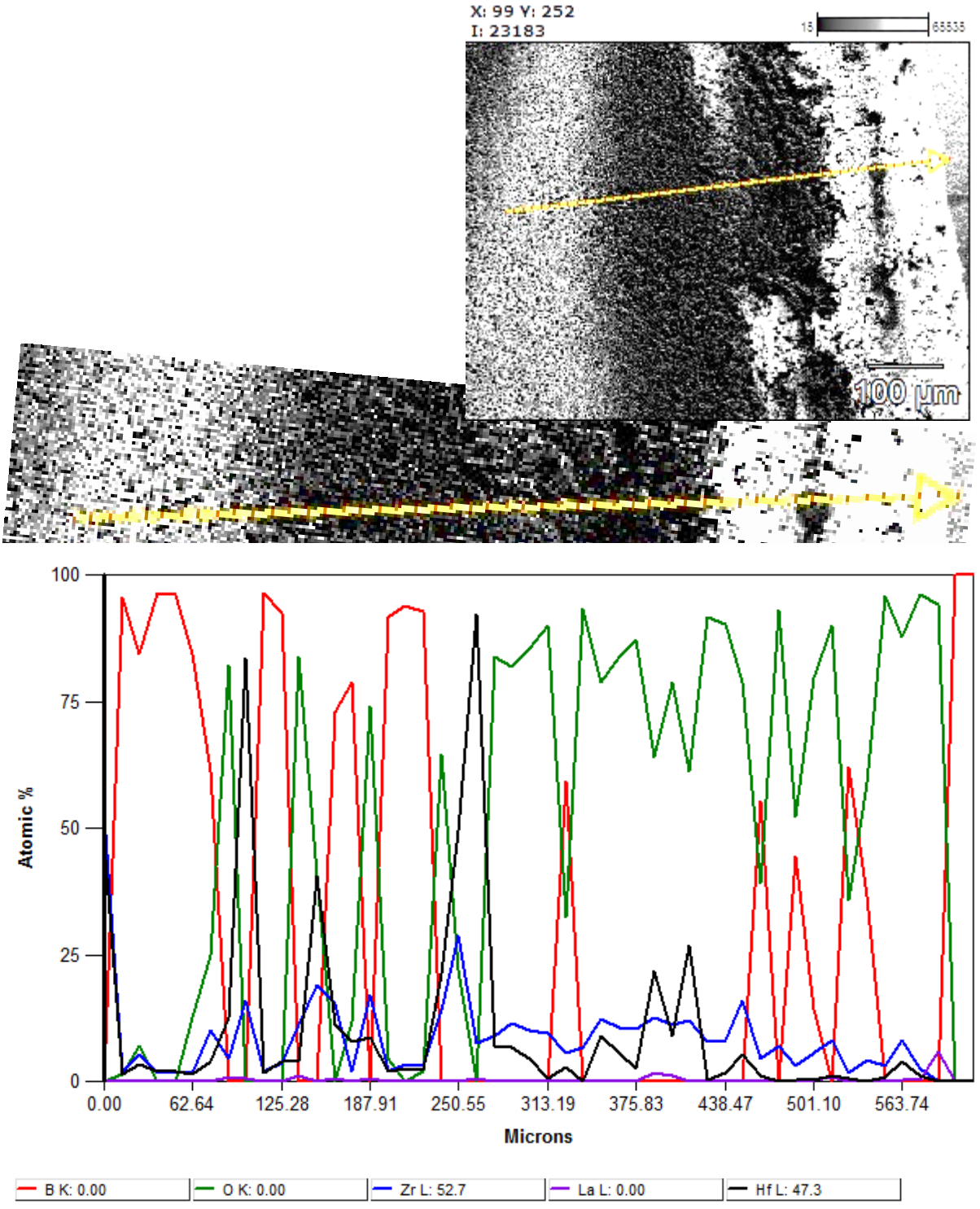

Figure 4.S14: EDS linescan of the anodized ABL sample coated with 2.5 mg/cm^2 K_2SO_4 salt after 8 hour TGA run at 1500 °C.

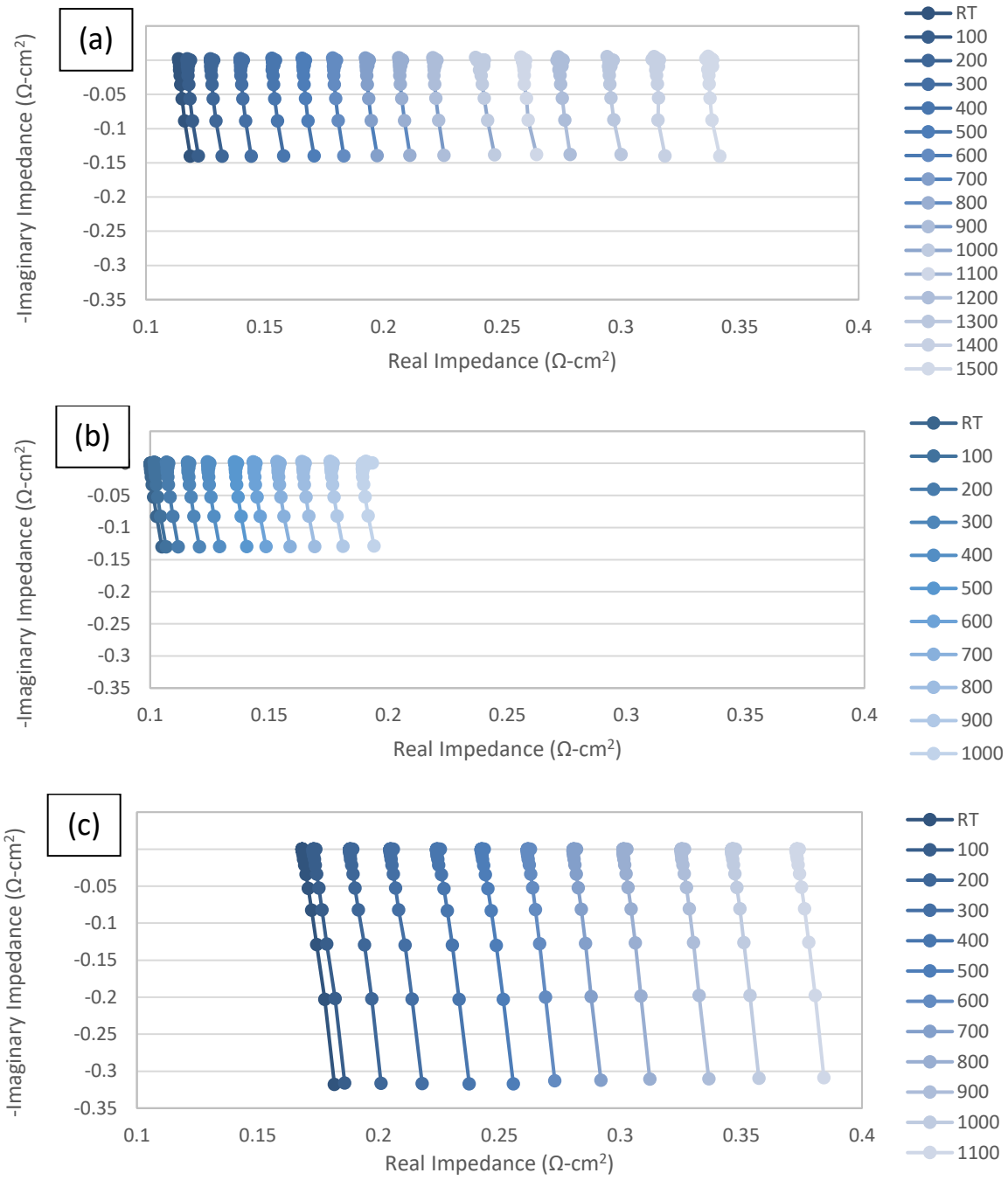

Figure 4.S15: Nyquist plots for the electrical conductivity samples in Figure 4.12. (a) Sample AB, (b) anodized sample AB, (c) sample ABL. The x and y scales have been equalized for all samples to easily compare.

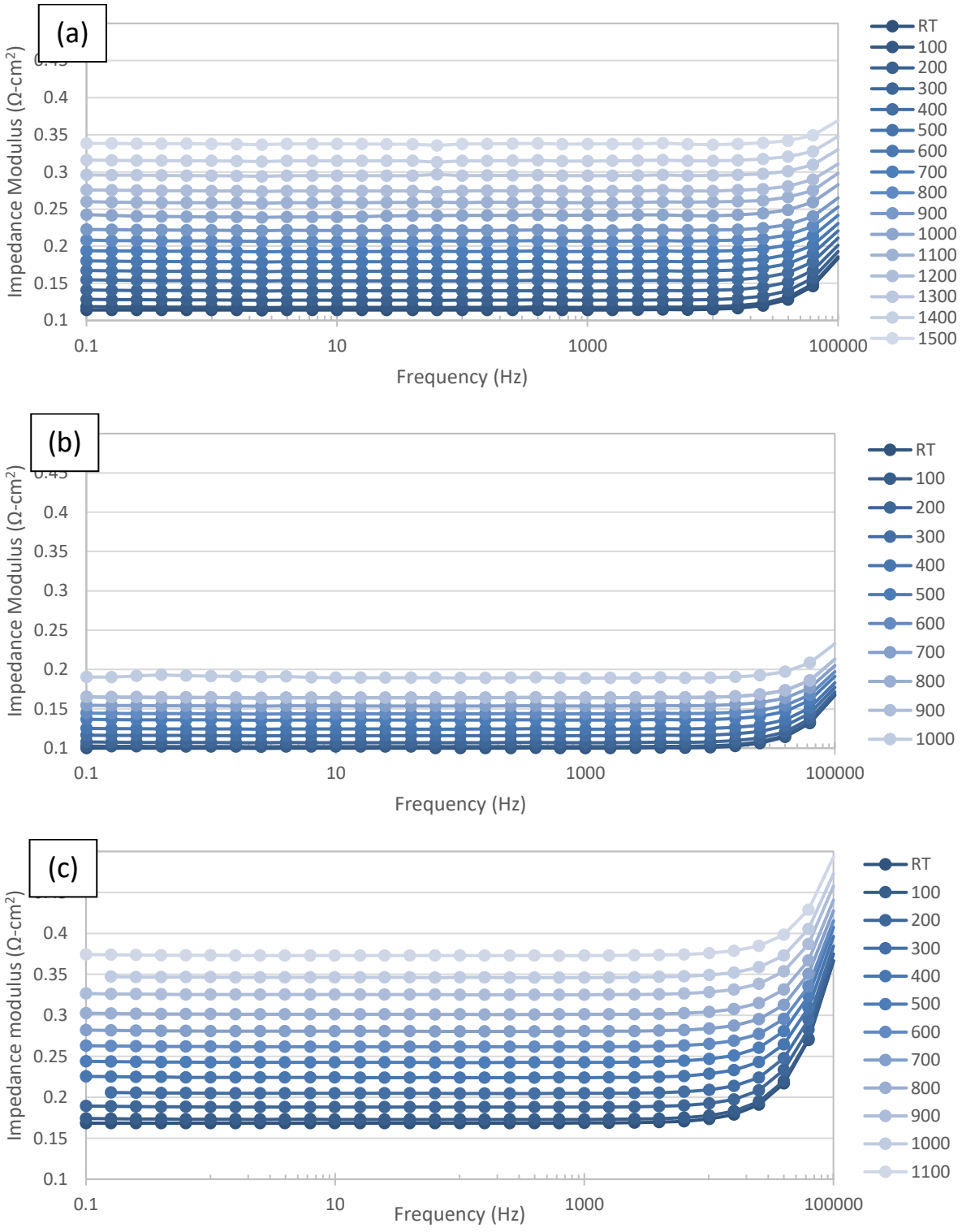

Figure 4.S16: Bode plots for the electrical conductivity samples in Figure 4.12. (a) Sample AB, (b) anodized sample AB, (c) sample ABL. The x and y scales have been equalized for all samples to easily compare.

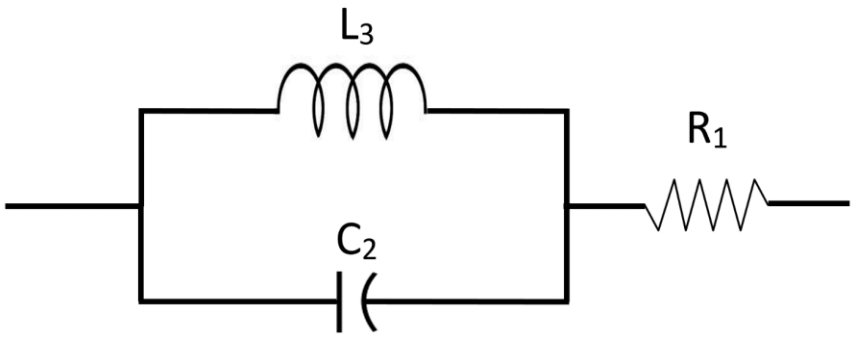

Figure 4.S17: Electrical equivalent circuit used to fit the EIS data, the results of which are found in Tables 4.5-4.7.

APPENDIX D: Supporting Information for Chapter 5

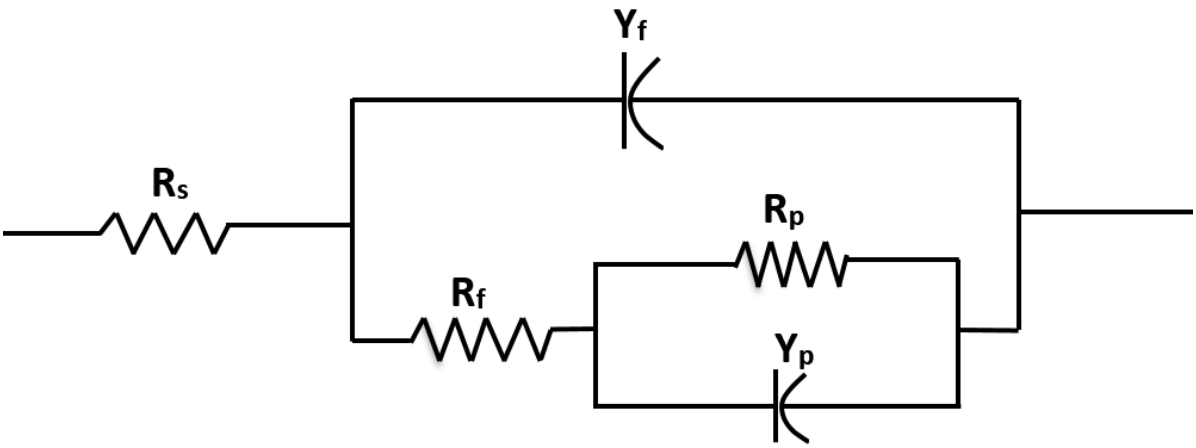

Figure 5.S1: Porous film equivalent circuit model used for fitting EIS data in Table 5.S4, 5.S5 and 5.S6.

The Density Functional Theory (DFT) calculations of HfB_2-ZrB_2 solid solutions found in Figures 5.S2-5.S4 were performed under the framework of DFT as implemented in the CASTEP module of Materials Studio® package. Initially, the geometry of the unit cell was optimized using Generalized Gradient Approximation (GGA) using Perdew-Burke-Ernzerhof (PBE) functional. The wave functions are expanded in a plane-wave basis set with an energy cutoff of 420 eV. The k-points in the Brillouin zone (BZ) of the primitive unit cell were sampled on a 12 x 12 x 12 mesh. The geometry was optimized for the convergence tolerance of energy = 0.5 x 10^{-6} eV/atom, Eigen energy convergence tolerance: 0.125 x 10^{-6} eV, Gaussian smearing scheme with a smearing width of 0.1 eV, and Fermi energy convergence tolerance of 0.125 x 10^{-7} eV. Electron–ion interactions were described by the norm-conserving pseudopotentials. 2 x 2 x 2 super cells were considered when introducing boron vacancies by deleting boron atoms.

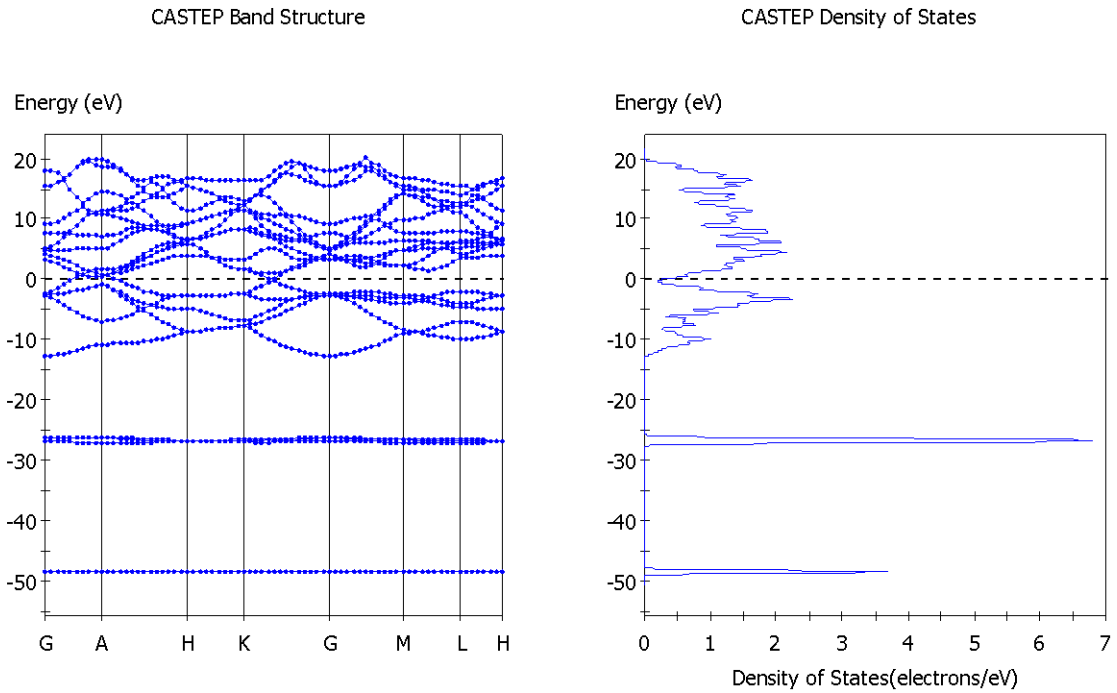

Figure 5.S2: (a) Band structure data of HfB_2 and (b) DOS of a unit cell of HfB_2.

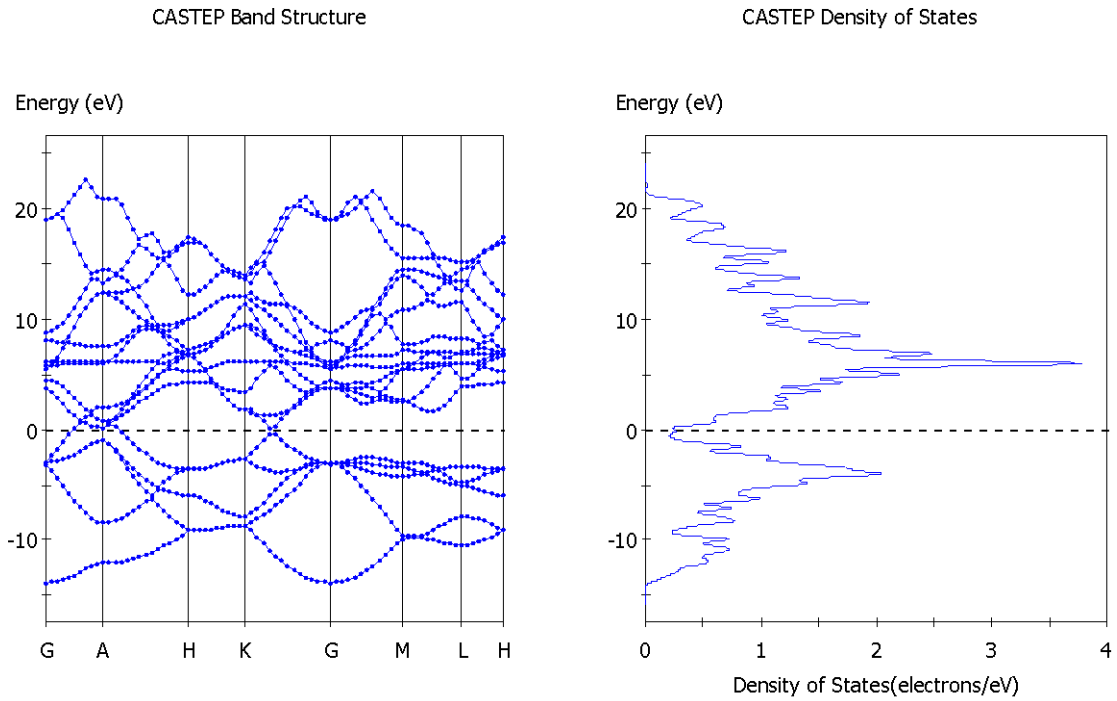

Figure 5.S3: (a) Band structure data of ZrB_2 and (b) DOS of a unit cell of ZrB_2.

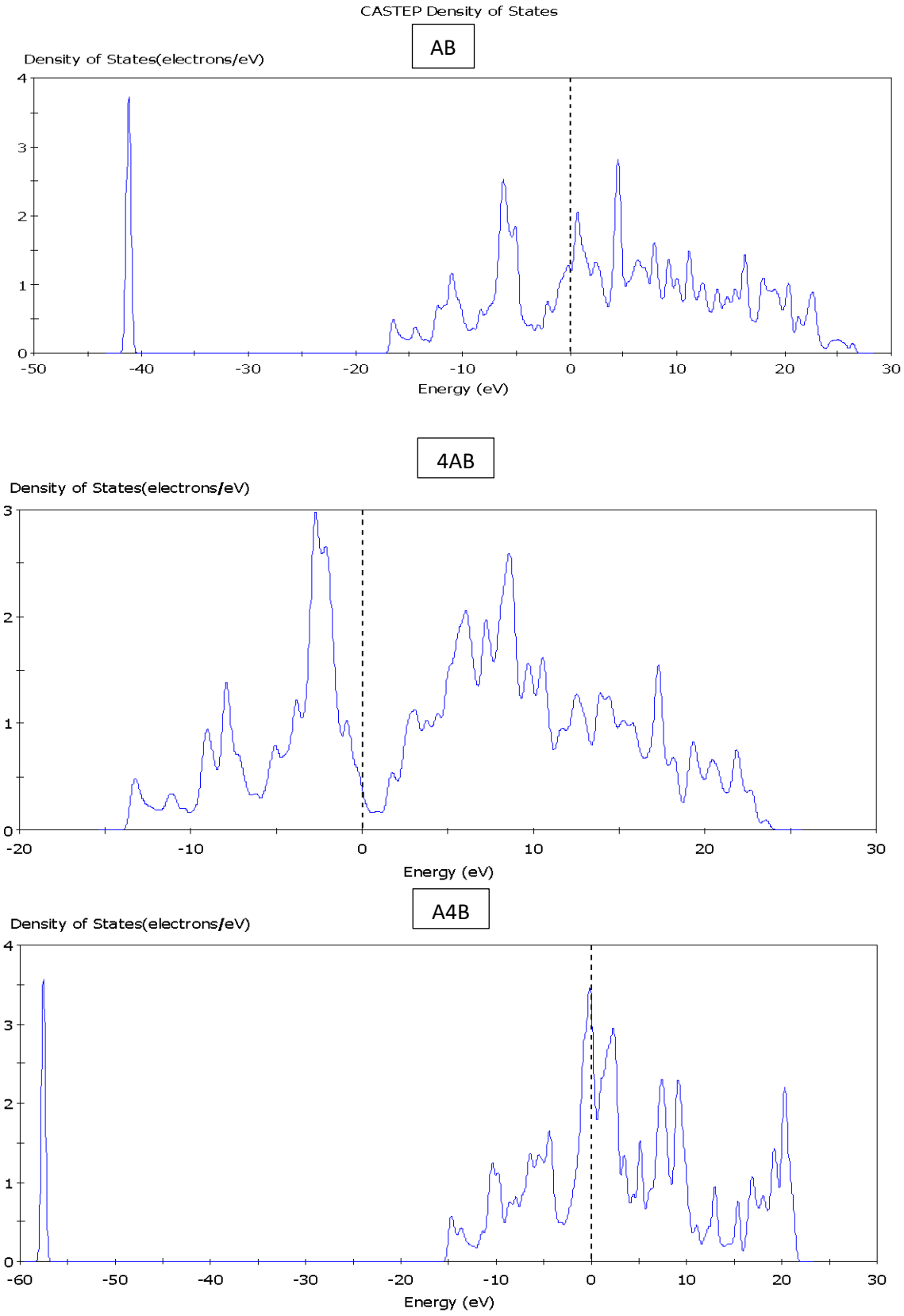

Figure 5.S4: DOS of a unit cell of (a) AB (b) 4AB and (c) A4B.

Table 5.S1: Lattice parameters calculated from the XRD results.

Identifier	*a (nm)*	*c (nm)*	*Cell Volume (nm³)*
A	0.313250	0.346146	0.029415
B	0.315917	0.351421	0.030372
AB	0.314642	0.348757	0.029901
4AB	0.315361	0.350250	0.030166
A4B	0.313929	0.347482	0.029657

Table 5.S2: Summary of HER behavior of the HfB_2-ZrB_2 solid solutions.

	1 M H_2SO_4			*1 M NaOH*		
Sample	Tafel slope, b mV/decade	Exchange current density, I_o mA/cm²	Over-potential, η at 10 mA/cm² V	Tafel slope, b mV/decade	Exchange current density, I_o mA/cm²	Over-potential, η at 10 mA/cm² V
A	380	5.0×10^{-2}	>1.0	100	2.0×10^{-4}	0.54
B	180	2.2×10^{-3}	0.69	270	3.5×10^{-2}	0.65
AB	150	1.1×10^{-3}	0.59	120	5.0×10^{-3}	0.42
4AB	150	2.5×10^{-3}	0.55	260	5.0×10^{-2}	0.61
A4B	160	7.0×10^{-4}	0.73	180	1.1×10^{-4}	0.90

Table 5.S3: EIS data fitted into a porous film equivalent circuit model 1 M H_2SO_4 at -0.6 V_{RHE}.

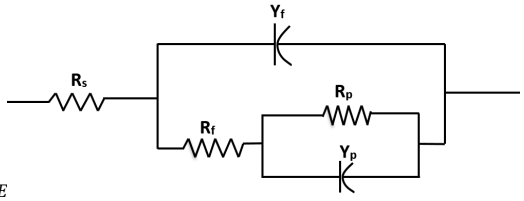

Equivalent Circuit Model for 1 M H_2SO_4 at -0.6 V_{RHE}

Sample	R_s (Ohm)	R_p (Ohm)	R_f (Ohm)	Y_p ($S \bullet s^n$)	n	Y_f ($S \bullet s^m$)	m	Goodness of fitting (χ^2)
A	266×10^{-9}	230	597.5	233×10^{-6}	0.65	4.23×10^{-9}	0.935	0.3×10^{-6}
B	3.144	8.6	4.425	331×10^{-6}	0.78	121×10^{-6}	0.727	8.1×10^{-3}
AB	43.84	27.07	3.3×10^{-9}	6.44×10^{-3}	1.00	374×10^{-6}	0.814	0.1×10^{-6}
4AB	2.054	0.442	0.849	608×10^{-6}	0.92	27.8×10^{-6}	1.000	2.5×10^{-3}
A4B	1.094	7.138	16.94	1.02×10^{-3}	0.75	30.6×10^{-6}	0.600	0.6×10^{-6}

Table 5.S4: EIS data fitted into a porous film equivalent circuit model 1 M NaOH at -0.2 V_{RHE}.

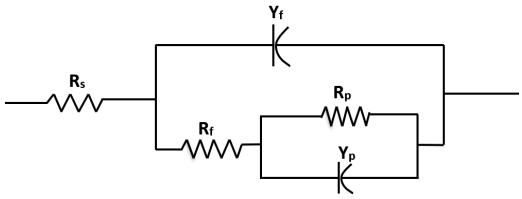

Equivalent Circuit Model for 1 M NaOH at -0.2 V_{RHE}

Sample	R_s (Ohm)	R_p (Ohm)	R_f (Ohm)	Y_p ($S \bullet s^n$)	n	Y_f ($S \bullet s^m$)	m	Goodness of fitting (χ^2)
A	13.08	74 x 10^6	1030	8.6 x 10^{-3}	0.641	129 x 10^{-6}	0.800	4.1 x 10^{-3}
B	5.862	118.3	170	1.38 x 10^{-3}	1.000	1.11 x 10^{-3}	0.600	0.9 x 10^{-3}
4AB	4.991	4.8 x 10^3	386	44.54	1.000	0.8 x 10^{-3}	0.635	4 x 10^{-3}

Table 5.S5: EIS data fitted into a porous film equivalent circuit model 1 M NaOH at -0.5 V_{RHE}.

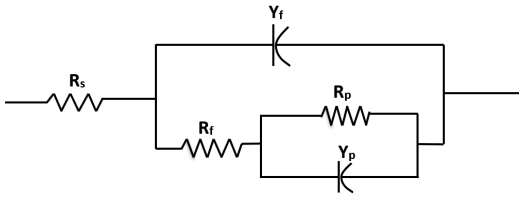

Equivalent Circuit Model for 1 M NaOH at -0.5 V_{RHE}

Sample	R_s (Ohm)	R_p (Ohm)	R_f (Ohm)	Y_p ($S \bullet s^n$)	n	Y_f ($S \bullet s^m$)	m	Goodness of fitting (χ^2)
A	13.55	1.419	6.633	1.021	0.976	21.5 x 10^{-6}	0.987	0.5 x 10^{-3}
B	5.796	1190	16.22	119 x 10^3	0.630	452 x 10^{-6}	0.657	0.7 x 10^{-3}
AB	161.5	103.4	59.68	39.93 x 10^{-3}	1.000	827 x 10^{-6}	0.641	8.2 x 10^{-3}
4AB	5.034	12.01	4.168	47.26 x 10^{-6}	1.000	14.87 x 10^{-6}	1.000	130 x 10^{-3}
A4B	6.228	86.72	8.151	332 x 10^{-6}	0.814	51.5 x 10^{-6}	0.660	59 x 10^{-3}

Table 5.S6: DFT geometrically optimized lattice parameters of HfB_2-ZrB_2 solid solutions.

Sample	*a (Å)*	*c (Å)*	*Cell Volume (nm^3)*
AB	3.036005	3.10019	0.024747
4AB	3.168500	3.49560	0.030392
A4B	2.705589	3.67493	0.023297

APPENDIX E: Supporting Information for Chapter 6

Table 6.S1: EIS data fitted into a porous film equivalent circuit model 1 M H_2SO_4 at -0.6 V_{RHE}.

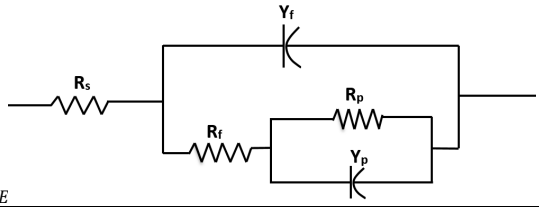

Equivalent Circuit Model for 1 M H_2SO_4 at -0.6 V_{RHE}

Sample	R_s (Ohm)	R_p (Ohm)	R_f (Ohm)	Y_p ($S \bullet s^n$)	n	Y_f ($S \bullet s^m$)	m	Goodness of fitting (x^2)
AB	43.84	27.07	3.3×10^{-9}	6.44×10^{-3}	1.000	374×10^{-6}	0.814	0.1×10^{-6}
ABG	5.08	3.192	1.501	543×10^{-6}	0.876	137×10^{-6}	0.907	1.2×10^{-3}
ABH	2.00	0.448	0.473	3.88×10^{-3}	0.806	81.5×10^{-6}	1.00	3.1×10^{-3}
ABL	3.678	7.1×10^{-3}	4.350	30×10^{-3}	1.000	364×10^{-6}	0.719	2.1×10^{-3}
ABT	2.628	257	65	118×10^{-6}	0.543	3.8×10^{-6}	0.836	188×10^{-6}

Table 6.S2: EIS data fitted into a porous film equivalent circuit model 1 M NaOH at -0.2 V_{RHE}.

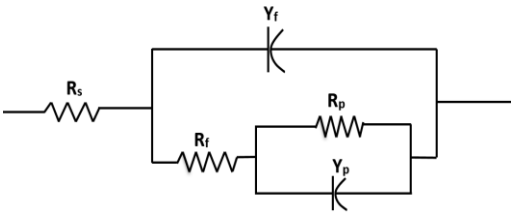

Equivalent Circuit Model for 1 M NaOH at -0.2 V_{RHE}

Sample	R_s (Ohm)	R_p (Ohm)	R_f (Ohm)	Y_p ($S \bullet s^n$)	n	Y_f ($S \bullet s^m$)	m	Goodness of fitting (x^2)
ABG	25.89	49.8(adsop)	27.88	632×10^{-6}	0.960	329×10^{-6}	0.823	6×10^{-3}
ABH	4.460	7.954	5.723	3.396×10^{-3}	0.826	1.42×10^{-3}	0.670	1.2×10^{-3}
ABL	4.716	14.47×10^{-3}	1120	72×10^{-3}	0.449	146×10^{-6}	0.798	9.9×10^{-3}
ABT	6.959	10.26	2.06	6.7×10^{-3}	0.588	1.3×10^{-3}	0.551	0.4×10^{-3}
ABZ	4.677	326.4	15.21	31.2×10^{-3}	1.000	4.14×10^{-3}	0.554	1.7×10^{-3}

Table 6.S3: EIS data fitted into a porous film equivalent circuit model 1 M NaOH at -0.5 V_{RHE}.

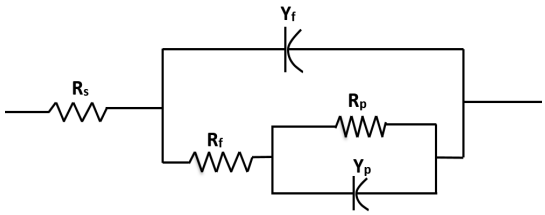

Equivalent Circuit Model for 1 M NaOH at -0.5 V_{RHE}

Sample	R_s (Ohm)	R_p (Ohm)	R_f (Ohm)	Y_p ($S \bullet s^n$)	n	Y_f ($S \bullet s^m$)	m	Goodness of fitting (x^2)
AB	161.5	103.4	59.68	39.93×10^{-3}	1.000	827×10^{-6}	0.641	8.2×10^{-3}
ABG	25.89	3.301	12.56	174.5×10^{-6}	1.000	272×10^{-6}	0.773	1.2×10^{-3}
ABH	4.614	1.732	1.346	803×10^{-6}	0.800	34.5×10^{-6}	0.957	2.5×10^{-3}
ABL	4.872	1.726	7.84	12.3×10^{-3}	0.128	70.3×10^{-6}	0.834	284×10^{-6}
ABT	7.344	4.754	1.590	2.53×10^{-3}	0.662	396×10^{-6}	0.644	0.3×10^{-3}
ABZ	4.998	4.200	2.101	555×10^{-6}	0.864	150×10^{-6}	0.823	1.6×10^{-3}

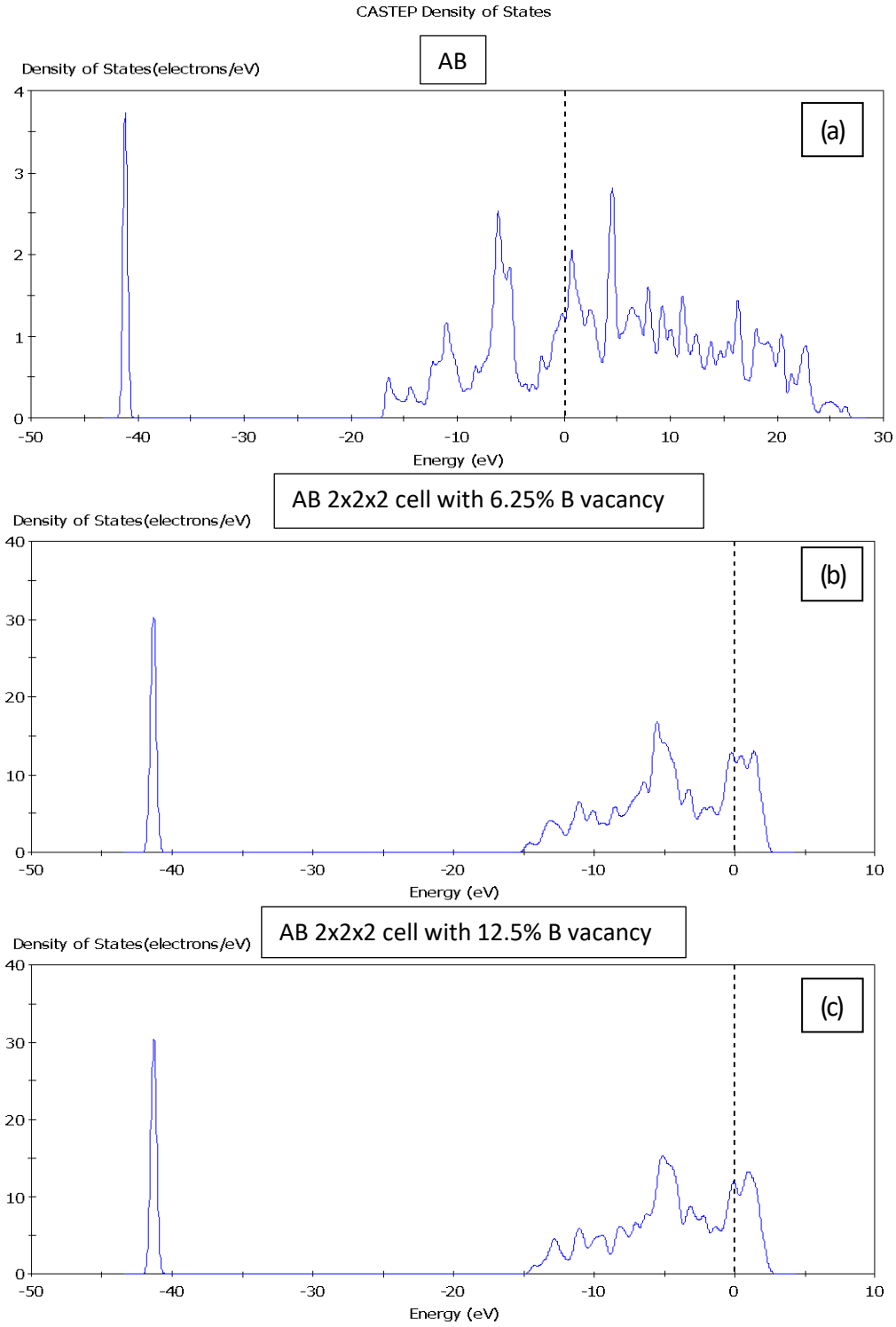

Figure 6.S1: Calculated DOS of AB (a) unit formula cell of AB without boron vacancies (b) 2 x 2 x 2 super cell of AB with 6.25 % boron vacancy and (c) 2 x 2 x 2 super cell of AB with 12.5 % boron vacancy.

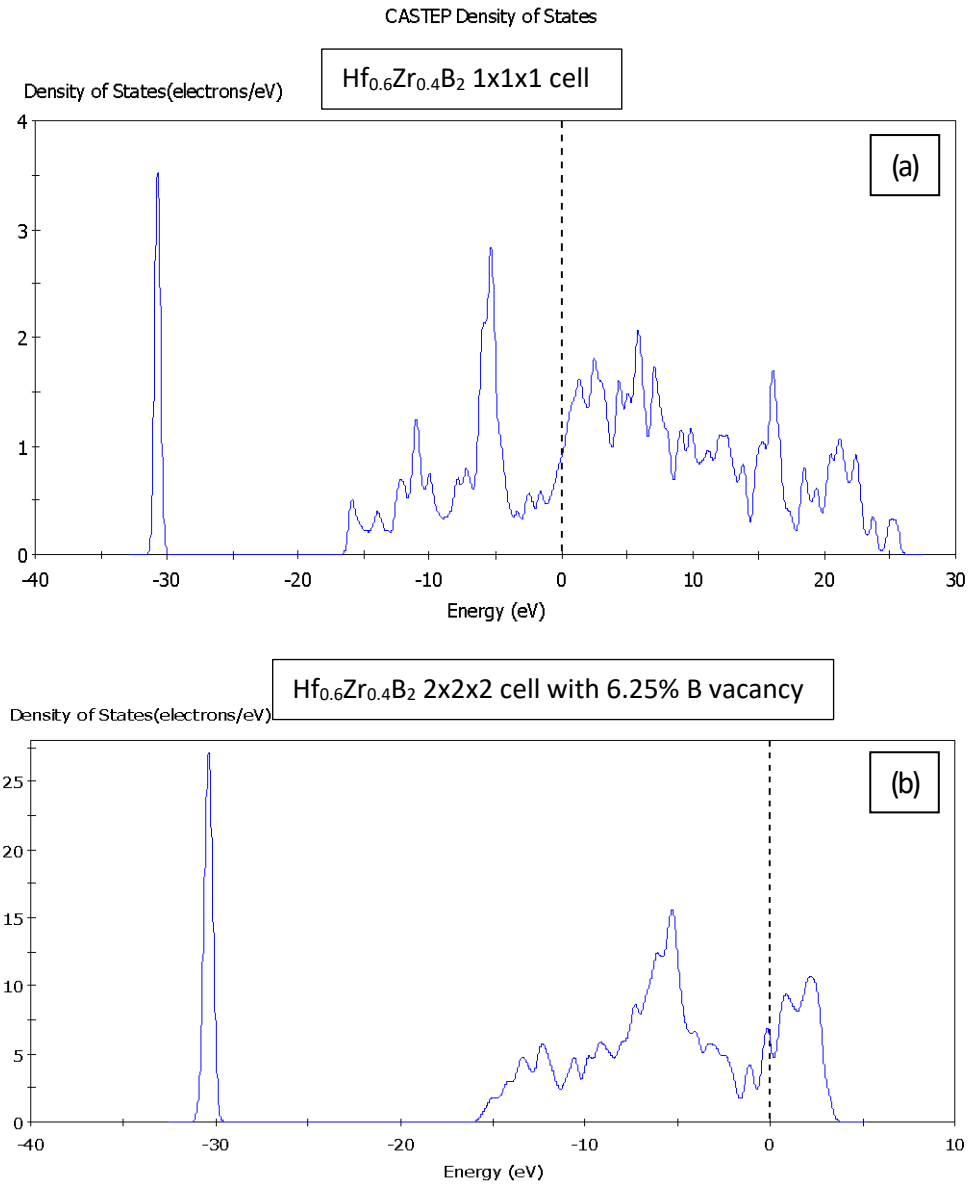

Figure 6.S2: Calculated DOS of $Hf_{0.6}Zr_{0.4}B_2$ (3A2B) (a) unit formula cell of 3A2B without boron vacancies and (b) 2 x 2 x 2 supercell of 3A2B with 6.25 % boron vacancy (simulating ABH condition).

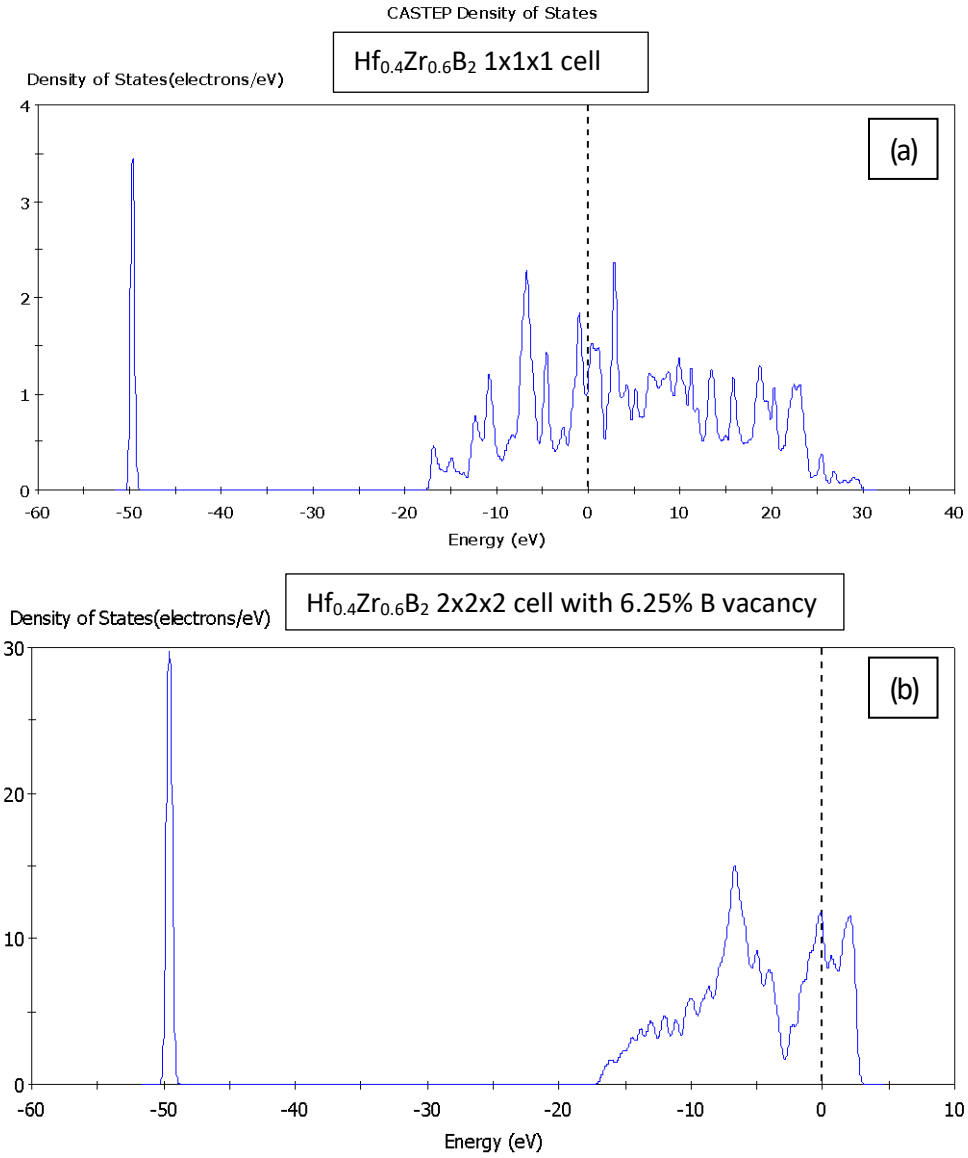

Figure 6.S3: Calculated DOS of $Hf_{0.4}Zr_{0.3}B_2$ (2A3B) (a) unit formula cell of 2A3B without boron vacancies and (b) 2 x 2 x 2 supercell of 2A3B with 6.25 % boron vacancy (simulating ABZ condition).

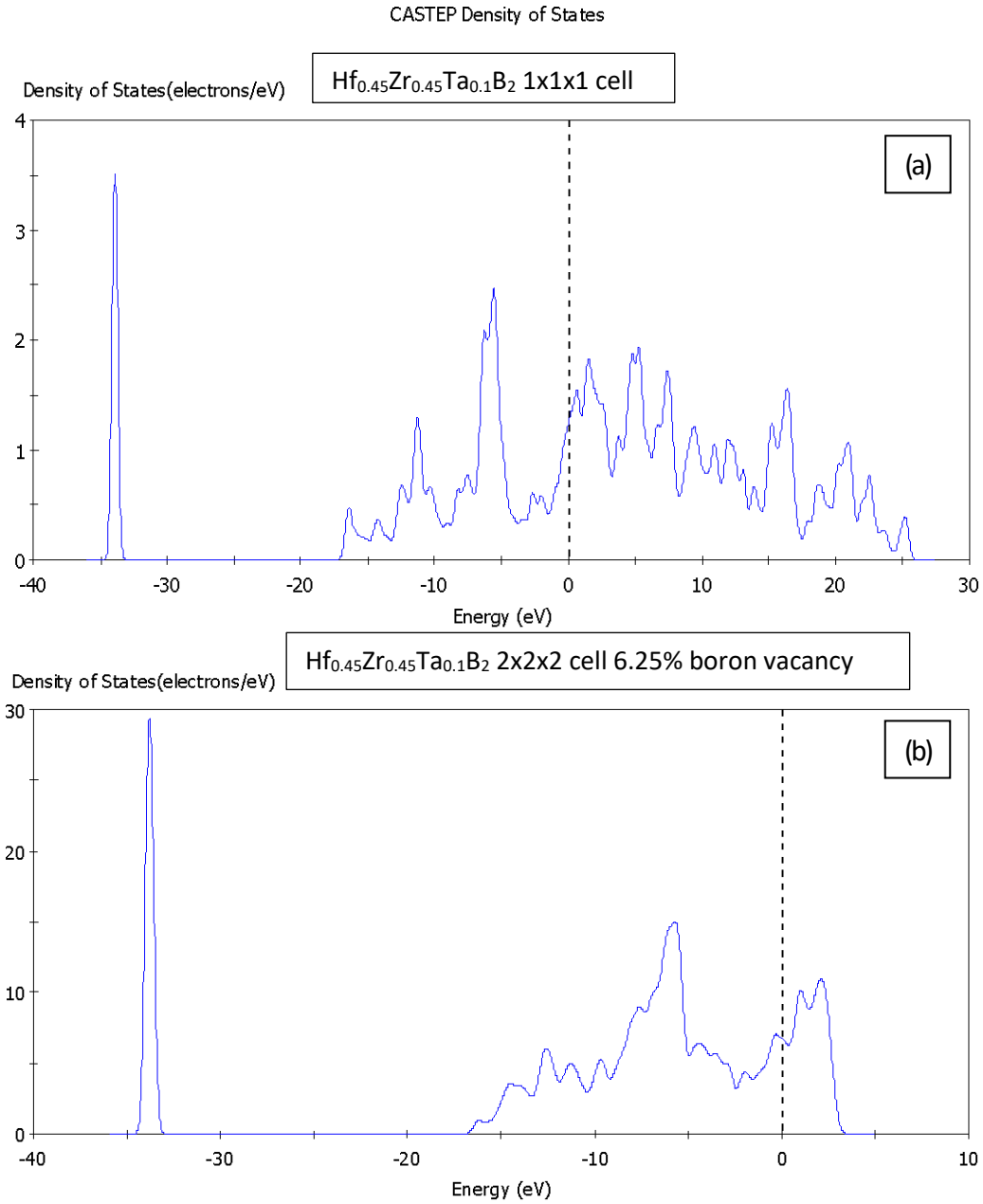

Figure 6.S4: Calculated DOS of $Hf_{0.45}Zr_{0.45}Ta_{0.1}B_2$ (ABT) (a) unit formula cell of ABT without boron vacancies and (b) 2 x 2 x 2 supercell of ABT with 6.25 % boron vacancy (simulating ABT condition).

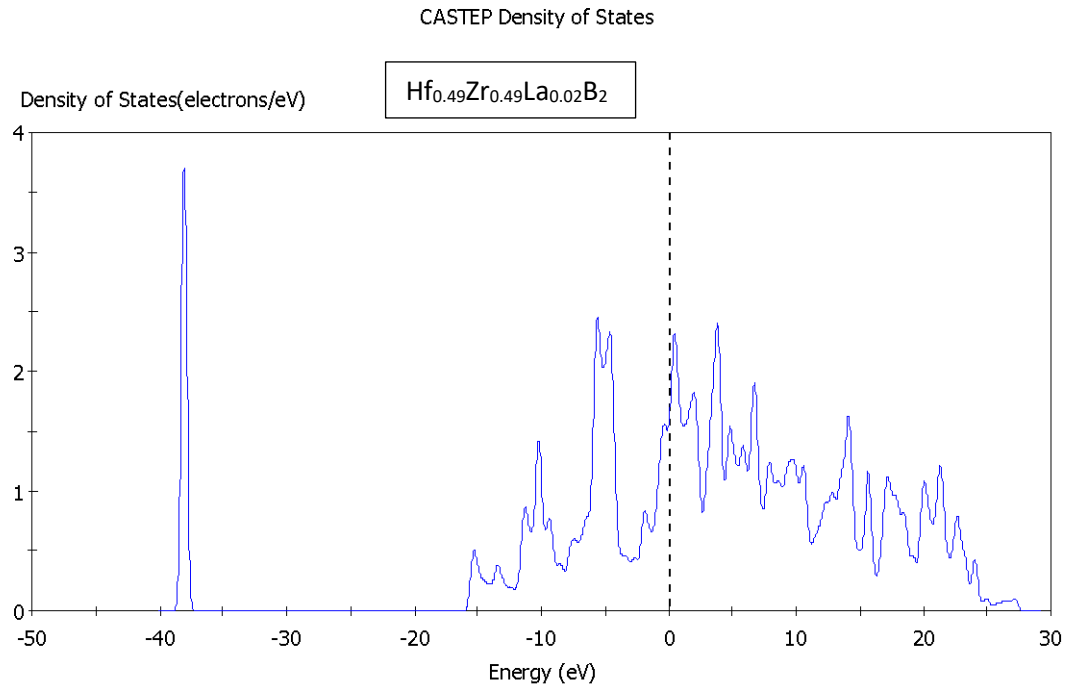

Figure 6.S5: Calculated DOS of a unit formula cell of $Hf_{0.49}Zr_{0.49}La_{0.02}B_2$ (ABL) without boron vacancies.

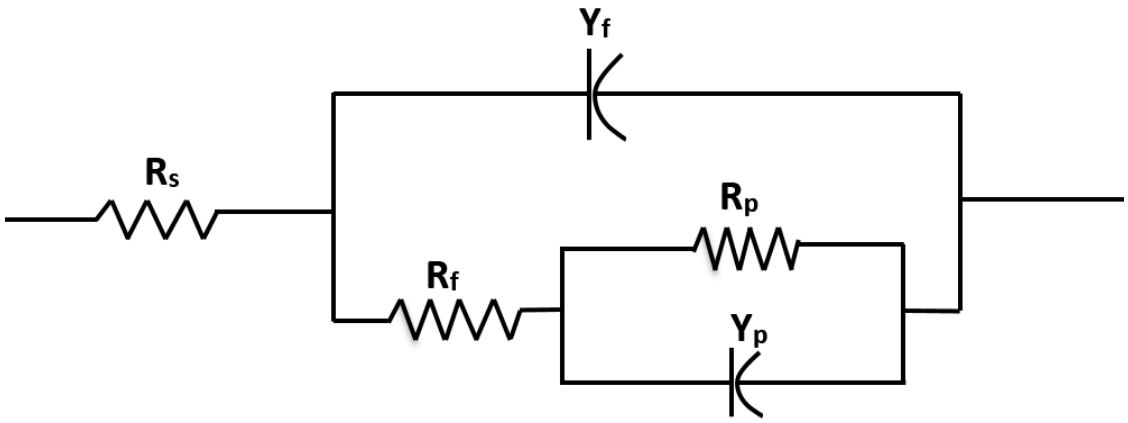

Figure 6.S6: Porous film equivalent circuit model used for fitting EIS data in Table 6.S1, 6.S2 and 6.S3.